

## **General Disclaimer**

### **One or more of the Following Statements may affect this Document**

- This document has been reproduced from the best copy furnished by the organizational source. It is being released in the interest of making available as much information as possible.
- This document may contain data, which exceeds the sheet parameters. It was furnished in this condition by the organizational source and is the best copy available.
- This document may contain tone-on-tone or color graphs, charts and/or pictures, which have been reproduced in black and white.
- This document is paginated as submitted by the original source.
- Portions of this document are not fully legible due to the historical nature of some of the material. However, it is the best reproduction available from the original submission.

(NASA-CR-144551) S-193 SCATTEROMETER  
BACKSCATTERING CROSS SECTION  
PRECISION/ACCURACY FOR SKYLAB 2 AND 3  
MISSIONS (Lockheed Electronics Co.)  
HC A11/MF A01

N77-16107

238 p  
CSCL 14B G3/19  
Unclas  
12666

S-193 SCATTEROMETER BACKSCATTERING CROSS SECTION  
PRECISION/ACCURACY FOR SKYLAB 2 AND 3 MISSIONS

(SENSOR PERFORMANCE EVALUATION  
TASK-SPE-S193-004)

Job Order 75-215



Prepared By

Lockheed Electronics Company, Inc.  
Aerospace Systems Division  
Houston, Texas

Contract NAS 9-12200

For

EARTH OBSERVATIONS DIVISION



*National Aeronautics and Space Administration*  
**LYNDON B. JOHNSON SPACE CENTER**  
*Houston, Texas*

June 1975

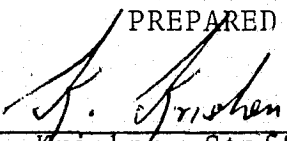
LEC-6119

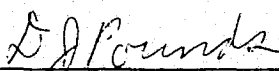
S-193 SCATTEROMETER BACKSCATTERING CROSS SECTION  
PRECISION/ACCURACY FOR SKYLAB 2 AND 3 MISSIONS

(SENSOR PERFORMANCE EVALUATION  
TASK-SPE-S193-004)

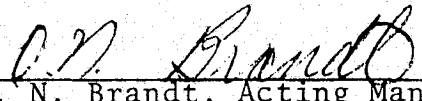
Job Order 75-215

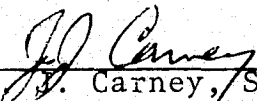
PREPARED BY

  
K. Krishen, Staff Scientist  
Earth Observations Exploratory  
Studies Department

  
D. J. Pounds, Principal Engineer  
Earth Observations Exploratory  
Studies Department

APPROVED BY

  
O. N. Brandt, Acting Manager  
Earth Observations Exploratory  
Studies Department

  
J. J. Carney, Supervisor  
Exploratory Investigations  
Section

Prepared By

Lockheed Electronics Company, Inc.

For

Earth Observations Division

NATIONAL AERONAUTICS AND SPACE ADMINISTRATION  
LYNDON B. JOHNSON SPACE CENTER  
HOUSTON, TEXAS

June 1975

LEC-6119

## ACKNOWLEDGMENTS

This document was prepared by Lockheed Electronics Company, Inc., Aerospace Systems Division, under Contract NAS 9-12200, Job Order 75-215 and was issued at the Johnson Space Center, Houston, Texas, in accordance with Job Order 63-0757-5215-19. Acknowledgment is made to Dr. K. Krishen and D. J. Pounds of Lockheed Electronics Company, Inc., for preparing this report. Acknowledgment is also made to Ken Eckel for computer programming support.



## ABSTRACT

The NASA Skylab Sensor Performance Evaluation task SPE-S193-004 is concerned with estimating the precision and accuracy with which the S-193 Scatterometer measured the backscattering cross section of ground scenes. These estimates were derived from data collected during Skylab missions. For this study, homogeneous ground sites were selected and S-193 Scatterometer backscattering cross section data analyzed. The precision was expressed as the standard deviation of the scatterometer-acquired backscattering cross section. In special cases, inference of the precision of measurement was made by considering the total range from the maximum to minimum of the backscatter measurements within a data segment, rather than the standard deviation. For Skylab missions 2 and 3 a precision better than 1.5 dB is indicated.

The indication of the measurement accuracy was derived from various comparisons. A theoretical scattering formula, most suitable to the surface model, was selected. Ground parameters were used to evaluate the theoretical values of backscattered cross sections of homogeneous sites. Aircraft-acquired backscattering cross sections were analyzed to verify and supplement the theoretical values. Through this tedious procedure, the most appropriate set of backscattering cross sections was generated for certain sites. As a final step, the differences between the actual measured values and those developed using aircraft-acquired data together with mathematical scattering models were computed. These differences were indicative of the accuracy of measurement.

This procedure indicates an accuracy of better than 3 dB for the Skylab 2 and 3 missions. The estimates of precision and accuracy given in this report are for backscattering cross sections from -28 to 18 dB. Outside this range the precision and accuracy decrease significantly.

# CONTENTS

Section	Page
ABSTRACT. . . . .	iv
1.0 <u>INTRODUCTION</u> . . . . .	1-1
2.0 <u>GROUND DATA USED FOR COMPARISON WITH S-193 SCATTEROMETER MEASUREMENTS</u> . . . . .	2-1
2.1 SKYLAB-ACQUIRED DATA . . . . .	2-3
2.2 AIRCRAFT-ACQUIRED DATA . . . . .	2-4
2.3 DATA ACQUISITION WITH GROUND-BASED SYSTEMS. . . . .	2-5
3.0 <u>THEORETICAL MODELS FOR RADAR CROSS SECTIONS FOR TERRESTRIAL SURFACES</u> . . . . .	3-1
3.1 SEMIEMPIRICAL MODELS . . . . .	3-2
3.2 GEOMETRICAL MODELS . . . . .	3-3
3.3 STATISTICAL MODELS . . . . .	3-3
3.4 APPLICABLE THEORY TO SCATTERING FROM SPE LAND AND OCEAN SITES . . . . .	3-7
3.4.1 Radar Scattering Theories . . . . .	3-8
3.4.2 Radar Return from the Sea - A Qualitative Approach. . . . .	3-19
3.4.3 Oceanic S-193 Targets - Applicable Theories . . . . .	3-25
4.0 <u>ATMOSPHERIC LOSSES</u> . . . . .	4-1
5.0 <u>S-193 SCATTEROMETER BACKSCATTER DATA ANALYSIS</u> . . . . .	5-1
5.1 LOW $\sigma_o$ DATA. . . . .	5-1
5.2 OCEAN $\sigma_o$ DATA. . . . .	5-13
5.2.1 EREP Pass 5, Gulf of Mexico . . . . .	5-13
5.2.2 EREP Pass 8, Gulf of Mexico . . . . .	5-27

Section	Page
5.2.3 EREP Passes 11 and 20, Gulf of Mexico . . . . .	5-32
5.2.4 Other $\sigma_0$ Data Over the Gulf of Mexico and Atlantic . . . . .	5-42
5.2.4.1 <u>EREP pass 13, Gulf of Mexico</u> . . . . .	5-42
5.2.4.2 <u>EREP pass 16, Gulf of Mexico</u> . . . . .	5-42
5.2.4.3 <u>EREP pass 7, Atlantic</u> . . . . .	5-44
5.3 LAND $\sigma_0$ DATA . . . . .	5-44
5.3.1 Great Salt Lake Desert Scatterometer Data . . . . .	5-46
5.3.1.1 <u>EREP pass 5</u> . . . . .	5-46
5.3.1.2 <u>EREP pass 12</u> . . . . .	5-54
5.3.2 Other Land Sites . . . . .	5-58
5.3.2.1 <u>Tennessee/Indiana, EREP pass 7</u> . . . . .	5-58
5.3.2.2 <u>Colorado/Kansas, EREP pass 13</u> . . . . .	5-58
5.3.2.3 <u>Kansas, EREP pass 15</u> . . . . .	5-59
6.0 <u>PRECISION/ACCURACY ESTIMATES</u> . . . . .	6-1
6.1 PRECISION ESTIMATES . . . . .	6-1
6.2 ACCURACY ESTIMATES . . . . .	6-10
6.2.1 Comparison of S-193 $\sigma_0$ Data with Other Experimental Data . . . . .	6-10
6.2.2 Comparison of S-193 $\sigma_0$ Data with Theoretical Results . . . . .	6-16
6.3 COMPARISON OF S-193 SCATTEROMETER PREFLIGHT PERFORMANCE AND PRECISION/ACCURACY ESTIMATES . . . . .	6-24

Section		Page
7.0	<u>CONCLUSIONS</u> . . . . .	7-1
8.0	<u>REFERENCES</u> . . . . .	8-1

## Appendix

A	THE S-193 SCATTEROMETER SENSOR BACKGROUND AND MATHEMATICAL MODEL . . . . .	A-1
B	DATA PROCESSING TECHNIQUES . . . . .	B-1

# TABLES

Table		Page
4-I	13.9 GHz SIGNAL ATTENUATION BY CLOUDS AND RAIN. . . . .	4-8
4-II	REFLECTIVITY OF UNIFORM RAIN, METER <sup>2</sup> / METER <sup>3</sup> (N OR $\Sigma\sigma_i^{**}$ ). . . . .	4-10
5-I	SCATTEROMETER NOISE INTEGRATION TIME (REFERENCE 32). . . . .	5-3
5-II	DEEP SPACE S-193 SCATTEROMETER DATA . . . . .	5-4
5-III	$\sigma_0$ VALUES FOR $\theta \approx 52.5^\circ$ EREP AVA PASS BEYOND 18:59:16 GMT . . . . .	5-10
5-IV	OCEAN SURFACE WINDSPEEDS FOR EREP PASS 5. . . . .	5-14
5-V	SURFACE AND ATMOSPHERIC CONDITIONS FOR SL-2 TARGET SITES . . . . .	5-24
5-VI	OCEAN SURFACE WINDSPEEDS FOR EREP PASS 8. . . . .	5-33
5-VII	SURFACE AND ATMOSPHERIC CONDITIONS FOR SL-3 TARGET SITES . . . . .	5-39
6-I	PRECISION ESTIMATES FOR SKYLAB 2 AND 3 SCATTEROMETER $\sigma_0$ DATA . . . . .	6-3
6-II	COMPARISON OF THEORETICAL AND EXPERIMENTAL $\sigma_0$ DATA FOR BEST COMPUTER FIT . . . . .	6-21
A-I	NOMINAL S-193 RADIOMETER/SCATTEROMETER MODES . . . . .	A-2
A-II	SCATTEROMETER INTEGRATION TIMES . . . . .	A-10
A-III	LIST OF SCATTEROMETER PARAMETERS. . . . .	A-20
A-IV	SCATTEROMETER MATHEMATICAL MODEL SUBROUTINES . . . . .	A-25
A-V	SCATTEROMETER MATHEMATICAL MODEL COMPUTER PROGRAM. . . . .	A-31

# FIGURES

Figure		Page
3-1	Scattering from the rough surface. [C(x,y,ξ) is any point on the rough interface and P <sub>1</sub> (x', y', z') is the observation point. (B) is the far field approximation of (A).] . . . . .	3-9
3-2	Polarization dependence for backscattering from a slightly rough surface for various dielectric constants (Valenzuela, 1967). . .	3-18
3-3	Depolarized backscattering cross section per unit area for a sea with directional wave spectrum for various windspeeds (Valenzuela, 1967) . . . . .	3-18
3-4	$\sigma_0$ versus $\theta$ for the sea (general observed dependence). . . . .	3-24
3-5	Comparison of NASA/JSC 0.4 GHz data with the composite scattering theory. . . . .	3-27
3-6	Values of $\beta_0$ [ $S = \tan \beta_0$ ] as a function of windspeed . . . . .	3-28
4-1	Absorption profiles for various altitudes for water vapor concentration = 7.5 g/m <sup>3</sup> (60 percent RH at 60°F) (R. A. LeFande, 1968). . . . .	4-2
4-2	Total absorption versus frequency for paths through the atmosphere at various antenna elevation angles (water vapor concentra- tion = 7.5 g/m <sup>3</sup> ) (R. A. LeFande, 1968) . . .	4-4
4-3	Total vertical path attenuation by atmos- pheric gases (water vapor concentration = 7.5 gm/m <sup>3</sup> ) (Haroules and Brown, 1968). . . .	4-5
4-4	Theoretical rainfall attenuation versus frequency for various rain rates (R. A. LeFande, 1968) . . . . .	4-7
5-1	Effect of A/D conversion on measurement uncertainty at low signal voltages . . . . .	5-7
5-2	Skylab pitch angle variation as a function of time (EREP Ava pass) . . . . .	5-11

Figure		Page
5-3	Zero degree filter bank response curves for low center frequency (LCF), middle center frequency (MCF), and high center frequency (HCF) Doppler filters. . . . .	5-12
5-4	Location of field-of-view (FOV) for S-193 Scatterometer VV data and NOAA aircraft data for Skylab 2, EREP pass 5 (Gulf of Mexico). . . . .	5-18
5-5	Backscattering cross section as a function of $\theta$ for data set I (pass 5). . . .	5-19
5-6	Backscattering cross section as a function of $\theta$ for data set II (pass 5) . . .	5-20
5-7	Backscattering cross section as a function of $\theta$ for data set III (pass 5). . .	5-21
5-8	Backscattering cross section as a function of $\theta$ for data set IV (pass 5) . . .	5-22
5-9	Location of field-of-view (FOV) for S-193 Scatterometer VV data and NOAA aircraft data for Skylab 2 EREP pass 8 (Gulf of Mexico) . . . . .	5-28
5-10	Backscattering cross section as a function of $\theta$ for data set I (pass 8). . . .	5-29
5-11	Backscattering cross section as a function of $\theta$ for data set II (pass 8) . . .	5-30
5-12	Backscattering cross section as a function of $\theta$ for data set III (pass 8). . .	5-31
5-13	Ground track and scatterometer data locations for EREP passes 11 and 20. . . . .	5-38
5-14	Backscattering cross section as a function of $\theta$ for EREP pass 11 . . . . .	5-40
5-15	S-193 Radiometer/Scatterometer field-of-view, pass 13. . . . .	5-43



Figure		Page
5-16	S-193 Radiometer/Scatterometer field-of-view, pass 16. . . . .	5-45
5-17	Field-of-view and ground track for Great Salt Lake Desert (EREP pass 5) . . . .	5-47
5-18	$\sigma_0$ versus $\theta$ for Great Salt Lake Desert, pass 5 (I) . . . . .	5-49
5-19	$\sigma_0$ versus $\theta$ for Great Salt Lake Desert, pass 5 (II). . . . .	5-50
5-20	Height of the surface in units for a segment of GSLD laser profiler data. . . . .	5-51
5-21	Frequency versus rms amplitude for a segment of laser profiler data over GSLD . . . . .	5-52
5-22	Autocorrelation for a segment of laser profiler data over GSLD. . . . .	5-53
5-23	FOV and S-193 Radiometer antenna temperature distribution over GSLD (pass 5) . . . . .	5-55
5-24	Comparison of S-194 and S-193 Radiometric antenna temperatures (nearly vertical incidence) for GSLD . . . .	5-56
5-25	FOV and S-193 Radiometer antenna temperature distribution over GSLD (pass 12) . . . . .	5-57
6-1	Radar cross section versus relative wind-heading (NASA-LaRC) . . . . .	6-7
6-2	Precision upper bound as a function of ( $\sigma_0$ ) from table 6-I . . . . .	6-9
6-3	Comparison of 13.9 GHz radiometer/scatterometer aircraft data and S-193 Scatterometer data (HH polarization) . . . .	6-11

Figure		Page
6-4	Comparison of 13.9 GHz radiometer/ scatterometer aircraft data and S-193 Scatterometer data (VV polari- zation). . . . .	6-12
6-5	Comparison of altimeter mode 2 $\sigma_0$ data and S-193 Scatterometer data. . . . .	6-14
6-6	Comparison of 13.3 GHz aircraft and S-193-acquired Scatterometer data. . . . .	6-15
6-7	Comparison of aircraft-acquired data ( $\sigma_0$ -15 dB) at 13.3 GHz and Skylab 13.9 GHz Scatterometer data. . . . .	6-17
6-8	Comparison of theoretical results using composite model and S-193 $\sigma_0$ data. . .	6-18
6-9	Comparison of S-193 Great Salt Lake data with theoretical results and 13.3 GHz data. . . . .	6-23
A-1	Intrack noncontiguous scan (ITNC) mode ( $\vec{n}$ is the normal to the surface at point $A_1$ ). . . . .	A-1
A-2	Crosstrack noncontiguous (CTNC) mode . . . .	A-4
A-3	Intrack contiguous (ITC) mode. . . . .	A-5
A-4	Crosstrack contiguous (CTC) mode . . . . .	A-7
A-5	S-193 Scatterometer functional block diagram. . . . .	A-12
A-6	Cross-polarization model . . . . .	A-14
A-7	Loss model . . . . .	A-15
A-8	Leakage model. . . . .	A-16
A-9	VSWR model . . . . .	A-17
A-10	S-193 Scatterometer volts output versus power input for two radiometric antenna temperatures . . . . .	A-41

Figure		Page
A-11	S-193 Scatterometer volts output versus power input for two modes - CTC R/S and ITNC . . . . .	A-42
A-12	S-193 Scatterometer volts output versus power input for a difference of 15 dB between vertical and horizontal input power. . . . .	A-43
A-13	S-193 Scatterometer volts output versus power input for a difference of 5 dB between vertical and horizontal input power. . . . .	A-44
B-1	S-193 Radiometer/Scatterometer data processing flow. . . . .	B-2
B-2	S-193 Radiometer/Scatterometer output product data flow. . . . .	B-3
B-3	S-193 Scatterometer resolution cell geometry. . . . .	B-5
B-4	13.3 GHz Scatterometer resolution cell geometry. . . . .	B-22

## ABBREVIATIONS, ACRONYMS, AND SYMBOLS

A/D	Analog-to-digital
AMT	Airlock Module Time
CCT	Computer compatible tapes
CTC	Crosstrack contiguous
CTNC	Crosstrack noncontiguous
CW	Continuous wave
dB	decibel
dBm	decibels referenced to 1 milliwatt
DOY	Day of year
DSAD	Data Systems and Analysis Division
DST	Data Stream Time
EREP	Earth Resources Experiment Package
FMC	Ferrite modulator constant
FOV	Field-of-view
GHz	gigahertz
GMT	Greenwich mean time
GSLD	Great Salt Lake Desert
HCF	High center frequency
i.f.	Intermediate frequency
IRIG A	Interrange Instrumentation Group Format A
IT	Integration time
ITC	Intrack contiguous
ITNC	Intrack noncontiguous
kbps	kilobits per second

kHz	kilohertz
km	kilometer
LC	Lunar calibration
LCF	Low center frequency
LaRC	Langley Research Center
MCF	Middle center frequency
MFMR	Multifrequency Microwave Radiometer
mHz	megahertz
MMC	Martin Marietta Company
msec	millisecond
NMi	nautical mile
NOAA	National Oceanographic and Atmospheric Administration
P/A	Precision/accuracy
PCM	Pulse code modulated
RAD/SCAT	Radiometer/scatterometer
rms	root mean square
R/S	Radiometer/scatterometer
rss	root sum squared
SKYBET	Skylab Best Estimate of Trajectory
SL-2	Skylab 2
SL-3	Skylab 3
SL-4	Skylab 4
SPE	Sensor Performance Evaluation
STBY	Standby

TC	Time constant
TDA	Tunnel Diode Amplifier
A	Area of the illuminated surface
a	Radius of a circle
$\alpha_a$	Attenuation coefficient per meter
$B(\tau)$	Surface correlation function
$C_t$	Contour of the illuminated area
$C_1, C_2, n$	constant
$D_i$	Droplet diameter
$\vec{E}$	Electric field on the surface
$\vec{E}_{P_1}(x', y', z')$	Electric field at the point $(x', y', z')$ scattered by the rough surface
$\epsilon_0, \mu_0$	Free space permittivity and permeability, respectively
$\vec{E}_1, \vec{H}_1$	Incident electric and magnetic fields, respectively
$E_2^*$	Complex conjugate of the magnitude of the scattered field
$\vec{E}_2, \vec{H}_2$	Reflected electric and magnetic fields, respectively
$g/m^3$	grams per meter cube
$\vec{H}$	Magnetic field on the surface
$H_0$	Altitude of the Skylab
h	Standard deviation or root mean square height of $\xi$
$J_1$	Bessel function of the first kind
k	Propagation constant of the incident electromagnetic wave

$K_1, K_2$	Functions of the angle of incidence $\theta$
$L$	Correlation distance of the small-scale roughness
$\ell$	Correlation length for the scattering rough surface
$\lambda$	Wavelength of the radar system
$L_1, L_2$	Atmospheric losses for transmission and reception, respectively
$\vec{n}$	Local normal to the surface at C
$\omega$	Radian frequency of the radar
$P(\xi)$	Gaussian surface height distribution function
$p, q$	Radian wave numbers in x and y directions on the sea surface
$\psi$	Crosstrack angle
$ R(o) $	Magnitude of the Fresnel reflection coefficient evaluated at $\theta=0$
$\rho$	Standard deviation
$\rho_0$	Water vapor density
$R_\theta$	Distance of the radar system from the illuminated area
$S$	Total root mean square slope of the rough surface
$\Sigma$	Root mean square height of the small-scale roughness
$\sigma_i$	Backscatter cross section of the $i$ th scatter
$\sigma_o$	Radar backscattering cross section of a target/site
$S_x, S_y$	Surface root mean square slopes in the x and y directions, respectively

$S_1$	Illuminated surface
$T$	Extent of the illuminated surface
$\tau$	Point on the surface $[(\Delta x)^2 + (\Delta y)^2]^{1/2}$ distance away from the point $(x,y)$
$\theta$	Angle of incidence in degrees
$V$	Ocean surface wind velocity
$V_A$	Aircraft ground velocity
$W(t)$	Sea surface roughness spectral density
$\xi$ or $\xi(x,y)$	Height from mean planar surface
$Z_R$	Reflectivity parameter associated with scatter from rain



## 1.0 INTRODUCTION

The goal of this investigation is to provide a statistically based estimate of the precision and accuracy with which the S-193 Scatterometer measured the scattering cross sections of the ground scenes.

The term precision is used to imply repeatability of data from sample-to-sample with no regard to the bias between the true value and the measured value of the scattering cross section. Thus, precision is of significance to investigators who are interested in differences between scattering cross sections for various ground scenes. The term accuracy, on the other hand, is used to imply a measure of the bias errors, plus the repeatability. The accuracy estimate is of importance to investigators who utilize the absolute value of the scattering cross sections for correlations with a phenomenon of interest.

The classical method for determining precision/accuracy would be to subject the system to a known environment and compare its output to a known standard. Additionally, an error analysis would be performed to place an upper bound on the measurement error of the system. However, accurate standard instruments are not available for S-193 Scatterometer data comparison. Original test data is also sometimes inadequate for placing the necessary bounds on the system parameters required for the classical analysis. This is due to the difficulty of knowing (and being able to simulate) the exact thermal environment that the S-193 Scatterometer experienced during the Skylab data-gathering missions.

Therefore, the estimates contained herein of the precision/accuracy of the scatterometer system, for the actual data-gathering periods, were based on the sensor analysis and comparisons of the actual S-193-acquired data with values of the backscattering cross sections obtained by aircraft sensors and the cross sections computed by analytical methods (using actual ground data).

The sensor specification control documents were studied to arrive at the latest configuration of the scatterometer system. The system performance has been summarized in appendix A. The realized antenna performance is also noted in this appendix. The relationship between input power to the antenna and the system output recorded on the tape was obtained by simulating the elements of the scatterometer system on a computer. Several parameters were changed to study their influence on the output. These results have been discussed in appendix A. The sensor mathematical model and the preflight system parameters gave the baseline precision value for the scatterometer measurements.

Since the estimates of precision/accuracy are based on the analysis of processed data, it is important to have an understanding of the data processing algorithms and possible sources of error due to processing. In appendix B the review of Skylab and aircraft scatterometer data processing is presented. The processing of the S-193 Scatterometer-acquired data has been reflected in the interpretation of the precision and accuracy estimates derived from processed backscattering cross section data.

In determining precision and accuracy, the crucial step is to locate homogeneous sites. This insures that the variance caused by the variability in surface roughness, biomass cover, intervening medium properties, and surface dielectric properties is minimum. The procedure for selecting homogeneous sites involved examination of the roughness and dielectric parameters as well as the intervening medium parameters. The medium and surface parameters were either measured by ground based sensors and/or airborne systems. The aircraft-acquired photographic, microwave, and laser profiler data was used to categorize the homogeneity of the scene viewed by the S-193 Scatterometer. The Skylab-acquired S-190 photographs, S-193 Radiometer, and S-194 Radiometer data supplemented the data derived from ground and aircraft measurements. The precision was then expressed as the variance or standard deviation of the scatterometer backscatter. In special cases, inference of the precision of measurement was made by considering the total range from maximum to minimum of the backscatter measurements within a data segment, rather than the standard deviation.

The determination of the measurement accuracy was accomplished by using various comparisons, including a theoretical scattering formula most suitable to the surface model being selected. Ground parameters were used to evaluate the theoretical values of backscattered cross sections of homogeneous sites. Aircraft-acquired backscattering cross sections were analyzed to verify and supplement the theoretical values. Through this tedious procedure, the most appropriate set of backscattering cross sections was generated for each site. As a final step, the

differences between the actual measured values and those developed using aircraft-acquired data, together with mathematical scattering models, were computed. These differences were indicative of the accuracy of measurement. It should be emphasized that any accuracy determination will be pessimistic because it will not be possible to specify the upper bound in the errors involved in arriving at the mathematical scattering cross section values. This problem is compounded by the fact that data from the sources considered are gathered from various vantage points, e.g., on the ground, from aircraft, and from spacecraft.

It should be noted that data for determining precision/accuracy was gathered over the same or quite similar ground sites during Skylab 2, 3, and 4 missions. The data analysis leads to the variation of the precision/accuracy of the sensor during the period of Skylab missions. This provides a useful input to the design of future spaceborne active microwave systems: Exact determination of the precision/accuracy is not possible. The values obtained with the procedure given in this report will enable the sorting of erroneous data. In fact, a number of S-193 cross section measurement values were found invalid with this procedure. Furthermore, the investigations also revealed the reason for this invalid data.

The study presented in this report is only for the Skylab 2 and 3 missions. A precision of better than 1.5 dB and an accuracy of better than 3 dB is shown for the scatterometer backscattering cross sections.

The review of the Skylab 4 data disclosed the presence of two problems:

- (1) The scatterometer received signal decreased by approximately 24 dB throughout the mission.
- (2) The roll scan operation began to malfunction on January 9, 1974.

As a result of these anomalies, special processing procedures were implemented in the NASA production data processing program. It is anticipated that the precision/accuracy of the scatterometer will have degraded during Skylab 4 mission. However, the extent of this degradation cannot presently be defined.

## 2.0 GROUND DATA USED FOR COMPARISON WITH S-193 SCATTEROMETER MEASUREMENTS

The estimation of the precision/accuracy of the scatterometer measurement requires a detailed knowledge of the ground scene. Proper consideration was given to the acquisition of the ground data during Skylab missions. These ground data requirements were specified in the Task Implementation Plan (reference 1). The Sensor Performance Evaluation (SPE) sites were chosen so that the values of backscattering cross section obtained by measurement using ground based/aircraft systems and/or theoretically evaluated using pertinent ground parameters, could be compared with confidence with the S-193 Scatterometer measurements. In particular, the following criteria were used for the selection of SPE sites (references 1 and 2):

- The site should be relatively uniform in such parameters as surface roughness and dielectric constant for at least one resolution cell.
- The roughness range and dielectric constant of the surface should be known so that the backscattering cross section ( $\sigma_0$ ) could be computed using theoretical techniques.
- The targets should be selected so that their  $\sigma_0$ 's cover the dynamic range of S-193 Scatterometer. For this, the high, medium, low, and no reflectivity sites were chosen.
- The scenes over which data was previously collected were preferred over those for which no  $\sigma_0$  data has been reported in the literature.

- Sites for which simultaneous data was gathered using S-190A, S-193 Radiometer, and S-194 Radiometer sensors were preferred to ones where these sensors were not operated.
- To reduce the effect of errors involved in computing exact attenuation because of heavy clouds and rain, no rain and cloud cover under 50 percent were specified as unique (mandatory) test conditions.

The SPE site criteria were satisfied by choosing ocean targets (high, medium, and low seas) and relatively smooth uniform ground targets (Great Salt Lake Desert and White Sands, New Mexico). Deep space was chosen to give the no reflectivity condition.

Detailed ground data requirements were stated in the S-193 Quick-Look II Plan (reference 3). Subsequently, these requirements were revised to reflect available resources for the SPE ground truth effort. In this section, a description of the ground data which will be utilized in this report will be presented. Actual ground data will be given when S-193 Scatterometer data comparisons are illustrated. The term "ground data" is used in this report for any data (other than that acquired by S-193 Scatterometer) which will be used in determining S-193 Scatterometer backscattering cross section precision/accuracy. In general, three types of ground data have been used to classify the scene sensed by the S-193 Scatterometer. These are discussed in sections 2.1, 2.2, and 2.3.

There are several experimental results of the backscattering cross sections from ocean and ground scenes reported in the literature. Theoretical models have also been given

for scattering from these surfaces. These theoretical and experimental results have also been used to generate data for comparison with Skylab-acquired S-193 Scatterometer data.

## 2.1 SKYLAB-ACQUIRED DATA

The data from the following sensors was used to gain an understanding of the site:

- S-190A photographs
- S-193 Radiometer/Altimeter
- S-194 Radiometer

The photographs helped to verify cloud conditions, rain, and general ground features such as vegetative cover and open water bodies. The photographs will not be reproduced in this report, but the results of the review of these photos will be utilized.

The S-193 and S-194 Radiometer data has been used to verify the homogeneity of the sensed area. Additionally, these measurements were employed to calculate the reflectivity of various ground scenes.

The S-193 Altimeter can yield the backscattering cross section for the following pitch angles:  $0^\circ$ ,  $0.4^\circ$ ,  $1.3^\circ$ ,  $2.65^\circ$ ,  $7.56^\circ$ , and  $15.6^\circ$ . Where available, this data has been used for comparison with the S-193 backscattering cross sections for similar sites.



## 2.2 AIRCRAFT-ACQUIRED DATA

The aircraft sensors specified for the collection of the data were:

- Metric camera
- Laser profiler
- Litton Industries LTN-51 Navigation Computer
- 13.3 GHz Scatterometer (or 13.9 GHz Radiometer/Scatterometer)
- Multifrequency Microwave Radiometer (MFMR)

The data from metric camera, 13.3 GHz Scatterometer, 13.9 GHz Radiometer/Scatterometer, and MFMR were used similarly to that of the Skylab-acquired support data (see section 2.1). The laser profiler data was used to categorize the roughness scale of the SPE site. Roughness power densities and surface correlation functions were computed from the laser profiler data. These parameters are vital to the selection and evaluation of the theoretical models of radar backscatter from ground scenes. The Litton Industries LTN-51 system can be used to determine the surface wind velocity.

In concluding this section, it should be noted that an anomaly (very high backscatter) was found in some portion of the aircraft-acquired 13.3 GHz Scatterometer and 13.9 GHz Radiometer/Scatterometer data. However, questionable data was not used for comparisons in this report.

## 2.3 DATA ACQUISITION WITH GROUND-BASED SYSTEMS

Direct measurements of environmental and surface conditions were also made within the limitations imposed by the necessary resources available to acquire and process the data. Fortunately, extensive weather data was compiled by the Space Meteorology Group (U.S. Weather Bureau). This group is located at the Johnson Space Center and provided much of the weather information needed to plan Earth Resources Experiment Package (EREP) passes during Skylab missions. The weather maps provided by the Space Meteorology Group present gross information about the ocean surface wind-speeds, cloud cover, and extent of rain on a global scale.

The requirements for the ground-based data acquisition were as follows:

- Ocean sites
  - Radiosonde data
  - Water temperature and salinity
  - Sea state (significant wave height)
  - Sea surface wind velocity
- Land sites
  - Radiosonde data
  - General surface characteristics, including dielectric properties (from available geological information).

National Oceanographic and Atmospheric Administration (NOAA) has taken wind and wave measurements using aircraft and surface instrumentation. These measurements were not taken for Skylab 3 (SL-3) mission. All NOAA data was reviewed and only applicable data was used.

Wind and wave data was also recorded at Buccaneer Tower (by NASA/JSC, Flight Operations Division) off Galveston Island. This data was utilized in this report.

For the ground sites, previous measurements made by U.S. Geological Survey were reviewed. Ground conditions were also ascertained using photographs and laser profiler data. In certain cases the weather at the time of the Skylab overpass was verified by calling the weather bureau nearest the SPE site.

### 3.0 THEORETICAL MODELS FOR RADAR CROSS SECTIONS FOR TERRESTRIAL SURFACES

Numerous approaches have been advanced to explain scattering from rough surfaces. The mathematical models which have shown considerable promise in explaining the experimental observations have several constraints. In general, these constraints are (reference 2):

- Most models assume a rough boundary between air and a homogeneous dielectric. Thus, the subsurface nonhomogeneities are not included in the models.
- The radar wavelength is assumed much smaller than the dimensions of the radar resolution cell.
- The radar system is assumed to be sufficiently far from the resolution cell. The incident wave at the surface of the site is assumed plane. Furthermore, the reflected wave at the radar is also assumed plane.
- The rough surface is considered to have isotropic statistical properties over the radar resolution cell.
- The rough surface is considered stationary random process.
- A uniform dielectric constant is assumed over the resolution cell.
- Most models assume only two or three statistical parameters to describe the rough surface (standard deviation, mean slope, correlation distance, etc.). In practice, these parameters are rather troublesome to obtain for terrestrial surfaces.

A summary of the available methods for calculating  $\sigma_0$  for rough surfaces is given by Barrick (reference 4). The mathematical models for the computations fall in three categories:

- Semiempirical models
- Geometrical models
- Statistical models

### 3.1 SEMIEMPIRICAL MODELS

Semiempirical models offer the simplest results and require little analytical derivations. These models involve one or more arbitrary constants which are determined from an agreement between the model and the measured results. These constants must be chosen for each class of rough surfaces. The most common semiempirical models use Lambert's law:

$$\sigma_0 = C_1 \cos^2 \theta \quad (1)$$

and the generalized Lambert's law:

$$\sigma_0 = C_2 (\cos \theta)^{2n} \quad (2)$$

where  $C_1$  and  $C_2$  are constants obtained by best fitting the equations to the measured data, as is the constant  $n$ .  $\theta$  is the angle of incidence (see figure B-3, appendix B). Both of these models apply to some terrestrial surfaces that scatter very diffusely (reference 4). These laws do not apply to the sites chosen for Sensor Performance Evaluation.

### 3.2 GEOMETRICAL MODELS

Geometrical models assume a surface composed of simple shapes arranged randomly on a planar area. From the knowledge of the scattering from simple shapes and proper boundary conditions, the field scattered from these surfaces can be calculated. These models partially take into account the multiple scattering, i.e., mutual interaction among the simple shapes. The scattered field is usually easily calculable. Among the various shapes considered in the literature are bosses on a conducting plane and infinite cylinders arranged with a random spacing upon a plane sheet (references 4 and 5). Beckmann (reference 5) has calculated the scattering cross section of a rough surface by approximating the surface with infinite half-planes tilted at variable angles with respect to the horizontal plane. These planes are all arranged in one direction. Purely geometrical models will not be considered in this report because one can seriously question how accurately such a model could be applied to rough terrestrial surfaces with composite roughness.

### 3.3 STATISTICAL MODELS

The model most applicable to the surfaces selected for the S-193 Sensor Performance Evaluation is the one where the roughness is characterized by suitable statistical parameters. Statistical models for a rough surface treat the height of the surface from the mean planar surface as a random variable. The most commonly used height distribution function is the

Gaussian distribution function  $P(\xi)$  given by (reference 4):

$$P(\xi) = \frac{1}{h\sqrt{2\pi}} \exp - \left( \frac{\xi^2}{2h^2} \right) \quad (3)$$

where  $\xi$  is the height from the mean planar surface and  $h$  is the standard deviation of this height. The roughness in the horizontal direction can be described by introducing a surface correlation function. The correlation equation requires that the height of the rough surface above every point ( $x$  and  $y$ ) in the mean surface plane be multiplied by the height above a point  $\tau$  distance away, and the product be integrated over  $x$  and  $y$  and divided by the area in the mean surface plane defined by the integration limits. The limits are permitted to become infinite (reference 6).

Mathematically, the correlation function can be expressed as (reference 6).

$$B(\tau) = \lim_{T \rightarrow \infty} \frac{1}{4T^2} \int_{-T}^T \int_{-T}^T \xi(x,y) \xi(x+\Delta x, y+\Delta y) d\tau \quad (4)$$

where  $\tau = [(\Delta x)^2 + (\Delta y)^2]^{1/2}$  and  $T$  denotes the extent of the surface.

The surface correlation function has the following properties (reference 6):

- $B(0) = h^2$
- As  $\tau \rightarrow \infty$ , the statistical dependence of the height at  $(x, y)$  and the height at  $(x+\Delta x, y+\Delta y)$  will decrease, i.e.,  $\lim_{\tau \rightarrow \infty} B(\tau) = \text{mean surface height} = 0$
- $-\left. \frac{d^2 B}{d\tau^2} \right|_{\tau=0} = \text{mean square surface slope} = S^2$

The surface can be categorized in terms of the root mean square (rms) height  $h$  (for the probability density function of equation (3), the rms height is equal to the standard deviation of the surface height  $\xi$  from the mean planar surface  $\xi=0$ ). The surface for which  $h \ll \lambda$  ( $\lambda$  is the wavelength of the radar system) is called "slightly rough." "Very rough" surfaces have  $h \gg \lambda$ .

Slightly rough surface scattering can be treated mathematically by using perturbation techniques, whereas for the very rough surface, the analysis involves an asymptotic method. Presently, no mathematical methods have been developed for the surface where  $h$  is of the order of a wavelength.

The choice of a correlation function for terrestrial surfaces has been a source of considerable controversy in the published literature on the subject of radar scattering (reference 2). Experimental determination of  $B(\tau)$  is cumbersome since it requires the knowledge of the surface



profile. Laser profiler data was requested as part of the ground data for the SPE sites. The laser data can be processed to yield the correlation function and the surface height distribution function. This is what was done.

For the theoretical investigations correlation functions are usually chosen on two bases — first to allow complicated integrations to be carried out in the analysis and second to yield a best fit between theoretical and experimental values of the  $\sigma_0$  versus  $\theta$  curve. One widely used correlation function with correlation length  $\ell$  is the Gaussian.

$$B(\tau) = h^2 \exp(-\tau^2/\ell^2) \quad (5)$$

Gaussian-correlated surfaces have continuous slopes at all points with a total mean square slope of

$$S^2 = \frac{4h^2}{\ell^2}$$

The exponential correlation function

$$B(\tau) = h^2 \exp(-|\tau|/\ell) \quad (6)$$

has also been used in many theoretical models (reference 5).

Surfaces with exponential correlation function are jagged and have vertical facets (jumps) (reference 4). For such surfaces, the surface slopes and all higher order surface derivatives can be undefined or infinite at many surface points.

Previous investigations by Krishen (reference 7) have shown that neither Gaussian nor exponential correlation functions gives an accurate fit to the backscatter versus  $\theta$  data from ocean surfaces. A better fit was observed with Gaussian correlation function for the gravity waves and exponential correlation for the capillary waves. For the land sites, the choice of a correlation function will entirely depend on the type of terrain.

The correlation distance  $\ell$  defines the region of statistical dependence of the surface height. The surface heights of two points separated by a distance greater than  $\ell$  are essentially statistically independent of each other. Points within the distance  $\ell$  are statistically dependent. Thus, the correlation distance is intuitively the average horizontal extent of ripples or irregularities in the rough surface.

### 3.4 APPLICABLE THEORY TO SCATTERING FROM SPE LAND AND OCEAN SITES

Three theories which have received attention and show promise of efficient interpretation of experimental data are the Kirchhoff method, the small perturbation theory, and the composite scattering theory. A discussion of these methods will be presented in this section. Most of this section has been taken directly from Kaufman's report (reference 2).

### 3.4.1 Radar Scattering Theories

#### Kirchhoff method

The field scattered by a rough surface  $\vec{E}_{p_1}(x', y', z')$  is formulated according to Huygen's principle and is given by the Stratton-Chu integral:

$$\begin{aligned} \vec{E}_{p_1}(x', y', z') = & \frac{1}{4\pi j\omega\epsilon_0} \oint_{C_t} \nabla\psi \cdot \vec{H} \cdot d\vec{l} \\ & - \frac{1}{4\pi} \int_{S_1} [-j\omega\mu_0 (\vec{n} \times \vec{H})\psi \\ & + (\vec{n} \times \vec{E}) \times \nabla\psi + (\vec{n} \cdot \vec{E}) \nabla\psi] ds \end{aligned} \quad (7)$$

In equation (7),  $S_1$  is the portion of the interface illuminated by the electric field  $\vec{E}$  and magnetic field  $\vec{H}$ , and  $C_t$  is contour of  $S_1$ . The coordinate system is illustrated in figure 3-1.  $\epsilon_0$  and  $\mu_0$  are respectively the free space permittivity and permeability, and

$$\psi = \frac{e^{-jk r}}{r}$$

$$\text{with } r = [(x' - x)^2 + (y' - y)^2 + (z' - \xi)^2]^{1/2} \quad (8)$$

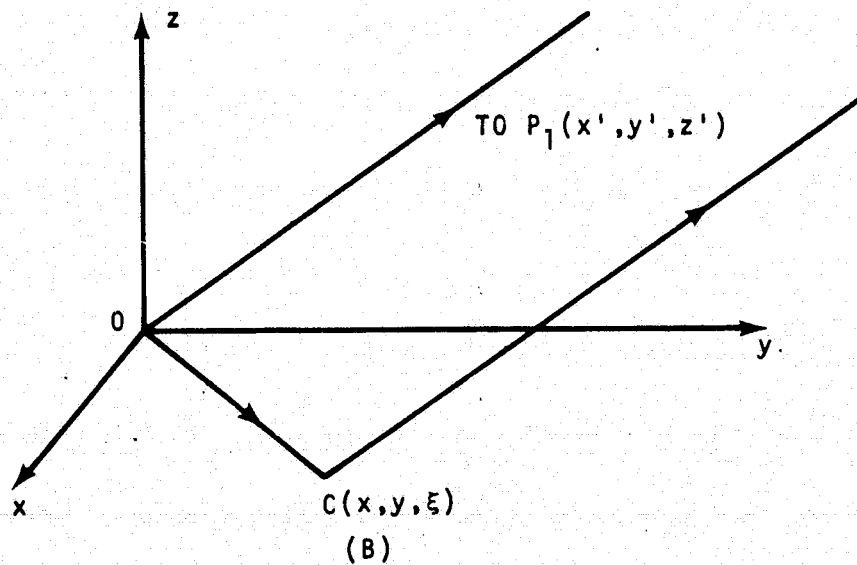
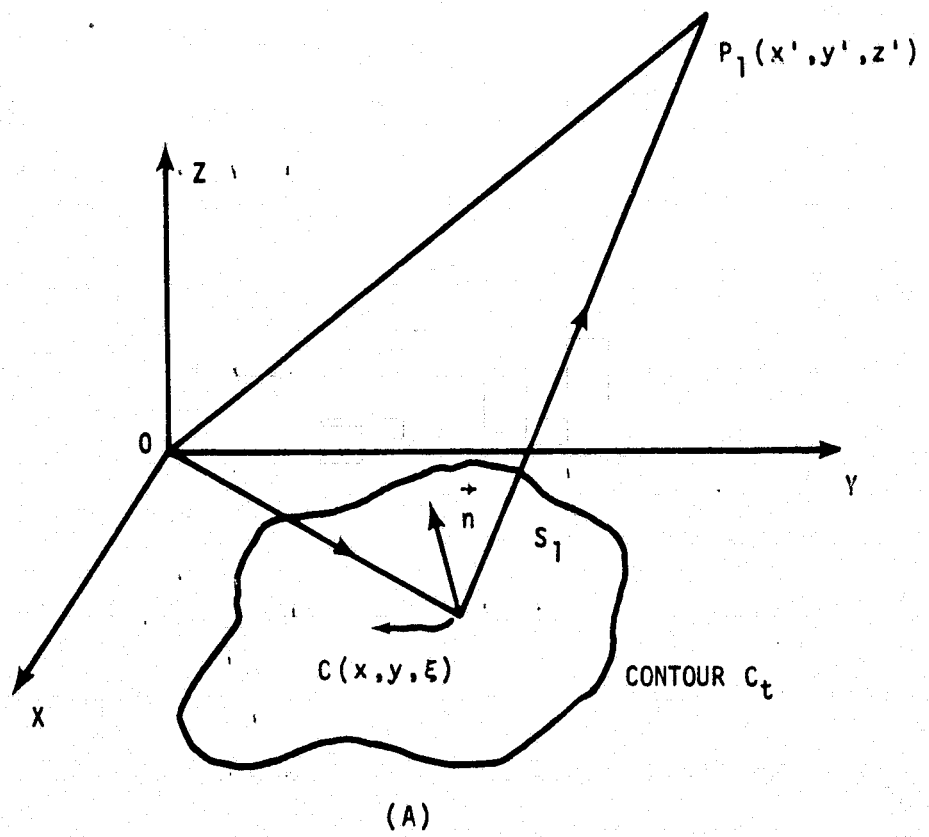


Figure 3-1. — Scattering from the rough surface. [ $C(x, y, \xi)$  is any point on the rough interface and  $P_1(x', y', z')$  is the observation point. (B) is the far field approximation of (A).]

$\vec{n}$  is the unit vector normal to the surface reflecting the incident wave  $\vec{E}_1$ ,  $\omega$  is the radian frequency of the radar,  $k$  is the propagation constant, and  $\xi$  is the rough scattering surface.

At each point  $C$  of the illuminated rough surface the fields  $\vec{E}$  and  $\vec{H}$  are the sum of an incident plane wave field ( $\vec{E}_1$  and  $\vec{H}_1$ ) and a reflected field ( $\vec{E}_2$  and  $\vec{H}_2$ ) so that

$$\begin{aligned}\vec{E} &= \vec{E}_1 + \vec{E}_2 \\ \vec{H} &= \vec{H}_1 + \vec{H}_2\end{aligned}\tag{9}$$

The fields on the surface are evaluated by tangent plane approximation. The assumption is that at the point  $C$ , the surface is locally flat. This approximation restricts the use of this method to surfaces where the radius of curvature of surface roughness is large compared with the radar wavelength. Under this assumption the incident and reflected fields can be related by using Fresnel reflection coefficients.

Once the fields at the rough surface have been established, these fields may be entered into the scattering integral and the scattering integral adapted for the calculation of the mean power,  $1/2\{(\epsilon_0/\mu_0)^{1/2}[\langle E_2 E_2^* \rangle]\}$  scattered from the surface to the radar system at a distance  $R_0$ . The brackets  $\langle \rangle$  indicate that an averaging process involving the statistical parameters of the surface must be carried out, while  $E_2$  and  $E_2^*$  are respectively the complex magnitude (involving both magnitude and phase) and the conjugate complex magnitude of the scattered field received at the radar.

In carrying out the averaging of the scattered power, it will be assumed that the surface height variation about the mean surface plane has the Gaussian distribution of equation (3) while the surface correlation function has the form of equation (5). A rather complicated integral is the result of the averaging process. Certain approximations required to facilitate its evaluation are:

- $\lambda \ll T$ , i.e., the correlation length of the surface roughness is much less than the dimension of the illuminated area.
- Kaufman's procedure (reference 8) requires also that all rough surface slopes not exceed 0.3 in magnitude and that the absolute value of the surface dielectric constant be much greater than 1.4 (at least 1.4).

Using the relation (reference 9),

$$\sigma_o = 4\pi R^2 \frac{\text{Average power scattered back to radar}}{\text{Power incident at rough surface}} \quad (10)$$

three normalized radar cross sections,  $\sigma_{oHH}$ ,  $\sigma_{oVV}$  and  $\sigma_{oC} = \sigma_{oHV} = \sigma_{oVH}$  can be calculated depending upon the polarization of the transmitted and incident waves.

Barrick gives the result (reference 4):

$$\sigma_{oHH} = \sigma_{oVV} = \frac{\sec^4 \theta}{2S_x S_y} |R(o)|^2 \exp\left(\frac{-\tan^2 \theta}{2S_x^2}\right) \quad (11)$$

and  $\sigma_{oC} = \sigma_{oHV} = \sigma_{oVH} = 0$ ,

where  $S_x, S_y$  are the root mean square (rms) slopes in x and y directions, (x direction being taken to lie along the surface in the plane of incidence),  $R(o)$  is the Fresnel reflection coefficient evaluated at  $\theta=0$ , i.e., at the normal angle of incidence.  $R(o)$  is given by:

$$R(o) = \frac{1 - \sqrt{\epsilon}}{1 + \sqrt{\epsilon}}$$

where  $\epsilon$  is the complex dielectric constant of the rough surface. For a surface with isotropic slope distribution  $S_x^2 = S_y^2 = S^2/2$ , where  $S^2$  is the total mean square slope given by  $S^2 = 4h^2/\ell^2$ .

Kaufman (reference 7) provides a more complicated but possibly more exact result since he does distinguish between  $\sigma_{oVV}$  and  $\sigma_{oHH}$ .

$$\sigma_{oHH} = \frac{1}{S^2} \left| R_h \sec^2 \theta + (R_h - 1) K_1 \tan \theta \right|^2 \exp \left( \frac{-\tan^2 \theta}{S^2} \right) \quad (12)$$

$$\sigma_{oVV} = \frac{1}{S^2} \left| R_v \sec^2 \theta + (R_v + 1) K_2 \tan \theta \right|^2 \exp \left( \frac{-\tan^2 \theta}{S^2} \right) \quad (13)$$

$$\sigma_{oC} = \sigma_{oHV} = \sigma_{oVH} = 0$$

REPRODUCIBILITY OF THE  
ORIGINAL PAGE IS POOR

where  $R_h$  and  $R_v$  are the Fresnel reflection coefficients:

$$R_h = \frac{\epsilon \cos \theta - (\epsilon - \sin^2 \theta)^{1/2}}{\epsilon \cos \theta + (\epsilon - \sin^2 \theta)^{1/2}}$$

and

$$R_v = \frac{\cos \theta - (\epsilon - \sin^2 \theta)^{1/2}}{\cos \theta + (\epsilon - \sin^2 \theta)^{1/2}}$$

The factors  $K_1$  and  $K_2$  are functions of  $\theta$ , and are given by:

$$\left. \begin{aligned} K_1 &= 1 - \frac{\cos \theta}{(\epsilon - \sin^2 \theta)^{1/2}} \tan \theta \\ K_2 &= \frac{\epsilon (1 - \epsilon) \sin \theta}{(\epsilon - \sin^2 \theta)(\epsilon \cos \theta + [\epsilon - \sin^2 \theta]^{1/2})} \end{aligned} \right\} \quad (14)$$

A few comments about the above equations are in order. For the case of a perfectly conducting surface, the Fresnel coefficients reduce to  $R_h = 1$  and  $R_v = -1$  so that Kaufman and Barrick's results are equivalent for such a surface. Essentially both sets of results can be interpreted as the radar cross sections available from a rough surface as the incident wavelength  $\lambda$  approaches zero. Also, the cross-polarized cross section is identically zero in the zero wavelength limit. Kaufman (reference 8) has shown, however, that the cross-polarized normalized radar cross



section behaves in the following manner as  $\lambda \rightarrow 0$  :

$$\sigma_{oC} = \frac{\lambda^2}{8\pi^2 h^2 \sin 2\theta} |R_h + R_v|^2 \exp \left( \frac{-\tan^2 \theta}{S^2} \right) \quad (15)$$

Experimental data gathered over gently undulating natural surfaces shows good agreement with Kirchhoff's scattering model up to the incidence angles of  $25^\circ$  for VV and HH polarizations.  $\sigma_{oC}$  from equation (15) does not show good agreement with the experimental data. This model has therefore been used in evaluating S-193 Scatterometer precision/accuracy at the lower incidence angles.

#### Small perturbation method

For surfaces where the rms height is smaller than the incident radar wavelength, a small perturbation technique can be applied. Two methods have been proposed in the literature. In the Bass and Bocharov method (reference 10), the homogeneous problem with boundary conditions on the rough surface is converted to a nonhomogeneous scattering surface with boundary conditions on a plane. For more detailed discussion and applicability of this method, the reader is referred to Krishen (reference 11) who applied this method to calculate scattering from a rough layer. Once the field on the surface is evaluated with this method, the field everywhere can be calculated using the Stratton-Chu integral.

Rice (reference 12) gave an extension of Rayleigh's scalar solution for solving vector problems. The method is based on mode representation of the scattered field. The scattering rough surface  $\xi(x,y)$  and the scattered field

are expanded into Fourier series. The coefficients of the scattered field are evaluated using boundary conditions on the surface. The following assumptions are involved in this method:

- $k \xi(x,y) < 1.0$ ; i.e., roughness height is small compared to wavelength  $\lambda$ ,  $\xi(x,y)$  is the height of the rough surface above the mean, and  $k$  the magnitude propagation vector.
- $\frac{\partial \xi}{\partial x}, \frac{\partial \xi}{\partial y} < 1.0$ , i.e., the slopes are relatively small.
- $\langle (\frac{\partial \xi}{\partial x})^2 \rangle = \langle (\frac{\partial \xi}{\partial y})^2 \rangle$ , i.e., the roughness is isotropic.  $\langle \rangle$  indicates average over an ensemble of surfaces. This is not essential to the solution but has been employed in developing cross section expressions.
- $T \gg \lambda, L$ , i.e., dimension of the illuminated area is large compared with the correlation distance  $L$  of the surface and wavelength  $\lambda$  of incident radiation.

In the small perturbation method, multiple scattering and shadowing are not neglected. For the Bass and Bocharov method, the third assumption above is not necessary.

Since the surface  $\xi(x,y)$  is a random variable, the Fourier coefficients associated with it are also random variables and may be averaged statistically. Such an averaging process yields an average value of  $\sigma_0$  for

small-scale roughness (reference 4):

$$\begin{aligned}\sigma_{oHH} &= 4\pi k^2 |\alpha_{hh}|^2 \cos^4 \theta W(t) \\ \sigma_{oVV} &= 4\pi k^2 |\alpha_{vv}|^2 \cos^4 \theta W(t) \dots\end{aligned}\quad (16)$$

and

$$\sigma_{oVH} = \sigma_{oHV} = 0 \quad (17)$$

where  $k = 2\pi/\lambda$ ,  $W(t)$  is the roughness spectral density of the surface with  $t$  defined as  $t = 2k \sin \theta$  and with  $\alpha_{hh}$  and  $\alpha_{vv}$  given by:

$$\begin{aligned}\alpha_{hh} &= \frac{\epsilon - 1}{\left[ \cos \theta + \left( \epsilon - \sin^2 \theta \right)^{1/2} \right]^2} \\ \alpha_{vv} &= \frac{(\epsilon - 1) \left[ (\epsilon - 1) \sin^2 \theta + \epsilon \right]}{\left[ \epsilon \cos \theta + \left( \epsilon - \sin^2 \theta \right)^{1/2} \right]^2}\end{aligned}$$

For rough terrestrial surfaces, the roughness spectral density appearing in equations (16) and (17) can be related to the correlation function of the surface through a Fourier transform. If the correlation function is Gaussian, i.e.,  $B(\tau) = \Sigma^2 \exp(-\tau^2/L^2)$  [see equation (4)], then the radar cross sections become:

$$\sigma_{oHH} = 4k^2 \Sigma^2 L^2 |\alpha_{hh}|^2 (\cos^4 \theta) \exp(-k^2 L^2 \sin^2 \theta) \quad (18)$$

$$\sigma_{oVV} = 4k^2 \Sigma^2 L^2 |\alpha_{VV}|^2 (\cos^4 \theta) \exp (-k^2 L^2 \sin^2 \theta) \quad (19)$$

where  $\Sigma$  and  $L$  are the rms height and correlation distance of the small-scale rough surface.

Valenzuela (reference 13) used Rice's theory to obtain depolarization from slightly rough surfaces. The depolarization is a second order effect. Figures 3-2 and 3-3 have been taken from Valenzuela's paper and illustrate the depolarization predicted using small perturbation theory. A Neumann spectrum for the fully developed sea has been used to arrive at the results given in figure 3-3.

The small perturbation method is useful in the low frequency limit and can therefore be employed to a class of slightly rough surfaces when large radar wavelengths are used. A comparison of the theoretical and experimental results over a slightly rough surface has been given by Wright (reference 14). As pointed out in his paper, the measured  $\sigma_o$  compare very well with those predicted by this theory. Experimental data over ocean surfaces for angles of incidence greater than  $20^\circ$  also shows reasonable agreement with the theoretical results predicted using small perturbation theory.

#### Composite scattering theory

Nearly all natural rough surfaces possess a composite structure where small-scale roughness appears superimposed on large-scale roughness. Mathematically, the treatment of

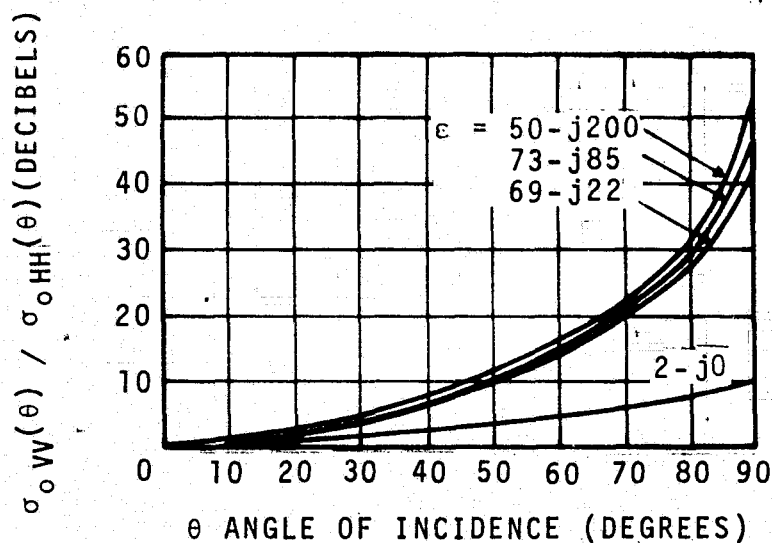


Figure 3-2. — Polarization dependence for backscattering from a slightly rough surface for various dielectric constants.  
(Valenzuela, 1967)

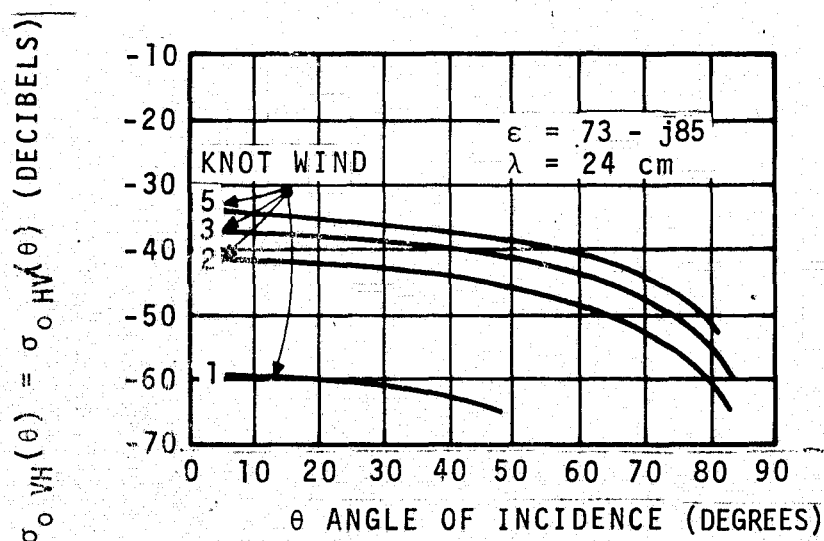


Figure 3-3. — Depolarized backscattering cross section per unit area for a sea with directional wave spectrum for various windspeeds.  
(Valenzuela, 1967)

such a surface is quite formidable, but to a first-order approximation one can merely add the cross section calculated for the large-scale roughness alone to that caused by small-scale roughness. Of course, as  $\theta$ , the angle of incidence, approaches zero, the return from the large-scale structure is dominant, especially for surfaces with gentle slopes.

Considerably more detail regarding the composite surface theory is given by Barrick (reference 4). In conclusion, returns given by equations (18) and (19) should be added to the returns given by the large-scale roughness for angles of incidence over  $20^\circ$ .

#### 3.4.2 Radar Return from the Sea - A Qualitative Approach

The calculation of radar return from the sea presents a challenge somewhat different but just as thorny as that for terrestrial targets. Because of the large number and variability of the parameters that produce a particular sea state, it is especially difficult to describe that state accurately. The windspeed, duration, fetch, and direction at the water surface, the ocean currents, contaminants such as oil, the effects of distant storms that propagate disturbances of the sea with low loss over vast distances, bottom variations, and local weather can all have an effect on radar return and are difficult to assess in practice.

Skolnik (reference 15) gives some of the more useful terms for describing the sea surface structure:

Wind wave — a wave resulting from the action of the wind on a water surface. While the wind is acting on it, it is a *sea*; thereafter, it is a *swell*.

Gravity wave — a wave whose propagation velocity is controlled primarily by gravity. Water waves more than 5 cm in length are considered gravity waves.

Capillary wave — a wave whose propagation velocity is controlled primarily by the surface tension of the liquid in which the wave is traveling. Water waves less than 2.5 cm long are capillary waves.

Fetch — (1) an area of the sea surface over which seas are generated by a wind having a constant direction and speed; (2) the length of the fetch area, measured in the direction of the wind, in which the seas are generated.

Duration — the length of time the wind blows in essentially the same direction over the fetch.

Swell — ocean waves that have traveled out of their fetch. A swell characteristically appears more regular for a longer period and has flatter crests than waves within their fetch.

Sea — waves generated or sustained by winds within their fetch; opposed to swell.

Wave spectrum — the distribution of wave heights (or square of the wave height) with respect to frequency of the wave.

Sea state — the numerical or written description of ocean roughness, often referred to as numerical code and expressed in terms of the significant wave height.

Significant wave height — the average height of the one-third highest waves of a given wave group. (Height is the vertical distance between a crest and a trough.)

Fully developed sea — the maximum height to which ocean waves can be generated by a given wind force blowing over sufficient fetch, regardless of duration, as a result of all possible wave components being present with their maximum amount of spectral energy.

Sea waves are generated by the wind and differ markedly from a swell in physical appearance and in their affect on radar return. Individual sea waves are more peaked than pure sine waves and are skewed in the direction of propagation. They are irregular, chaotic, short-crested (length along the crest is of the same order of magnitude as the wavelength), mountainous, and unpredictable except in a statistical sense. Sea waves contain many small waves superimposed on the larger waves, and their spectrum covers a wide range of frequencies and directions.

Swells are more regular than sea waves, longer crested, more rounded tops, and more predictable. Their spectrum covers a narrow range of frequencies and directions, with periods falling between 30 seconds to 5 minutes.



Both wind-generated sea waves and swells can be included in the category of gravity waves. Typically, the period of gravity waves varies from about 1 to 30 seconds. Gravity waves are also dispersive, i.e., waves of longer wavelength propagate faster than waves of shorter wavelength. Ultragravity waves (also known as high frequency gravity waves) have periods of about .1 second to 1 second.

Capillary waves have periods less than approximately 0.1 second. Like sea waves, they are generated by the wind, but surface tension rather than gravity is the force controlling their characteristics. Capillary waves are fairly sensitive to the wind. In contrast, if the wind-generating gravity waves stop, they continue to run and become swells. When capillary waves interact with the longer gravity waves, the capillary waves appear to be concentrated, at times, on the forward face of the gravity wave just before the sharp crest. Capillary waves are significant in radar return at the higher microwave frequencies (X band or greater).

Wave height is not fixed in relation to the wavelength but depends on the wind generating it. Any wave becomes unstable and breaks if the angle formed by the crest exceeds  $120^\circ$ ; wave height also can be no greater than one-seventh the wavelength. Once the wind is blowing, it takes a finite time for a sea to develop. The term *fully developed sea* describes the condition which exists when the ocean waves have reached their maximum height generated by a given wind force over a given fetch.

A typical plot of  $\sigma_0$  versus  $\theta$ , the angle of incidence, would appear as in figure 3-4. In the quasi-specular region near vertical incidence, the radar echo is fairly large with measured values at  $\theta = 0$  lying between 0 and +18 dB. As in the case of the "very rough" terrestrial targets, this enhanced return near vertical is apparently due to specular-like return from facet-like areas on the sea surface that are oriented in the direction of the radar.

Above some transition angles (in the order of  $20^\circ$  incidence angle) there is little likelihood of significant return from the facets making up the sea surface. Most of the return now appears to be due to sea surface small-scale structure such as spray, foam, and capillary waves. Such return is relatively isotropic and accounts for the plateau region of the  $\sigma_0$  versus  $\theta$  plot. At still higher angles of incidence  $\sigma_0$  falls sharply, but this region is of no concern in the S-193 Scatterometer measurements and will not be discussed in this report.

At near normal incidence, measurements (reference 16) indicate that  $\sigma_0$  decreases with increasing wind on the sea. Little difference is seen between  $\sigma_{oHH}$  and  $\sigma_{oVV}$  at near normal incidence. In the plateau region  $\sigma_0$  increases as the wind rises. At low windspeeds  $\sigma_{oHH}$  in the plateau region is considerably less than  $\sigma_{oVV}$ , but as the wind increases,  $\sigma_{oHH}$  increases faster than  $\sigma_{oVV}$ , so that with rough-sea conditions there is relatively little difference between the two returns.

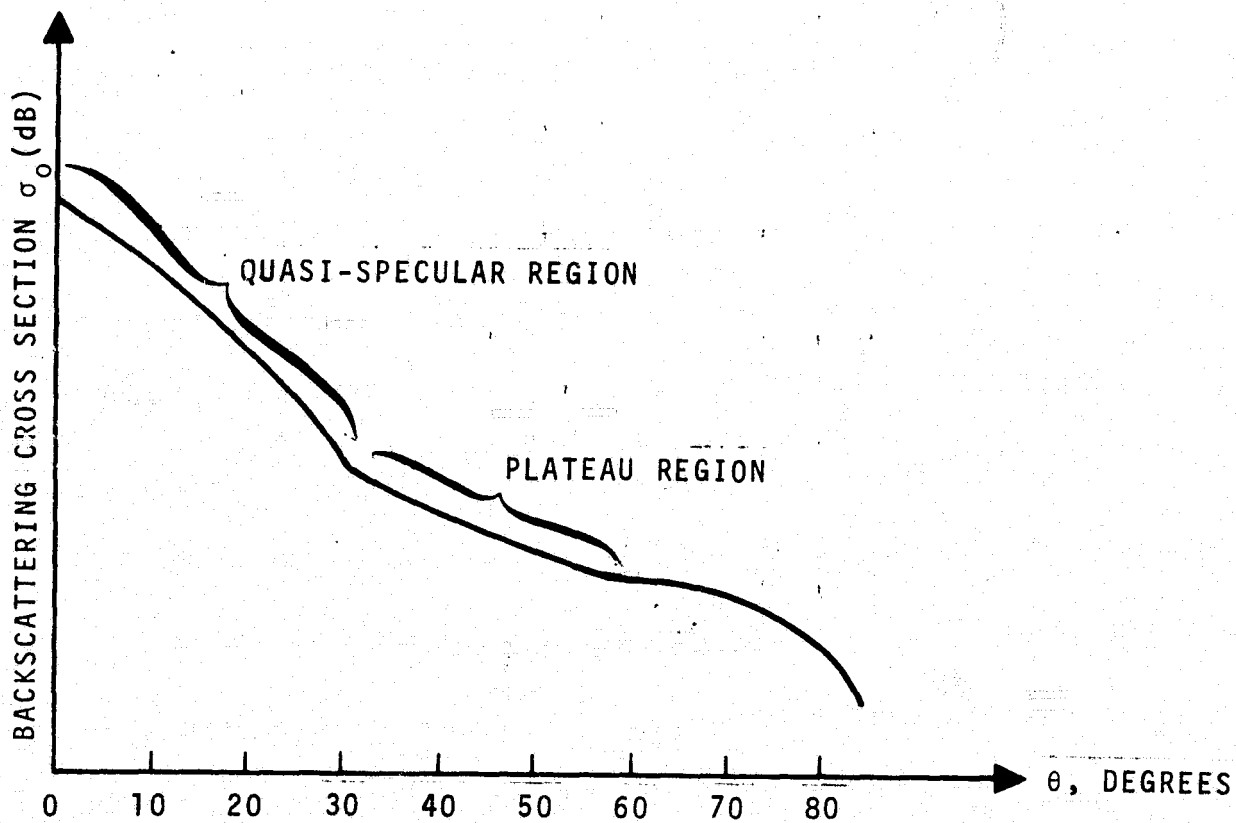


Figure 3-4. -  $\sigma_0$  versus  $\theta$  for the sea (general observed dependence).

### 3.4.3 Oceanic S-193 Targets - Applicable Theories

Since the sea state is so sensitive to wind, it is to be expected that no single model can predict  $\sigma_o$  for the sea. Thus, this section will discuss three models, each pertaining to a particular range of sea state, that can be used to theoretically determine  $\sigma_o$ . These are (1) low sea (rms wave height less than  $\lambda/4\pi$ ), (2) medium sea ( $h > \lambda/4\pi$  and  $W(t)$ , the roughness spectral density of the surface, dependent strongly upon the wind magnitude), and (3) rough sea ( $h \gg \lambda/4\pi$  with  $W(t)$  weakly dependent upon wind).

For low seas the radar return contains a coherent and a noncoherent return. The noncoherent return is quite small and diffused and can be calculated by equations (18) and (19) if the sea rms height is known. The coherent component has a strong return at  $\theta = 0$ , with side lobes elsewhere, and is given by the following equation. (The results of Barrick (4) and Kerr (17) suggest this expression.)

$$\sigma_o = \frac{4\pi A^2}{\lambda^2} \left[ \frac{J_1(2ka \sin \theta)}{ka \sin \theta} \right]^2 \cos^2 \theta \exp(-4k^2 \Sigma^2 \cos^2 \theta) \quad (20)$$

where it is assumed that the illuminated area of the sea is a circle of area  $A = \pi a^2$ ,  $J_1$  is a Bessel function of the first kind.

For the moderate sea, the composite rough surface model will apply; the resultant cross section is the sum of the cross sections due to large ( $h \gg \lambda$ ) and small ( $\Sigma \ll \lambda$ )

scale roughness. Comparison of the composite model theory and NASA/Johnson Space Center 0.4 GHz data is shown in figure 3-5 (reference 7). In this figure the total rms slope of the large-scale structure is

$$S = 0.1763$$

and the small-scale parameters are

$$k\Sigma = 0.5$$

$$kL = 20.0$$

Near  $\theta = 0$ , the large-scale roughness predominates and equations (11), (12), and (13) can be used to predict  $\sigma_0$ . The required value of  $S$ , the total root mean slope, can be estimated from the work of Schooley (reference 18), Cox and Munk (reference 19), or Krishen (reference 7), who have related the mean sea slope to wind. Figure 3-6 has been taken from Krishen (reference 7). In this figure the rms slope is  $\beta_0$  in degrees where  $S = \tan \beta_0$ . For large values of  $\theta$  the return is largely due to small-scale sea structure and is given by equations (18) and (19). Unfortunately,  $W(t)$ , the roughness spectral density of the surface, has no simple functional form (reference 7). It must be evaluated from rather slender experimental evidence (reference 20).

As wind rises and the sea becomes rough, an upper limit exists for the height of a wave of fixed length whether in the gravity or capillary range. For portions of the ocean where the wave height is limited, the roughness spectral density  $W(t)$  assumes the form  $W(t) = Bt^{-4}$  (reference 21) where  $t^2 = p^2 + q^2$ ,  $p$ ,  $q$  are the

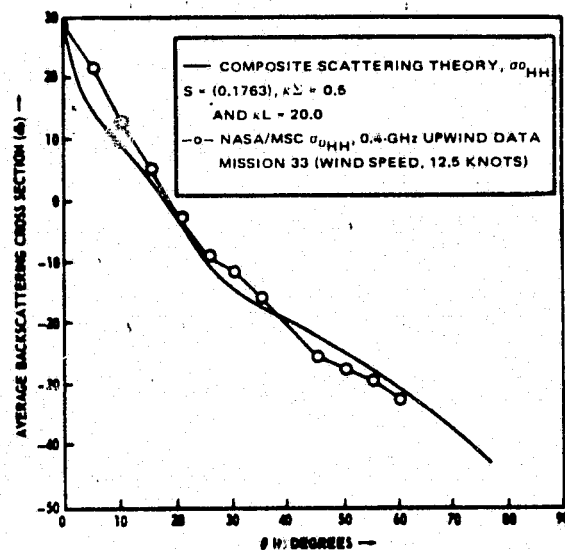


Figure 3-5. — Comparison of NASA/JSC 0.4 GHz data with the composite scattering theory. (Krishen, 1971)

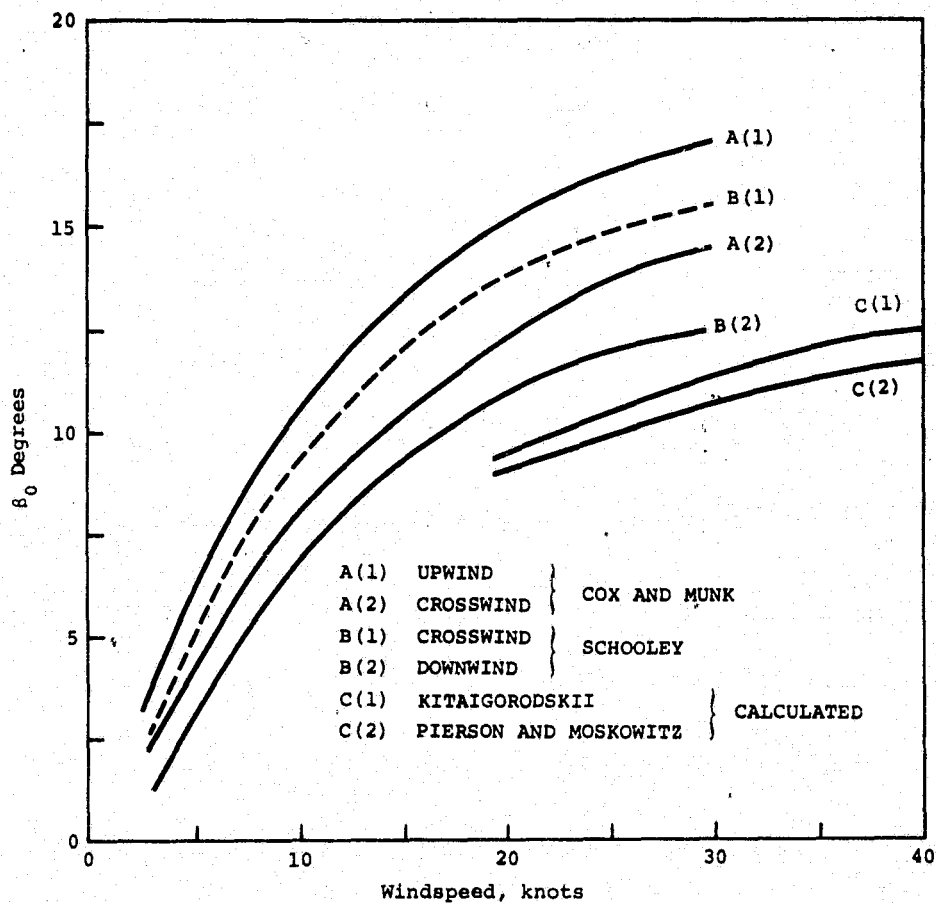


Figure 3-6. - Values of  $\beta_0$  [ $s = \tan \beta_0$ ] as a function of windspeed.  
(Krishen, 1971)

radian wave numbers in x and y directions on the surface. The value of  $B$  for the capillary waves given in reference 21 is  $1.5 \times 10^{-2}$ . Thus, for rough seas, a composite surface model again suffices, with returns due to the two roughness structures contributing to the radar cross section over a wide range of angles, including small values of  $\theta$ .

Regarding the matter of a theory that can be used to calculate  $\sigma_{\text{OVH}}$  and  $\sigma_{\text{OHV}}$ , no satisfactory one currently exists. Most theoretical treatments of electromagnetic wave scattering from a rough surface indicate negligible depolarized scatter into the plane of incidence, although experimental measurements show that this scatter component is present. Some investigators, such as Rouse (reference 22), have postulated that depolarization is largely a volume scattering effect. Rouse's analysis, however, includes parameters that are not physically meaningful in an inspection of the surface.



#### 4.0 ATMOSPHERIC LOSSES

The computation of the backscattering cross sections involves corrections for path losses for transmission and reception through the intervening atmosphere. These losses appear as constants  $L_1$  and  $L_2$  in the  $\sigma_0$  equation (see appendix B, equation B-9). Atmospheric losses are not included in the JSC production processed S-193 data where  $L_1 = L_2 = 1$ . It is therefore important to include (where atmospheric losses are significant) proper corrections in the  $\sigma_0$  computation. In the  $K_u$  band (S-193 operates in this band) of microwave frequencies, the radar energy is absorbed by atmospheric oxygen, water vapor, and rainfall. Rainfall can also cause scattering of the microwave energy.

The loss due to the atmosphere has been studied intensively in literature (references 15, 23, 24, 25, 26, 27, and 28). Experimental data has also been gathered to verify theoretical models. In general, the atmospheric loss depends on the atmospheric temperature, pressure, and water vapor density. Large variations normally occur over long intervals and are associated with major changes in air mass type at the observing site. LeFande (reference 27) divided the atmosphere into a series of 110 spherical shells of exponentially increasing thickness to a height of 30 kilometers. His theoretical results for 60 percent relative humidity at 60°F (which gives a ground-level water vapor density  $\rho_0$  of 7.5 g/m<sup>3</sup>) are shown in figure 4-1. The attenuation per unit path length increases with frequency. For the range of frequencies up to 100 GHz, there is a water vapor peak at 22.3 GHz and oxygen absorption peak at 60 GHz.

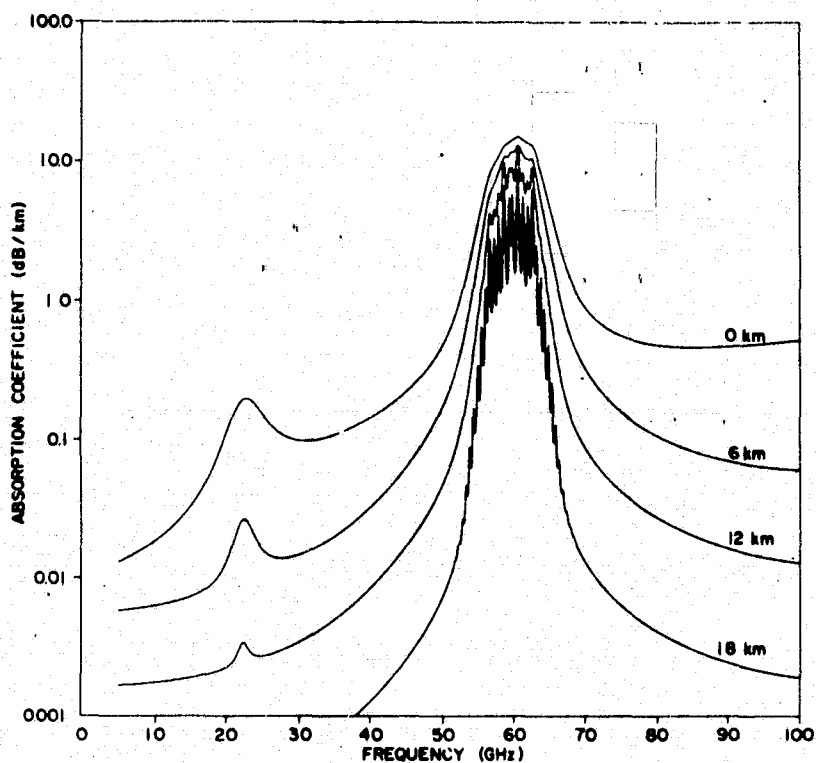


Figure 4-1. — Absorption profiles for various altitudes for water vapor concentration =  $7.5 \text{ g/m}^3$  (60 percent RH at  $60^\circ\text{F}$ ). (R. A. LeFande, 1968).

The final results of LeFande's (reference 27) calculations giving a total attenuation due to atmospheric oxygen and water vapor are shown in figure 4-2. The formulation was developed from classical laws on electromagnetic attenuation in gases and a known oxygen, water vapor, pressure, and temperature distribution of the troposphere. Experimental data gathered thus far confirms the attenuations shown in figure 4-2 (see references 24 and 25). Another computation by Haroules and Brown (reference 23) yields the results of figure 4-3 for vertical incidence ( $\theta = 0$ ). The agreement between figures 4-2 and 4-3 is evident.

The two-way attenuation can be expressed in terms of an exponential law over propagation paths where pressure and atmosphere composition are uniformly distributed. The attenuation for this case is (reference 15):

$$L_1 L_2 = \exp \left( -2 \frac{R_\theta}{H_o} \int_0^{H_o} \alpha_a dH_o \right) \quad (21)$$

where  $\alpha_a$  is the attenuation coefficient per meter,  $R_\theta$  is the distance between the S-193 antenna and ground resolution cell and  $H_o$  is the Skylab altitude. For the U.S. Standard Atmosphere, the data needed to calculate the value of the integral of equation (21) has been given in reference 28. For the U.S. Standard Atmosphere, equation (21) can be evaluated as

$$L_1 L_2 = \exp \left( \frac{-0.0364047 R_\theta}{H_o} \right) \quad (22)$$

at the frequency of 13.9 GHz.

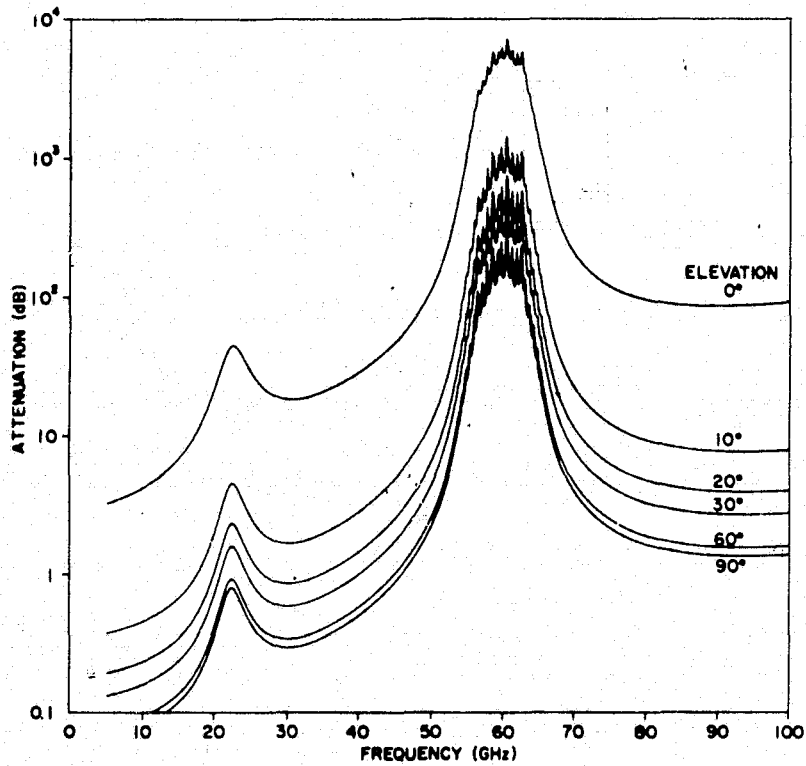


Figure 4-2. — Total absorption versus frequency for paths through the atmosphere at various antenna elevation angles (water vapor concentration =  $7.5 \text{ g/m}^3$ ). (R. A. LeFande, 1968)

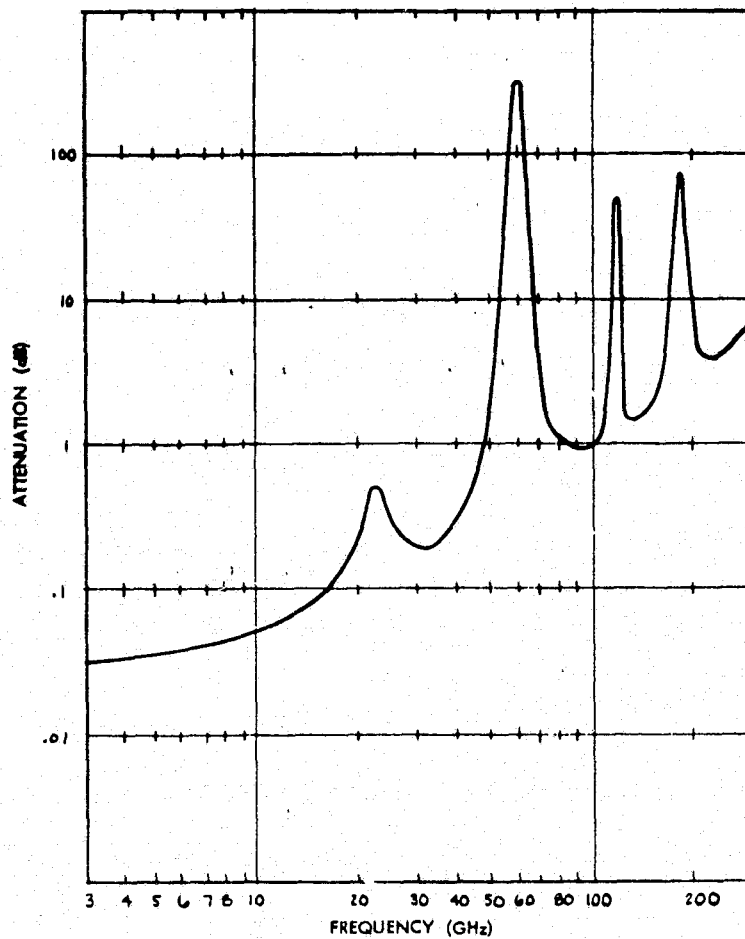


Figure 4-3. — Total vertical path attenuation by atmospheric gases (water vapor concentration =  $7.5 \text{ gm/m}^3$ ). (Haroules and Brown, 1968)

Under normal circumstances where no heavy precipitation is present, the S-193 radar energy suffers a two-way attenuation of approximately 0.16 dB at vertical incidence and approximately 0.24 dB at the highest scan angle of 48°. It should be noted that the mission requirements for Sensor Performance Evaluation data-takes were such that no data was to be taken in the presence of heavy precipitation and cloud cover. The data analyzed in this report belongs to this category. In the presence of clouds and heavy rain, the  $\sigma_0$ 's will be used with proper recognition given to the atmospheric conditions.

Considerably more attenuation is caused by the presence of clouds and rainfall over the observation site. The rainfall attenuation for frequencies from 4 to 100 GHz has been calculated theoretically by Oguchi (reference 29). His results were interpolated by LeFande (reference 27). These results are shown in figure 4-4. No resonances have been noted. Stafford (reference 30) computed the attenuation constant due to a cloud deck from 6,000 to 12,000 feet with moderate-to-heavy rain below. His results are given in table 4-I. A review of various experimental and theoretical results (reference 31) indicates that attenuation because of rainfall cannot be ignored at 13.9 GHz.

For accurate measurements of  $\sigma_0$ 's from ground scenes, it is necessary to consider false returns from heavy precipitation. The backscatter from heavy rain or clouds can cause more return than the ground, under certain ground conditions, and antenna look angle. Typical backscatter

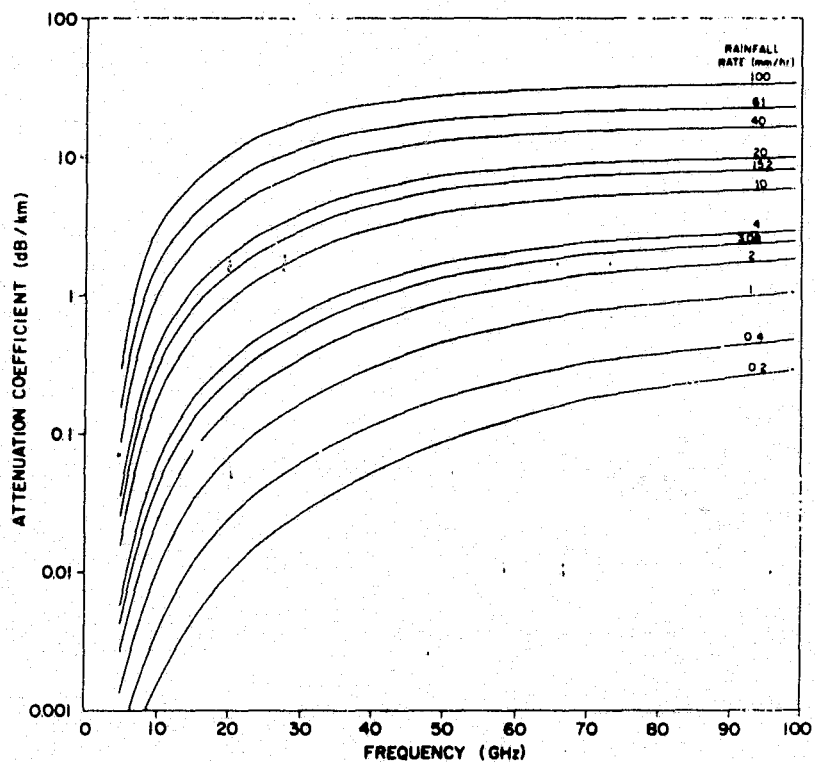


Figure 4-4. — Theoretical rainfall attenuation versus frequency for various rain rates.  
(R. A. LeFande, 1968)

TABLE 4-I. - 13.9 GHz SIGNAL ATTENUATION BY CLOUDS AND RAIN

(two-way-path attenuation, in dB)

Angle from nadir (degrees)	Rainfall rate, inches/hour					
	Drizzle .001 mm/hr	Light rain .04 mm/hr	Moderate rain .16 mm/hr	Moderate-to- heavy .39 mm/hr	Heavy rain .63 mm/hr	Very heavy rain 1.6 mm/hr
0	$2.9 \times 10^{-2}$	$1.0 \times 10^{-1}$	$6.2 \times 10^{-1}$	2.6	4.8	10.2
12.5	$3.0 \times 10^{-2}$	$1.0 \times 10^{-1}$	$6.3 \times 10^{-1}$	2.6	4.8	10.4
20	$3.2 \times 10^{-2}$	$1.1 \times 10^{-1}$	$6.7 \times 10^{-1}$	2.8	5.1	11.0
32.1	$3.6 \times 10^{-2}$	$1.2 \times 10^{-1}$	$7.6 \times 10^{-1}$	3.1	5.8	12.5
35	$3.6 \times 10^{-2}$	$1.2 \times 10^{-1}$	$7.7 \times 10^{-1}$	3.2	5.9	12.7
43.2	$4.3 \times 10^{-2}$	$1.4 \times 10^{-1}$	$9.1 \times 10^{-1}$	3.8	7.0	15.1
52	$5.5 \times 10^{-2}$	$1.8 \times 10^{-1}$	1.2	4.8	8.9	19.2



from rain is given in table 4-II (reference 31). The reflectivity parameter  $Z_R$  is defined as:

$$Z_R = \sum_{i=1}^N D_i^6$$

where  $N$  is the number of scatterers per unit volume and  $D_i$  is the droplet diameter. The combined backscattering effects of a unit volume are :

$$\eta = \sum_{i=1}^N \sigma_i$$

where  $\sigma_i$  is the backscatter cross section of the  $i$ th scatter.

The reflectivity of uniform rain is expressed in terms of radar cross section per unit volume  $\eta$  (or  $\sum \sigma_i$ ) in table 4-II. The rainfall rates are given in millimeters per hour (mm/hr).

The  $\sigma_o$ 's over rainfall will not be used to determine precision/accuracy of S-193 Scatterometer. The uncertainties due to the backscatter caused by the rainfall will prevent drawing any conclusions on the performance of the sensor. Mission requirements were stated so that data would be gathered over Sensor Performance Test sites under almost clear conditions (less than 50 percent cloud cover).

TABLE 4-II. — REFLECTIVITY OF UNIFORM RAIN, METER<sup>2</sup>/METER<sup>3</sup> ( $\eta$  OR  $\Sigma\sigma_i^{**}$ )

$Z_R^*$ (dB)	Type	$\Sigma\sigma_i$ , dB m <sup>-1</sup> transmit frequency, GHz			
		S 3.0	C 5.6	X 9.3	Ku 15.0
-3	Heavy cumulus clouds 4 gm/m <sup>3</sup>	-118	-108	-98	—
14	Drizzle, 0.25 mm/hr	-102	- 91	-81	-69
23	Light rain, 1 mm/hr	- 92	- 81.5	-72	-60
32	Moderate rain, 4 mm/hr	- 83	- 72	-62	-50
41	Heavy rain, 16 mm/hr	- 73	- 62	-53	-43

\*Assumes drop diameter  $\ll \lambda$ 

\*\*Tropospheric attenuation not included

## 5.0 S-193 SCATTEROMETER BACKSCATTER DATA ANALYSIS

The data which will be used to determine precision/accuracy (P/A) will be reviewed in this section. The range of the values of  $\sigma_0$  which should be examined for determining precision/accuracy will be determined by examining data from various SPE ground sites. Selection of data for the determination of the sensor performance will be based on the analysis of data from typical ground scenes. Parameters which influence the data will be outlined. Correlation of backscattering cross section data with the ground location will be discussed.

### 5.1 LOW $\sigma_0$ DATA

Scatterometer data was collected with antenna scanning the deep space in several radiometer/scatterometer operating modes. There were three lunar calibration (LC) passes during Skylab 2 and 3 missions. Analysis of this data is given in reference 32. However, the relationship between the precision/accuracy performance and the deep space data was not discussed in this reference. It is this aspect that will be discussed in this section.

Deep space has been assumed to be an excellent "no backscatter" target. Therefore, for  $V_S$  and  $V_N$ , the only inputs to the scatterometer receiver were the receiver noise and the radiometric temperature of the deep space. The average scatterometer power ( $V_S'$ ) and scatterometer noise power ( $V_N'$ ) when normalized to account for integration time, time constant, and filter and amplifier gains should be equal. Using

this argument and the equation:

$$\langle V_S' \rangle = \langle V_N' \rangle \frac{(IT)_S}{(IT)_N} \cdot \frac{(TC)_N}{(TC)_S} \cdot \frac{F_S}{F_N} \cdot \frac{G_S}{G_N} \quad (23)$$

where  $\langle \rangle$  denotes average,  $(IT)_N$ ,  $(IT)_S$  denote the integration times for noise and signal,  $F_N$ ,  $F_S$  scatterometer filter gains for noise and signal, and  $G_N$ ,  $G_S$  are the scatterometer gains for noise and signal, respectively, Martin Marietta Company (MMC) personnel recommended that the integration times for the scatterometer noise be changed in the production data processing program (reference 32). The new integration times (table 5-I) were used in the NASA S-193 Production Processing Program. Approximately half of the corrected signal and noise power minus noise power values were negative. This is to be expected since  $V_S'$  and  $V_N'$  are randomly varying about the same average values. Computation of  $P_R/P_T$  using the Production Data Processing equations in this case would lead to a negative value (see appendix B) which is not possible. Therefore, these computations are suppressed.

When signal plus noise power minus noise power is positive, the positive values of  $P_R/P_T$  for deep space provide an opportunity to examine the variance of  $\sigma_0$  for zero returned power. To accomplish this, these  $P_R/P_T$  values were used to calculate the backscattering cross sections. The program assumes that the sensor is looking at the earth (in this case an "earth" which absorbs all the energy and returns none). This hypothetical concept allows the computation of the angle of incidence and range needed for evaluating  $\sigma_0$ . No computation is done for the case where  $P_R/P_T$  would be calculated to be negative or zero. The extreme values of  $\sigma_0$  and approximate average which result from such a computation are given in table 5-II.  $\sigma_0$  data does not show any particular dependence on polarization or roll/pitch angle.

TABLE 5-1. — SCATTEROMETER NOISE INTEGRATION TIME (Reference 32)

Mode	Angle (°)	Time constant (TC) (ms)	Integration time (IT) (ms)	
			Preflight	New
ITNC, CTNC	0	10.22	26.582	24.094
ITNC, CTNC	15.6 29.4	33.00	61.532	57.990
CTC-R/S	N/A	10.22	16.000	13.686
CTC-S (only)	N/A	4.00	6.813	6.544

TABLE 5-II. — DEEP SPACE S-193 SCATTEROMETER DATA

Mission/ day of year/ time GMT start/stop	Mode	Positive $P_R/P_T$		
		Extreme values of $\sigma_o$ (dB)		Approximate average of $\sigma_o$ data (dB)
		Maximum	Minimum	
SL2 165 15:42:11.5 15:44:10.7	CTC R/S	-33.67	-48.06	-39.5
SL2 165 15:44:34.8 15:45:32.1	ITC R/S	-38.14	-51.46	-41.0
SL2 165 15:49:11.8 15:49:59.6	ITNC R/S	-37.83	-52.47	-40.5
SL2 165 15:52:0.4 15:54:41.8	CTNC R/S	-33.14	-51.72	-38.5
SL3 224 15:55:16 15:57:16	CTNC R/S	-33.97	-51.63	-39.5
SL3 224 15:53:56 15:54:52	ITNC R/S	-39.77	-48.45	-41.93

TABLE 5-II. — DEEP SPACE S-193 SCATTEROMETER DATA (Concluded)

Mission/ day of year/ time GMT start/stop	Mode	Positive $P_R/P_T$		
		Extreme values of $\sigma_o$ (dB)		Approximate average of $\sigma_o$ data (dB)
		Maximum	Minimum	
SL3 224 15:49:35 15:50:32	ITC R/S	-36.82	-50.90	-41.9
SL3 224 15:47:10 15:49:10	CTC R/S	-34.07	-47.90	-40.33
SL3 224 15:41:16 15:42:10	CTC /S	-34.58	-48.77	-41.4
SL3 254 13:58:24 13:59:17	CTNC R/S	-34.04	-50.43	-40.2
SL3 254 13:53:05 13:54:01	CTC R/S	-34.17	-41.64	-39.26
SL3 254 13:48:44 13:49:57	ITNC R/S	-38.24	-50.07	-41.8
SL3 254 13:57:06 13:58:00	ITC R/S	-34.00	-44.72	-37.00

The data in table 5-II shows that below -33 dB the back-scattering cross section precision decreases considerably. From the accuracy standpoint, a ground site for which  $\sigma_0$  is -33 dB and below, the S-193 Scatterometer essentially predicts a "no return" target. The accuracy and precision are influenced not only by the S-193 Scatterometer but by the analog-to-digital (A/D) converter. It is interesting to examine the uncertainty caused by A/D converter alone in the very low signal range.

The uncertainty is caused by a finite voltage range for which only one output count number will result (see figure 5-1). In computing  $\sigma_0$  the noise voltage is subtracted from the signal voltage. The difference between signal and noise voltages will be the same under each of the following three conditions (figure 5-1):

- When signal and noise voltage ( $V_{Snom}$ ) and noise ( $V_{Nnom}$ ) are in the middle of the voltage range for a particular count, respectively
- When signal and noise voltage  $V_{Smax} = V_{Snom} + 1/2$   
signal count and noise voltage  $V_{Nmin} = V_{Nnom} - 1/2$   
noise count
- When signal and noise voltage  $V_{Smin} = V_{Snom} - 1/2$   
signal count and noise voltage  $V_{Nmax} = V_{Nnom} + 1/2$   
noise count

This will assume importance when signal + noise voltage is so low that the difference between signal + noise and noise counts are no longer accurately related to the difference in actual voltages. The uncertainties caused can be examined for a particular case, e.g., when  $G_S = G_N = 1$  (highest gain)



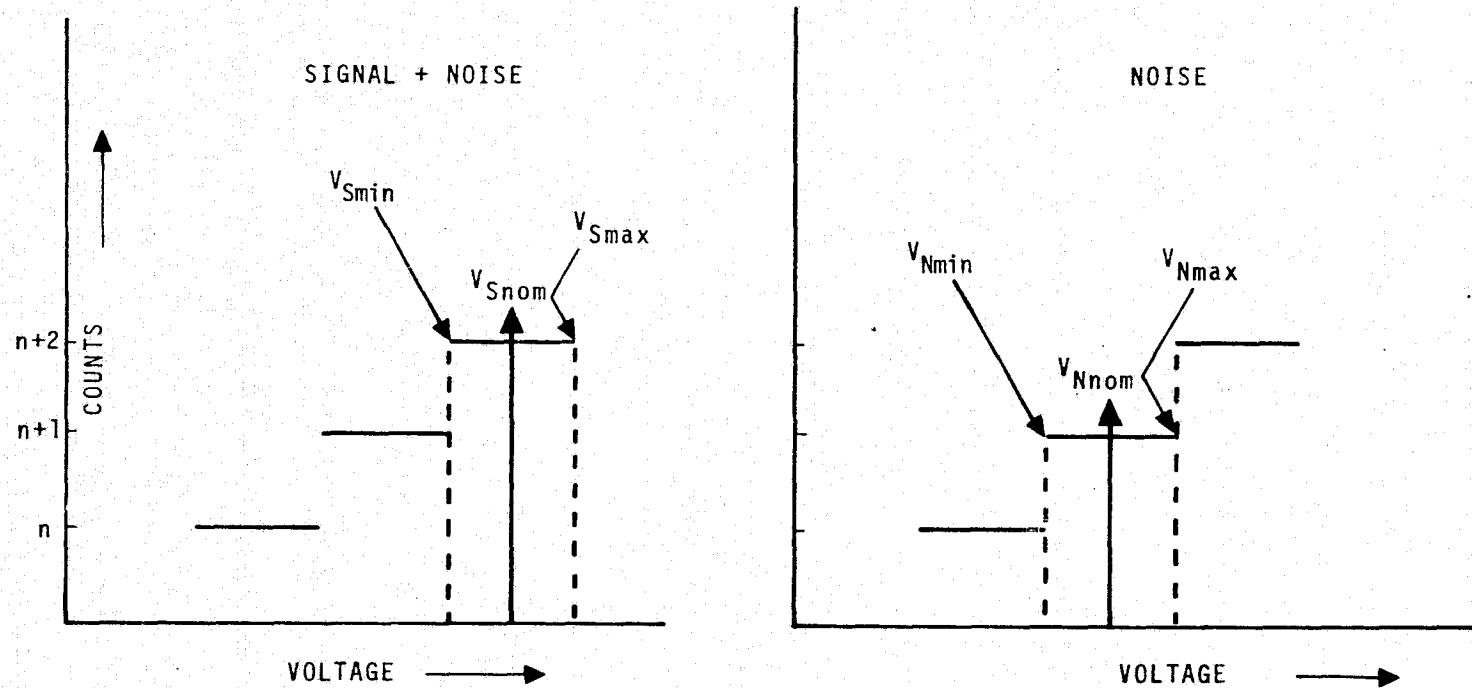


Figure 5-1. — Effect of A/D conversion on measurement uncertainty at low signal voltages.

and  $F_S = F_N$ . Under these conditions (see appendix B)

$$\sigma_o = \text{constant } (V_S'' - V_N'') \quad (24)$$

Now a maximum difference of  $(V_{S\text{max}}'' - V_{N\text{min}}'')$  will result in only  $(V_{S\text{nom}}'' - V_{N\text{nom}}'')$  at the output. Using equation (24) the uncertainty in the measurement of  $\sigma_o$  in dB (on the higher side) will be:

$$A' = 10 \log_{10} \left\{ \left[ V_{S\text{max}}'' - V_{N\text{min}}'' \right] / \left[ V_{S\text{nom}}'' - V_{N\text{nom}}'' \right] \right\} \quad (25)$$

On the other hand,  $(V_{S\text{min}}'' - V_{N\text{max}}'')$  difference causes the same nominal difference  $(V_{S\text{nom}}'' - V_{N\text{nom}}'')$  to be output. Hence, the uncertainty in  $\sigma_o$  (on the lower side) will be:

$$B' = 10 \log_{10} \left\{ \left[ V_{S\text{min}}'' - V_{N\text{max}}'' \right] / \left[ V_{S\text{nom}}'' - V_{N\text{nom}}'' \right] \right\} \quad (26)$$

provided  $V_{S\text{min}}'' > V_{N\text{max}}''$ . As a consequence, the real value of  $\sigma_o$  in dB could range from  $(\sigma_o + A')$  to  $(\sigma_o - B')$  but if  $V_{S\text{min}}'' \leq V_{N\text{max}}''$  only the upper limit  $(\sigma_o + A')$  can be determined. Equations (25) and (26) were used to find the range of uncertainties for the Ava pass data. At GMT 18:59:16.901 the value of  $\sigma_{o\text{VV}}$  is -37.43 dB. However, due to A/D conversion characteristics, the actual  $\sigma_o$  can range from a maximum of -35.85 dB to a minimum of -39.95 dB. At GMT 18:59:1.639 the reported  $\sigma_o$  is -29.46 dB for VV polarization. The actual  $\sigma_o$  will be within a range of (including extremes) -29.19 to -29.75 dB. Computations similar to these make it obvious that essentially the data below -33 dB will suffer an uncertainty of 2 dB or more because of A/D conversion alone. This uncertainty reduces to approximately 0.5 dB at a  $\sigma_o$  of -29 dB. It is because of this that the use of all  $\sigma_o$  data below approximately -33 dB should be avoided.

Although this section primarily referenced the deep space data, all very low values of  $\sigma_0$  are being discussed. One such example is the  $\theta = 52.5^\circ$  (approximately) data over Hurricane Ava. The spacecraft was in a solar inertial mode. Because of this a pitch angle variation was introduced (figure 5-2). S-193 was operated in CTNC/right-only mode. Thus only the  $0^\circ$  Doppler filters were used. The response curves for the  $0^\circ$  Doppler filters are shown in figure 5-3 (reference 33). Computations show that beyond approximately 18:59:16 GMT the sensor was receiving only a small amount of energy mainly through the side lobes of the antenna. (A complete discussion of why this happens can be found in reference 33.) The values of  $\sigma_0$  for the Ava pass, beyond 18:59:16 are given in table 5-III. The data is quite similar to that of deep space. Polarization dependence is lost. For this data the uncertainty due to A/D conversion alone is approximately 4 dB. The variance in the data is due to the poor S/N ratio at the input to the antenna. For this data the range of half standard deviation is from -36.67 to -32.96 dB, and therefore corrections to this data are useless.

There are many instances where the  $\sigma_0$  value suddenly drops very low (approximately -37 dB or below). During some of these periods, the scatterometer was in a standby mode (i.e., transmitter off), thus no scattered signal was received, only noise. (Note: the scatterometer was put in the standby mode before the radiometer; however, the data processing is continued up to the time radiometer was put in standby mode.) Two such examples are:

- EREP pass 11 14:49:29.415 GMT  $\sigma_{0VH}$  after this time are -37.47 and -42.60 dB.

TABLE 5-III. -  $\sigma_o$  VALUES FOR  $\theta \approx 52.5^\circ$  EREP AVA PASS  
BEYOND 18:59:16 GMT

Time GMT	$\sigma_o$	Polarization
18:59:16.9	-37.43	VV
	-36.01	HV
	-30.98	HH
	-36.50	VH
18:59:32.145	-36.01	VV
	-37.40	HV
	-33.03	HH
	-34.10	VH
18:59:47.989	-37.37	HV
	-29.56	HH
	-36.48	VH
19:00:3.233	-36.76	HV
	-29.98	HH
	-36.45	VH
19:00:17.895	-35.83	VV
	-35.81	HV
	-39.37	HH
	-39.14	VH

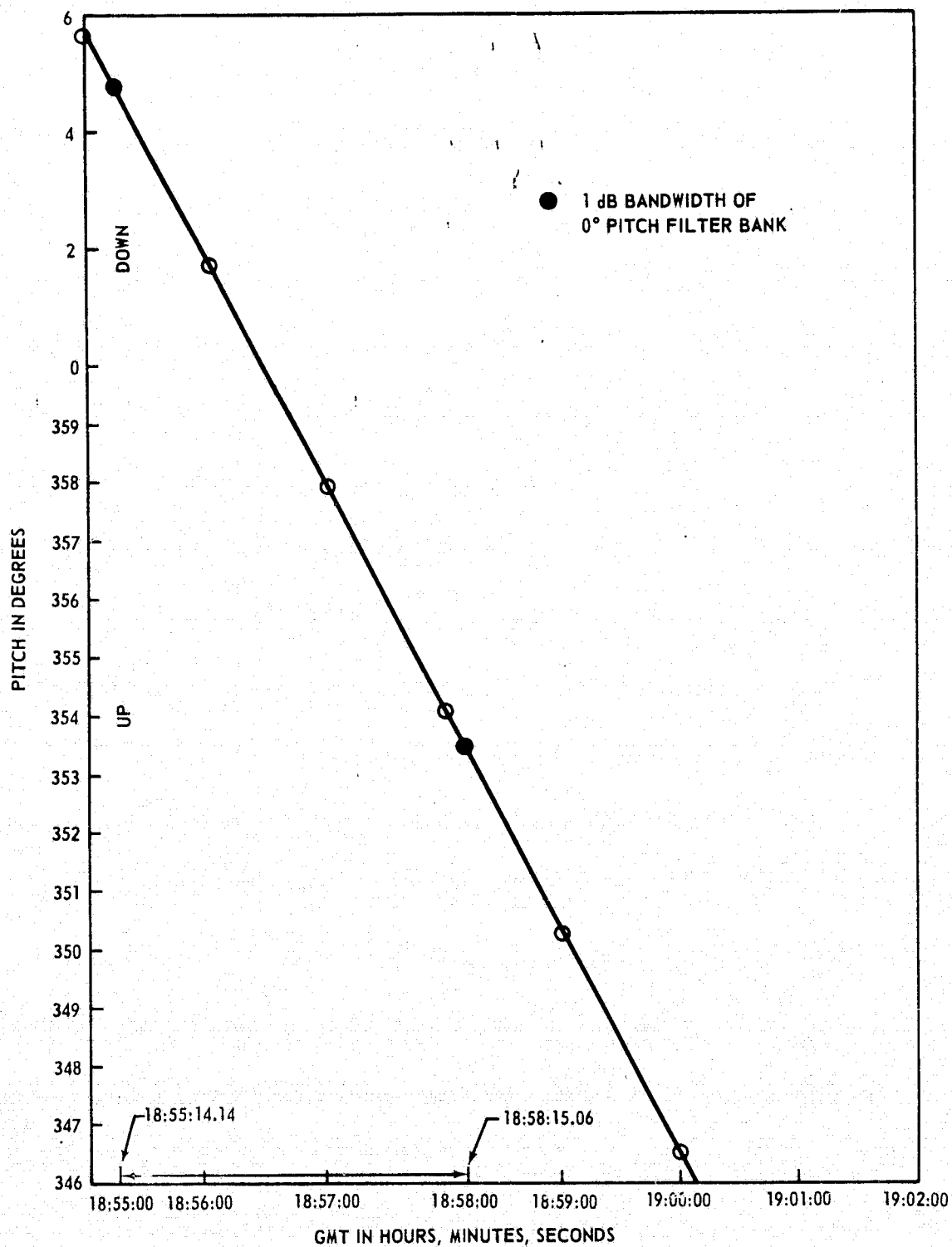


Figure 5-2. — Skylab pitch angle variation as a function of time (EREP Ava pass).

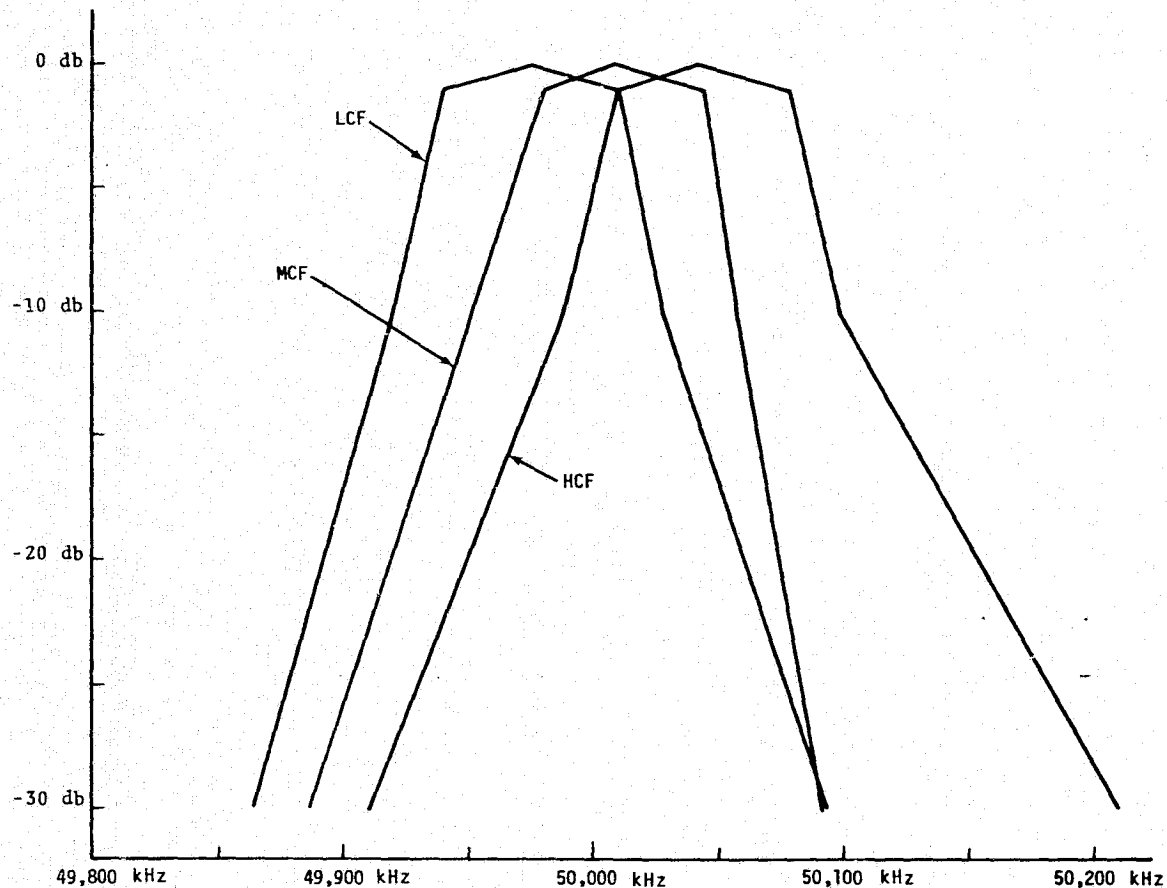


Figure 5-3. — Zero degree filter bank response curves for low center frequency (LCF), middle center frequency (MCF), and high center frequency (HCF) Doppler filters.

- EREP pass 20 14:53:1.45 GMT  $\sigma_{oVV}$  after this time are -43.87 and -50.46 dB.

Unfortunately, this invalid data has been used in determining the average  $\sigma_o$  and the standard deviation of  $\sigma_o$  (product S062-8). It is therefore recommended that caution be exercised in using product S062-8 for data segments where  $\sigma_o$  plunges to low values.

## 5.2 OCEAN $\sigma_o$ DATA

### 5.2.1 EREP Pass 5, Gulf of Mexico

The data over the Gulf of Mexico provides a better opportunity to study the precision/accuracy of the S-193 Scatterometer. This is because of the homogeneity of the electrical and surface roughness properties. This aspect of the data will be addressed here.

Extensive ground truth was collected by NOAA during the Skylab data take. The location where ground data was gathered by the NOAA aircraft is shown in figure 5-4. This data was taken nearly simultaneously with the EREP data. To assign the data to the proper location on the ground, the S-193 Scatterometer data from GMT 18:2:24.155 to 18:4:24:104 was sorted. Thus four sets (I through IV) were located at four ocean locations. The locations for VV data are shown in figure 5-4, along with the Skylab ground track. Since the 48° pitch angle was not achieved, this data is displaced from the data corresponding to other four-pitch angles. The backscatter data corresponding to these locations is given in figures 5-5, 5-6, 5-7, and 5-8. The ocean surface wind data is given in table 5-IV. This data was discussed with D. Ross (NOAA/Miami)

TABLE 5-IV. — OCEAN SURFACE WINDSPEEDS FOR EREP PASS 5

(a) Data Set: I, Pass 5

Date	Time GMT	Latitude	Longitude	Windspeed measured at A/C altitude	Wind at 20 meters
73 06 05	18:51:01.2	26.104	-93.439	16.0	
	18:52:51.0	26.164	-93.494	16.0	
	18:55:51.0	26.263	-93.598	20.0	
	18:57:39.0	26.318	-93.664	17.0	
	18:58:51.1	26.356	-93.708	18.0	
	19:03:39.1	26.301	-93.647	15.0	
	19:06:35.5	26.290	-93.598	20.0	
	19:09:39.1	26.362	-93.784	17.0	
	19:12:39.1	26.433	-93.851	16.0	
	19:15:04.9	26.488	-93.950	17.0	
	19:19:40.9	26.510	-94.021	18.0	
	19:52:24.2	26.757	-93.878	2.0	
	19:54:12.2	26.829	-93.785	12.0	
	19:57:12.2	26.944	-93.625	17.0	
	20:00:12.2	27.076	-93.444	16.0	
Average				15.8	14.22



TABLE 5-IV. — OCEAN SURFACE WINDSPEEDS FOR EREP PASS 5 (Continued)

(b) Data Set: II, Pass 5

Date	Time GMT	Latitude	Longitude	Windspeed measured at A/C altitude	Wind at 20 meters
73 06 05	18:26:21.6	25.477	-92.933	17.0	
	18:27:33.6	25.461	-92.889	19.0	
	18:29:21.6	25.439	-92.823	12.0	
	18:32:21.6	25.488	-92.829	18.0	
	18:35:21.6	25.587	-92.933	18.0	
	18:37:09.6	25.642	-92.904	18.0	
	18:38:57.6	25.697	-93.054	13.0	
	18:40:47.4	25.757	-93.115	17.0	
	18:43:49.2	25.856	-93.214	16.0	
	18:45:37.2	25.917	-93.268	17.0	
	18:48:01.2	25.999	-93.345	17.0	
Average				16.54	14.89

TABLE 5-IV. — OCEAN SURFACE WINDSPEEDS FOR EREP PASS 5 (Continued)

(c) Data Set: III, Pass 5

Date	Time GMT	Latitude	Longitude	Windspeed measured at A/C altitude	Wind at 20 meters
73 06 05	18:00:28.1	24.714	-92.230	15.0	
	18:01:40.1	24.758	-92.269	16.0	
	18:02:52.1	24.796	-92.307	13.0	
	18:05:16.1	24.879	-92.384	18.0	
	18:06:28.1	24.922	-92.422	15.0	
	18:08:17.2	24.983	-92.483	14.0	
	18:10:41.9	25.065	-92.560	15.0	
	18:13:41.9	25.164	-92.659	19.0	
	18:15:33.5	25.225	-92.719	17.0	
	18:17:57.5	25.307	-92.802	17.0	
	18:19:45.5	25.367	-92.862	16.0	
	18:21:33.5	25.433	-92.922	14.0	
Average				15.75	14.175

TABLE 5-IV. — OCEAN SURFACE WINDSPEEDS FOR EREP PASS 5 (Concluded)

(d) Data Set: IV, Pass 5

Date	Time GMT	Latitude	Longitude	Windspeed measured at A/C altitude	Wind at 20 meters
73 06 05	16:20:06.8	24.774	91.708	17	
	16:21:22.4	24.788	91.791	17	
	16:22:35.0	24.642	91.868	17	
	16:23:53.6	24.565	91.95	17	
	16:25:09.2	24.494	92.021	17	
	16:28:56.0	24.472	92.098	13	
	16:39:42.8	24.510	91.917	4	
	16:34:36.2	24.565	91.846	14	
	16:36:29.6	24.593	91.978	7	
	16:39:36.9	24.543	92.038	8	
	16:49:39.9	24.554	92.071	15	
	16:50:55.5	24.549	91.994	12	
	16:52:11.1	24.543	91.917	11	
	16:54:04.5	24.505	91.95	12	
	16:55:57.9	24.527	92.075	11	
	16:59:44.7	24.505	92.071	11	
	16:05:08.7	24.423	91.989	10	
	16:26:08.8	24.401	91.978	12	
	16:32:46.6	24.384	92.016	12	
	16:45:24.5	24.478	92.131	13	
Average				12.5	11.25

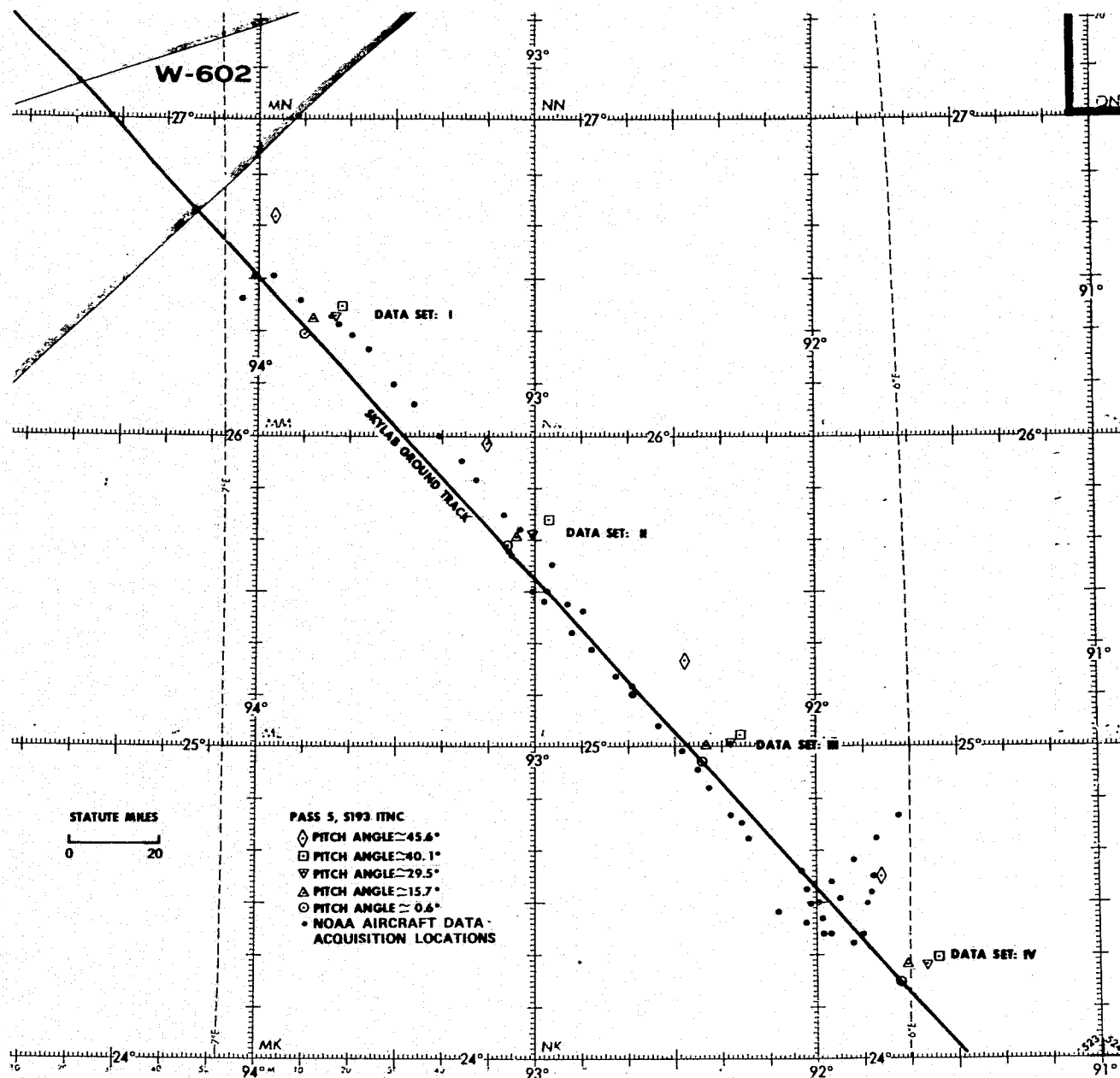


Figure 5-4. — Location of field-of-view (FOV) for S-193 Scatterometer VV data and NOAA aircraft for Skylab 2, EREP pass 5 (Gulf of Mexico).

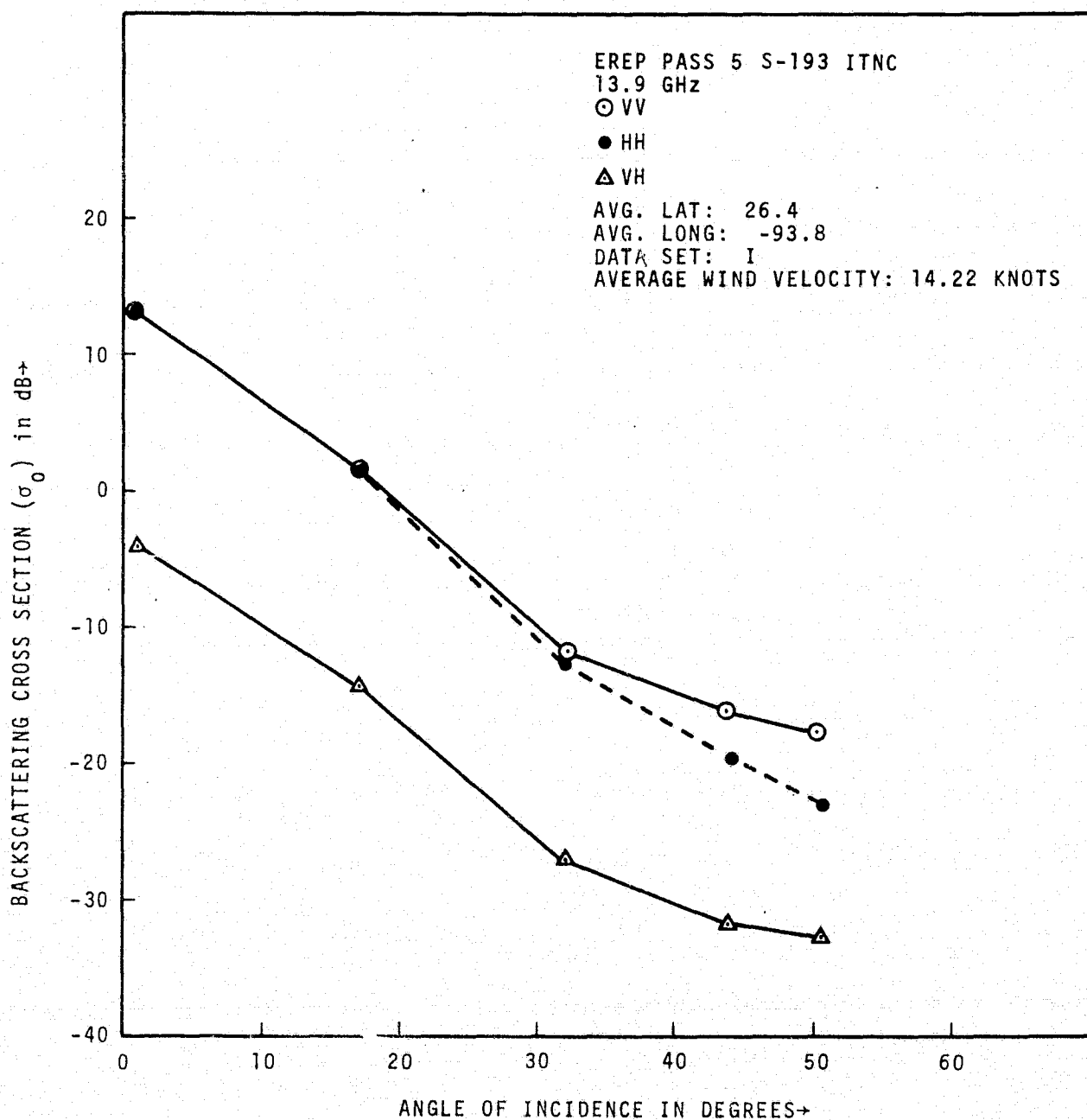


Figure 5-5. — Backscattering cross section as a function of  $\theta$  for data set I (pass 5).

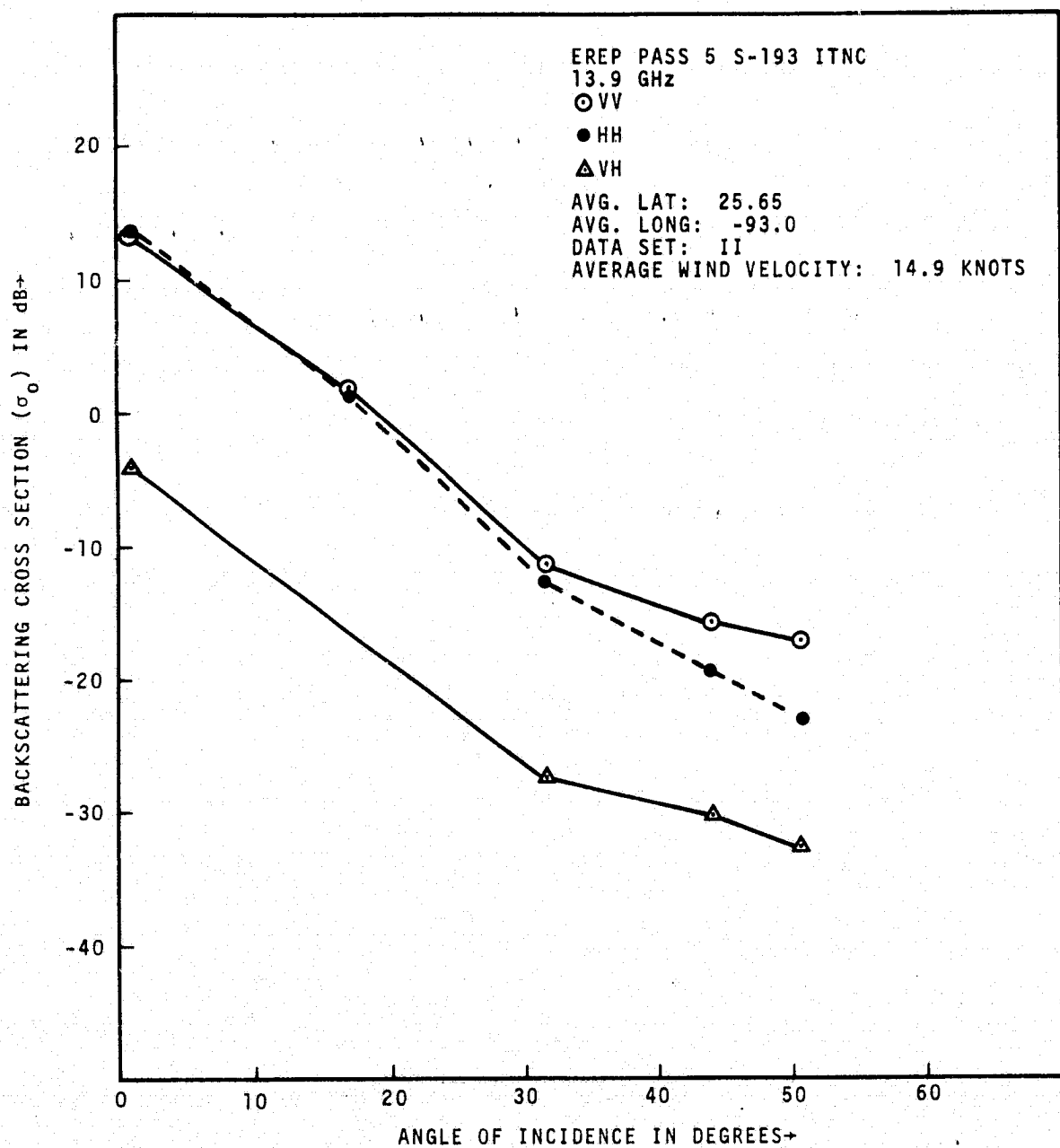


Figure 5-6. — Backscattering cross section as a function of  $\theta$  for data set II (pass 5).

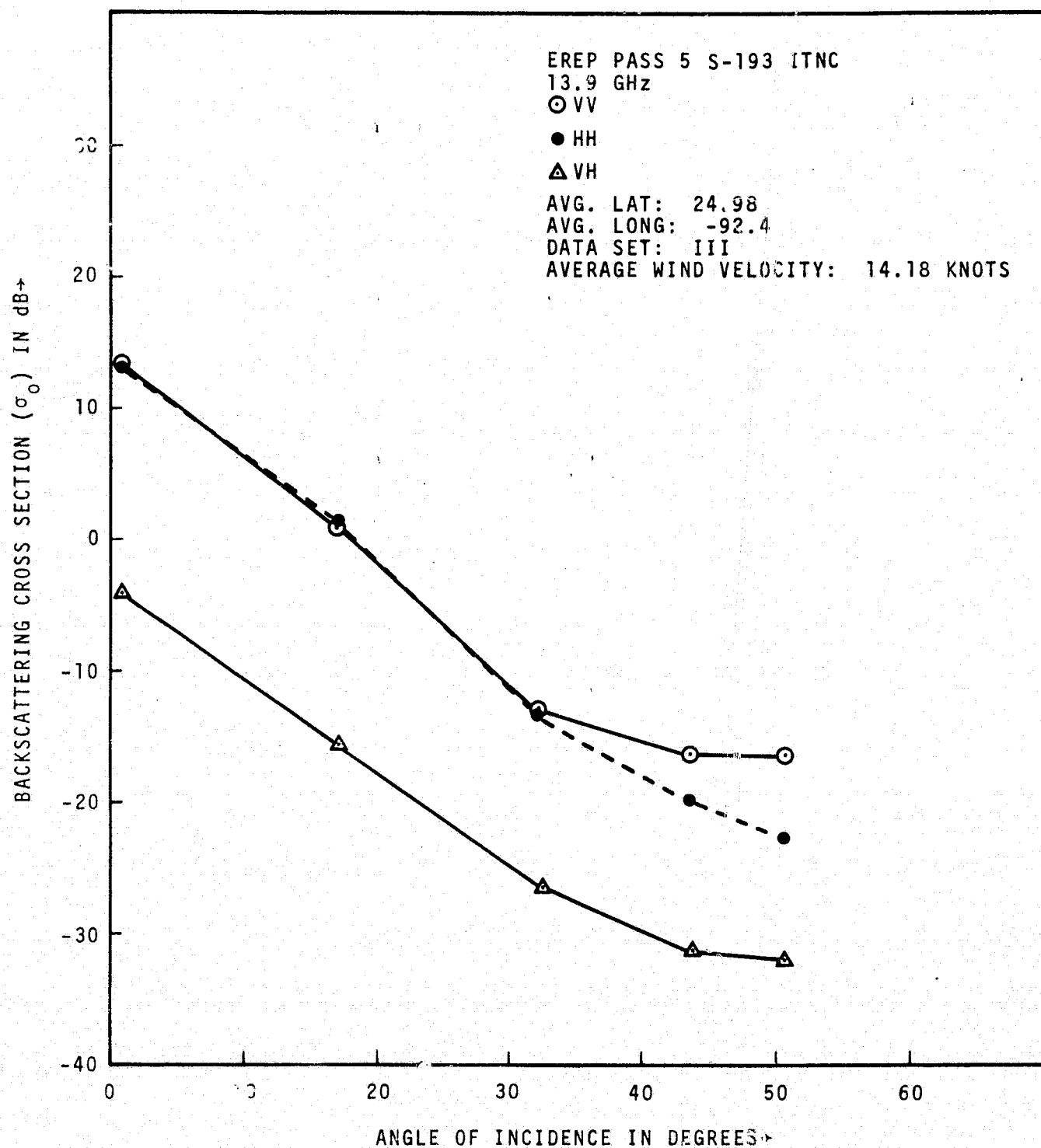


Figure 5-7. — Backscattering cross section as a function of  $\theta$  for data set III (pass 5).

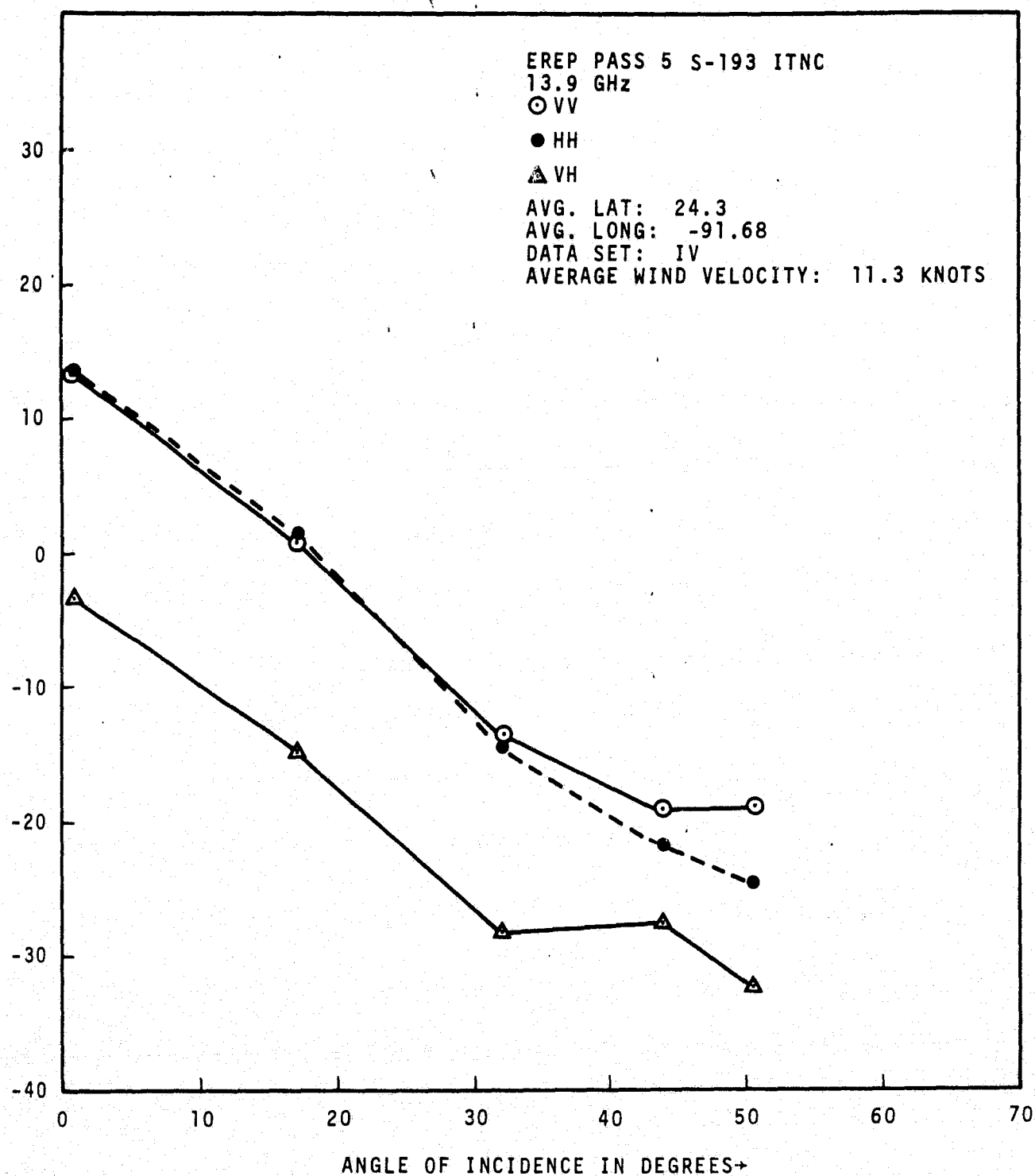


Figure 5-8. — Backscattering cross section as a function of  $\theta$  for data set IV (pass 5).



and the winds were scaled to 20 meters from the ocean surface according to his recommendation. The wind direction was not uniform for the small resolution cells sensed by the aircraft sensors. The weather maps from the U.S. Weather Bureau show an average ocean surface wind velocity of 12 knots from 90° in this region (table 5-V was compiled by J. Carney/LEC). The data of tables 5-IV and 5-V shows the homogeneity of the ocean wind field to within 4 knots (standard deviation). The  $\sigma_o$  data also shows consistence, in that the dependence on  $\theta$  and polarization is as expected at this wind velocity. The values of  $\sigma_{oVH}$  and  $\sigma_{oHV}$  are equal to within 0.5 dB (rms). The precision/accuracy of this data will be reported in section 6 of this report.

The homogeneity of the dielectric properties can be assessed by analyzing the L-band S-194 Radiometer data. For this vertical-looking sensor, the effects of ocean surface wind velocity (which varies from 9 to approximately 16 knots within one sigma standard deviation) are negligible. The measured antenna temperature varies from 105.9 to 105.0°K over a period from GMT 18:03:32.35 to 18:04:36.56. These radiometric temperatures have a constant offset because of sun angle correction. This correction will reduce all temperatures by a few degrees. The standard deviation for 184 data samples is less than 0.3°K. The approximate reflectivity  $R(o)$  can be calculated using the equation:

$$T_A = L_2 \left[ T_s |R(o)|^2 + (1 - |R(o)|^2) T_g \right] + T_{ATM} \quad (27)$$

where  $L_2$  is the transmittance of the atmosphere,  $T_A$  is the radiometric antenna temperature,  $T_s$  the sky background temperature,  $T_g$  the ground temperature, and  $T_{ATM}$  the radiometric temperature of the atmosphere. For  $T_s = 4^\circ K$ ,  $L_2 = 0.99$ ,  $T_g = 300^\circ K$  (from table 5-V),  $T_A = 105^\circ K$ ,  $T_{ATM}$  is

TABLE 5-V. — SURFACE AND ATMOSPHERIC CONDITIONS FOR SL-2 TARGET SITES

Site number	Site name	Skylab pass number	Cloud cover	Visibility	Pressure (MB)	Air temperature (°F)	Dew point	Average winds and direction	Significant wave height (feet)	Water temperature (°F)
750598	Gulf of Mexico	1	8/10*	N/A	N/A	82.4	23	12 knots from 80°	2	73.4
750598	Gulf of Mexico	5	6/10*	N/A	N/A	80.6	24	12 knots from 90°	2	75.2
750598	Gulf of Mexico	8	6/10*	N/A	N/A	82.4	24	11 knots from 90°	2	73.4
750598	Gulf of Mexico	11	4/10*	N/A	N/A	82.4	24	14 knots from 130°	3	73.4
750233	Great Salt Lake Desert	5	Clear	20 miles	1,022.0	74	21	5 knots at 210° SSW	—	—

\*These cloud covers were reported only for some portion of the ground site. The cloud cover over all the ground site area used was less than 50 percent. The duration of the winds was long (fully developed seas).

taken 1.5°K for U.S. Standard Atmosphere; the value of  $|R(o)|$  is equal to 0.812. Furthermore, the variability of  $|R(o)|$  for 0.9°K change in  $T_A$  is negligible. It is interesting to compare this value of  $|R(o)|$  with those measured and quoted in literature. From Von Hippel (reference 34) the value of dielectric constant is:

$$\epsilon = 76.7 (1 + j 0.157)$$

for water at 25°C at a frequency of 3 GHz. The value of  $|R(o)|$  for this case is:

$$|R(o)| = 0.80$$

This value of  $|R(o)|$  at S-band shows good agreement with that predicted from S-194 L-band Radiometer measurement since a slight decrease is expected as the frequency increases.

The S-193 Radiometer data for  $\theta \approx 0.9^\circ$  varies from 125.31 to 127.96°K for GMT from 18:2:24.155 to 18:4:24.104. Taking  $T_S = 10^\circ\text{K}$  and  $T_g = 297^\circ\text{K}$ ,  $L_2 = 0.98$ ,  $T_{\text{ATM}} = 4.8^\circ\text{K}$  for U.S. Standard Atmosphere  $|R(o)| = 0.777$  for  $T_A = 127^\circ\text{K}$ . It is interesting to compare this with the value of  $|R(o)|$  calculated from  $\epsilon = 55 (1 + j 0.55)$  quoted in reference 4 for sea surface at X-band. For this  $\epsilon$ ,  $|R| = 0.78$ .

This  $|R(o)|$  is slightly higher than that calculated at 13.9 GHz. This is in accord with the dependence of  $\epsilon$  on frequency.

No dielectric constant measurements of water with salt concentrations have been quoted in literature at 13.9 GHz. Paris (reference 35) has compiled a table of aqueous sodium chloride dielectric constants measured by various investigators. At 10 GHz the value of the dielectric constant (reference 36) for aqueous sodium chloride at 21°C is:

$$\epsilon = 65(1 + j 0.44)$$

and for 23.7 GHz at 20°C (reference 37)

$$\epsilon = 42.97 (1 + j 0.74)$$

A linear interpolation between these frequencies yields a value of

$$\epsilon = 59 (1 + j 0.66)$$

for the dielectric constant of aqueous sodium chloride at 20.5°C for a frequency of 13.9 GHz. The reflection coefficient using this value of the dielectric constant is:

$$|R(o)| = 0.779$$

which is reasonably close to the predicted value of 0.777 using S-193 Radiometer data.

The following conclusions can be drawn by analyzing the S-194 and S-193 Radiometer data:

- The value of the reflectivity  $|R(o)|$  predicted using L-band S-194 Radiometer data shows a reasonably good agreement with those calculated at a slightly higher frequency (3 GHz) (considering, of course, the frequency dependence).
- The value of  $|R(o)|$  calculated using S-193 Radiometer data is reasonably in agreement with values calculated near this frequency.
- $|R(o)|$  shows proper frequency dependence behavior from S-193 and S-194 Radiometer data.
- The S-194 Radiometer data shows that the dielectric properties of the Gulf of Mexico were homogeneous. The S-193 Radiometer also shows homogeneity. The interpretation (taking into account the frequency dependence of the dielectric properties) of S-194

and S-193 Radiometer data was necessary. The L-band frequencies are sensitive to salinity changes (reference 38) compared with the  $K_u$ -band frequencies which are sensitive to the sea state (reference 39). Hence, it was deemed proper to analyze data at both frequencies to arrive at the stated conclusion of reflectivity homogeneity of the Gulf of Mexico for the data examined.

### 5.2.2 EREP Pass 8, Gulf of Mexico

The ITNC mode was exercised on June 11, 1973, to gather radiometer and scatterometer data over the Gulf of Mexico. The location of the FOV for the S-193 scatterometer vertical-transmit, vertical-receive data is shown in figure 5-9 for GMT 15:21:6.286 to 15:22:50.991. The wind measurements were taken with the LTN 51 airborne sensor by NOAA. The aircraft was flown at 200 feet altitude and corrections made to calculate winds at a height of 20 meters. The scatterometer data corresponding to the three locations shown in figure 5-9 is given in figures 5-10, 5-11, and 5-12. The  $\sigma_0$  versus  $\theta$  figures indicate that the general appearance of dependence is as expected from theoretical and previous experimental data considerations. The polarization dependence is also normal.

The homogeneity of the dielectric properties (or reflectivity) can be examined by reviewing the S-194 and S-193 Radiometer data. For GMT 15:21:9.93 to 15:22:59.07 the minimum radiometric antenna temperature for S-194 is 90.3°K with a maximum of 92.1°K. This small range of values shows that no significant nonhomogeneities were present. The average temperature was approximately 91°K. Using equation (27)

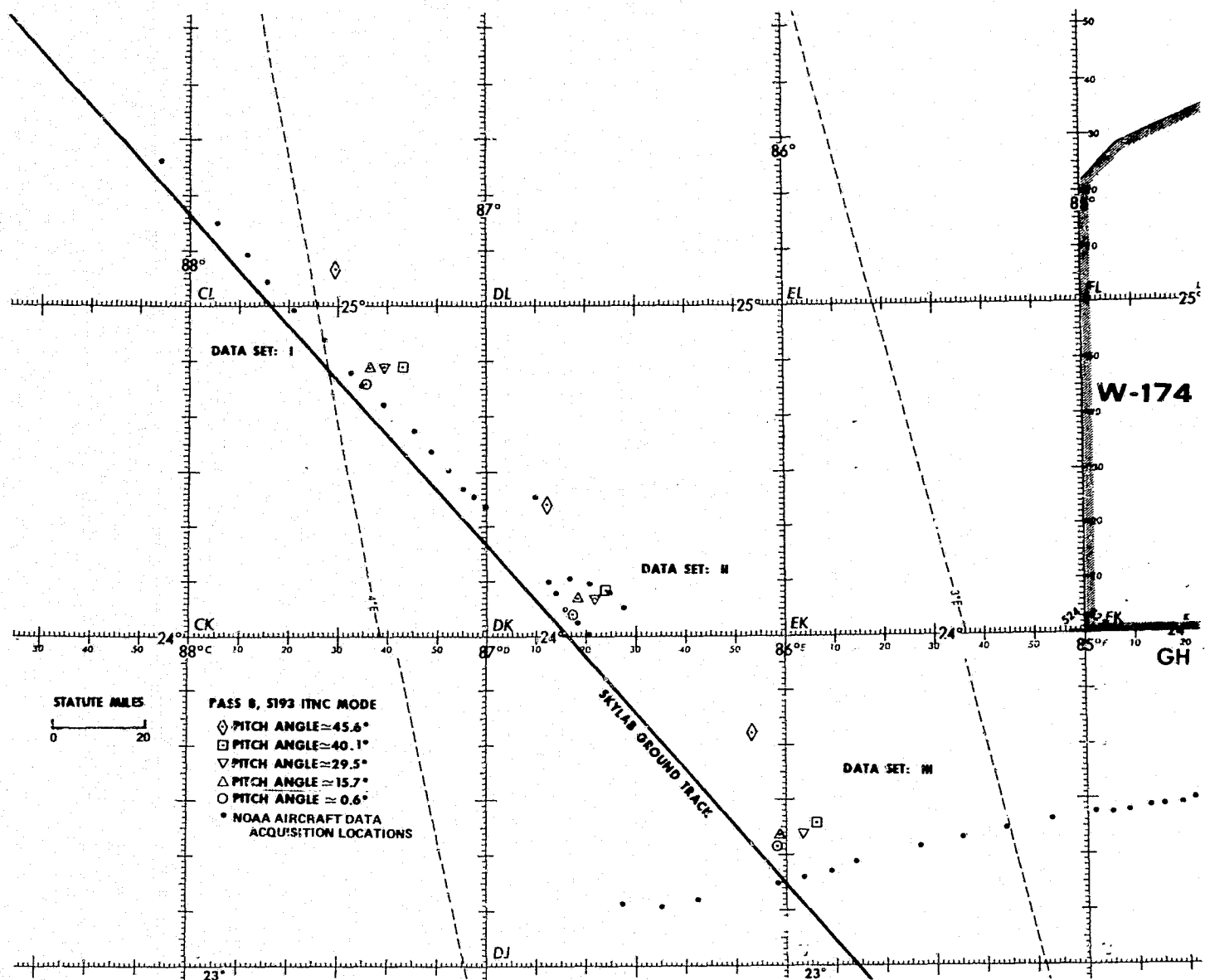


Figure 5-9. — Location of field-of-view (FOV) for S-193 Scatterometer VV data and NOAA aircraft data for Skylab 2, EREP pass 8 (Gulf of Mexico).

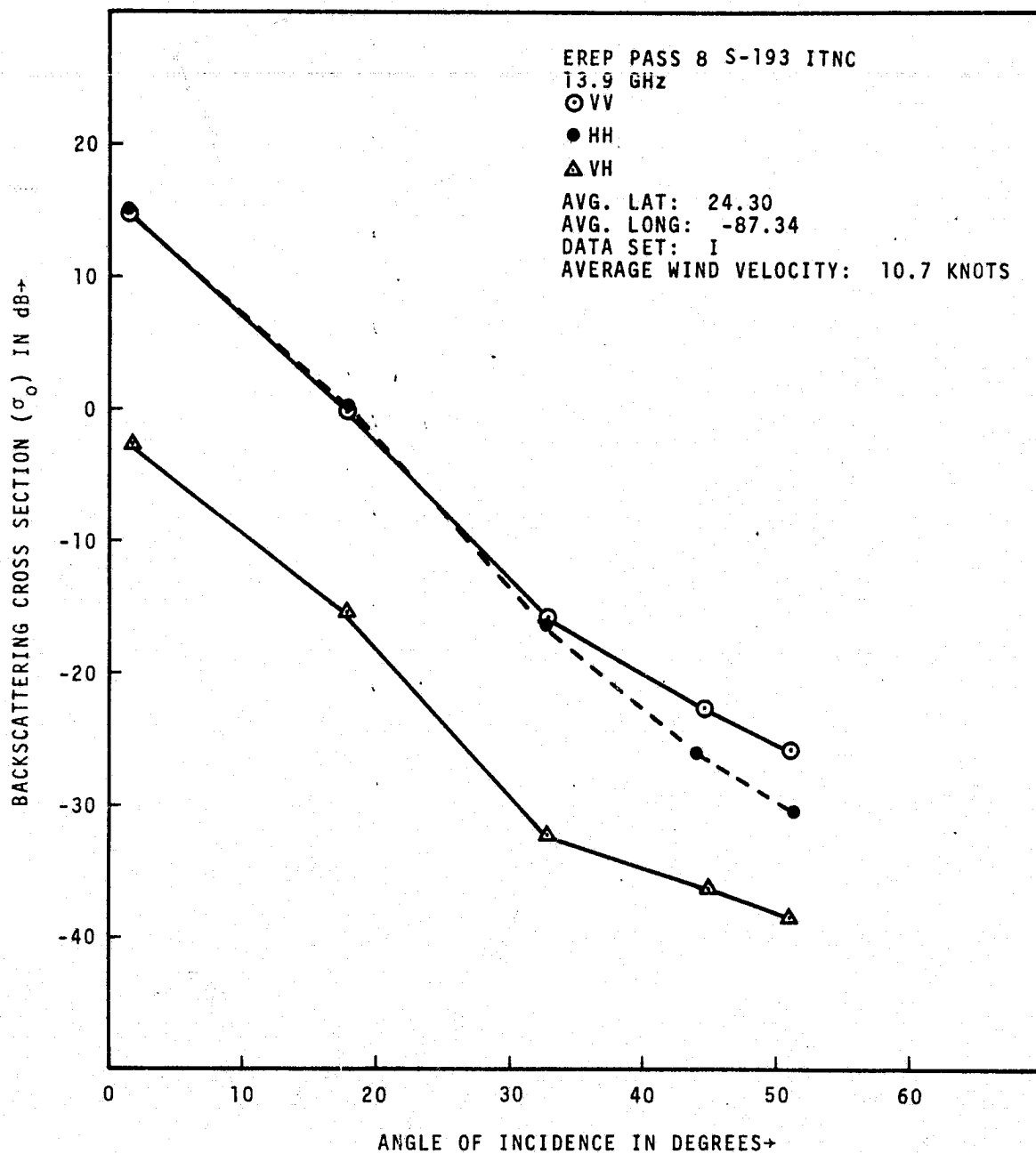


Figure 5-10. — Backscattering cross section as a function of  $\theta$  for data set I (pass 8).

C-2

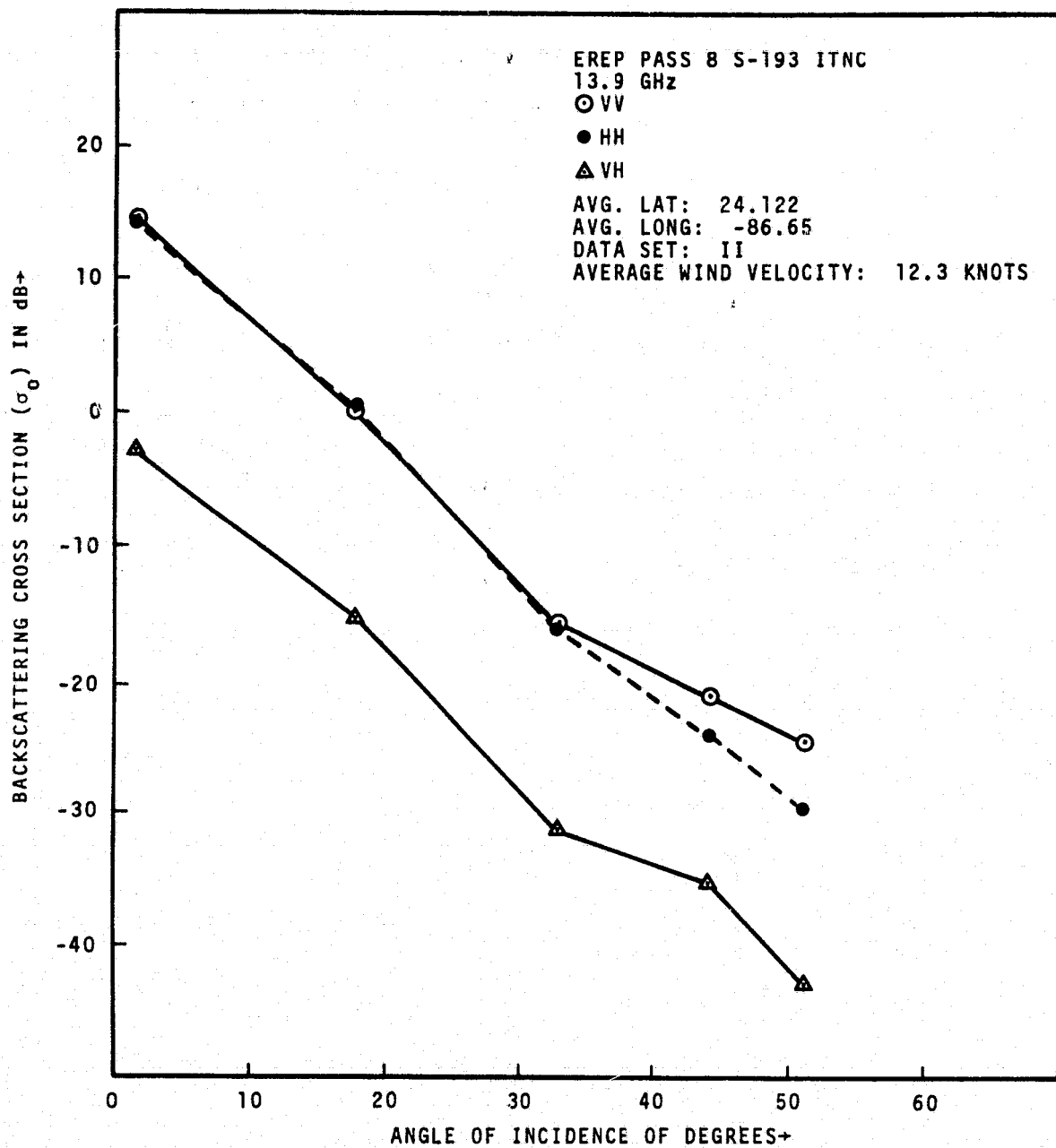


Figure 5-11. — Backscattering cross section as a function of  $\theta$  for data set II (pass 8).



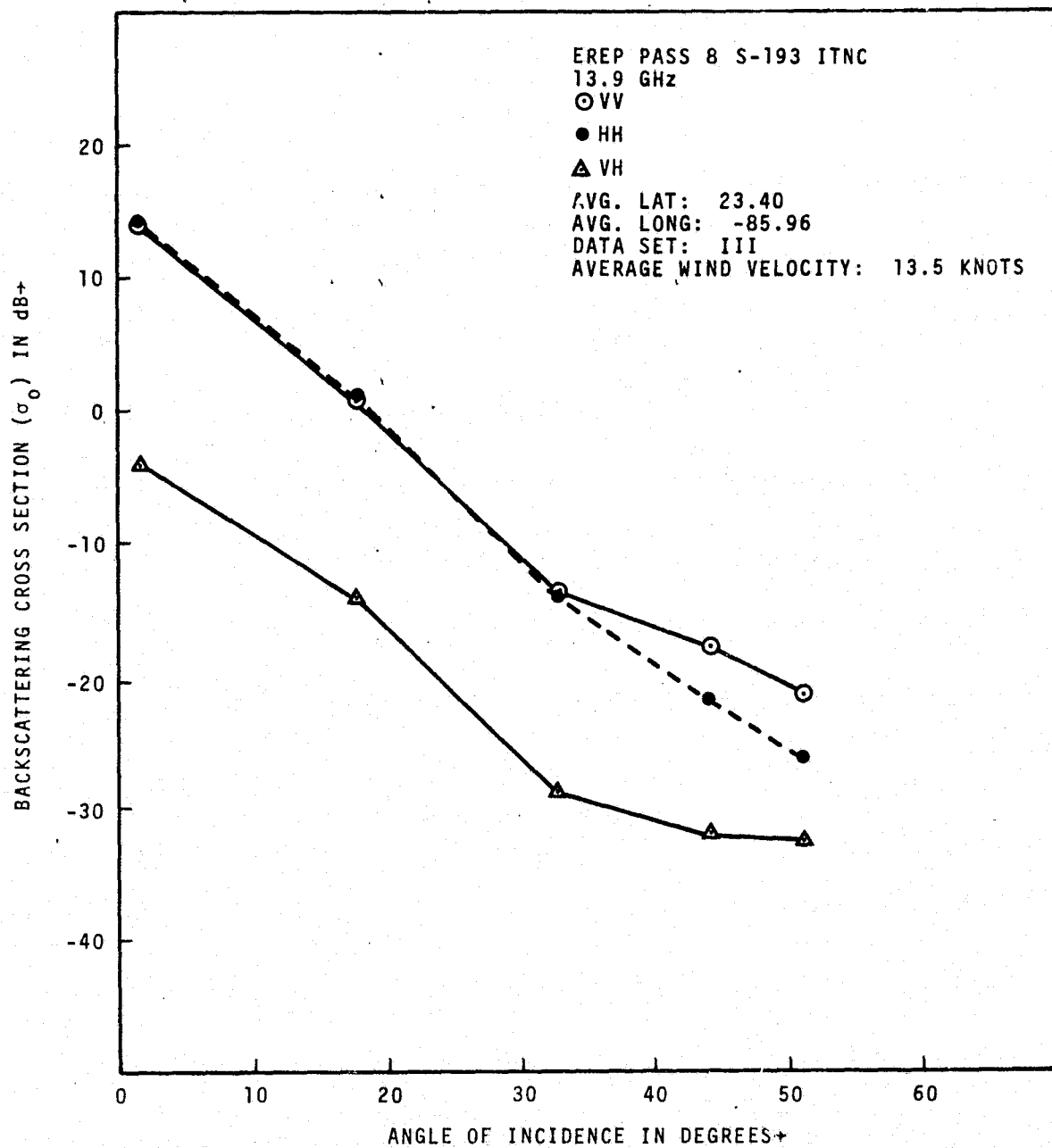


Figure 5-12. — Backscattering cross section as a function of  $\theta$  for data set III (pass 8).

and table 5-V, the value of reflectivity  $C|R(o)|$  is 0.839. This is in agreement with the values given in section 5.2.1. The S-193 Radiometer temperature for  $0^\circ$  incidence shows a variance of approximately  $2^\circ\text{K}$  with an average value of approximately  $125^\circ\text{K}$ . The reflectivity computed from equation (27) is  $|R(o)| = 0.768$ . This is in excellent agreement with EREP pass 5 data.

The wind measurements reported by the U.S. Weather Bureau at NASA/JSC (see table 5-V) are quite in agreement with NOAA detailed measurements (see table 5-VI) taken almost simultaneously ( $\pm 1$  hour). The noteworthy aspect of the wind fields for this pass is that these are very close to the winds present at the time of EREP pass 5 over the Gulf of Mexico. This will permit comparisons of this data and provide insight into the precision/accuracy performance of the S-193 Scatterometer. The ocean wind variations for the data shown in figures 5-10, 5-11, and 5-12 are also small (approximately 5 knots standard deviation). The homogeneity of the ocean wind field is very much like that of EREP pass 5.

The preceding paragraph leads to the conclusion that the dielectric constant of the ocean surface is very nearly the same as for EREP pass 5 over the Gulf of Mexico. Furthermore, a fairly high degree of homogeneity was shown for the ocean surface for the EREP pass 8.

### 5.2.3 EREP Passes 11 and 20, Gulf of Mexico

Data from passes 11 (SL-2) and 20 (SL-3) offers an opportunity to study the performance of the scatterometer in intrack contiguous (ITC) mode. During pass 11 the data

TABLE 5-VI. — OCEAN SURFACE WINDSPEEDS FOR EREP PASS 8

(a) Data Set: I, Pass 8

Date	Time GMT	Latitude	Longitude	Windspeed measured at A/C altitude	Wind at 20 meters
73 06 11	15:48:10.8	24.395	87.001	14	
	15:48:48.8	24.412	87.023	14	
	15:49:22.8	24.428	87.045	12	
	15:49:58.8	24.45	87.061	12	
	15:50:36.6	24.467	87.083	11	
	15:51:48.6	24.505	87.127	12	
	15:52:24.6	24.521	87.144	14	
	15:53:00.6	24.543	87.122	14	
	15:53:36.6	24.56	87.187	13	
	15:55:24.6	24.62	87.248	27	
	15:57:12.7	24.703	87.347	15	
	15:57:48.7	24.73	87.38	14	
	15:58:24.7	24.763	87.413	12	
	15:59:00.7	24.796	87.446	14	
	15:59:36.7	24.829	87.479	12	
	16:00:50.5	24.895	87.55	12	
	16:01:26.5	24.922	87.578	9	
	16:02:02.5	24.961	87.610	11	
	16:02:38.5	24.988	87.649	11	
	16:03:14.5	25.021	87.676	10	
	16:03:50.5	25.054	87.709	10	
	16:04:26.5	25.087	87.742	10	
	16:05:02.5	25.129	87.775	9	
	16:05:38.5	25.158	87.808	8	
	16:08:14.5	25.186	87.841	8	
	16:06:50.5	25.219	87.869	10	
	16:07:28.3	25.252	87.907	8	
	16:08:04.3	25.280	87.940	7	
	16:08:40.3	25.312	87.968	9	
	16:11:06.1	25.444	88.099	7	

TABLE 5-VI. — OCEAN SURFACE WINDSPEEDS FOR EREP PASS 8 (Continued)

(a) Data Set: I, Pass 8

Date	Time GMT	Latitude	Longitude	Windspeed measured at A/C altitude	Wind at 20 meters
73 06 11	16:12:19.9	25.510	88.165	8	
	16:12:55.9	25.543	88.198	4	
	16:13:31.9	25.571	88.231	6	
	16:14:07.9	25.604	88.264	6	
	16:15:19.9	25.664	88.330	7	
	16:15:55.9	25.697	88.363	7	
	16:16:31.9	25.730	88.391	7	
	16:17:43.9	25.796	88.456	7	
	16:18:99.9	25.829	88.484	11	
	16:19:31.9	25.895	88.550	6	
Average				11.9	10.71

TABLE 5-VI. — OCEAN SURFACE WINDSPEEDS FOR EREP PASS 8 (Continued)

(b) Data Set: II, Pass 8

Date	Time GMT	Latitude	Longitude	Windspeed measured at A/C altitude	Wind at 20 meters
73 06 11	15:22:55.2	24.005	86.660	12	
	15:23:31.2	24.027	86.682	16	
	15:24:07.2	24.044	86.699	14	
	15:24:43.2	24.066	86.721	14	
	15:25:21.0	24.088	86.737	15	
	15:25:57.0	24.104	86.759	14	
	15:26:33	24.126	86.776	16	
	15:27:09.0	24.148	86.797	12	
	15:27:45	24.164	86.797	12	
	15:29:33	24.170	86.726	11	
73 06 11	15:30:09.0	24.164	86.704	13	
	15:30:45.0	24.153	86.682	9	
	15:53:09.0	24.126	86.583	10	
	15:53:45.0	24.115	86.561	11	
	15:34:21.0	24.109	86.539	11	
	15:34:57.0	24.088	86.539	13	
	15:35:33.0	24.082	86.517	13	
	15:36:09	24.104	86.528	16	
	15:36:45	24.109	86.556	15	
	15:37:21	24.115	86.583	17	
	15:37:57	24.126	86.611	15	
	15:38:33	24.131	86.638	16	
	15:39:09	24.142	86.666	15	
	15:39:45	24.153	86.693	15	
	15:40:21	24.159	86.721	15	
	15:40:57	24.170	86.748	14	
	15:41:33	24.186	86.770	14	
	15:42:09	24.203	86.792	17	
	15:42:45	24.225	86.814	14	
	15:43:21	24.241	86.836	13	
Average				13.7	12.33

TABLE 5-VI. — OCEAN SURFACE WINDSPEEDS FOR EREP PASS 8 (Concluded)

(c) Data Set: III, Pass 8

Date	Time GMT	Latitude	Longitude	Windspeed measured at A/C altitude	Wind at 20 meters
73 06 11	14:23:23.8	23.5	84.633	19	
	14:23:59.8	23.494	84.694	20	
	14:24:35.8	23.483	84.749	18	
	14:25:11.8	23.478	84.809	18	
	14:25:49.6	23.472	84.864	14	
	14:26:25.6	23.461	84.919	10	
	14:27:03.4	23.456	84.974	10	
	14:28:51.4	23.439	85.128	19	
	14:38:27.4	23.286	85.853	21	
	14:39:39.4	23.264	85.946	11	
	14:40:51.5	23.242	86.034	11	
	14:44:27.5	23.192	86.287	16	
	14:46:15.5	23.181	86.424	10	
	14:48:03.5	23.187	86.545	13	
Average				15	13.5

was collected in VV and then in VH polarization mode, while VV polarization was exercised during pass 20. The ground track and locations where data was taken for the pitch angles of approximately  $39.5^\circ$  and  $42^\circ$  are shown in figure 5-13.

The ocean surface conditions at the time of pass 11 are summarized in table 5-V. Aircraft data with 13.3 GHz Scatterometer was also acquired during this pass. The data from pass 11 is shown in figure 5-14. The polarization and angle dependence of the backscattering cross sections are predictable from mathematical models. Detailed correlations with ground and aircraft data will be presented in section 6.

The ocean parameters for Skylab-3 data-takes over the Gulf of Mexico were compiled by J. Carney (LEC/ASD) and are given in table 5-VII. This data was collected by the U.S. Weather Bureau. The winds did not exceed 18 knots in the area for which the data will be analyzed in this report. Typical data is shown in figure 5-14. It should be noted here that in the ITC mode the data is taken over a large area for a plot of  $\sigma_0$  versus  $\theta$ . This makes it possible to have relative changes in  $\sigma_0$  from angle-to-angle due to entirely different ground locations. Fortunately, for passes 11 and 20, the variations in ocean surface wind velocity were insignificant. This is also reflected in the plots of figure 5-14 since the dependence on  $\theta$  is as expected from a homogeneous rough target.

One unique aspect of the data for passes 11 and 20 is the land/water interface caused by Yucatan Peninsula (figure 5-13). At GMT 14:49:0.08 of pass 11 the FOV was closest to the land/water interface. If one assigns  $\sigma_{0VH}$  of -34.8 dB

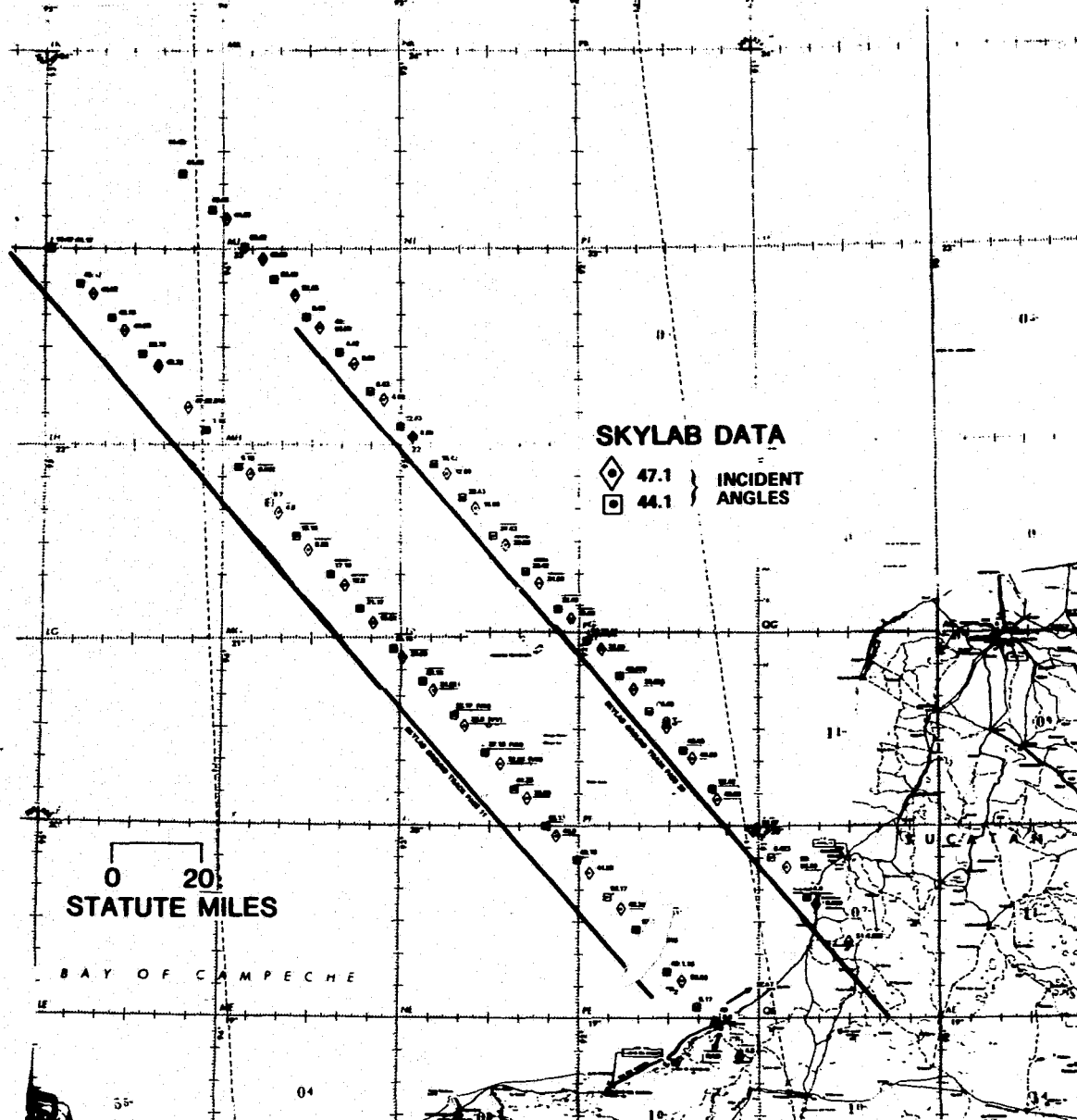


Figure 5-13. — Ground track and scatterometer data locations for EREP passes 11 and 20.



TABLE 5-VII. — SURFACE AND ATMOSPHERIC CONDITIONS FOR SL-3 TARGET SITES

Site number	Site name	Skylab pass number	Cloud cover	Visibility	Pressure (MB)	Temperature (°F)	Dew point	Winds	Significant wave height (feet)	Water temperature (°F)
750598	Gulf of Mexico	13**	Overcast* (precipitation)	N/A	1,019	81	75	8 knots from 130°	2	86
750598	Gulf of Mexico	16**	3/10	N/A	1,018	87	74	10 knots from 90°	2	85
750598	Gulf of Mexico	20**	5/10	N/A	1,016	82	76	12 knots from 130°	4	87
746508	Tennessee/ Indiana/ North Carolina	7	Clear	—	—	—	—	Below 18 knots	—	—
—	South Atlantic	7**	Less than 4/10	—	—	—	—	Below 18 knots	—	—
750233	Great Salt Lake Desert	12	Scattered at 11,000 feet	35 miles	1,014	83	47	4 knots from 110°	—	—

\*Data used in this report for precision/accuracy analysis did not include areas of overcast/precipitation.

\*\*Fully developed seas.

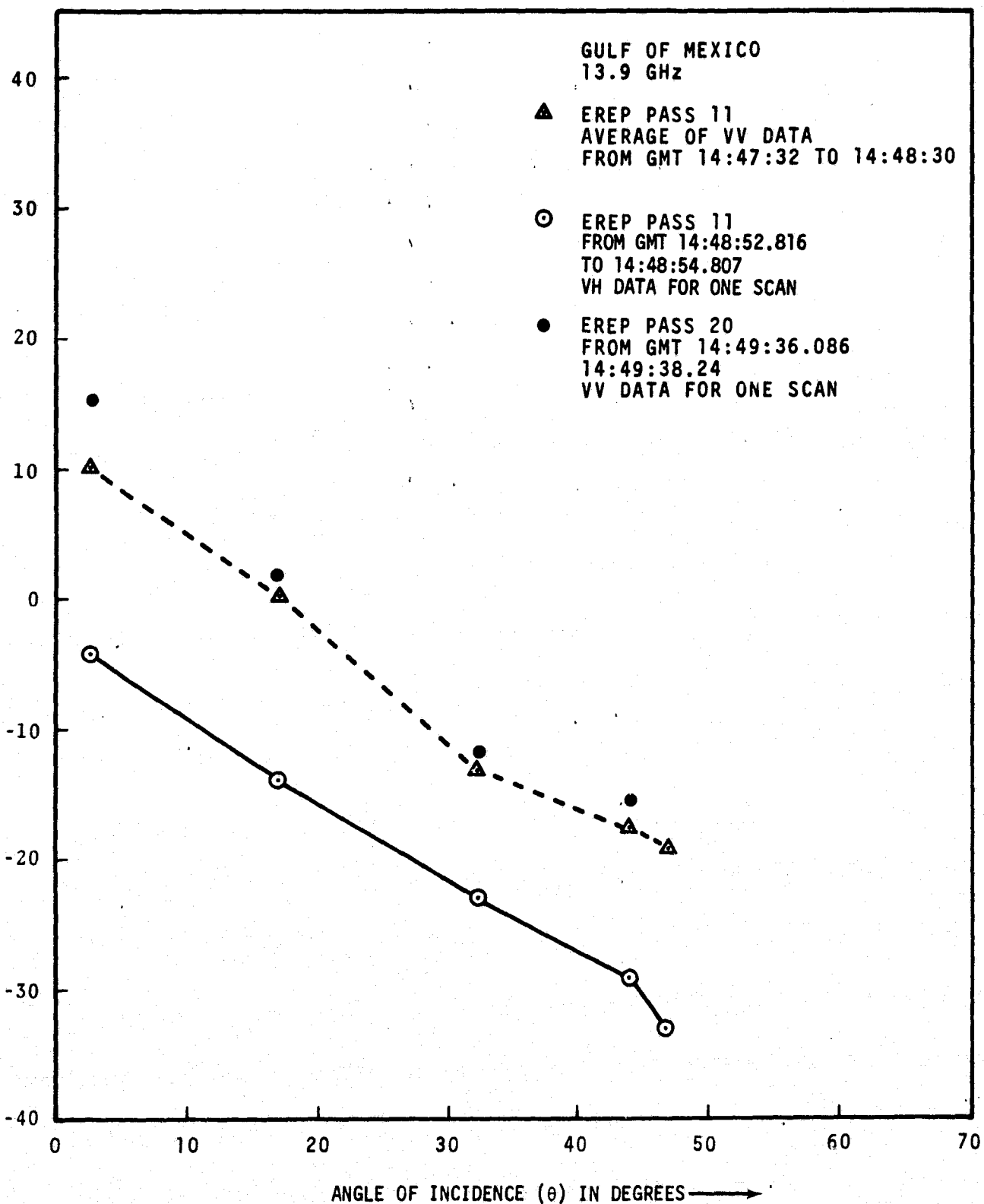


Figure 5-14. — Backscattering cross section as a function of  $\theta$   
for EREP pass 11.

to water at  $47^\circ$  incidence angle (see figure 5-13) and -15.92 dB to the land surface as measured by S-193 Scatterometer, it is interesting to calculate the value of  $\sigma_{\text{OVH}}$  at GMT 14:49:0.08. Taking the value of a water-illuminated area of 60 percent with land the remaining 40 percent of the resolution cell, the predicted value of  $\sigma_{\text{OVH}}$  is -19.8 dB. The measured value of  $\sigma_{\text{OVH}}$  at GMT 14:49:0.08 was -21.7 dB. For pass 20, the closest point to the land/water interface was at GMT 14:51:0.089. The ocean and land  $\sigma_{\text{OVV}}$ 's for  $\theta \approx 47^\circ$  were taken, respectively, as -19.09 and -9.79 dB. as measured by S-193 Scatterometer. Assuming one-half beam was illuminating the ocean surface (figure 5-13), the calculated value of  $\sigma_{\text{OVV}}$  is -12.32 dB. The measured value for  $\sigma_{\text{OVV}}$  pass 20, GMT 14:51:0.08 is -13.96 dB.

The reasonable agreement between the calculated and measured values of backscattering cross sections at the land/water boundary leads to two conclusions:

- The FOV computation is reasonably accurate as specified in TR 524 (reference 40).
- The response of S-193 Scatterometer to land/water interfaces is reasonably accurate.

For the analysis of precision/accuracy, the  $\sigma_0$ 's over the ocean will be used from these two passes.

For pass 11 from GMT 14:48:7 to 14:49:41, the S-194 Radiometric antenna temperatures range from 89.1 to 91.9°K. The average value is 90.6°K. The reflectivity is fairly constant

with an average of  $|R(o)| = 0.835$ . The S-193 Radiometric antenna temperatures also show homogeneity of the surface dielectric properties. Skylab pass 20 shows a minimum of 90.4°K and a maximum of 92.3°K for the S-194 measured radiometric antenna temperature (GMT 14:49:58 to 14:51:42). The S-193 Radiometer-acquired data also confirms the uniformity of the surface reflectivity.

#### 5.2.4 Other $\sigma_o$ Data Over the Gulf of Mexico and Atlantic

5.2.4.1 EREP pass 13, Gulf of Mexico. A CTC radiometer/scatterometer (pitch and roll offsets equal to zero) mode was exercised during EREP pass 13. Figure 5-15 shows the field-of-view plot for a data segment. The data to be considered in analyzing precision/accuracy will be HH data from GMT 17:27:01 to 17:29:00 and VV data from GMT 17:25:36.84 to 17:26:21.3. During these times, negligible precipitation was present. The overcast precipitation (table 5-VII) was primarily centered over field-of-view (FOV) around GMT 17:25:00. The data is for low windspeeds (below 10 knots). The theoretical models are most appropriate for comparisons since tangent plane approximations are valid in this case. The mean radiometric temperature over all angles of incidence for S-193 is 133.8°K with a standard deviation of 2.4°K (GMT 17:27:00 to 17:29:00). This is encouraging, since it verifies the uniformity of surface wind field as well as the homogeneity of surface reflectivity.

5.2.4.2 EREP pass 16, Gulf of Mexico. Two modes were exercised during pass 16 over the Gulf of Mexico. The intrack noncontiguous (ITNC) radiometer/scatterometer, VV mode was exercised from GMT 16:04:50 to 16:07:21. Part of this data

S193RS FIELD OF VIEW  
 PROJ. PASS 13 CTC R/S 1 3A-151-325-13  
 SCAN MODE: CTC P=0.0 R=0.0  
 RS OF MODE: RAD / SCAT

PAGE 2  
 DATE 23-JAN-75  
 PRODUCT NO. 5063-1

MISSION 3  
 PASS 13  
 SITE 0

SENSOR S-193 RS  
 RECORDING FORM S-193 RS  
 FLIGHT DATE 4-AUG-73  
 START TIME 17:27:45.5402  
 STOP TIME 17:28:29.6886

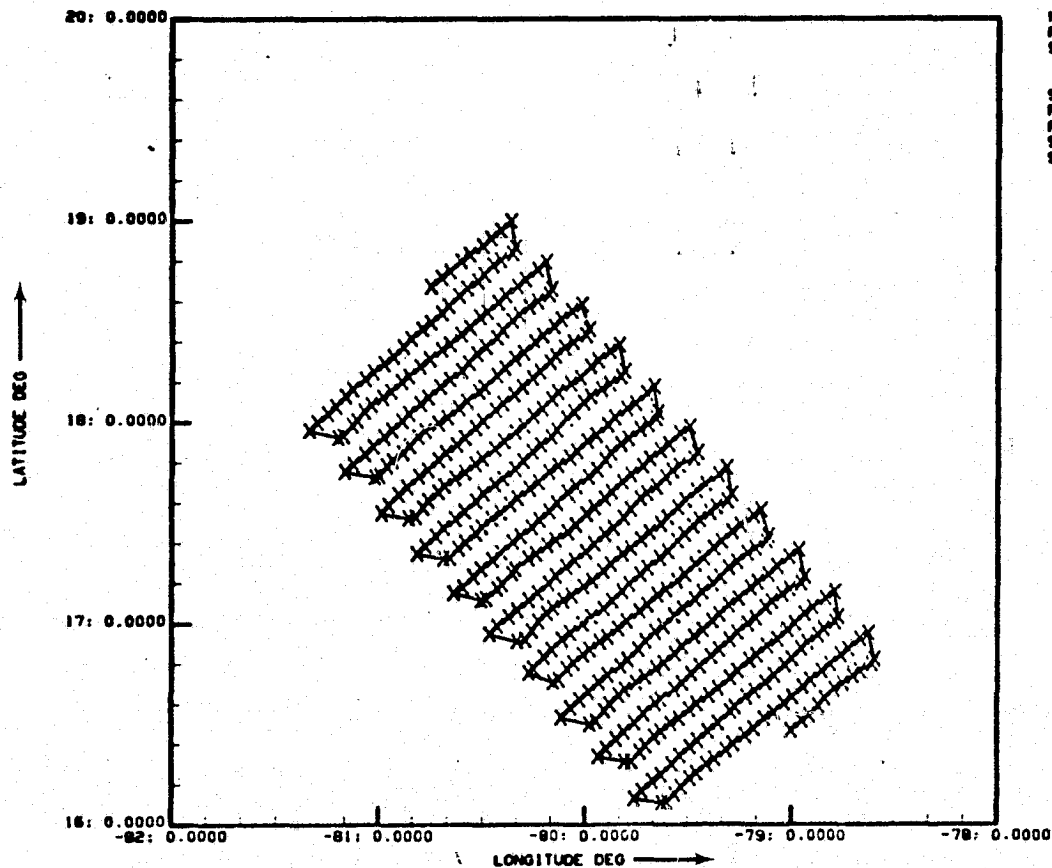


Figure 5-15. — S-193 Radiometer/Scatterometer  
 field-of-view, pass 13.

was taken over land. This part was excluded from the analysis of backscatter precision/accuracy. The average ocean surface winds were approximately 10 knots. The second mode exercised was the CTNC left radiometer/scatterometer. Only HH polarization data was gathered. Figure 5-16 shows the FOV of the sensor. The data averaging was performed on only the ocean data; data gathered over land (last scan) was not considered. The homogeneity of the surface properties was once again checked (as in section 5.2.4.1). Similar results were obtained for the surface reflectivity.

5.2.4.3 EREP pass 7, Atlantic. The CTC scatterometer-only mode was exercised over South Atlantic from GMT 14:44:3.6 to 14:44:24.188. The ocean surface winds were below 18 knots (exact velocity not known). The pitch offset was  $29.4^\circ$ . The angle of incidence varied from  $33.11$  to  $35.46^\circ$ . This aspect of the data is very important, since the variability in the data caused by  $\theta$  variation is almost minimum for this mode with the pitch offset. Since no significant atmospheric effects predominated (cloud cover less than 40 percent), the variance of this data was studied as a possible measure of the precision. The variation in angle of incidence ( $2.35^\circ$ ) and polarization mixing (see appendix B) were taken into account in the data interpretation. The location of the data was around latitude- $13.9^\circ$  and longitude  $-37.0^\circ$ .

### 5.3 LAND $\sigma_0$ DATA

The Sensor Performance Evaluation sites were chosen on the basis of homogeneity in roughness and surface dielectric properties. Great Salt Lake Desert (GSLD) and uniform crop

PROJ. S193RS FIELD OF VIEW  
PASS 15 CTNC L R/S 1 3A-351-14-16  
SCAN MODE 1 CTNC (LEFT)  
RS OP MODE: RAD / SCAT

PAGE 1  
DATE 22-NOV-74  
PRODUCT NO. 5063-1

MISSION 3  
PASS 16  
SITE 0

SENSOR S-193 RS  
RECORDING FORM S-193 RS  
FLIGHT DATE 8-AUG-73  
START TIME 16: 7:39.2468  
STOP TIME 16: 9:17.5675

(\*DATA NOT  
PROCESSED)

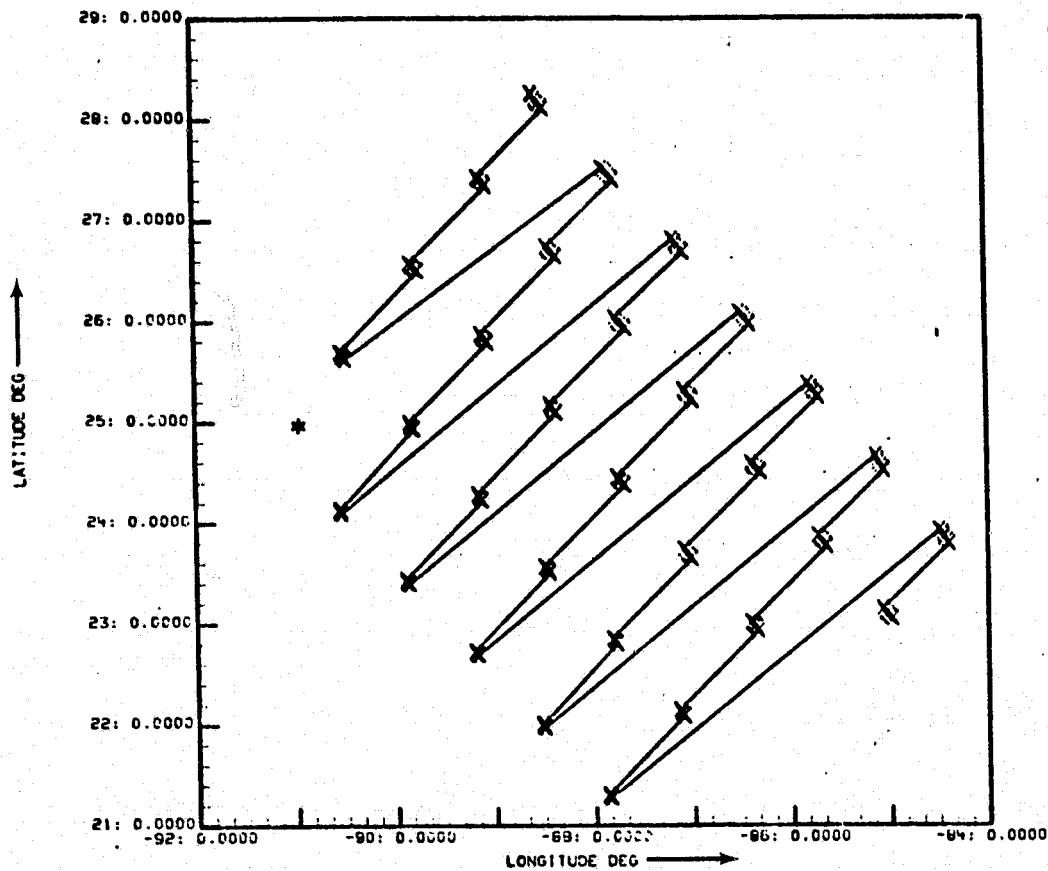


Figure 5-16. - S-193 Radiometer/Scatterometer field-of-view, pass 16.

or forest areas were considered prime sites. In this section a discussion of the data will be presented. The detailed comparisons with theory and other experimental data will be given in section 6.0.

### 5.3.1 Great Salt Lake Desert Scatterometer Data

5.3.1.1 EREP pass 5. During EREP pass 5, a CTC zero-pitch, zero-roll offset mode was exercised over the GSLD site. Scatterometer data corresponding to horizontal-transmit, horizontal-receive (HH) and radiometer H-polarization was acquired.

The coverage for six selected scans (not successive) is shown in figure 5-17. The finite period of measurement extends the ground coverage. This extension is shown for the scatterometer by the dashed area. The center of main beam intersection with the ground is shown as "S" for scatterometer and "R" for the radiometer. There is approximately 40 percent overlap between the scatterometer- and radiometer-sensed area at a particular pitch angle. In general, the instantaneous resolution cell on the ground is elliptic in shape, but for the CTC mode with zero-degree pitch, zero-degree roll offsets, the differences between circles and actual shapes are negligible. Because of this, the instantaneous scatterometer FOV has been shown as a circle in figure 5-17. The numbers associated with the center point of selected cells show the GMT data acquisition time in seconds.

The FOV for the L-band radiometer operating at a wavelength of 21 cm is also shown in figure 5-17. The radiometer energy received by the antenna is sampled at a rate of three per second. At the nominal altitude of 440 km the antenna



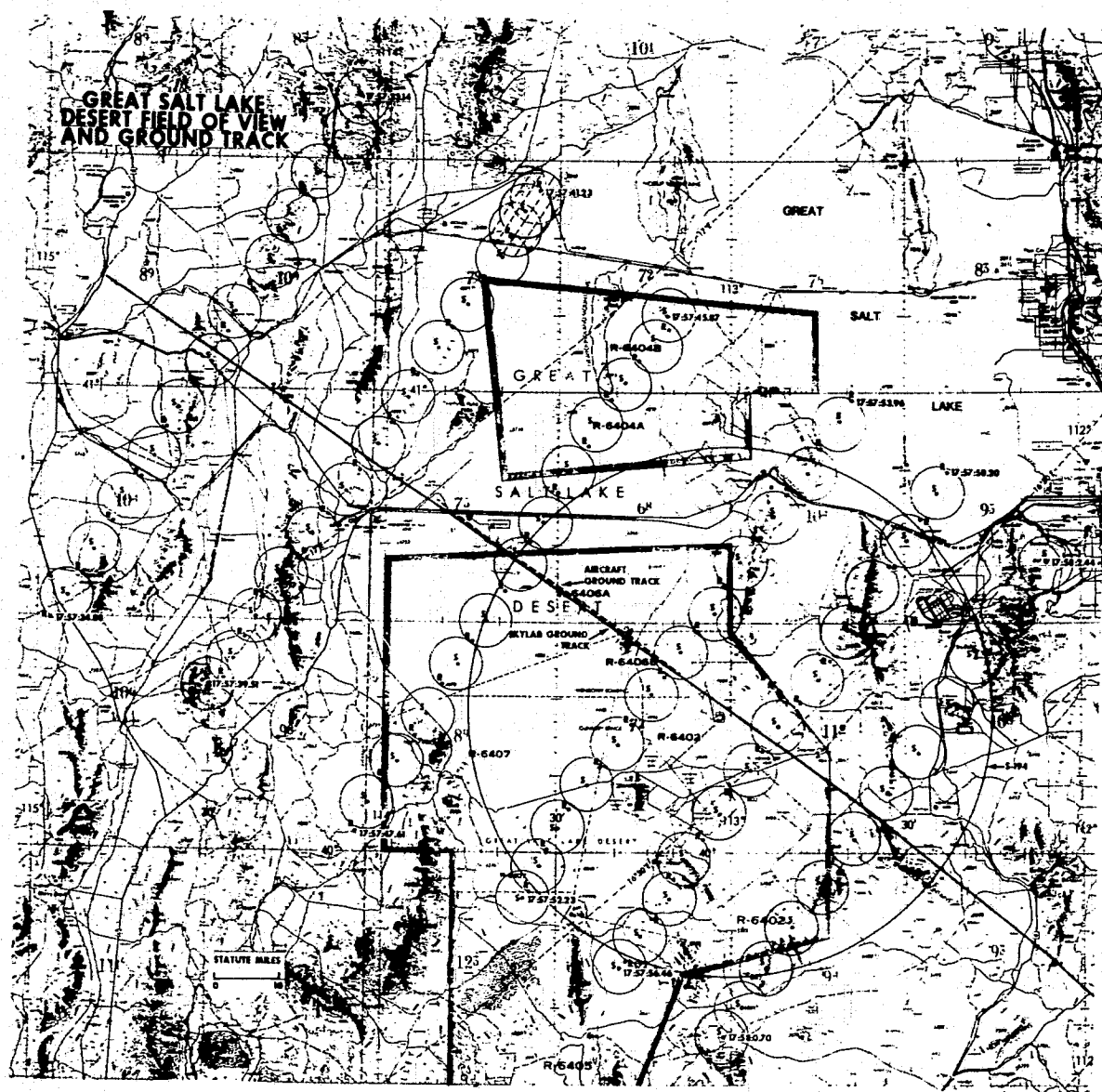


Figure 5-17. — Field-of-view and ground track for Great Salt Lake Desert (EREP pass 5).

receives energy from approximately a 60-mile radius circle on the ground. There is a 97 percent overlap between two successive measurements.

The  $\sigma_0$  data for several scans is shown in figures 5-18 and 5-19. From this data and photographs, it is obvious that the GSLD area shown in figure 5-17 is not homogeneous in surface roughness and dielectric properties. Ground data was also gathered over Great Salt Lake. It was a warm day with no overcast (table 5-V). To select a uniform area, the aircraft-acquired data and Skylab S-193 and S-194 Radiometer data were reviewed. The 13.3 GHz scatterometer data showed good uniformity over the flight line shown in figure 5-17 except over the Wildcat Mountain (see the figure 5-17 area marked R-6406B). This aircraft and spacecraft data will be compared in section 6. The laser profiler data shows most areas are smooth over the flight line. A typical smooth surface data is shown in figure 5-20. Power spectral densities and the autocorrelation function of the surface were also computed from the laser data. The results from two time segments are shown in figures 5-21 and 5-22. The laser data showed data corresponding to two scans from GMT 17:57:45.875 to 17:57:47.611 gathered over the smoothest area. Furthermore, in this area, the Kirchhoff approximation could be used, and the correlation distance ( $\ell$ ) would be approximately 8 meters and rms height ( $h$ ) of 1 meter. The values of  $h$  and  $\ell$  are typical and are suggested by the data shown in figures 5-20, 5-21, and 5-22. Accurate values of  $h$  and  $\ell$  for the entire flight line have not been determined. Even if these were determined, they would not necessarily be completely representative of the area covered by S-193 Scatterometer for the scans from GMT 17:57:45.875 to 17:57:47.611.

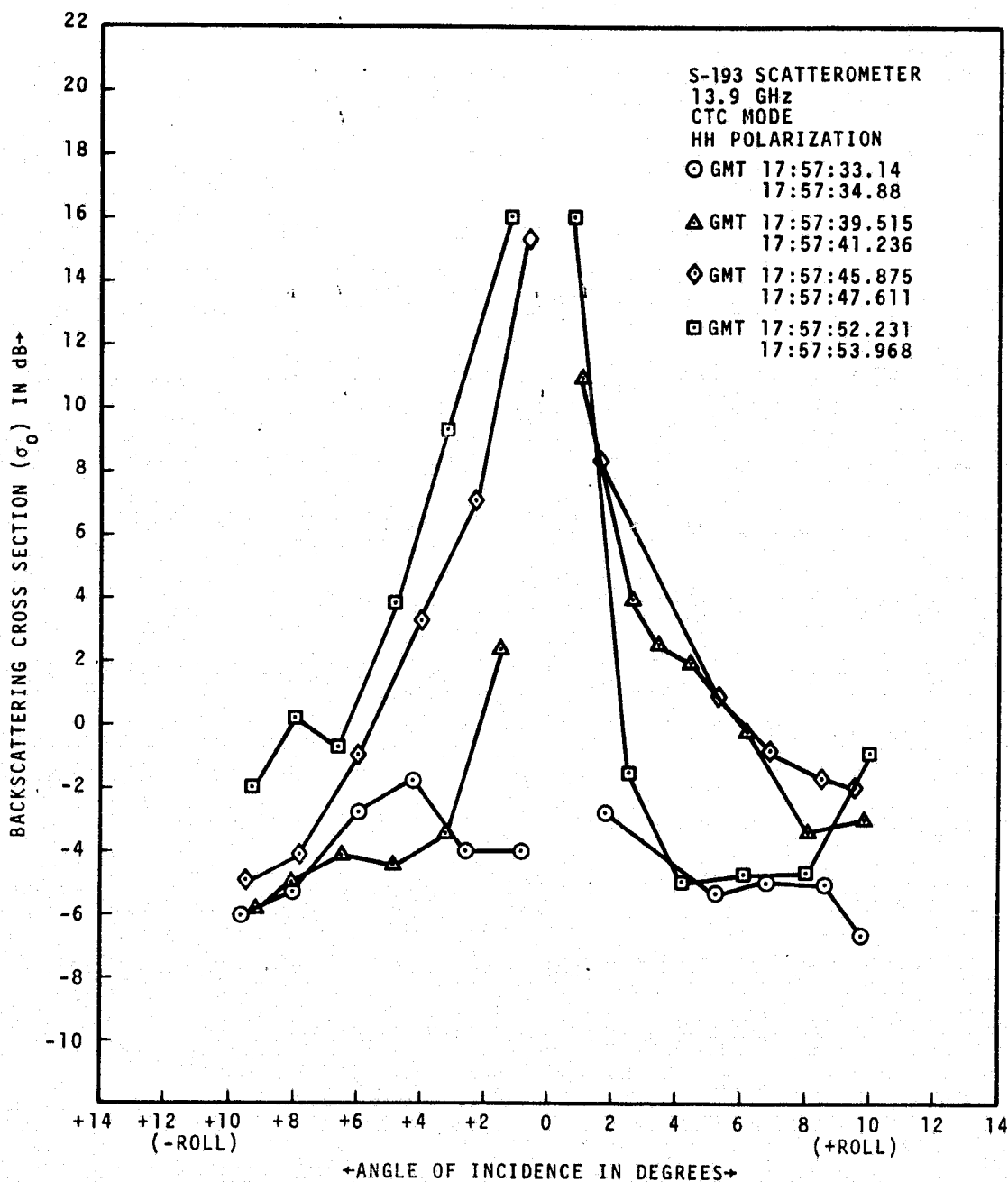


Figure 5-18. -  $\sigma_0$  versus  $\theta$  for Great Salt Lake Desert, pass 5 (I).

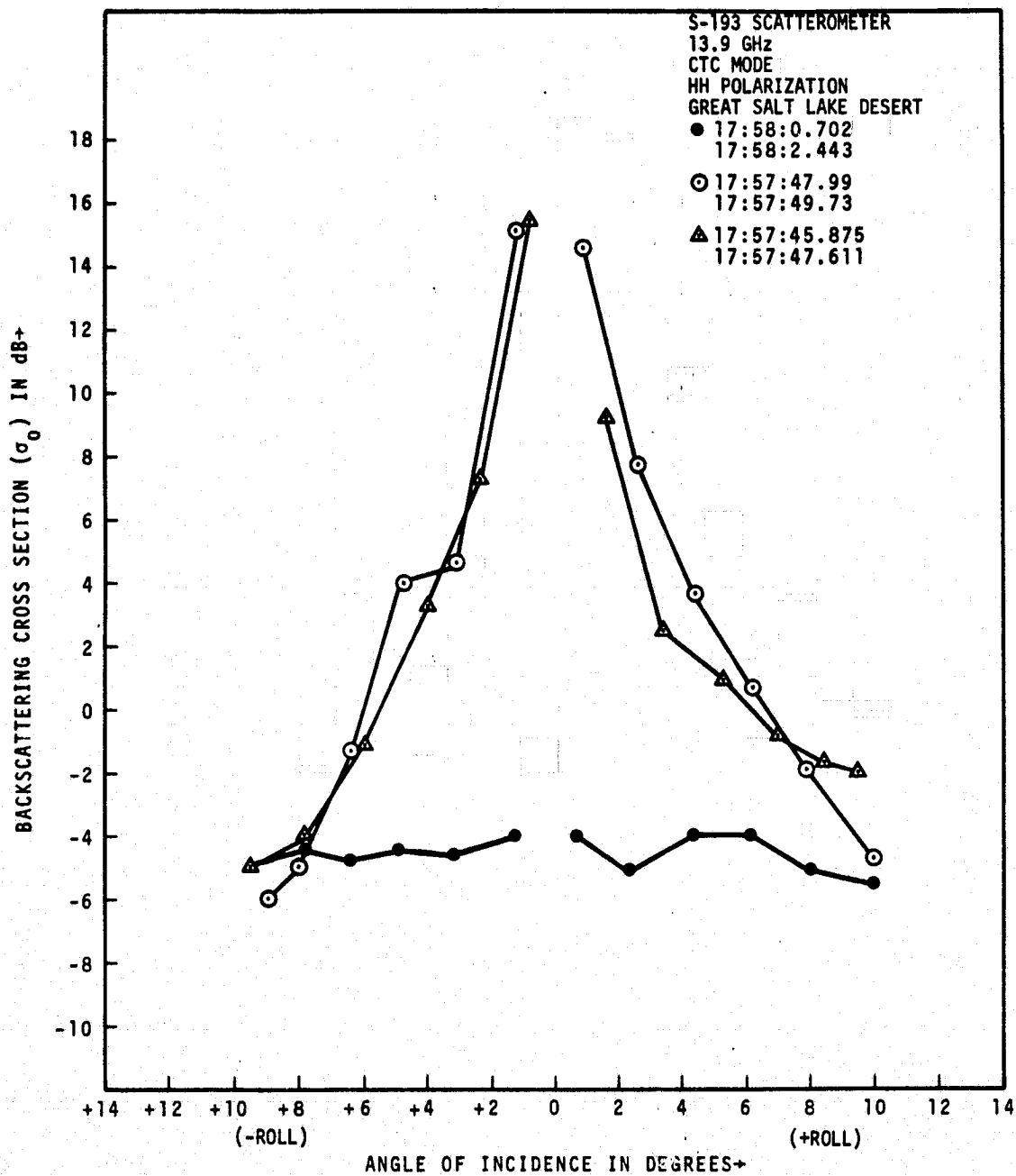


Figure 5-19. -  $\sigma_0$  versus  $\theta$  for Great Salt Lake Desert, pass 5 (II).



# AIRCRAFT VELOCITY 180 KNOTS

SENSOR - SURFACE PROFILER LASH 235 042E  
LOW-PASS FILTER USED .0  
NORM. STD. DEVIATION... .00914  
FILTER BANDWIDTHS... 9.0346  
FILTER START POINTS. .0000

TIME SLICE (HR-MIN-SEC) 14 50 23.7424 TO 14 50 29.9990  
STANDARD DEVIATION.. 6.4302  
DATE PROCESSED:..... 31JUL79  
INPUT TAPE NUMBER...

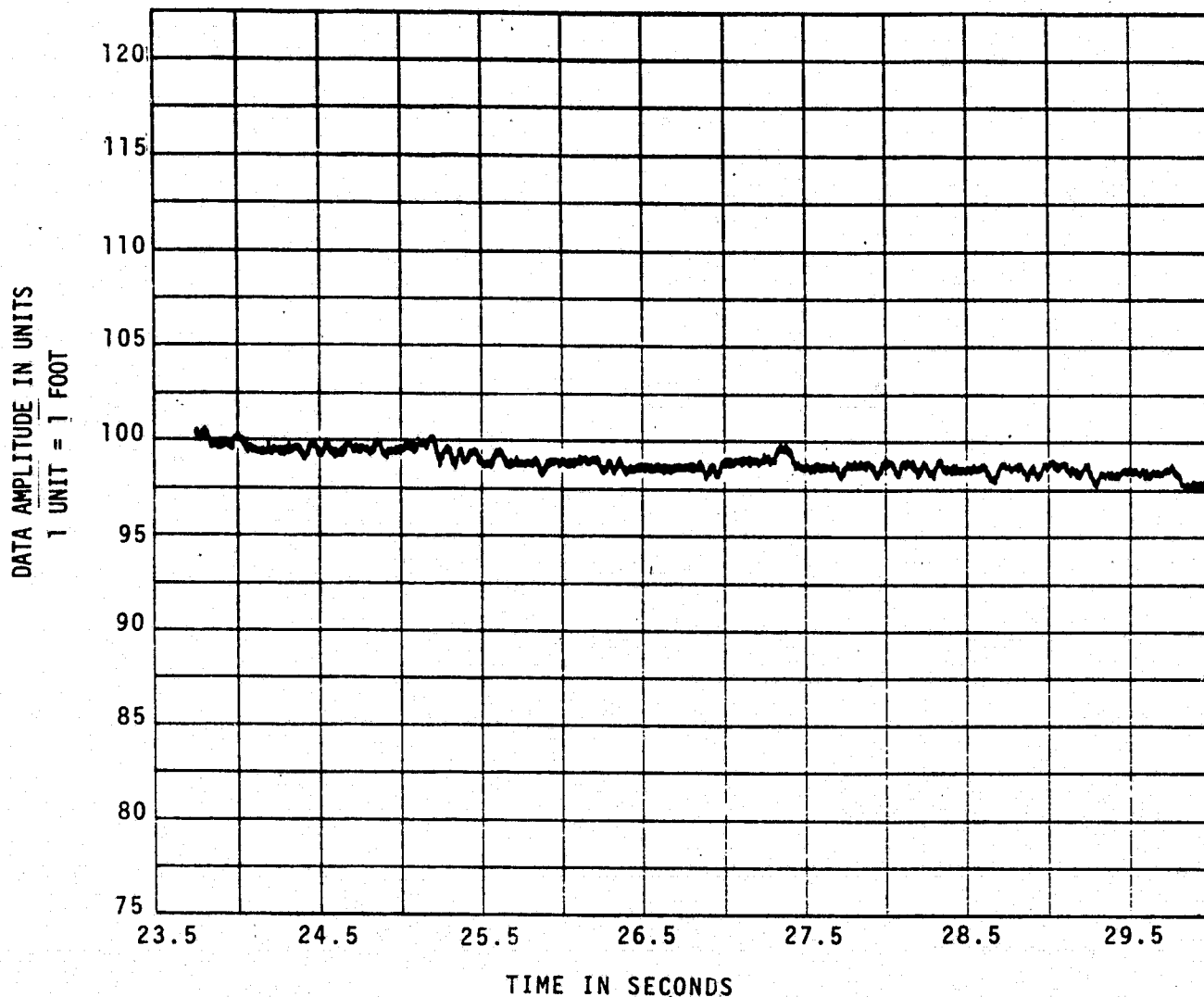


Figure 5-20. — Height of the surface in units for a segment of GSLD laser profiler data.

# AIRCRAFT VELOCITY 180 KNOTS

SENSOR - SURFACE PROFILER LASR 295 062D  
 LOW-PASS FILTER USED .0  
 NORM. STD. ERROR.... .06913  
 FILTER BANDWIDTHS... 5.0346  
 FILTER START POINTS. .0000

TIME SLICE (HR-MIN-SEC) 15 53 15.0000 TO 15 53 40.0000  
 STANDARD DEVIATION.. 7.7976

DATE PROCESSED..... 30JUL74  
 INPUT TAPE NUMBER...

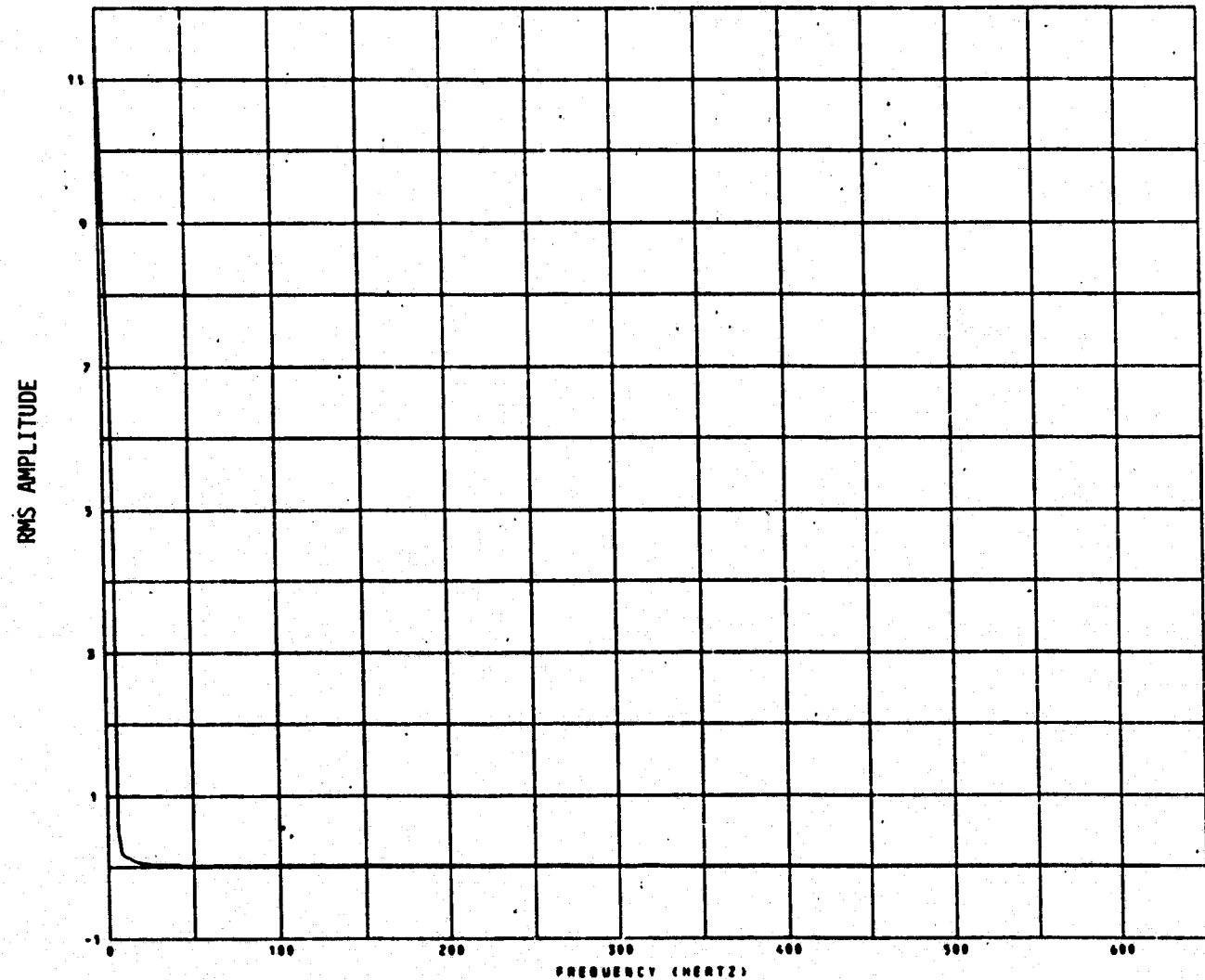


Figure 5-21. - Frequency versus rms amplitude for a segment of laser profiler data over GSLD.

# AIRCRAFT VELOCITY 180 KNOTS

SENSOR - UNCORRECTED PROFILE  
LOW-PASS FILTER USED .0  
NORM. STD. ERROR.... .02913  
FILTER BANDWIDTHS... 5.0346  
FILTER START POINTS. .0000

TIME SLICE (HR-MIN-SEC) 15 53 15.0000 TO 15 53 40.0000  
STANDARD DEVIATION.. 7.2167

DATE PROCESSED..... 30JUL74  
INPUT TAPE NUMBER...

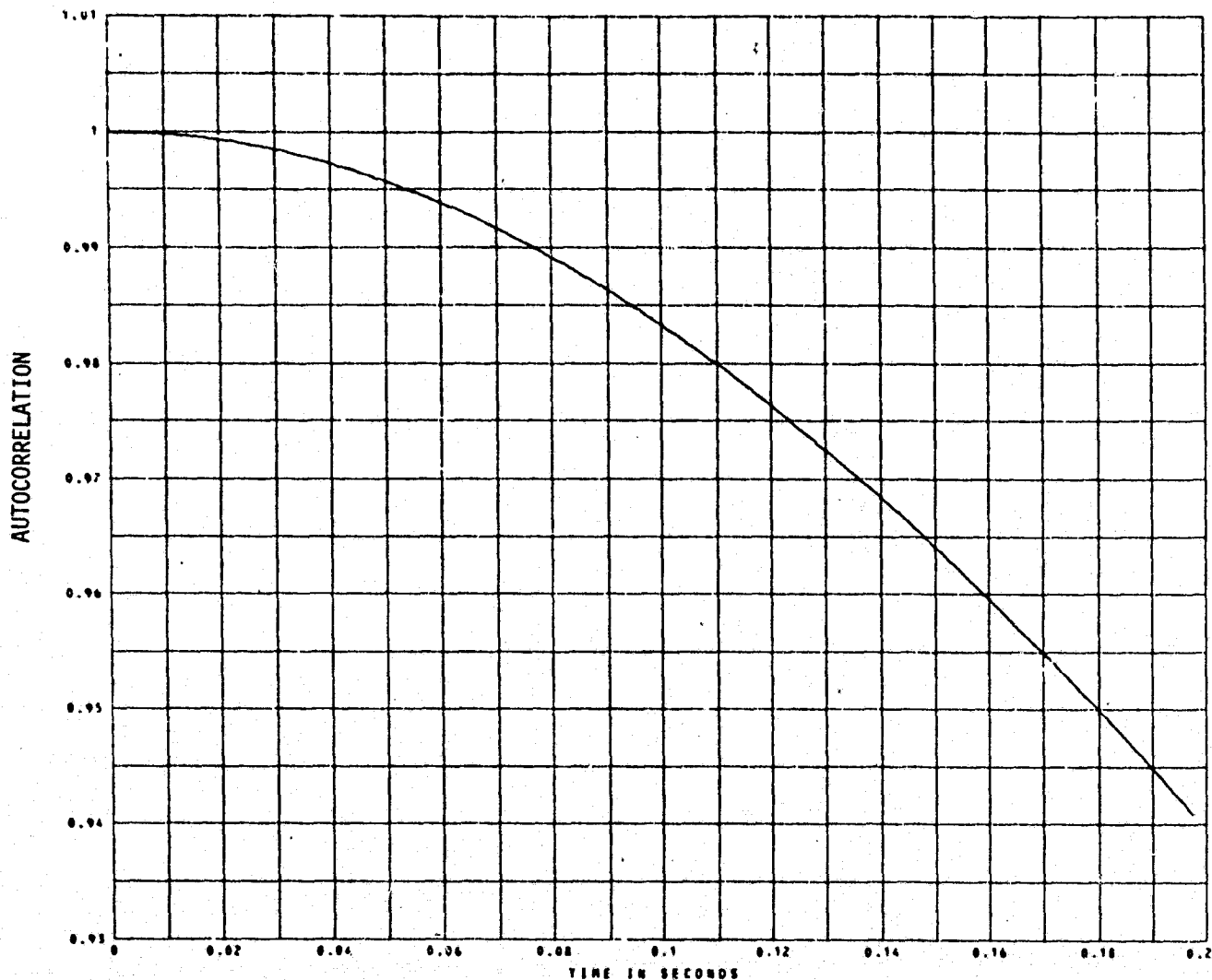


Figure 5-22. — Autocorrelation for a segment of laser profiler data over GS LD.

The S-193 Radiometer data was plotted on the FOV scan plot (figure 5-23). Radiometer antenna temperatures were coded for five ranges. This representation showed unexpectedly low temperature ranges for the shaded areas shown in the figure. This was indicative of surface and subsurface moisture. S-194 Radiometer-sensed antenna temperature also dipped in this area (figure 5-24). It should be emphasized here that the footprint of S-194 is quite large, and the dip near GMT 17:57:47 does not necessarily mean that L-band-sensed radiometric temperature is higher than that measured at the  $K_u$ -band. Most significantly, both data in figure 5-24 show presence of moisture within the same ground area. Aircraft-acquired MFMR X-band data also showed similar results. The surface nonhomogeneity in dielectric properties presented a serious limitation. Only the data from GMT 17:57:45.875 to 17:57:49.73 was selected for the comparisons needed to estimate accuracy.

The data from the first scan, GMT 17:57:33.14 to 17:57:34.88, and the last scan (figure 5-17), GMT 17:58:0.702 to 17:58:2.443 when compared with the remaining data (figures 5-18 and 5-19), shows that the area within these two scans gives a nearly specular return.

5.3.1.2 EREP pass 12. A CTC radiometer/scatterometer VV mode with pitch offset of  $29.4^\circ$  was exercised during pass 12. In this mode the  $\theta$  variation was only approximately  $2.5^\circ$  ( $\theta$  varies from  $31.8$  to  $34.3$ ). Because of this, the variance in  $\sigma_0$  was considerably reduced. Figure 5-25 shows the S-193 Radiometric antenna temperature distribution over the sensed area. Once again, the presence of moisture in the shaded area was indicated.



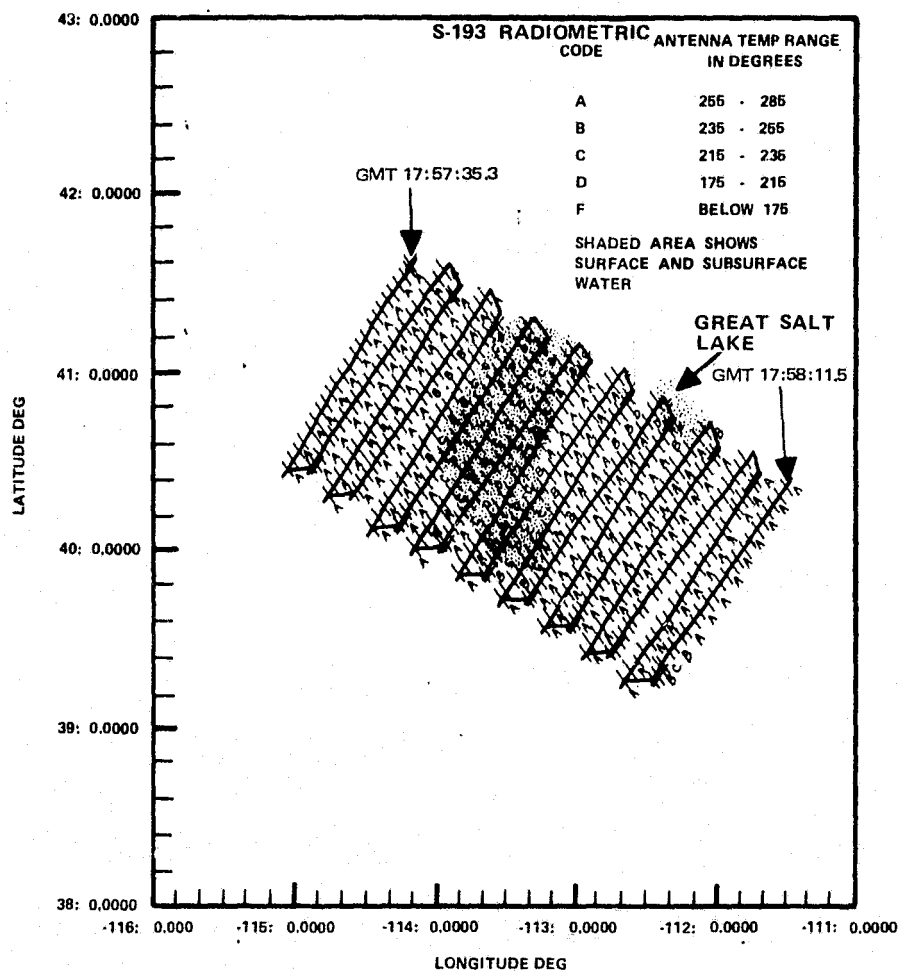


Figure 5-23. — FOV and S-193 Radiometer antenna temperature distribution over GSLD (pass 5).

5-56

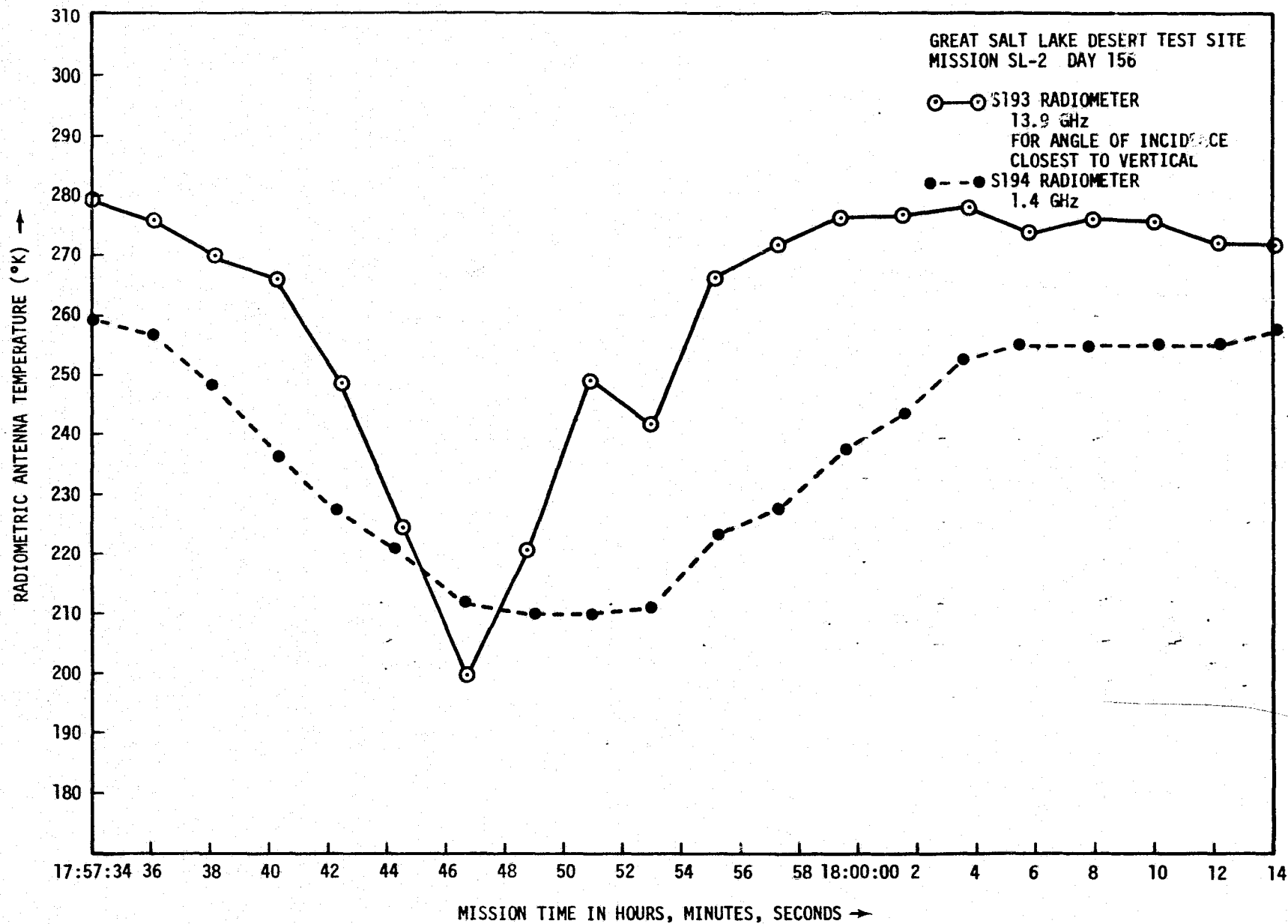


Figure 5-24. — Comparison of S-194 and S-193 Radiometric antenna temperatures (nearly vertical incidence) for GSLD.

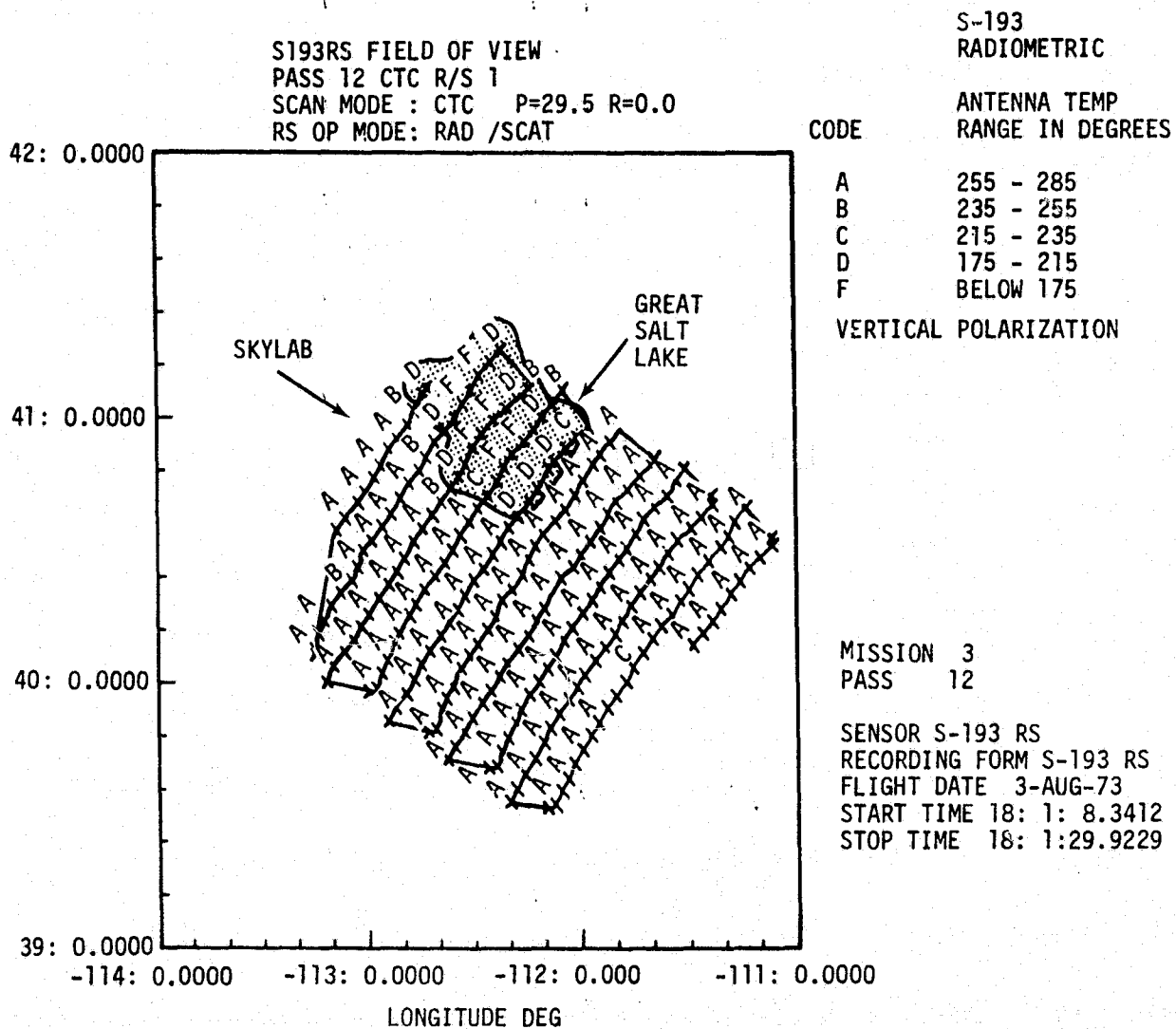


Figure 5-25. — FOV and S-193 Radiometer antenna temperature distribution over GSLD (pass 12).

For the area where no moisture was indicated (after the fifth scan), the maximum and minimum  $\sigma_0$  were -10.78 and -7.22, respectively. This was indicative of some degree of uniformity. Since the Kirchhoff approximation is not appropriate for angles of incidence greater than approximately  $25^\circ$  (unless small structure is absent), no adequate comparisons could be made between theoretical models and this data. Furthermore, this data could not be compared with pass 5 data because of different incidence angles and polarization.

### 5.3.2 Other Land Sites

Three land sites covered during Skylab missions 2 and 3 indicated a fairly high degree of homogeneity. These were (1) EREP pass 7, Tennessee/Indiana area; (2) the EREP pass 13 Colorado/Kansas Area around latitude  $37.4^\circ$  and longitude  $-102.35^\circ$ ; and (3) the area in the vicinity of latitude  $37^\circ$  and longitude  $-97^\circ$ , EREP pass 15 in Kansas. Although no attempt will be made to model these sites for accuracy determination, some insight into the precision can be gained from this data.

5.3.2.1. Tennessee/Indiana, EREP pass 7. An ITC, HH-polarization mode was operated in the vicinity of  $37^\circ$  latitude and  $-85^\circ$  longitude. The radiometer data indicated homogeneity of the surface. The scatterometer  $\sigma_{\text{HH}}$  data was highly consistent. The area had no cloud cover.

5.3.2.2 Colorado/Kansas, EREP pass 13. A CTC Radiometer/Scatterometer mode was exercised with pitch-offset of  $15.6^\circ$  and roll-offset of  $0^\circ$ .

The S-193 Radiometer H-polarization antenna temperature averaged approximately 272° with a standard deviation of approximately 11° for data from GMT 17:19:50 to 17:20:40. This is expected, since the site consisted of dry grass lands, sand, and wheat fields and was relatively smooth.

The scatterometer backscatter ( $\sigma_{\text{HH}}$ ) has an average value of -5.95 dB and the standard deviation range is from -8.24 to -4.46 dB. It should be noted that at  $\theta \approx 17^\circ$  scatterometer backscatter is relatively less sensitive to the surface roughness than at other angles. The averages and standard deviation for radiometer and scatterometer data were taken over 260 data samples.

5.3.2.3 Kansas, EREP pass 15. A CTC R/S, HH-polarization mode with roll-offset 0° and pitch-offset 29.4° was exercised in the southeastern corner of Kansas. This area is mostly smooth with a fairly small area covered by surface water. Other than being used as pasture, parts of the area are used to grow wheat and milo. The S-193 Radiometer measured average antenna temperature from GMT 16:37:39 to 16:38:20 of 280°K with a standard deviation of 5.7°K. The  $\sigma_{\text{HH}}$  had a total variation from a minimum of -12.35 dB to a maximum of -7.11 dB. The average value of  $\sigma_{\text{HH}}$  is -9.099 and the standard deviation range is from -10.17 to -8.24 dB.

## 6.0 PRECISION/ACCURACY ESTIMATES

The parameters which influence the backscattering cross sections belong to one or more of the following categories: sensor, intervening medium, and the ground scene. Considerable effort was expended to select data over uniform scenes with minimum atmospheric attenuation (clear skies or less than 50 percent cloud cover with no rain). This made it possible to study the variation of  $\sigma_0$  caused predominantly by the S-193 Scatterometer system. Obviously it is very difficult, if not impossible, to find a completely uniform site (including the intervening medium) and, therefore, the values of precision/accuracy are the worst case estimates (or pessimistic upper bounds).

### 6.1 PRECISION ESTIMATES

Precision is given in terms of one standard deviation computed from data for a given mode and polarization (assuming a homogeneous ground scene, including intervening medium). The precision estimates are given in table 6-1. From the  $\sigma_0$  (dB) data the mean value was computed by converting the dB values into numbers, averaging, and finally converting back to dB values. For the standard deviation,  $\sigma_0$ 's (not in dB) were used in the following formula.

$$\rho \text{ (standard deviation)} = \frac{n \sum (\sigma_0)^2 - (\sum \sigma_0)^2}{n (n-1)}$$

where  $n$  is number of data values used. The standard deviation range was computed from  $[\text{mean } \sigma_0 \pm \rho]$  in dB. The

precision was expressed as the larger of the two values of  $\{[\text{mean } \sigma_0 \pm \rho] \text{ dB minus } [\text{mean } \sigma_0] \text{ dB}\}$ . The range of the values of  $\sigma_0$  measurements is also given in table 6-I. In the interpretation of the results given in this table, the following remarks should be kept in view:

- For the EREP passes 5, 8, and 11 over the Gulf of Mexico, only  $17^\circ$  angle of incidence data was used. Out of the five angles at which data was collected, the  $17^\circ$  angle shows the least variation with ocean surface winds/sea state. This has been established theoretically and experimentally. The dependence of  $\sigma_0$  on polarization is as expected.
- For the CTC, pitch offset =  $29.4^\circ$ , roll offset =  $0^\circ$ , mode there are variations due to two factors which contribute to the data variance. First, the angle of incidence varies by about  $2.4^\circ$  within a scan. At an angle of incidence of  $33^\circ$  this could cause a variation up to 2 dB for ocean winds up to 15 knots (pass 7, GMT 14:44:3.6 to 14:44:24.188) (references 7, 41, and 42). Second, the antenna motion is such that the polarization states for the received and transmitted signals are not horizontal or vertical but in between. This effect, however, is small for this mode since the maximum angle of cross-track motion is  $11^\circ$ , and the backscattering cross sections for VV and HH polarizations are approximately the same for moderate ocean windspeeds. Despite these variations because of angle of incidence and polarization, the  $\sigma_0$  data shows small variation (table 6-I, EREP passes 7 and 15). This is indeed

TABLE 6-I. -- PRECISION ESTIMATES FOR SKYLAB 2 AND 3 SCATTEROMETER

 $\sigma_0$  DATA

EREP pass/day of year (DOY)	GMT		Area	Mode/polar- ization	Average angles of incidence degrees	Number of samples	Mean $\sigma_0$ (dB)	$\sigma_0$ Standard deviation range (dB)		$\sigma_0$ Variation (dB)		Precision better than (dB)
	From	To						Minimum	Maximum	Minimum	Maximum	
5/156	18:02:34	18:07:10	Gulf of Mexico	ITNC/VV	17.0	15	0.98	0.67	1.27	0.47	1.58	0.31
				ITNC/HH	17.0	15	1.36	1.12	1.59	0.85	1.76	0.27
				ITNC/VH	17.0	15	-14.9	-15.37	-14.47	-15.84	-14.43	0.47
7/161	14:44:36	14:44:24.188	South Atlantic	CTC/VV (R=0, P=29.4)	From 33.11 to 35.46	117	-14.39	-15.29	-13.65	-16.41	-12.75	0.90
				CTC/HH (R=0, P=29.4)	From 33.11 to 35.46	116	-15.42	-16.22	-14.74	-17.47	-14.4	0.80
	14:26:2.827	14:27:6.821	Tennessee Indiana North Carolina	ITC/HH	46.7	17	-6.18	-6.9	-5.56	-7.17	-4.93	0.72
					43.7	17	-7.7	-8.6	-6.93	-9.38	-6.5	0.90
					32.0	17	-6.36	-7.11	-5.72	-7.7	-5.35	0.75
					16.75	17	-6.50	*	-5.02	-7.3	-4.72	1.48
					2.6	16	1.57	*	4.69	-2.5	8.6	3.12
	15:20:45	15:23:50	Gulf of Mexico	ITNC/VV	17.7	13	-0.36	-1.86	0.74	-3.11	1.34	1.5
				ITNC/HH	17.8	13	-0.04	-1.47	1.03	-2.96	1.43	1.43
				ITNC/VH	17.7	13	-15.44	-16.78	-14.42	-18.5	-13.94	1.34
11/165	14:47:42	14:48:27	Gulf of Mexico	ITC/VV	16.9	12	-0.07	*	1.94	-2.56	2.7	2.0
	14:48:30	14:49:27	Gulf of Mexico	ITC/VH	17.0	15	-14.02	-14.34	-13.73	-14.6	-13.58	0.32

\*The standard deviation is large and therefore [mean  $\sigma_0$  -  $\rho$ ] is either negative or yields a value which is even smaller than the minimum  $\sigma_0$  in the data set.



TABLE 6-1. — PRECISION ESTIMATES FOR SKYLAB 2 AND 3 SCATTEROMETER (Continued)

 $\sigma_o$  DATA

EREP pass/day of year (DOY)	GMT		Area	Mode/polar- ization	Average angles of incidence degrees	Number of samples	Mean $\sigma_o$ (dB)	$\sigma_o$ Standard deviation range (dB)		$\sigma_o$ Variation (dB)		Precision better than (dB)
	From	To						Minimum	Maximum	Minimum	Maximum	
13/216	17:25: 36.84	17:26: 21.3	Gulf of Mexico	CTC/VV (P=0°, R=0°)	Minus roll	21	5.6	2.92	7.25	0.65	7.77	2.68
					Plus roll	21	-15.19	-14.64	15.67	14.62	16.29	0.55
13/216	17:19:50	17:20:46	Colorado/ Kansas	CTC/HH (P=15.6° R=0°)	17.5	264	-5.95	-8.24	-4.46	-9.53	-2.05	1.49
15/217	16:37:39	16:38:20	Kansas	CTC/HH (P=29.4°, R=0°)	From 32.69 to 34.07	223	-9.1	-10.17	-8.24	-12.35	-7.11	1.07
16/220	16:6: 24:006	16:7: 21:179	Gulf of Mexico	ITNC/R/S VV	49.59	14	-22.22	-23.56	-22.0	-24.8	-21.0	1.34
					43.0	16	-20.1	-21.42	-19.07	-21.65	-18.95	1.41
					31.41	16	-14.0	-14.46	-13.61	-14.65	-13.4	0.46
					16.44	16	1.5	1.33	1.73	1.15	1.87	0.23
					0.85	12	13.8	13.54	14.06	13.26	14.13	0.26

TABLE 6-I. - PRECISION ESTIMATES FOR SKYLAB 2 AND 3 SCATTEROMETER (Concluded)

 $\sigma_o$  DATA

EREP pass/day of year (DOY)	GMT		Area	Mode/polar- ization	Average angles of incidence degrees	Number of samples	Mean $\sigma_o$ (dB)	$\sigma_o$ Standard deviation range (dB)		$\sigma_o$ Variation (dB)		Precision better than (dB)
	From	To						Minimum	Maximum	Minimum	Maximum	
16/220	16:07:39	16:09:16	Gulf of Mexico	CTNC L(R/S) HH	49	20	-29.74	-31.15	-28.68	-32.7	-28.45	1.41
					41.4	24	-23.36	-26.09	-21.74	-28.75	-19.97	2.73
					30.4	20	-17.47	-19.66	-16.02	-21.91	-15.23	2.19
					15.94	20	0.87	0.4	1.3	0.08	1.53	0.43
					0.28	16	13.96	13.66	14.24	13.63	14.59	0.3

encouraging. All the comments made thus far also apply to EREP pass 13, GMT 17:19:50 to 17:20:46 when a CTC, pitch offset = 15.6°, roll offset = 0° was exercised.

- For the ocean  $\sigma_0$  data, the windspeeds remained fairly constant within the areas viewed by the antenna during the times used in table 6-I. However, no accurate measurements of wind direction were available.  $\sigma_0$  is a function of the wind direction. Figure 6-1 shows data taken with 13.9 radiometer/scatterometer aircraft system. This data was collected by NASA/Langley Research Center. Though the variations in wind direction during Skylab passes over the ocean were relatively small, it is clear that up to 1 dB variation in  $\sigma_0$  could have resulted from wind direction alone.
- The data used in computing the precision estimates in table 6-I was carefully correlated with the ground scene. There were several land/water boundaries causing sudden changes in  $\sigma_0$  data. In these instances, the data was sorted according to land or water site. All data within the time intervals shown in table 6-I was used except for pass 16, day of the year (DOY) 220 GMT 16:07:39 to 16:09:16. From this data, two sets of four  $\sigma_0$  data values were dropped corresponding to GMT 16:8:10.072 to 16:8:12.525 for the highest angle, and GMT 16:9:8.427 to 16:9:9.137 for the lowest angle. These data were abnormally different from the remaining data. The lowest angle data was dropped because the sensor FOV was on land. However, no particular reason was determined for the behavior of the highest angle data.

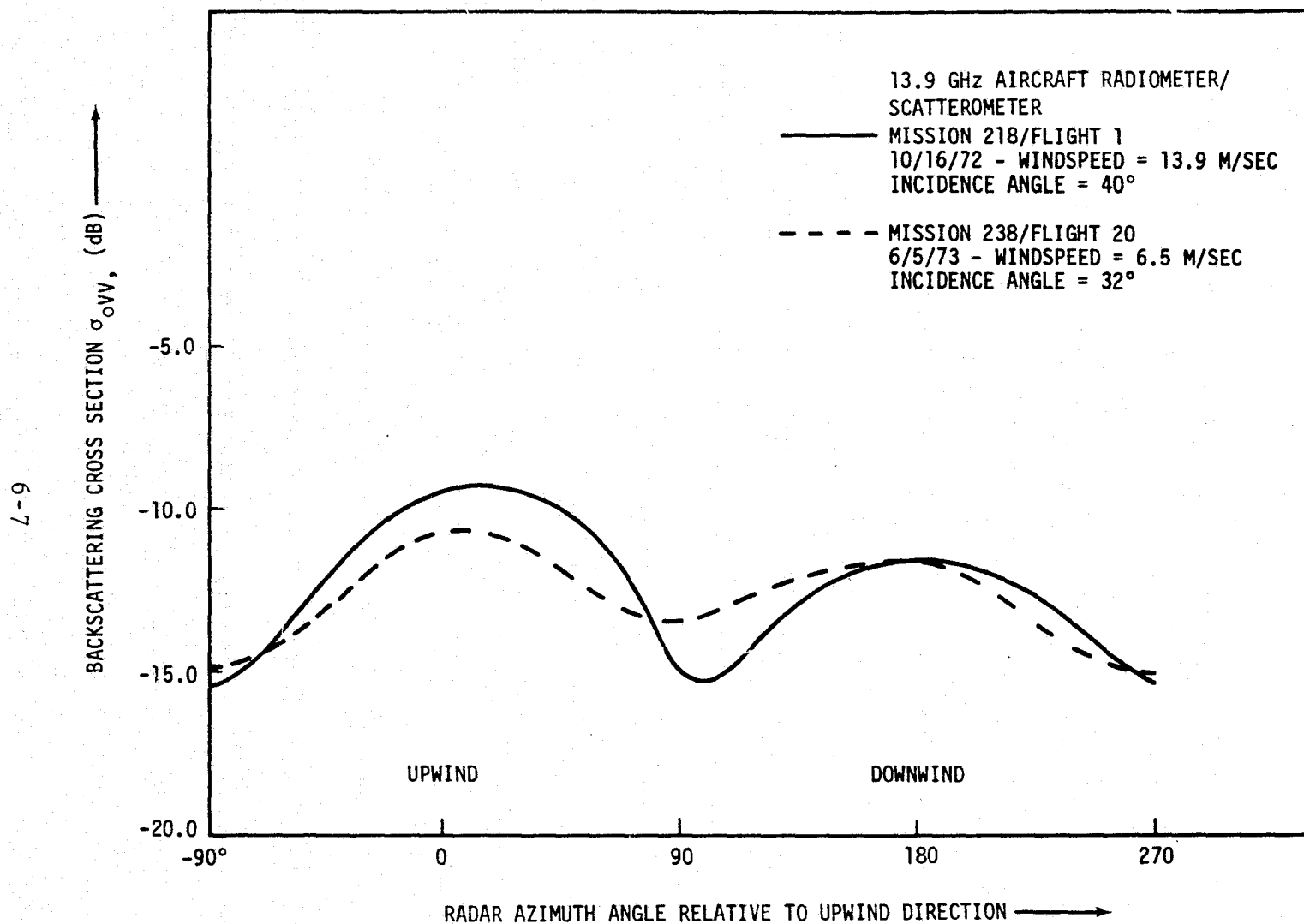
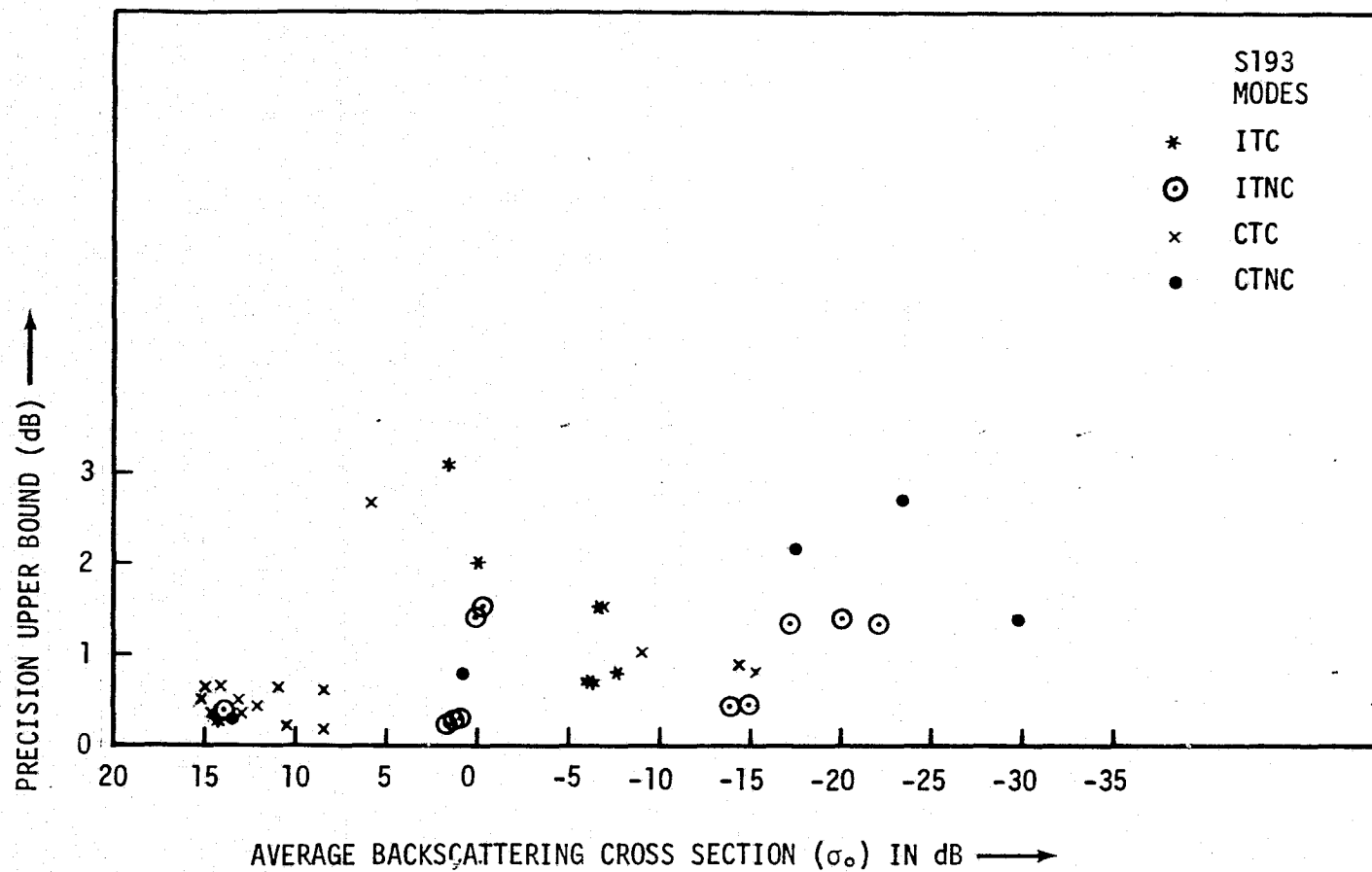


Figure 6-1. — Radar cross section versus relative wind-heading (NASA/LaRC).

- One aspect of table 6-I warrants special explanation. It is the angle of incidence which has been used in sorting the data. The pitch and roll gimbal angles are used to determine the angle of incidence. The gimbal angles did not stay constant during data runs. In modes which included  $48^\circ$  command angles, the flex harness stiffness prevented the antenna from reaching this angle. The attained angle ranged from  $43$  to  $46^\circ$ . The analysis of gimbal angles is given in reference 43. It appears that variations of the pitch and roll gimbal angles ranged up to  $0.5^\circ$  for SL-2 and SL-3 during a pass. The variations for individual data takes analyzed in table 6-I are smaller. However, any variation in these angles causes a corresponding variation in  $\theta$ . Thus, in the presence of a homogeneous scene, the  $\sigma_0$  will show some variation since it is dependent on the angle of incidence. This is therefore one reason for variance of  $\sigma_0$  caused by the system.
- The variance of the  $\sigma_0$  values given in table 6-I is the sum of variances caused by the sensor and the ground scene, since these two effects are independent. Because of this the precision estimates given in this table should be considered upper bounds. Each scatterometer  $\sigma_0$  is a result of several independent measurements (see appendix A). Therefore, the precision of  $\sigma_0$  is expected to be good.

The values of the precision upper bound from table 6-I have been plotted in figure 6-2. Out of 39 values only five are greater than or equal to 2 dB. For the remaining



34 sets of data, the precision upper bound is 1.5 dB. The trend for these 34 data points (figure 6-2) is such that precision upper bound is lower for  $\sigma_0$  greater than 0 dB and higher for  $\sigma_0$  less than 0 dB. This is expected since the signal-to-noise ratio deteriorates for low  $\sigma_0$ . From the data analyzed, it can be concluded that the precision upper bound is 1.5 dB for S-193 Scatterometer for a  $\sigma_0$  range of 18 to -30 dB.

## 6.2 ACCURACY ESTIMATES

The remarks made in section 6.1 are also true for the accuracy estimates. Accuracy will be inferred by two methods. The first is the comparison of S-193  $\sigma_0$  data with other experimental data; the second compares theoretical values of  $\sigma_0$  calculated using ground truth with S-193 data.

### 6.2.1 Comparison of S-193 $\sigma_0$ Data with Other Experimental Data

During the period of Skylab missions 2 and 3, data was gathered over selected sites with 13.9 GHz radiometer/scatterometer aircraft-borne system. In figures 6-3 and 6-4 the comparison of data for nearly the same ocean surface winds is given. The data was taken within 1 hour of the Skylab overpass. The data shows excellent consistency. The two types of data (Skylab and aircraft) show a difference of approximately 2 dB. It should be noted that 13.9 GHz radiometer/scatterometer aircraft Mission 247 data was gathered over an area part of which was under cloud cover and moderate shower activity. The aircraft-scatterometer data was processed at NASA/Langley Research Center.

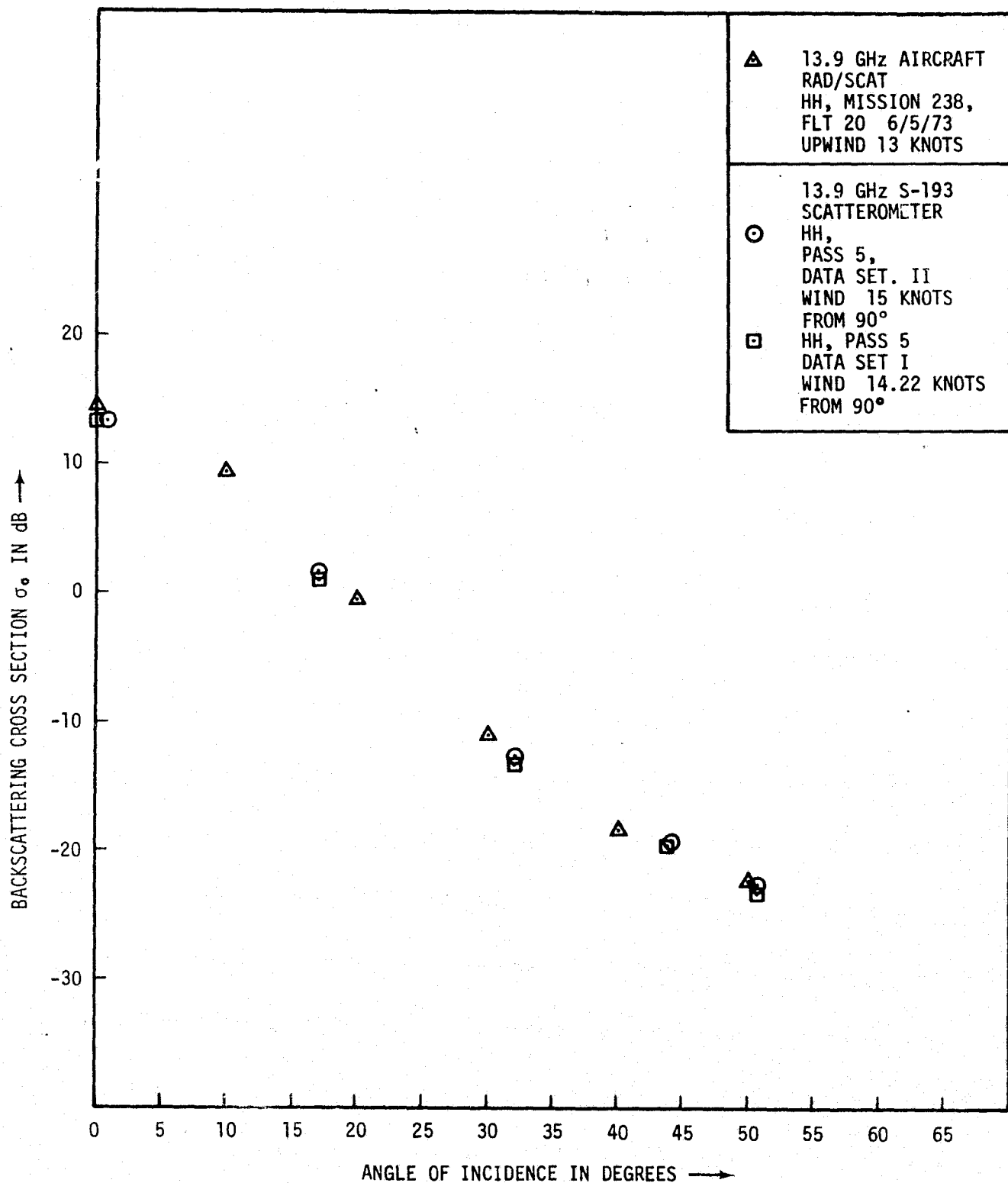


Figure 6-3. — Comparison of 13.9 GHz radiometer/scatterometer aircraft data and S-193 Scatterometer data (HH polarization).



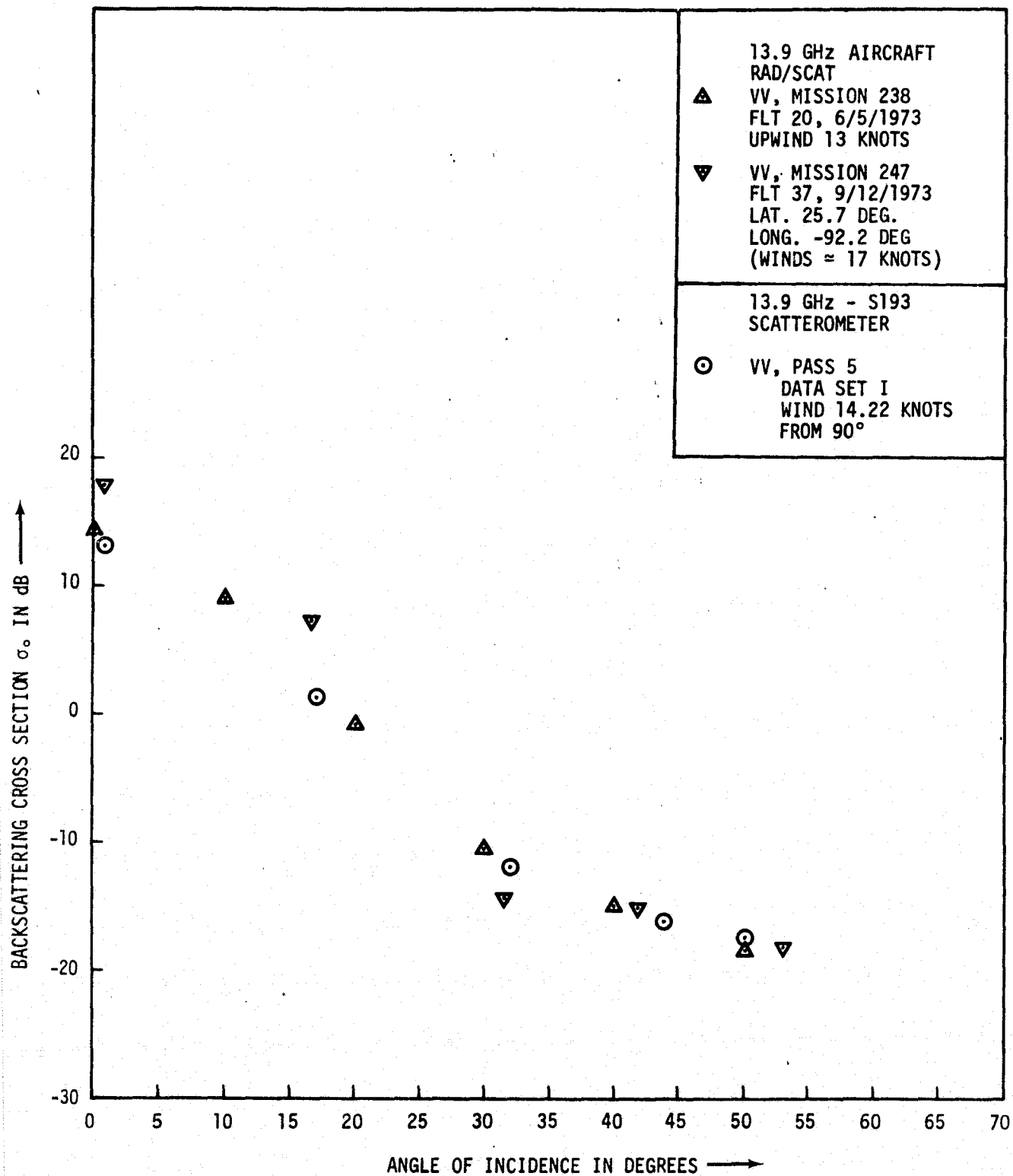


Figure 6-4. — Comparison of 13.9 GHz radiometer/scatterometer aircraft data and S-193 Scatterometer data (VV polarization).

The second comparison was made with S-193 altimeter-acquired  $\sigma_0$  data. The S-193 altimeter is a high signal-to-noise system (18 to 30 dB, depending on mode). It was therefore felt that the performance of S-193 Scatterometer could also be verified by a comparison such as is given in figure 6-5. Details of the computations for the altimeter  $\sigma_0$  are given in reference 44. These data were not taken simultaneously, but over nearly the same ocean windspeeds. Only a limited number of values were available for the  $\sigma_0$  calculated from S-193 altimeter data (through NASA/Wallops Space Center). The S-193 Scatterometer data is close to the altimeter  $\sigma_0$  (at the most a difference of 2.8 dB). It is not intended here to provide a number for the accuracy using figure 6-5, but rather to verify general agreement between the two kinds of data gathered under nearly similar ocean surface conditions.

For several years, a number of aircraft missions have been flown by NASA/JSC to study the dependence of radar return on such parameters as local windspeed, wind direction, and the spectrum of the sea. In figure 6-6, the comparison of the data from one of these missions (13.3 GHz NASA/JSC aircraft mission 119) and S-193 Scatterometer is presented. Mission 119 was conducted over the North Atlantic in 1970. Once again the three data sets are within 2.5 dB. The maximum difference between the aircraft and Skylab data is from 0 to 5° angles of incidence.

Nearly simultaneous data was obtained with 13.3 GHz scatterometer over the Gulf of Mexico during EREP pass 11. When the two sets of data (from aircraft 13.3 GHz scatterometer and S-193 Scatterometer) were compared, a 15 dB constant

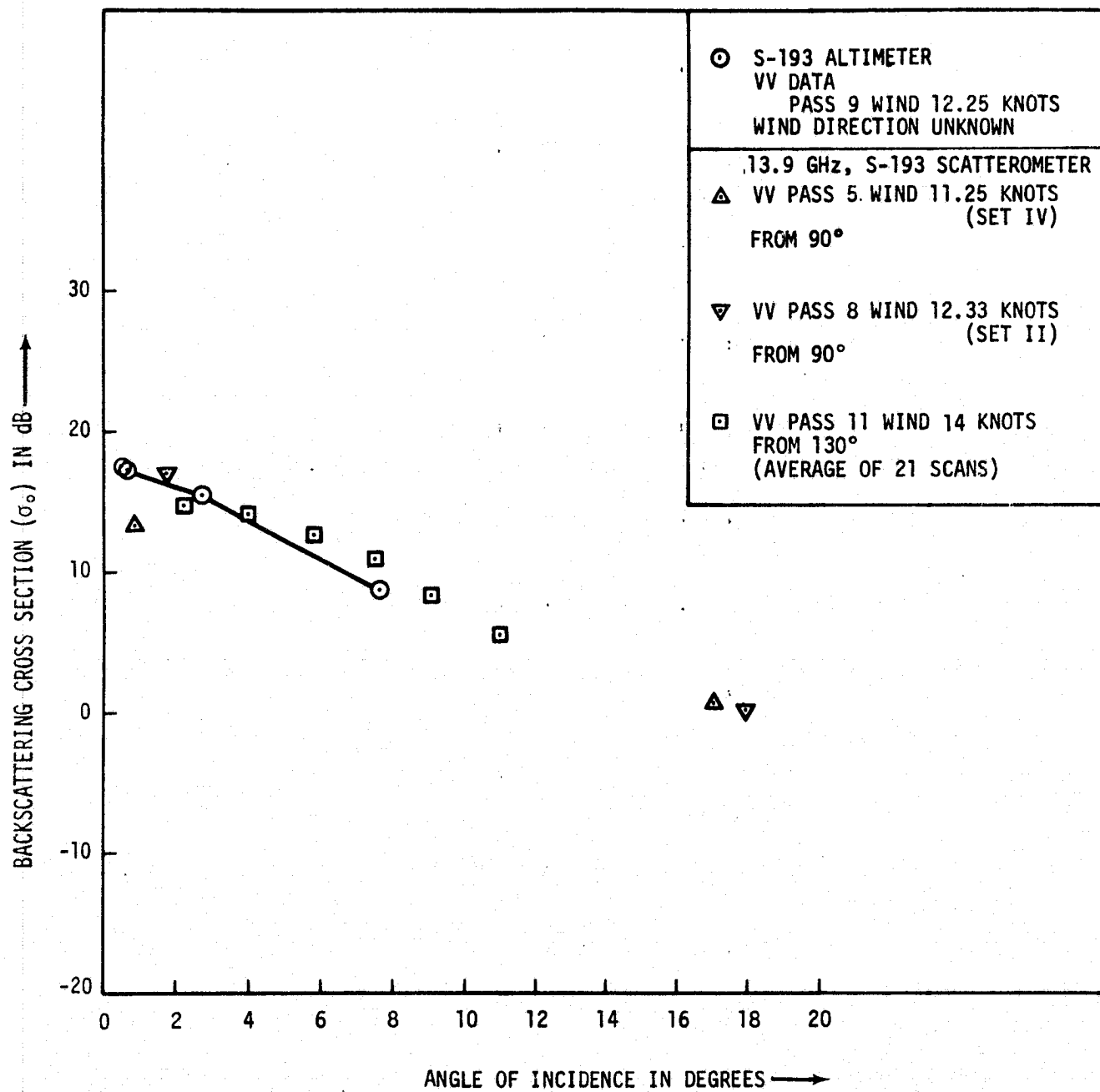


Figure 6-5. — Comparison of altimeter mode 2  $\sigma_0$  data and S-193 Scatterometer data.

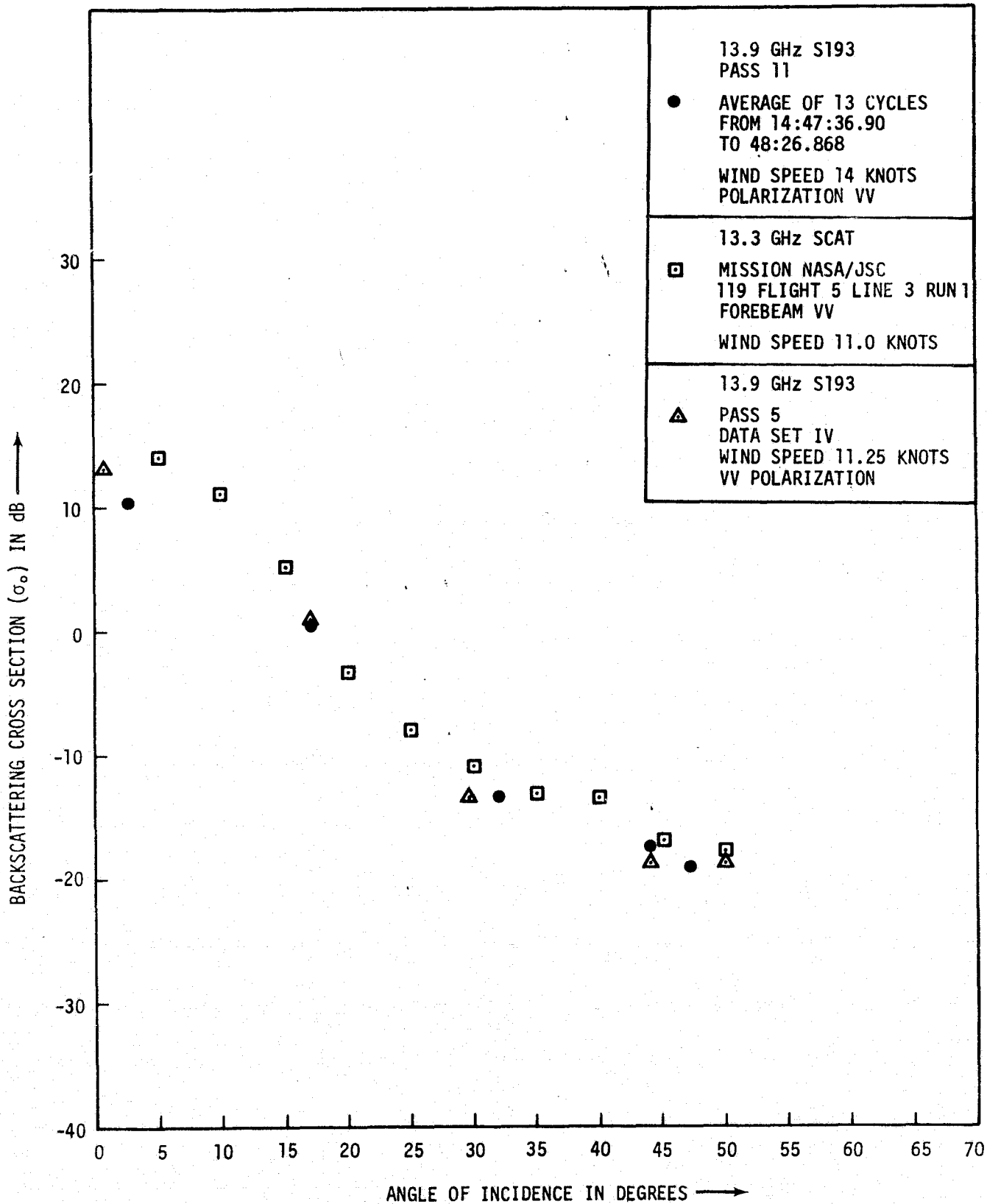


Figure 6-6. — Comparison of 13.3 GHz aircraft and S-193-acquired Scatterometer data.

difference was noted. It has been suggested that the 15 dB higher 13.3 GHz data was due to new system calibration, which was not perhaps reflected in the data processing. Further evaluation could not be pursued due to the lack of time. However, it was felt that a comparison of ( $\sigma_o$  -15 dB) from 13.3 GHz with S-193  $\sigma_o$  data could verify the general dependence on the angle of incidence. The resulting comparison is shown in figure 6-7. The  $\sigma_o$  dependence of S-193 data on the angle of incidence compares very well with that of the aircraft-acquired data.

Additional data sources were not found in the literature at or close to 13.9 GHz frequency. This is why no further comparisons could be made.

#### 6.2.2 Comparison of S-193 $\sigma_o$ Data with Theoretical Results

In section 3.4 the applicable theories to the scattering from ocean surfaces were discussed. The composite surface model was selected here for the comparison with the experimental data. The  $\sigma_o$  data from three Skylab passes is shown in figure 6-8. The average wind velocity for these data is approximately 14 knots. The total mean square slope ( $S_g^2$ ) was calculated for waves longer than approximately 1 foot from the following equation (reference 45):

$$S_g^2 = 0.01 (0.8 + 0.08V) \quad (28)$$

where  $V$  is ocean surface wind velocity in knots.

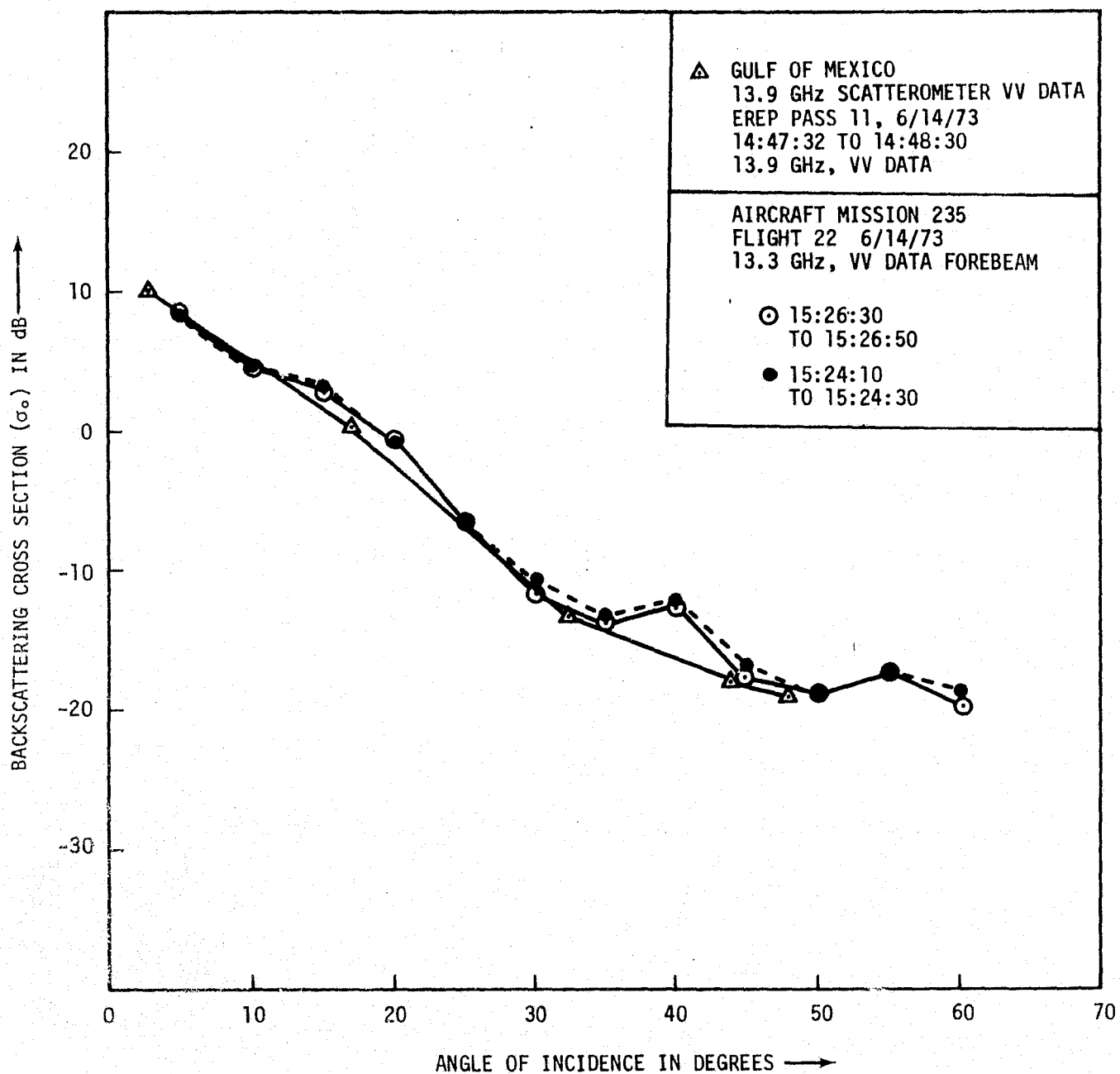


Figure 6-7. — Comparison of aircraft-acquired data ( $\sigma_0$  -15 dB) at 13.3 GHz and Skylab 13.9 GHz scatterometer data.

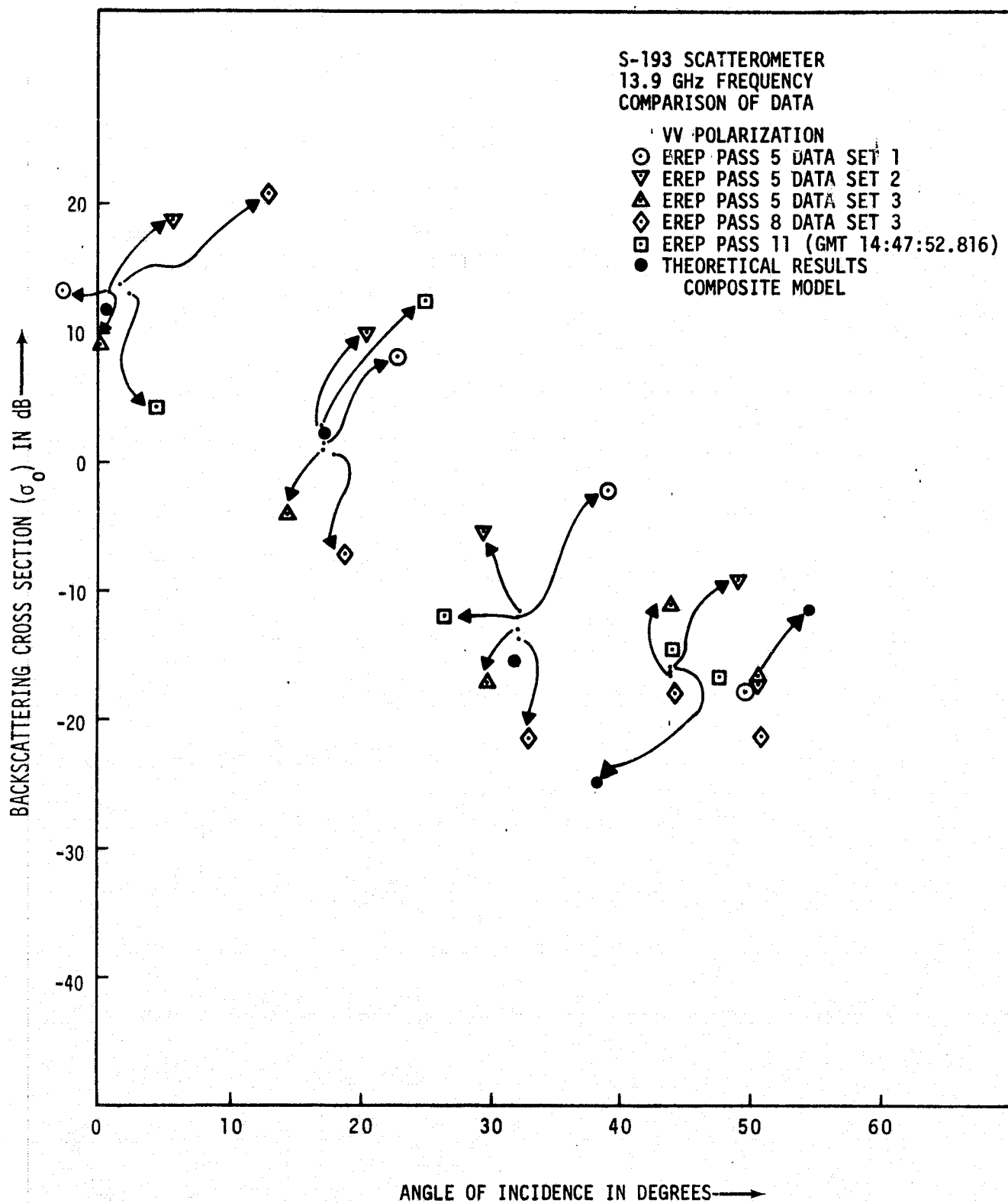


Figure 6-8. — Comparison of theoretical results using composite model and S-193  $\sigma_0$  data.

The total mean square slope ( $S^2$ ) for all waves (high frequency and gravity waves) was computed from the following equation (reference 45):

$$S^2 = 0.01 (0.3 + 0.264V) \quad (29)$$

The high frequency waves (includes capillary and high frequency gravity waves) are sensitive to wind velocities much more than the low frequency gravity waves (reference 46). The total root-mean-square slope for these high frequency waves was computed by subtracting the values of  $S_g^2$  from  $S^2$ . For the 14-knot wind velocity, this yielded the total mean-square slope ( $S_1^2$ ) of 0.0192. Wu has given the following relationship between  $S_1^2$  and the root mean square height ( $\Sigma$ ) (reference 46),

$$S_1^2 = 0.01 (0.4 \ln \Sigma + 3.38) \quad (30)$$

Equation (30) is valid up to the ocean wind velocity of approximately 7 meters per second. In this report it will be used up to 7.2 m/sec. For the Gaussian distributed high frequency waves, the correlation length (L) can be calculated from

$$S_1^2 = \frac{4\Sigma^2}{L^2} \quad (31)$$



For the 14-knot ocean surface wind, equations (28) through (31) yield the following values:

$$S^2 = 0.04$$

$$k\Sigma = 0.087$$

$$kL = 1.233$$

For  $\epsilon = 55 + j30$  and  $R = 0.78$ , the backscattering cross sections were computed from the following equation

$$\sigma_{oVV} = \exp \left( \frac{-0.0364 R_{\theta}}{H_o} \right) \left\{ (\sigma_{oVV})_h + (\sigma_{oVV})_{\Sigma} \right\} \quad (32)$$

where  $R_{\theta}$  is the distance from S-193 antenna to the illuminated area and  $H_o$  the Skylab altitude.

The first factor on the right side gives the atmospheric losses for the clear atmosphere.  $(\sigma_{oVV})_h$  is the backscatter from equation (11) and  $(\sigma_{oVV})_{\Sigma}$  from equation (19) for large and small-scale ocean surface roughness, respectively. The results are shown in figure 6-8. The theoretical and experimental values are within 3 dB. This result is quite encouraging. Comparison of theoretical  $\sigma_o$  for HH polarization combination and S-193  $\sigma_{oHH}$  data showed agreement to within 3 dB for a  $\sigma_o$  range of 14 to -28 dB.

The comparison of theoretical results and S-193  $\sigma_o$  data is based on the relationship between  $S_1^2$  (mean square slope) and  $\Sigma$  (the root mean square height of the high frequency waves) given by Wu (reference 46). However,

experimental verification of the dependence of  $\Sigma$  on the ocean surface wind velocity has not been reported. The theoretical results should therefore be considered only approximate. It is interesting to note that the best computer fit to the data set I of pass 5 (VV polarization) was obtained for the following roughness parameters:

$$S^2 = 0.032$$

$$k\Sigma = 0.11$$

$$kL = 2.25$$

A comparison of the theoretical and experimental results is given in table 6-II.

TABLE 6-II. — COMPARISON OF THEORETICAL AND EXPERIMENTAL  $\sigma_0$  DATA FOR BEST COMPUTER FIT

$\theta$	EREP pass 5 polarization VV (dB)	Theoretical results (dB)
0.919	13.21	12.52
17.1	1.42	0.85
32.17	-11.9	-12.76
43.7	-16.22	-16.3
50.1	-17.65	-18.56

The best computer fit is within 1 dB of the value of the S-193  $\sigma_0$  data. The set of roughness parameters is also quite reasonable. From this it would seem that the

capillary and small-gravity structure has a larger correlation length than what is predicted from Wu's (reference 46) analysis. It should be noted that the direction of wind relative to the Skylab ground track also influences the backscattering cross section (see figure 6-1). The effect of wind direction was not included in Wu's experiments and has not been reflected in the accuracy analysis given in this report.

The gently undulating profile of the Great Salt Lake Desert satisfies the requirements of the tangent plane approximation. The backscattering cross sections can therefore be calculated from equation (11) of section 3.4. The comparison of theoretically computed values of  $\sigma_0$  for  $S^2 = 0.08$ ,  $\epsilon = 3.4 + j0.6$  and S-193 data is shown in figure 6-9. This dielectric constant is typical of sandy surfaces (reference 47). The difference between the two sets of data shown in figure 6-9 is less than 3 dB. Also shown on the same figure is the aircraft-acquired 13.3 GHz data. The three sets of  $\sigma_0$  values are very consistent regarding the dependence on the angle of incidence.

From the analysis and comparisons presented in this section, it can be concluded that the accuracy of  $\sigma_0$  is better than 3 dB. Furthermore, this estimate of accuracy is expected to be valid for  $\sigma_0$ 's from -28 to 18 dB. The signal-to-noise ratio increases for higher  $\sigma_0$ 's. This is why  $\sigma_0$ 's up to the saturation limit of 18 dB are included. It is not possible to further tighten the limits of this estimate by theoretical modeling, since the ground truth required for such a calculation is not available (correlation distance, root mean square slope for high frequency

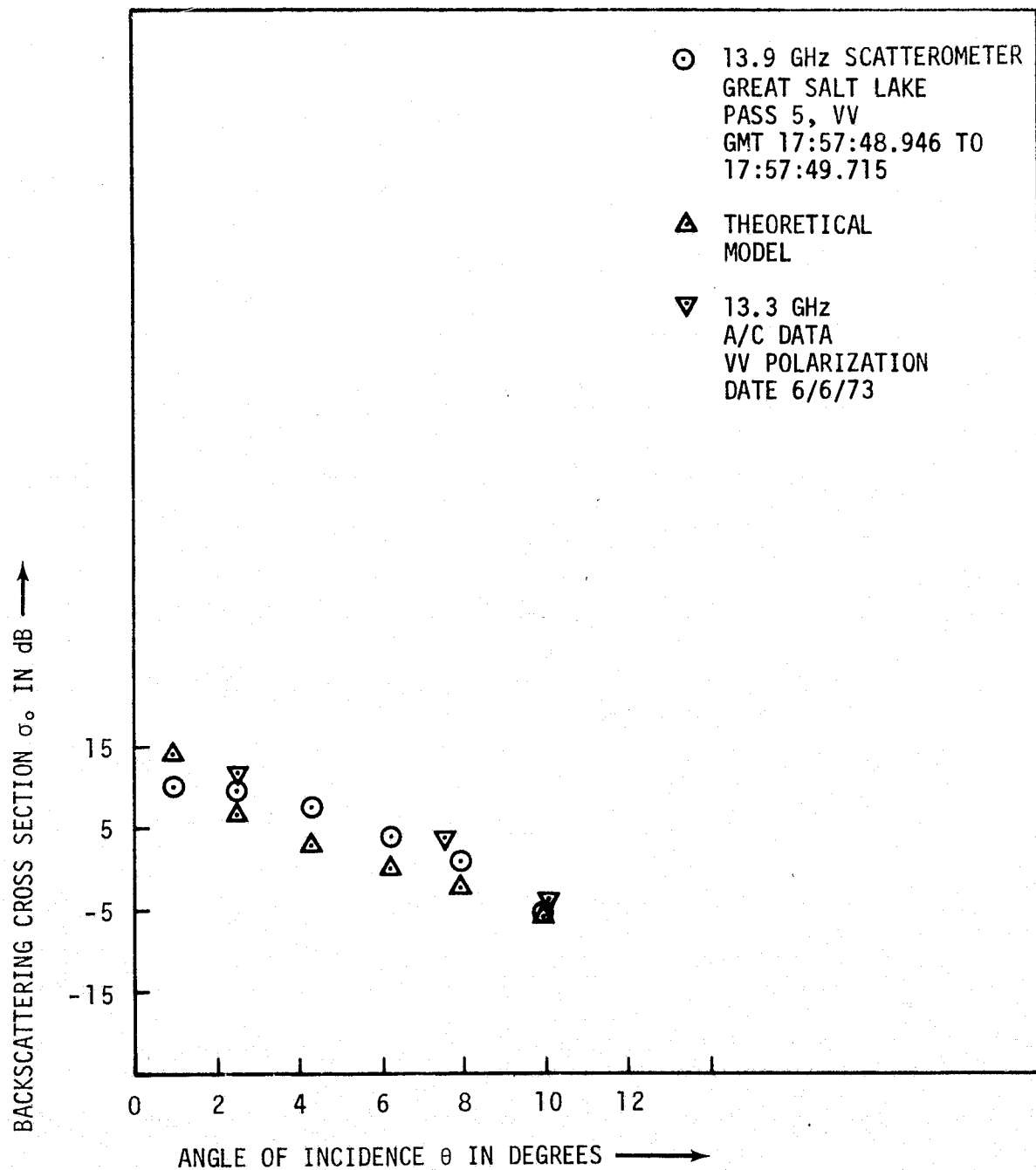


Figure 6-9. — Comparison of S-193 Great Salt Lake data with theoretical results and 13.3 GHz data.

capillary and gravity-waves, and exact atmospheric attenuation). In view of the limitations imposed on the mathematical models, it is felt that the accuracy of S-193  $\sigma_0$  data is certainly better than the upper bound of 3 dB.

### 6.3 COMPARISON OF S-193 SCATTEROMETER PREFLIGHT PERFORMANCE AND PRECISION/ACCURACY ESTIMATES

An error analysis of the scatterometer system was performed by Moore (reference 48) using measured preflight sensor parameters. The following assumptions are involved in his analysis:

- There are two basic types of errors: bias or systematic errors, both known and unknown, and random errors.
- Known bias errors can be calibrated out of the system with data processing.
- Unknown bias errors, such as switch insertion loss and short term temperature variations, etc., are fixed during any one measurement sequence but change randomly from one measurement sequence to the next.
- Random and unknown bias errors are independent and will be root-sum-squared (rss) to provide a most probable measure of their total effect.
- Those components which are not temperature-controlled will be monitored to determine their temperature so that the error introduced will be of the known bias type.

- Losses before any amplifier in a chain will be lumped together.
- Rotary joint insertion loss variation due to position occurs at a rate slower than the radiometer chopping rate and will be rejected. For the scatterometer calibration, it will be considered an unknown bias error.
- Intermediate frequency bandpass filters will be assumed to be ideal rectangular bandpass filters and bandwidth as specified. They will otherwise be subject to drift and variation in their other parameters such as insertion loss, bandwidth, etc.
- RF unknown bias errors will be rss together to compute a single unknown bias error.

The following error sources have been identified by Moore (reference 48).

- Transmitted power error

The mean loss in the transmit path is 1.323 dB known bias with an unknown bias error of  $\pm 0.059$  dB. This variational error is attributed to the circulator unit whose long term drift is slow but will not be able to be calibrated inflight and the unknown bias error due to switch indexing. The rotary joint error is also assumed to be cyclic in nature, i.e., a bias error whose peak level is known but there being no way to calibrate its affect except statistically by data processing. For these reasons,

the variations in the transmit path have been rssi together and considered an unknown bias error with random distribution.

- Calibration path loss from transmitter to circulator D (see appendix A)

The attenuation in the path is 105.87 dB with an unknown bias error of  $\pm 0.028$  dB.

- Transmitter leakage

Leakage from the transmitter may enter the scatterometer receiver through circulator D. The total isolation is 120 dB minimum with an unknown bias error of  $\pm 10$  dB.

- Rotary joint leakage

The rotary joints have a maximum radiation leakage of 95 dB below the power level transmitted through them. Assuming the leakage to emanate from the most undesirable spatial point and the leakage opening to act as an isotropic radiator, the free-space loss at 13.9 GHz from the rotary joint will be 45.02 dB/foot. The rotary joints are about 1 foot behind the dish edge. It will be assumed that the dish will also act as an isotropic antenna in the near field behind the dish. Therefore, the leakage signal due to two rotary joints is 95 dB +45 dB -3 dB (two joints) equal to 137 dB below the transmitted power through the joint.

- Coupling between channels

The dual-channel rotary joints leave 95 dB maximum leakage between channels. The output of the scatterometer transmitter couples directly into the

down converter input as seen in figure A-5. Since there are two dual-channel rotary joints, there are two paths of leakage, i.e., -95 dB/path +3 dB/two joints = -92 dB leakage into the down converter. The expected power level of the scatterometer calibration signal at the output of the TDA is -105.87 dB before TDA +30 dB TDA gain = -75.87 dB.

- Loss from circulator E to TDA input (see figure A-5)  
The loss is 6.369 dB with an unknown bias error of  $\pm 0.058$  dB.
- Loss/gain of down converter i.f. ampere power splitters  
The gain of the i.f. amplifier is 20 dB  $\pm 0.1$  dB. The uncertainty is a long term known bias. The power splitters have a loss of 7.035 dB  $\pm 0.42$  dB, but these uncertainties were known before flight.
- Scatterometer processor errors (dynamic range error)  
The scatterometer processor error is 2.52 percent and distributed as follows:

Mixer variation	82.9 percent
Gate isolation	15.7 percent
50 MHz ampere variation	<u>1.4</u> percent
Total	100.0 percent

Component variations after the three-range-gate amplifier section are reduced by the gain of the amplifier in use since the variation only affects the finite range of  $\sigma_0$  computed after the coarse selection of the range of  $\sigma_0$ . For example, the range of  $\sigma_0$  will be known to lie between +10 to -10 dB, -10 to -30 dB, -30 to -50 dB exactly



by selecting the proper range-gate amplifier. The variational error will apply only to the resolution of the 20 dB range chosen.

- Scatterometer error

The error variations discussed thus far have been shown as unknown bias errors which, while constant for a measuring sequence, are distributed randomly from one sequence to another. The best estimate of scatterometer accuracy is a root-sum-squared estimate of these errors as follows:

Receiver signal error (circulator unit)	$\pm 0.055$ dB 1.2 percent
Transmitted power error	$\pm 0.059$ dB 1.3 percent
Calibration path error	$\pm 0.028$ dB 0.6 percent
Calibration error, (undesired signals)	$\pm 0.03$ dB 0.7 percent
Signal path loss error	$\pm 0.058$ dB 1.3 percent
Processor errors	<u><math>\pm 0.11</math> dB 2.52 percent</u>
	rss = 3.46 percent

or  $\pm 3.46$  percent of the calibration signal. Besides this unknown bias uncertainty, one should consider the signal power contributed by undesired signals in relation to the desired signal.

<u>Undesired (dB)</u>	<u>Desired (dB)</u>	<u>Difference (dB)</u>	<u>Error percent</u>
Switch isolation - 120 dB	-106	-14	±3.98
Rotary joint leakage - 137 dB	-106	-31	±0.07
Coupling between channels - 92 dB maximum	-75.87	-16.13	±2.36

The antenna gain error (squared) is ±12.1 percent.

Total systematic (unknown

$$\begin{aligned}
 \text{bias) error (rss)} &= (3.46 \text{ percent}^2 + 3.98 \text{ percent}^2 \\
 &\quad + 0.07 \text{ percent}^2 + 2.36 \text{ percent}^2 \\
 &\quad + 12.1 \text{ percent}^2)^{1/2} \\
 &= \pm 13.4 \text{ percent}
 \end{aligned}$$

The total unknown bias error estimate of ±13.4 percent would correspond to approximately ±0.55 dB. In addition to these systematic errors there are several sources of random errors. General Electric personnel (reference 48) have evaluated two error sources.

These are:

Statistical error due to noise	±12.2 percent
Scatterometer processor (differential channel error)	±2.3 percent

A significant error source is due to antenna pointing. Accurate value of the antenna pointing error is not available. However, ground tests conducted during Skylab missions indicate a pointing accuracy of 0.3° (reference 43). This angular error can cause the  $\sigma_0$  to be computed for incorrect angles. The error in computing  $\sigma_0$  due to  $R_\theta$  (the range) and  $\theta$

(the angle of incidence) are indeed small (less than 0.05 dB) for the highest  $\theta$ ). But the error due to assigning an incorrect angle to a  $\sigma_0$  value could amount to a significant error depending on the ground scene and the angle of incidence. Maximum errors will result for very flat surfaces. For actual rough ground surfaces this error is small (approximately 2 dB in the worst case).

To meet the constraints of the shroud envelope, the focal length to diameter ratio of the S-193 antenna was reduced. This factor, plus the limitations in the antenna feed and microwave switching network, resulted in low isolation between the vertical and horizontal antenna polarization ports. Based on the estimates of cross coupling from the University of Kansas, the ratio of power received in the desired polarization and the cross-polarization for the S-193 Radiometer was only approximately 10 to 13 dB.

For the radiometer an attempt to make a first order correction for this mixing of energy from two polarizations was performed in production data processing. For the scatterometer the condition is more complex. Small errors are generated in the vertical-transmit, vertical-receive (VV) and horizontal-transmit, horizontal-receive (HH) modes. However, in the cross-polarized modes, vertical-transmit, horizontal-receive (VH) and horizontal-transmit, vertical-receive (HV), the situation is extremely difficult.

Cross-polarized return signals are generally 10 to 15 dB below the level of like-polarized return signals (see  $\sigma_0$  data given in section 5). Since the antenna provided only approximately 20 dB of isolation on transmission or

reception between polarizations, extraneous-like polarized return signals typically 5 to 10 dB below the power of the desired cross-polarized signals are introduced into the data. An undesired signal (5 dB lower in power) added to a desired signal of the same frequency can cause errors as large as +1 to -3.5 dB depending upon the phase relationships between the two. The stochastic nature of the return signals may contribute to increasing this error. Consequently, an uncertainty must be assigned to the cross-polarized scatterometer data.

The preflight error estimates lend enough evidence as to the suitability of the results derived from the flight data. Considering the preflight performance, the precision better than 1.5 dB and accuracy better than 3 dB, as estimated in this report, are reasonable. It should be emphasized that for short segments of data (over a test site) precision as well as accuracy will approximate the preflight values given in appendix A.

## 7.0 CONCLUSIONS

A precision estimate was generated by computing the standard deviation of the backscattering cross sections over selected uniform surfaces. A worst-case estimate of 1.5 dB was found. For the estimation of accuracy two methods were adopted. The S-193 Scatterometer was compared to the existing microwave data at or near 13.9 GHz frequency. Theoretical values of  $\sigma_0$  were also computed using a composite scattering model and ground data. The comparisons showed the accuracy estimate to be better than 3 dB. It should be emphasized that these estimates apply to  $\sigma_0$  data for VV and HH polarization for the backscattering cross section range of 18 to -28 dB. For  $\sigma_0$ 's greater than 18 dB, saturation of scatterometer further degrades the precision/accuracy. For  $\sigma_0$ 's below -28 dB the analog-to-digital converter and the system noise combined degrade the accuracy and precision of the measurement.

The dependence of backscattering cross sections on angle of incidence and surface roughness was found to be consistent with the theoretical and experimental results quoted in the literature. From the detailed analysis of S-193 Scatterometer data presented in section 5.0, it is possible to conclude that the quality of  $\sigma_0$  data is more than adequate for most applications for which the sensor was designed. In fact, significant applications have been reported in the area of ocean and land remote sensing (reference 19). For applications requiring an accuracy of more than 1 dB, the data must be evaluated carefully for specific data segments to ascertain the data accuracy.

One advantage of the S-193 Scatterometer precision/accuracy analysis was in evaluating the algorithms and production data processing programs. As a result of data analysis which was undertaken for precision/accuracy determination, several anomalies were found. These anomalies were investigated and resulted in several modifications to the NASA S-193 production processing programs. The S-193 Scatterometer data was reprocessed for analysis by principal investigators.

For the evaluation of the scatterometer algorithm, a method was developed to model the sensor on a time-sharing computer system. The effects of polarization isolation were studied using this model. With the existing polarization isolation of 20 dB, errors could result in the cross-polarized backscattering cross section. The magnitude of these errors depends on the polarization characteristics of the scattered energy from the target.

## 8.0 REFERENCES

1. Krishen, K. and D. J. Pounds: Skylab Program, EREP Sensor Performance Evaluation Implementation Plan. Task Number SPE-S193-004, NASA/Johnson Space Center, Document Number JSC-SPE-00412, Houston, Texas, May 1973.
2. Kaufman, D.: RF Link Equation for the Skylab S-193 Radiometer/Scatterometer. Technical Report LEC-4119, Lockheed Electronics Company, Inc., Houston, Texas, August 1974.
3. Krishen, K.: S-193 Quick-Look II Data Verification Plan. Lockheed Electronics Company, Inc., Technical Report LEC/HASD 640-TR-063, April 1971.
4. Ruck, George T., et al.: *Radar Cross Section Handbook*. Volume II, Plenum Press, New York, 1970.
5. Beckmann, P. and A. Spizzichino: *The Scattering of Electromagnetic Waves from Rough Surfaces*. Pergamon Press, New York, 1963.
6. Beckmann, P.: *Probability in Communication Engineering*. Harcourt, Brace and World, Inc., New York, 1967.
7. Krishen, K.: Correlation of Radar Backscattering Cross Sections with Ocean Wave Height and Wind Velocity. *Journal of Geographical Research*, Volume 76, Number 27, pages 6,528-6,539, September 1971.
8. Kaufman, D. E.: The Scattering of Electromagnetic Waves from a Rough Surface of Arbitrary Dielectric Constant. Technical Report EE-TR-6, Department of Electrical Engineering, Kansas State University, Manhattan, Kansas, May 1967.
9. Blacksmith, P., R. E. Hiatt, and R. B. Mack: Introduction to Radar Cross Section Measurements. *Proceedings IEEE*, Volume LIII, August 1965, pages 901-920.
10. Bass, G. and V. G. Bocharov: On the Theory of Electromagnetic Wave Scattering from a Statistically Uneven Surface. *Radio Engineering and Electronics* (Translated from *Radiotekhnika i Elektronika*), Volume 3, pages 251-258, 1958.

11. Krishen, K.: Reflection from Rough Layers. Ph.D. dissertation, also published as Kansas State University Technical Report EE-TR-11, June 1968.
12. Rice, S. O.: Reflection of Electromagnetic Waves by Slightly Rough Surfaces. In Kline, M.: The Theory of Electromagnetic Waves. John Wiley (Interscience), New York, 1951; also Dover, New York, 1963.
13. Valenzuela, G. R.: Depolarization of EM Waves by Slightly Rough Surfaces. IEEE Transactions on Antennas and Propagation, AP-15, pages 552-557, 1967.
14. Wright, J. W.: Backscattering from Capillary Waves with Application to Sea Clutter. IEEE Transactions on Antennas and Propagation, AP-14, pages 749-754, 1966.
15. Skolnik, M. I.: Sea Echo. Chapter 26, Radar Handbook, McGraw-Hill, New York, 1970.
16. Grant, C. R. and B. S. Yaplee: Backscattering from Water and Land at Centimeter and Millimeter Wavelengths. Proceedings IRE, Volume XLIV, July 1957, pages 972-982.
17. Kerr, D. E.: Propagation of Short Radio Waves. Boston Technical Publishers, Lexington, Massachusetts, 1964.
18. Schooley, A. H.: A Single Optical Method for Measuring the Statistical Distribution of Water Surface Slopes. Journal Optical Society of America, Volume XLIV, 1954, pages 37-40.
19. Cox, C. and W. Munk: Measurement of the Roughness of the Sea Surface from Photographs of the Sun's Glitter. Journal Optical Society of America, Volume 44, 1954, pages 838-850.
20. Neumann, G. and W. J. Pierson: Principles of Physical Oceanography. Chapter 12, Prentice-Hall, Inc., Englewood Cliffs, New Jersey, 1966.
21. Phillips, O. M.: *The Dynamics of the Upper Ocean*. Cambridge University Press, London, 1966.
22. Rouse, J. W.: The Effect of the Subsurface on the Depolarization of Rough-Surface Backscatter. Radio Science, Volume VII, Number 10, October 1972, pages 889-895.



23. Haroules, G. G. and W. Brown III: Radiometric Measurements of Attenuation and Emission by the Earth's Atmosphere at Wavelengths from 4 cm to 8 mm. IEEE Transactions on MIT, Number 6, September 1968.
24. Rosenblum, E. S.: Atmospheric Absorption of 10 to 400 KMCPS Radiation. The Microwave Journal, March 1961.
25. Benoit, A.: Signal Attenuation Due to Neutral Oxygen and Water Vapor, Rain, and Clouds. The Microwave Journal, II, 1968.
26. Thompson III, W. I. and G. G. Haroules: A Review of Radiometric Measurements of Atmospheric Attenuation at Wavelengths from 75 Centimeters to 2 Millimeters. NASA Technical Note, NASA TN D-5087, NASA, Washington, D.C., April 1969.
27. LeFande, R. A.: Attenuation of Microwave Radiation for Paths through the Atmosphere. Department 6766, Naval Research Laboratory, Washington, D.C., November 1968.
28. Paris, J.: MOADAP Microwave Atmospheric and Oceanic Data Analysis Program. Technical Report, 640-TR-078, Lockheed Electronics Company, Inc., HASD, December 1971.
29. Oguchi, T.: Attenuation of Electromagnetic Waves Due to Rain with Distorted Raindrops. Journal of Radio Research Laboratory (Japan), Volume II, Number 19, September 1964.
30. Stafford, L.: Scatterometer Signal-to-Noise Ratio Considerations. Private Communication.
31. Nathanson, F. E.: Radar Design Principles. McGraw-Hill Book Company, New York, 1969.
32. Earth Resources Experiment Package, Sensor Performance Report, S-193 Radiometer/Scatterometer. National Aeronautics and Space Administration, Johnson Space Center, Houston, MSC 05528, Volume IV, October 1974.

33. S-193 SL-4 Scatterometer Algorithm Modification.  
(Prepared jointly by Lockheed Electronics Company, Inc., and the University of Kansas), Lockheed Electronics Co., Inc., Technical Report LEC-5247, December 1974.
34. Hippel, Von (ed.): *Dielectric Materials and Applications*. The M.I.T. Press, Massachusetts Institute of Technology, Cambridge, Massachusetts, 1954.
35. Paris, Jack F.: Transfer of Thermal Microwaves in the Atmosphere. Department of Meteorology, Texas A&M University, College Station, Texas, Volume I, May 1971.
36. Hasted, J. B., D. M. Ritson, and C. H. Collie: Dielectric Properties of Aqueous Ionic Solutions. *Journal Chemical Physics*, Volume 16, pages 1-21, 1948.
37. Hasted, J. B. and S. M. El-Sabeh: The Dielectric Properties of Water in Solutions. *Transactions of the Faraday Society*, Volume 49, pages 1,003-1,011, 1953.
38. Paris, Jack F.: Salinity Surveys Using an Airborne Microwave Radiometer. *Proceedings of the Eighth International Symposium on Remote Sensing of Environment*, Ann Arbor, Michigan, pages 665-676, 1972.
39. Hollinger, J. T.: Passive Microwave Sensing of Marine Windspeed. (Paper communicated to NASA Active Microwave Workshop, held in July 1974). Naval Research Laboratory, Washington, D.C., July 1974.
40. Earth Resources Production Processing Requirements for EREP Electronic Sensors. PHO-TR524, Revision A., Change, National Aeronautics and Space Administration, Lyndon B. Johnson Space Center, Houston, Texas, May 1973.
41. Grant, C. R. and B. S. Yaplee: Backscattering from Water and Land at Centimeter and Millimeter Wavelengths. *Proceedings IRE*, Volume 45, July 1957, pages 972-982.

42. Daley, J.: An Empirical Sea Clutter Model. Naval Research Laboratory Report 2668, October 1973.
43. NASA Johnson Space Center, Earth Resources Experiment Package Sensor Performance Evaluation Final Report. Volume IV (S-193 Radiometer/Scatterometer), MSC-05546, January 1975.
44. Krishen, K.: Determination of the Backscattering Cross Section from the S-193 Altimeter-Acquired Data. Lockheed Electronics Company, Inc., Technical Memorandum LEC-3095, March 1974.
45. Pilon, R. O.: Determination of Ocean Surface Descriptors Using Sea Photo Analysis Techniques. Naval Research Laboratory, Washington, D.C., July 1973.
46. Wu, Jin: Sea-Surface Slope and Equilibrium Wind-Wave Slope. The Physics of Fluids, Volume 15, Number 5, May 1972.
47. Krishen, K.: Remote Sensing of Surface Parameters Using Skylab S-193 Radiometer/Scatterometer Data. Proceedings of the URSI Specialist Meeting on Microwave Scattering and Emission from the Earth, University of Berne, Berne, Switzerland, September 1974.
48. Moore, J. H.: Radiometer/Scatterometer Error Analysis and Error Distribution. Program Information Request/Release, PIR Number U-1J85-S-193-016, General Electric Missile and Space Division, Philadelphia, July 1970.
49. Krishen, K.: The Significance of the S-193 Skylab Experiment Using Preliminary Data Evaluation. Lockheed Electronics Company, Inc., Technical Memorandum LEC-4250, August 1974.
50. Historical Logbook, S-193 Microwave Radiometer/Scatterometer/Altimeter. General Electric Corporation, Document Number 72SD4234, Revision A, Volumes 1 through 10, October 1972.
51. Calibration Data Report, Flight Hardware, S-193 Microwave Radiometer/Scatterometer/Altimeter. General Electric Corporation, Document Number 72SD4207, Revision D, March 1973.

52. Akima, Hiroshi: A New Method of Interpolation and Smooth Curve Fitting Based on Local Procedures. Journal of the Association for Computing Machinery, Volume 17, Number 4, October 1970, pages 589-602.
53. Krishen, K. and D. J. Pounds: S-193 Radiometer and Scatterometer Sensor Mathematical Models. Lockheed Electronics Company, Inc., Technical Report LEC-1741, Houston, Texas, February 1974.
54. Cook, A. C. and A. Sobti: Development of an Algorithm for Evaluating the Scatterometer Illumination Integral. Technical Memorandum 236-1, University of Kansas Space Technology Laboratories, Lawrence, Kansas, February 1973.
55. Skylab Instrumentation Calibration Data Book. National Aeronautics and Space Administration, Johnson Space Center, Houston, Texas, Volume IV, Revision B, Chapter 2, January 1974.
56. Earth Resources Production Processing Requirements for Aircraft Electronic Sensors. PHO-TR523, Revision A, Channel 2, National Aeronautics and Space Administration, Lyndon B. Johnson Space Center, Houston, Texas, October 1974.
57. Krishen, K., N. Vlahos, O. Brandt, and G. Graybeal: Results of Scatterometer Systems Analysis for NASA/MSC Earth Observation Sensor Evaluation Program. Proceedings of the Seventh International Symposium on Remote Sensing of Environment, The University of Michigan, Ann Arbor, Michigan, May 1971.

ORIGINAL PAGE IS FOR...

## APPENDIX A

### THE S-193 SCATTEROMETER SENSOR BACKGROUND AND MATHEMATICAL MODEL

APPENDIX A  
THE S-193 SCATTEROMETER SENSOR  
BACKGROUND AND MATHEMATICAL MODEL

1.0 THE S-193 RADIOMETER/SCATTEROMETER OPERATIONAL MODES

The radiometer and scatterometer can operate in various scanning and polarization modes jointly and separately (reference 50). A summary of these modes is given in table A-I and briefly explained in the following sections.

1.1 INTRACK NONCONTIGUOUS (ITNC) MODE

This mode is used for a joint radiometer and scatterometer operation. In this mode, only the pitch angle is varied. A resolution cell on the ground (figure A-1) is seen by the radiometer and scatterometer at approximately the following pitch angles:  $0^\circ$ ,  $15.6^\circ$ ,  $29.4^\circ$ ,  $40.1^\circ$ , and  $48^\circ$ . The complete scan cycle time in this mode is 15.25 seconds. The roll angle is always zero.

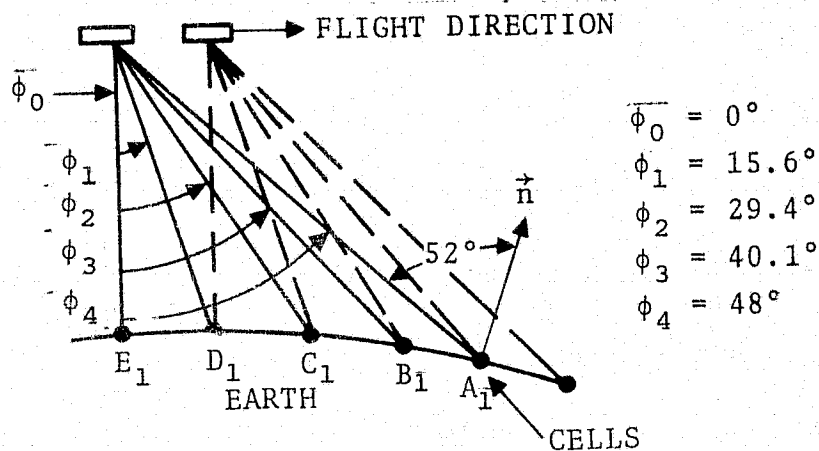


Figure A 1. Intrack noncontiguous (ITNC) scan mode  
( $\vec{n}$  is the normal to the surface at point  $A_1$ ).

TABLE A-I. -- NOMINAL S-193 RADIOMETER/SCATTEROMETER MODES

Operation	Scanning mode choice	Polarization choice	Pitch/roll angles
Radiometer/scatterometer	1. Intrack noncontiguous mode (ITNC)	1. Scatterometer VV, HH, VH, and HV Radiometer V and H 2. One polarization combination (VV or HH or HV or VH) for scatterometer and V or H for radiometer	0°, 15.6°, 29.4°, 40.1°, and 48° (pitch)
Radiometer/scatterometer	1. Crosstrack contiguous (CTNC) left/right 2. CTNC, left 3. CTNC, right	Same as for ITNC	Same as for ITNC (roll)
Radiometer/scatterometer	1. Intrack contiguous (ITC) mode	1. One polarization combination for scatterometer (VV or HH or VH or HV) and V or H for radiometer	Same as for ITNC (pitch)
Radiometer/scatterometer	1. Crosstrack contiguous (CTC) left/right	1. VV or HH for scatterometer and V or H for radiometer	+11° to -11° (roll)
Scatterometer only	1. CTC	1. V and H radiometer data	+11° to -11° (roll)
Scatterometer only	1. CTC	1. Scatterometer data for VV and HH	+11° to -11° (roll)

In reviewing the S-193 Radiometer/Scatterometer Skylab-acquired data, it was determined that some scan angle positions in this mode were different from the nominal prelaunch values. The angles,  $0^\circ$ ,  $15.6^\circ$ , and  $29.4^\circ$ , are not markedly different. However, the  $40.1^\circ$  and  $48^\circ$  angles show noteworthy change. In particular, the last angle remains, for most part, within  $46$  to  $47^\circ$ . The  $40.1^\circ$  angle is within  $1.5^\circ$  of the nominal value.

On the Earth Resources Experimental Package (EREP) pass 40 the antenna gimbals malfunctioned. The ITNC mode was not used subsequently.

## 1.2 CROSSTRACK NONCONTIGUOUS (CTNC) MODE

In this mode, the roll angle is varied identically to the intrack noncontiguous mode, and the pitch angle remains zero. The motion of the field-of-view (FOV) is shown in figure A-2, where it can be seen that individual cells are viewed from only one antenna position. Because of the motion of the antenna in the pitch direction, the cells lie on a curved arc. There are three forms of this mode — left scan, right scan, and left/right scan as shown in the figure. The outermost cell is viewed at approximately  $52^\circ$  (corresponding to  $48^\circ$  gimbal angle) and the innermost cell at approximately  $0^\circ$  at all times. The total scan time for a complete cycle is 15.25 seconds. The selection of polarizations is given in table A-1.

The S-193 data for the CTNC mode shows that the antenna scan angles are approximately the same for  $0^\circ$ ,  $15.6^\circ$ , and  $29.4^\circ$  angles. The  $40.1^\circ$  pitch angle reaches only approximately



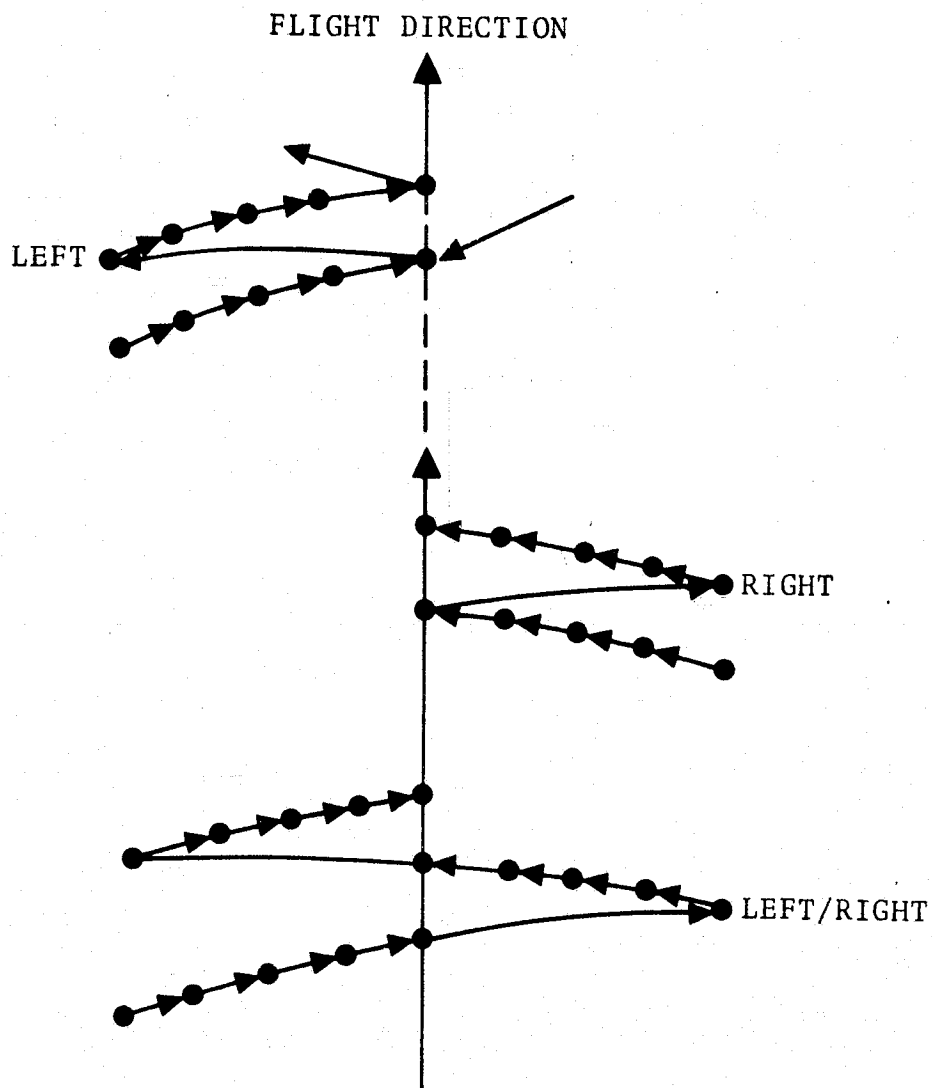


Figure A-2. — Crosstrack noncontiguous (CTNC) mode.

37.5° for the Skylab-acquired data. The right scan extends up to approximately 43° instead of the nominal value of 48°, and the left scan extends up to approximately 46° instead of 48°. Some oscillation in the antenna pitch angle is also noticeable at each dwell angle. However, actual antenna angles were recorded. Skylab-4 mission antenna scan motion was also variable.

### 1.3 INTRACK CONTIGUOUS (ITC) MODE

The pattern is similar to the intrack noncontiguous mode (figure A-3), except that the antenna is scanned much faster and there is no dwell at any antenna pitch angle. The entire inflight path is eventually scanned at all incidence angles with this process.

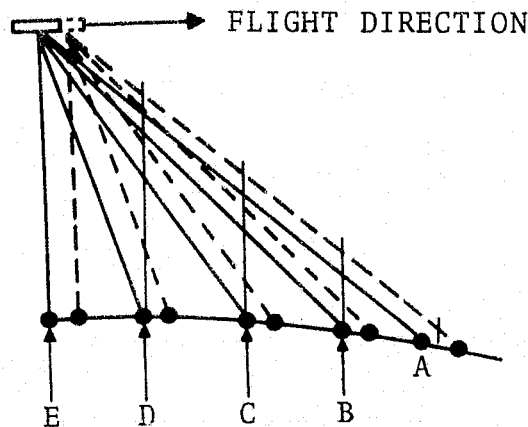


Figure A-3. — Intrack contiguous (ITC) mode.

The scan cycle time is chosen so that at the vehicle velocity the resolution cell at incidence angle  $48^\circ$  overlaps the previous cell by approximately 25 percent, the  $40.1^\circ$  cell overlaps its predecessor by less than 20 percent, etc., down to the  $0^\circ$  incidence angle case where gapping rather than overlap occurs. The complete cycle for one scan takes approximately 4.0 seconds.

As the vehicle progresses on successive scans, the entire path is viewed at  $48^\circ$  and less, except for gapping at lowest angles. Table A-I gives the selection of modes and polarizations.

In the ITC mode, the starting angle was about  $43^\circ$  (the nominal prelaunch value was  $48^\circ$ ) during the Skylab-2 and 3 missions. Since the Doppler filters are centered around  $48^\circ$ , the scatterometer data recorded for  $43^\circ$  is highly attenuated. Corrections for the Doppler filter attenuation have been implemented into the NASA/Data Systems and Analysis Division S-193 processing program. Other angles are also slightly off. The difference increases with increasing pitch angle. However, no correction to the scatterometer data is needed at the angles other than the highest angle (approximately  $43^\circ$ ).

During the Skylab-3 mission, a malfunction occurred in the antenna gimbals. The pitch gimbal was disabled as a fix. Consequently, no data was gathered in the ITC mode after the fix.

#### 1.4 CROSSTRACK CONTIGUOUS (CTC) MODE

This mode contains three submodes and further selection of polarizations (see table A-I). It provides a side-to-side linear scan covering  $\pm 11.375^\circ$  and a turnaround to repeat. As can be seen in figure A-4, this is a mapping mode. To compensate for the satellite forward velocity which could cause skewing of the pattern perpendicular to the flightpath, the pitch gimbal is scanned backwards slightly as the roll angle oscillates between its limits. Measurements are made for every  $1.896^\circ$  of beam center motion, ranging from  $-11.375^\circ$  to  $+11.375^\circ$  in roll. The total time of one cycle is 4.24 second. The pitch offset angles for this mode can be chosen as  $0^\circ$ ,  $15.6^\circ$ ,  $29.4^\circ$ , or  $40.1^\circ$ . The roll offset angles can be chosen from  $0^\circ$ ,  $+15^\circ$ ,  $-15^\circ$ ,  $-29.4^\circ$ , and  $+29.4^\circ$ . Either pitch or roll offset angle is selectable.

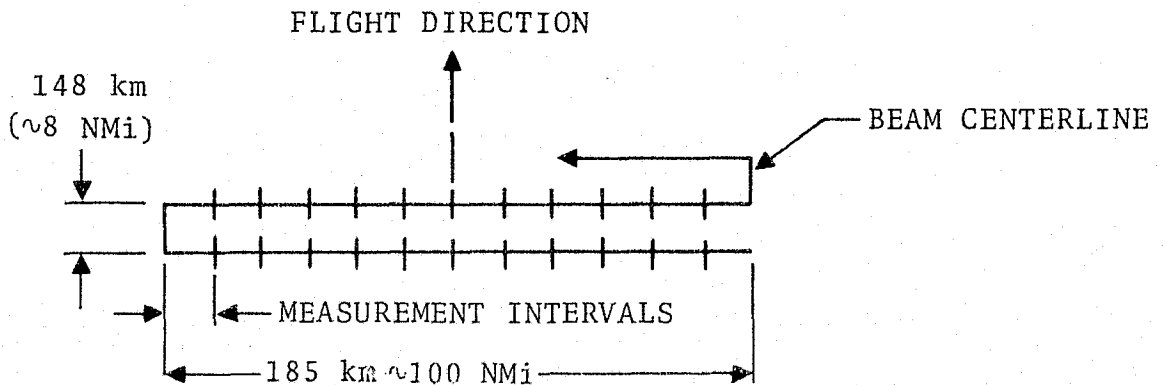


Figure A-4. — Crosstrack contiguous (CTC) mode.

A study of Skylab-acquired data in the CTC mode revealed that the scan extends only up to a total of approximately 20.6° instead of 22.75°. The repeatability of the timing sequence also differs from that indicated by figure A-4.

Because of the antenna malfunction during the Skylab-3 mission, the pitch gimbal was pinned at 0°. Consequently, the ground scans are not parallel for the Skylab-4 (SL-4) mission. The roll angles are also different in SL-4 data.

## 2.0 SUMMARY OF SCATTEROMETER SUBSYSTEM PARAMETERS

The nominal scatterometer parameters, in addition to those described in 2.1, are as follows (reference 50):

Data rate (radiometer/ scatterometer)	10.66 kbps (effective) Biphase
--	--------------------------------

### Transmitter

Frequency	13.9 GHz
Output tube	TWT
Peak power of tube	20 W (minimum)
Power losses to antenna input port	1.5 dB (maximum)
Pulse width	5.05 milliseconds for all scan angles in all modes
Pulse shape	100 µsec rise time maximum 100 µsec fall time maximum
Pulse repetition frequency	125 pps for all scan angles in all modes

## Receiver

Center frequency	13.9 GHz
First i.f.	500 MHz
Second i.f.	50 MHz
System noise	1,200°K (maximum)
Second i.f. bandwidths	Function of pitch angle only

<u>Pitch angle (degree)</u>	<u>Minimum i.f. bandwidth (kHz)</u>
0.0	68.4
15.6	66.6
29.4	61.0
40.1	54.7
48.0	47.5

Number of i.f. filters per pitch angle	3
--	---

Signal plus noise integration times (milliseconds)	41 (see table A-II)
--	---------------------

Noise integration times (milliseconds)	6 (see table A-II)
--	--------------------

Measurement precision	Maximum standard deviation of 0.0708 $\mu$ , where $\mu$ is mean of measurement, at 52° incidence angle, $\sigma_0 = 30$ dB.
-----------------------	--

Integration rate	2.207 milliseconds wide, turned on 5.3195 milliseconds after start of transmit pulse for all scan angles except 48°, for which the width is 2.351 milliseconds, turned on 5.61 milliseconds after start of transmit pulse
------------------	---

Detection	Square law device
-----------	-------------------

TABLE A-II. - SCATTEROMETER INTEGRATION TIMES

\*1 = Maximum gain curve  
 2 = Second highest gain curve  
 3 = Third highest gain curve  
 4 = Lowest gain curve

<sup>†</sup>Revised upon discussions with  
 General Electric engineers

Mode	Integration time per pulse	Scatterometer curve gain*	Scatterometer gain ( $G_S$ )	Number of pulses integrated	Total scatterometer (signal + noise) integration time (I.T.'s)	Scatterometer noise integration time (I.T.) <sub>N</sub>	Scatterometer and scatterometer noise integration time constant
CTC scatterometer only	2.187 ms	1	1.0			6.813 ms	(T.C.) <sub>S</sub> = (T.C.) <sub>N</sub>
		2	0.1007135	8	17.496		4.0 ms
		3	0.0082848	7	15.309		
		4	0.0008044	6	13.122		
ITC 48°	2.353 ms	1	Same as above	9	21.177	27.063	4.0
		2		8	18.824		
		3		7	16.471		
		4		6	14.118		
ITC less than 48°	2.187 ms	1		9	19.683	27.063	4.0
		2		8	17.496		
		3		7	15.303		
		4		6	13.122		
CTC radiometer/scatterometer	2.187 ms	1		14	30.618	16.735 <sup>†</sup>	10.22
		2		13	28.432		
		3		12	26.244		
		4		11	24.057		
Scatterometer calibration		4	1 ms for first pulse + 4.872 ms for next four pulses		20.488	N/A	10.22
NC radiometer/scatterometer or scatterometer only 0.0°	2.187 ms	1		23	50.301	26.582	10.22
		2		22	48.114		
		3		21	45.927		
		4		20	43.740		
15.6°	2.187 ms	1		39	85.293	61.532	33.0
		2		38	83.106		
		3		37	80.919		
		4		36	78.732		
29.4°	2.187 ms	1		57	124.659	61.532	33.0
		2		56	122.472		
		3		55	120.285 <sup>†</sup>		
		4		54	118.098		
40.1°	2.187 ms	1		64	139.968	125.532	33.0
		2		63	137.781		
		3		62	135.594		
		4		61	133.407		
48.0°	2.358 ms	1		74	174.122	125.532	33.0
		2		73	171.769		
		3		72	169.416		
		4		71	167.063		

Dynamic range

-66.2 to -131.2 dBm, measured  
at antenna output terminals  
(65 dB range overall)

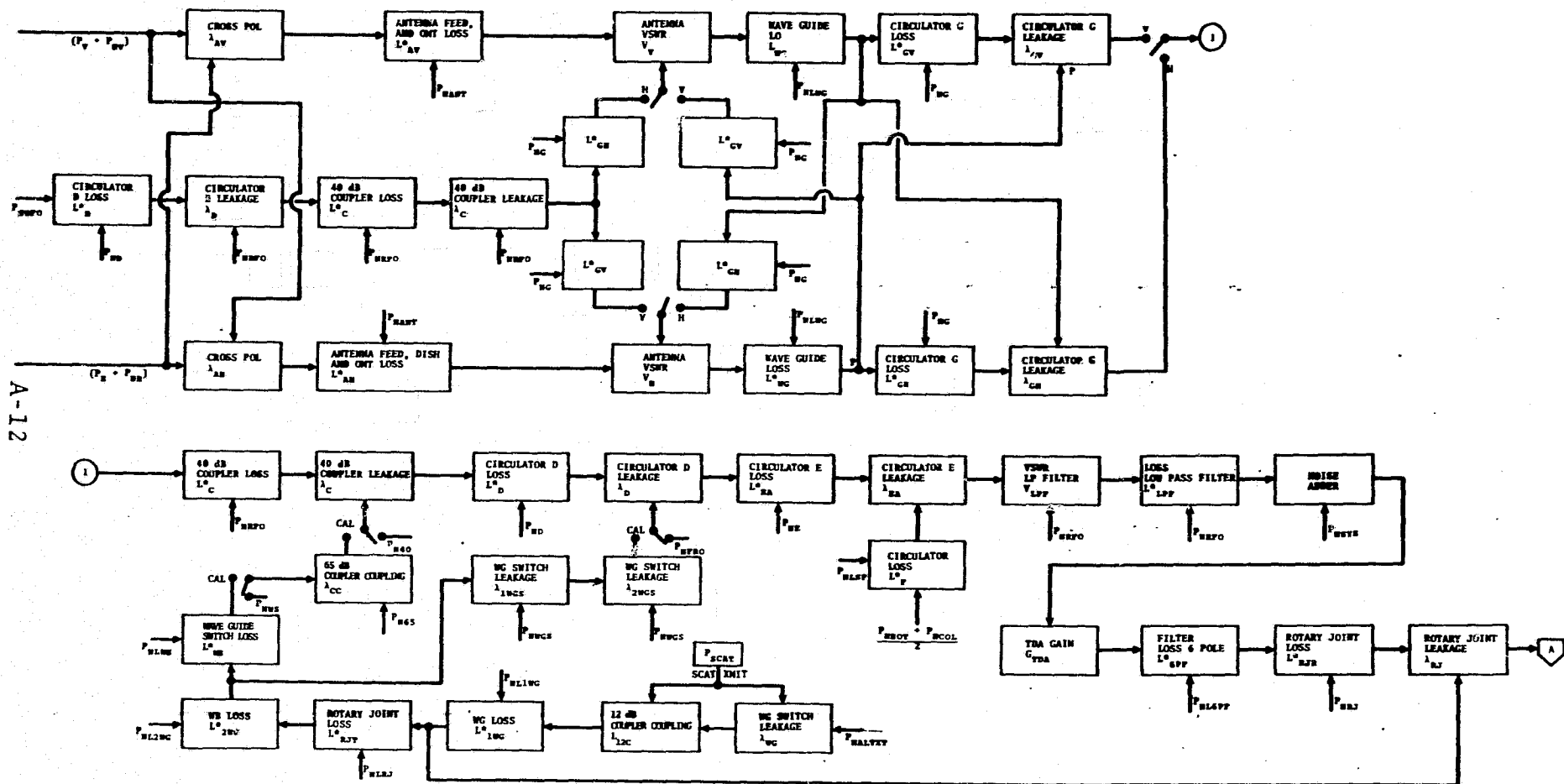
### 3.0 THE S-193 SCATTEROMETER SYSTEM MATHEMATICAL MODEL

#### 3.1 GENERAL DESCRIPTION

The S-193 documents by General Electric Corporation describe the scatterometer system one part at a time. From these subsystem details a functional block diagram was prepared for the purpose of developing a sensor mathematical model. The sensor has been broken into a series of "elements" which represent accurately a particular component characteristic. By combining one or more of these elements, a component is simulated. The simulated components are combined into a subsystem. Together, the subsystems represent the system. The functional block diagram of the S-193 Scatterometer system is given in figure A-5.

The input to the antenna is the vertically and horizontally polarized scattered power ( $P_V$ ,  $P_H$ , respectively). Passive microwave vertically and horizontally polarized powers emitted by the surrounding scene are denoted by  $P_{NV}$  and  $P_{NH}$ , respectively. These are added to the radar return power. The cross-polarization effects caused by the antenna and orthomode transducer are accounted for by introducing leakage factors  $\lambda_{aV}$  and  $\lambda_{aH}$  (figure A-6).  $\lambda_{aV}$  is the per unit cross-polarized power (i.e., horizontal) present when the antenna is switched to receive vertically polarized signals.  $\lambda_{aH}$  can be defined similarly.





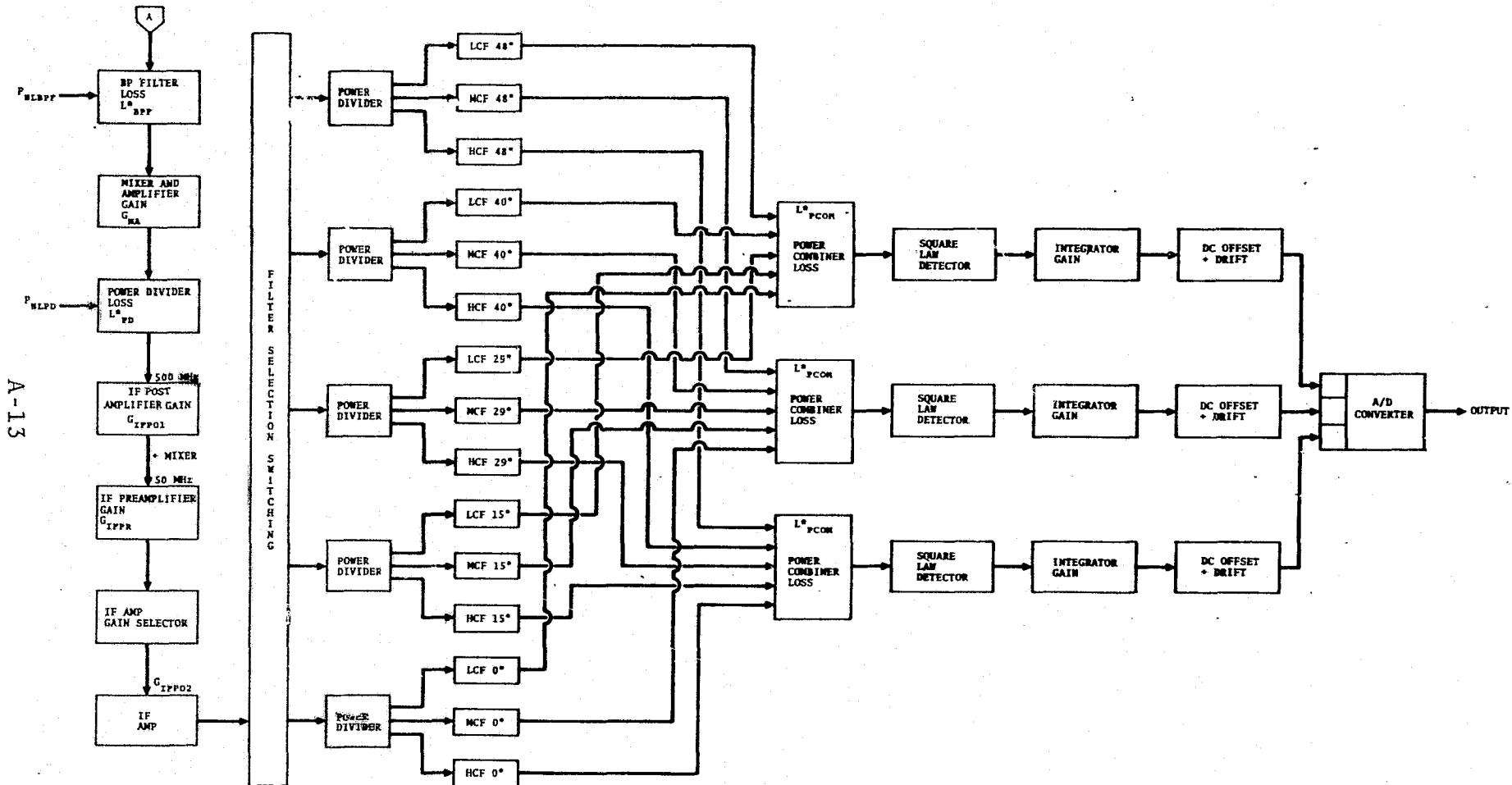


Figure A-5. - S-193 Scatterometer functional block diagram (concluded).

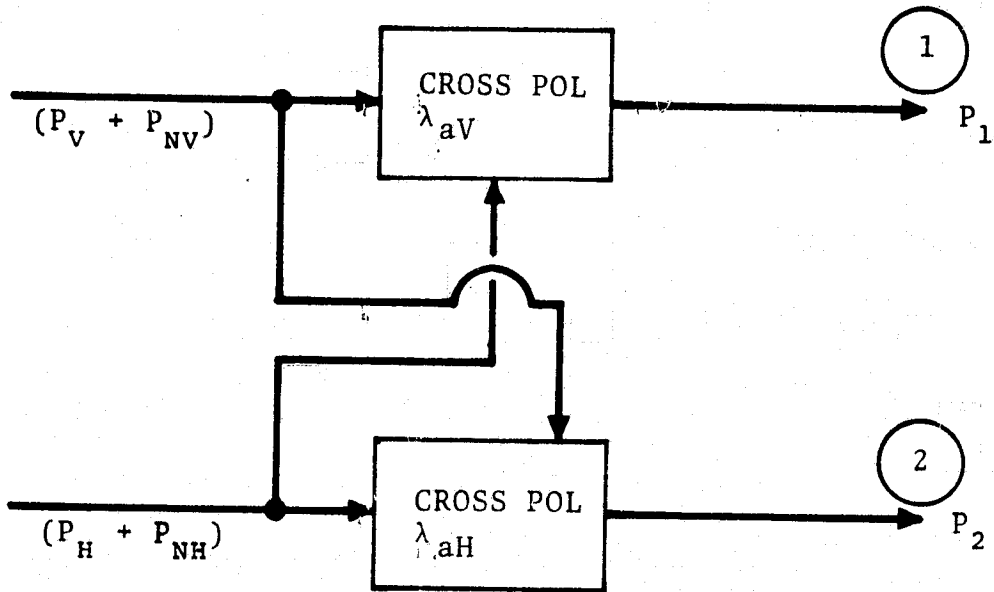


Figure A-6. — Cross-polarization model.

The following equations were used to take the cross-polarization into account:

$$P_1 = (P_V + P_{NV})(1 - \lambda_{aV}) + \lambda_{aV}(P_H + P_{NH}) \quad (A-1)$$

$$P_2 = (P_H + P_{NH})(1 - \lambda_{aH}) + \lambda_{aH}(P_V + P_{NV}) \quad (A-2)$$

In arriving at equations (A-1) and (A-2), the following assumptions were made:

- The antenna is a linear element.
- The ratios of the mixing of the polarization of the antenna remain constant and have been correctly measured.

- There is zero correlation between the vertical input signal, the horizontal input signal, the vertical noise received, and the horizontal noise received.

The losses in the circuits (figure A-7) were modeled using the following equation:

$$P_j = \frac{P_i}{L^*} + \frac{P_n(L^* - 1)}{L^*} \quad (A-3)$$

$P_i$  = Input power

$P_j$  = Output power

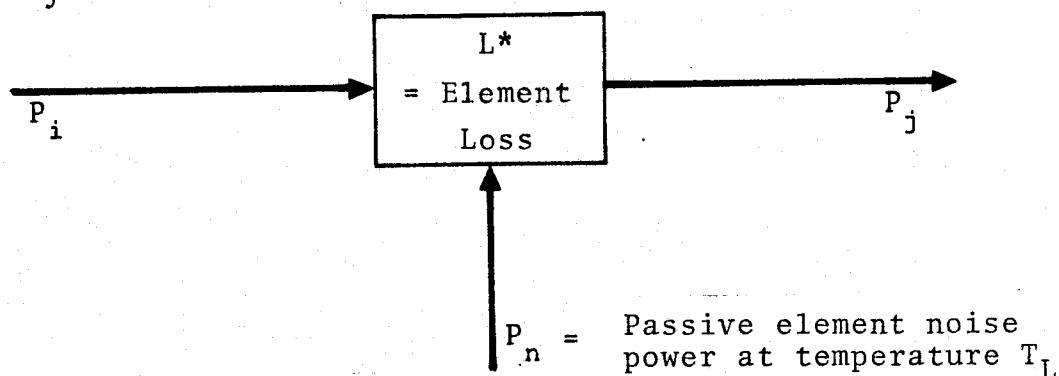


Figure A-7. — Loss model.

In equation (A 3)  $P_n$  is the passive noise power due to the element (loss  $L^*$ ) being at temperature  $T_L$ . The noise powers were computed using the Boltzmann's equation

$$P_N = kTB_n \quad (A-4)$$

where  $k$  is the Boltzmann constant ( $1.38 \times 10^{-23}$  watts - sec/°K),  $T$  the element temperature °K, and  $B_n$  the noise bandwidth.

The leakage factor has been modeled (figure A-8) using the following equation:

$$P_o = P_1(1 - \lambda) + \lambda P_X \quad (A-5)$$

where  $P_X$  is the leakage power into the element.

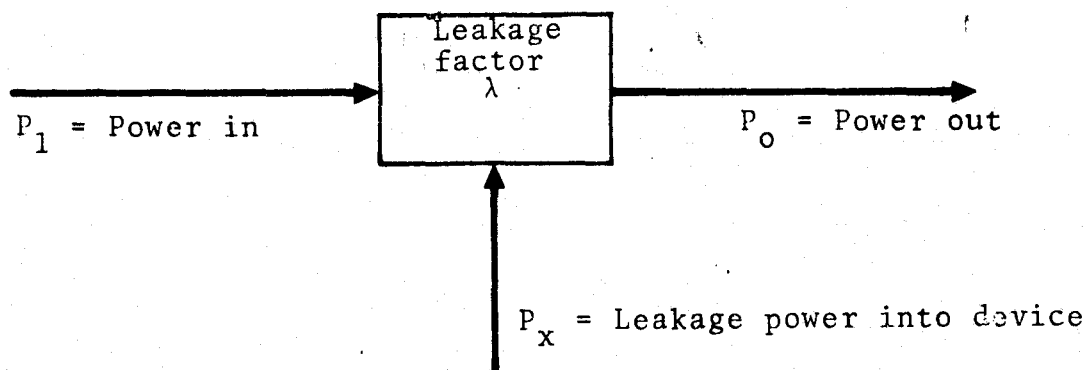


Figure A-8. — Leakage model.

The amplifier gains have been treated by computing outputs as the product of input and the gain.

The equation used for the antenna voltage standing wave ration (VSWR)  $V_v$  is as follows (see figure A-9)

$$P_B = P_A \frac{4V_V}{(1 + V_V)^2} + P_C \frac{(V_V - 1)^2}{(V_V + 1)^2} \quad (A-6)$$

where  $P_C$  is the power in the cross-polarized channel leaked into the channel under consideration.

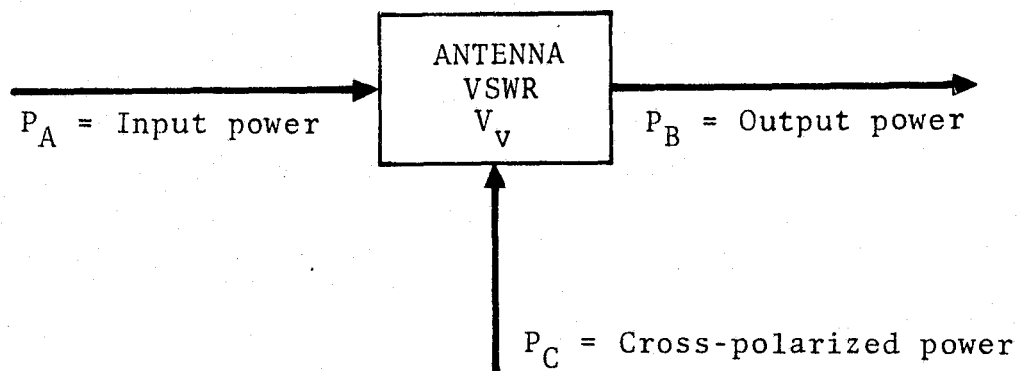


Figure A-9. — VSWR model.

The basic elements of the functional block diagram include the following types:

- Cross polarization
- Dissipative loss
- Discontinuities (reflections)
- Imperfect isolation (leakage)
- System noise
- Gains (constant and temperature dependent)
- DC offset
- Integrator drift

- Square law detection
- Analog-to-digital conversion

In the scatterometer model the radiometric noise temperatures have been converted to the noise powers. The advantage of treating the scatterometer in this manner is that the noise power for the system is adequately simulated. The output noise power from the scatterometer system depends not only on the system thermal state but also on the radiometric temperature of the surrounding scene.

The DC offset and the integrator drift were taken into account by adding voltages calculated from the following expression:

$$(IT) \cdot \text{drift} + \frac{IT}{TC} (\text{DC offset})$$

where IT is the integration time and TC is the time constant. Proper integration times and time constants have to be taken into account for noise plus signal, noise, and calibration data.

The computer model automatically selects paths and parameters to compute outputs corresponding to each S-193 mode and submode. Amplifier gains, filters, integrators, command angles, scan modes, etc., are selected, depending on the desired output. The calibration data used in the mathematical model was taken from references 50 and 51. Temperature dependence of the filter gains has been programmed. Since the DC offset term is only slightly dependent on the temperature, a constant temperature of 77°F was assumed.

This can cause a maximum error of 0.9 millivolts in the output based on actual results obtained from the computer model. The list of parameters used in the mathematical model is given in table A-III. This table also relates the symbols in the program to those in the scatterometer functional block diagram. The element losses, leakages, and gains have been assumed constant, as reported in reference 51.

The sensor simulation also included the analog-to-digital converter. Complete calibration data was not available for the analog-to-digital converter. There are only 20 calibration points instead of 1,024. In the analog-to-digital converter input, the voltage values are taken as each of the 10 bits is switched individually from 0 to 1. After the most significant bit reaches 1, each bit in turn is switched from 0 to 1 until a full count of 1,023 is obtained. In the simulation program since only 20 points were available, an interpolation technique, developed by Akima (reference 52), was used to convert each input voltage to counts. Three A/D curves (reference 51) were used in the scatterometer simulation model.

### 3.2 SCATTEROMETER COMPUTER MODEL AND RESULTS

The analytical models presented in section 3.1 of this appendix were coded into FORTRAN (or XTRAN) statements for each functional block of the scatterometer model. These statements, subroutines, subroutine calls, selection logic, and other statements were combined into a computer program. A list of the scatterometer model subroutines and a brief description of each are given in table A-IV (reference 53).



TABLE A-III. - LIST OF SCATTEROMETER PARAMETERS

Computer symbol	Mathematical symbol	Value	Comments
PV	$P_V$	$1.0 \times 10^{-10}$	1.
PH	$P_H$	$1.0 \times 10^{-10}$	1.
TNV	$T_{NV}$	$1.0 \times 10^2$	1.
TNH	$T_{NH}$	$1.0 \times 10^2$	1.
PSCAT		$2.0 \times 10^1$	
IFIL		1	2.
IGAIN		1	3.
ICMDA		1	4.
IMODE		1	5.
LAH	$\lambda_{AH}$	$7.8412 \times 10^{-2}$	
LAV	$\lambda_{AV}$	$6.0145 \times 10^{-2}$	
TNANT	$T_{NANT}$	$2.3665 \times 10^2$	7.
LSAV	$L^*_{AV}$	1.055626	
LSAH	$L^*_{AH}$	1.072161	
TND	$T_{ND}$	$2.9995 \times 10^2$	6.
LSD	$L^*_D$	1.048409	
TNRFO	$T_{NRFO}$	$2.9775 \times 10^2$	6.
LSC	$L^*_C$	1.027845	
LC	$\lambda_C$	$1.23288 \times 10^{-4}$	
TNSCATX	$T_{NSCATX}$	$2.8015 \times 10^2$	6.
LSGV	$L^*_{GV}$	1.0218550	

TABLE A-III. — LIST OF SCATTEROMETER  
PARAMETERS (Continued)

Computer symbol	Mathematical symbol	Value	Comments
TNG	$T_{NG}$	$2.991 \times 10^2$	
VH	$VSWR_H$	1.263	
TNLWG	$T_{NLWG}$	$2.3665 \times 10^2$	
LSWGV	$L^*_{WGV}$	1.0	
LSWGH	$L^*_{WGH}$	1.0	
VV	$VSWR_V$	1.262	
LGV	$\lambda_{gv}$	$4.39 \times 10^{-4}$	
TNE	$T_{NE}$	$2.9865 \times 10^2$	6.
LSGH	$L^*_{gh}$	1.01935	
LGH	$\lambda_{gh}$	$1.72 \times 10^{-4}$	
TNALTX	$T_{NALTX}$	$3.0 \times 10^2$	6.
L12C	$\lambda_{12c}$	$6.3895 \times 10^{-2}$	
TNL12C	$T_{NL12C}$	$2.764 \times 10^2$	6.
TNL1WG	$T_{NL1WG}$	$2.764 \times 10^2$	6.
LS1WG	$L^*_{1WG}$	1.051404908	
LSRJ	$L^*_{RJ}$	1.051961874	
TNLRJ	$T_{NLRJ}$	$2.70 \times 10^2$	
LRJ	$\lambda_{RJ}$	$1.874 \times 10^{-10}$	
TNL2WG	$T_{NL2WG}$	$2.9775 \times 10^2$	6.
LS2WG	$L^*_{2WG}$	1.037265659	

TABLE A-III. — LIST OF SCATTEROMETER  
PARAMETERS (Continued)

Computer symbol	Mathematical symbol	Value	Comments
TNLWS	$T_{NLWS}$	$2.9775 \times 10^2$	6.
LSWS	$L^*_{WS}$	1.009252886	
LCC	$\lambda_{CC}$	$1.90546 \times 10^{-7}$	
TN65	$T_{N65}$	$2.9775 \times 10^2$	6.
TNWGS	$T_{NWGS}$	$2.9775 \times 10^2$	6.
L1WGS	$\lambda_{1WGS}$	$6.3095734 \times 10^{-7}$	
L2WGS	$\lambda_{2WGS}$	$5.6234 \times 10^{-7}$	
Ld	$\lambda_d$	$9.1877 \times 10^{-4}$	
TNF	$T_{NF}$	$2.992 \times 10^2$	6.
LSEANT	$L^*_{EANT}$	1.051869	
TNHOT	$T_{NHOT}$	$3.922 \times 10^2$	6.
TNCOL	$T_{NCOL}$	$3.183 \times 10^2$	6.
TNLSF	$T_{NLSF}$	$2.992 \times 10^2$	6.
LSF	$L^*_F$	1.028532	
LEA	$\lambda_{EANT}$	$3.5495 \times 10^{-3}$	
VLPPF	$VSWR_{LPPF}$	1.1451	
LSLPPF	$L^*_{LPPF}$	1.059863656	
TNSYS	$T_{NSYS}$	$1.250 \times 10^3$	8.
GTDA	$G_{TDA}$	$7.70312 \times 10^2$	9.
TNLGPF	$T_{NL6PF}$	$2.9775 \times 10^6$	6.

TABLE A-III. — LIST OF SCATTEROMETER  
PARAMETERS (Continued)

Computer symbol	Mathematical symbol	Value	Comments
LS6PF	$L^*_{6PF}$	1.462117	
TNLBPF	$T_{NLBPF}$	$2.893 \times 10^2$	6.
LSBPF	$L^*_{BPF}$	1.0	
GMA	$G_{MA}$	4.7315	
TNLPD	$T_{NLPD}$	$2.893 \times 10^2$	
LSPD	$L^*_{PD}$	1.0	
GIFPO1	$G_{IFPO1}$	$1.045 \times 10^8$	10.
GIFPO2	$G_{IFPO2}$	1.	10.
GIFPR	$G_{IFPR}$	1.	10.
TNFILT	$T_{NFILT}$	$2.7685 \times 10^2$	6.
LSPDFIL	$L^*_{PDFIL}$	1.	11.
TNLPCM	$T_{NLPCM}$	$2.7685 \times 10^2$	6.
LSPCOM	$L^*_{PCOM}$	1.	12.
GIF	$G_{IF}$	1.	10.
GPLDET	$G_{PLDET}$	1.	13.
IT	$I_T$	1.74122	14.
TNWS	$T_{NWS}$	$2.9775 \times 10^2$	6.
TN40	$T_{N40}$	$2.9775 \times 10^2$	6.
TC	TC	$3.30 \times 10^1$	15.
DRIFT	DRIFT	$27 \times 10^{-6}$	16.
DC	DC	$1 \times 10^{-3}$	17.

TABLE A-III. - LIST OF SCATTEROMETER  
PARAMETERS (Concluded)

COMMENTS
1. Inputs to simulated sensor
2. LCF = 1, MCF = 2, HCF = 3
3. 1→Maximum gain, 4→Minimum gain
4. 1→48°, 2→40°, 3→29°, 4→15°, 5→0°
5. 1→ITC; 2→ITNC; 3,4,5→CTNC; 6→R/S CTC; 7→S CTC
6. Housekeeping data
7. Computed from housekeeping data
8. System noise temperature
9. Gain of TDA
10. Gain at i.f.
11. Loss in power divider and filter (dB)
12. Loss in power combiner
13. Gain of square law detector
14. Integration time
15. Time constant
16. Drift rate
17. DC offset of integrator

TABLE A-IV. — SCATTEROMETER MATHEMATICAL MODEL SUBROUTINES

Subroutine	Purpose
ACPT	<p>Acts as a driver routine to accept changes of parameter values (if any), typed in from the demand terminal.</p> <p>Input: Changes of program parameters.</p> <p>Output: Terminal display/printout of current value.</p>
ADCON	<p>Provides calibration data to convert an analog voltage to number of counts.</p> <p>Input: Analog voltage and filter number.</p> <p>Output: Number of counts.</p>
GAINT	<p>Interpolates the filter gain ratio as a function of temperature.</p> <p>Input: Command angle, temperature, filter, and mode number.</p> <p>Output: Gain ratio.</p>
GAINS	<p>Automatically selects gain value to be used as a function of polarization, mode, and input power <math>P_V</math> or <math>P_H</math>.</p> <p>Input: Signal power, polarization mode, and current gain.</p> <p>Output: Gain factor.</p>

TABLE A-IV. -- SCATTEROMETER MATHEMATICAL MODEL  
SUBROUTINES (Continued)

Subroutine	Purpose
AKITRP	<p>Uses the 20 input calibration points from A/D converter as a basis to interpolate the complete output calibration of A/D converter.</p> <p>Input: Calibration points and counts, analog input voltage, number of calibration points.</p> <p>Output: Number of counts.</p>
CX	<p>Computes the power output for a leakage element.</p> $PO = PI + (PX - PI) * AL$ <p>Input: Input power (PI), power through leakage "element" (PX), the leakage (AL).</p> <p>Output: Power output from leakage element.</p>
CL	<p>Computes power at the output of a lossy element.</p> $PO = [PI + PN * (AL - 1)] / AL$ <p>Input: Input power (PI), thermal noise power of the "element" (PN), and element loss (AL).</p> <p>Output: Power output from lossy element.</p>

TABLE A-IV, — SCATTEROMETER MATHEMATICAL MODEL  
SUBROUTINES (Continued)

Subroutine	Purpose
VSWR	<p>Computes the output power at a reflection boundary.</p> $PO = PI*4*V/(V + 1)**2 + PR*[(V - 1)/(V + 1)]**2$ <p>Input: Input power (PI), VSWR (V), power presented to the function by the thermal radiation of the components following the function (PR).</p> <p>Output: Power at the "output" side of the reflection boundary.</p>
CPOL	<p>Accounts for the cross-polarization of the antenna.</p> $P1 = (PV + PNV)*(1 - LAV) + LAV*(PH + PNH)$ $P2 = (PH + PNH)*(1 - LAH) + LAH*(PV + PNV)$ <p>Input: Signal and noise powers, cross-polarization leakage.</p> <p>Output: Power at the output of the antenna for each polarization channel.</p>
PNOISE	<p>Converts the element temperature and effective noise bandwidth to noise power</p> $PN = (1.38*10^{-23})*TN*BW$ <p>Input: Element temperature and bandwidth.</p> <p>Output: Noise power.</p>



TABLE A-IV. — SCATTEROMETER MATHEMATICAL MODEL  
SUBROUTINES (Continued)

Subroutine	Purpose
FILTER	<p>Table lookup to filter bandwidth.</p> <p>Input: Command angle, scan mode, and filter number.</p> <p>Output: Filter bandwidth.</p>
FILG	<p>Performs the normalization of the Doppler filter gains.</p> <p>Input: Signal power, command angle, scan mode, and filter number.</p> <p>Output: Signal power relative to the middle center frequency filter of the 0° Doppler filter set.</p>
DETTTC	<p>Performs logical selection of time constant.</p> <p>Input: Scan mode, polarization, command angle.</p> <p>Output: Time constant.</p>
DETIT	<p>Performs logical selection of the integration time.</p> <p>Input: Scan mode, polarization, command angle, and signal gain.</p> <p>Output: Integration time.</p>

TABLE A-IV. — SCATTEROMETER MATHEMATICAL MODEL  
SUBROUTINES (Concluded)

Subroutine	Purpose
DDRIFT	<p>Determine voltage drift rate via a logical selection and table lookup.</p> <p>Input: Filter number and time constant.</p> <p>Output: Voltage drift rate.</p>
DDC	<p>Simple logical lookup for DC offset value.</p> <p>Input: Signal gain, filter number, and time constant.</p> <p>Output: DC offset value.</p>

A complete listing of the S-193 Scatterometer computer model is given in table A-V. Several runs were made to illustrate the usefulness of the computer model. The results of the data runs are given in figures A-10 through A-13.

The scatterometer output, calculated using the sensor mathematical model, for CTC radiometer/scatterometer mode is shown in figure A-10. The input power level has been varied from -135 to -70 dBm. This graph has been drawn for the vertical polarization case. The radiometric brightness temperature of the sensed scene was assumed to be 4°K and 270°K. Figure A-10 illustrates the effect of radiometric brightness of the target on the output of the scatterometer system. As expected, the brightness temperature is of significance only for the lowest signals (or the highest gain curve). The linear behavior of the curves at high power levels is expected, since the model does not simulate nonlinear behavior at the dynamic range extreme. Note, however, that the output limits at 5 volts when the A/D converter hits maximum counts. The dashed part of the curves in figure A-10 is the expected output-versus input-power relationship since a linear system is simulated.

To illustrate the effect of integration time, time constant, and filter characteristics, two input versus output plots have been drawn in figure A-11. These plots correspond to CTC and ITNC modes. In these computer runs the radiometric temperature of the surrounding ( $T_{NV}$ ) scene is assumed to be 270°K. The input versus output curves for CTC and ITNC modes are not the same. In the S-193 Scatterometer data processing, the difference in the input versus output is properly accounted for.

TABLE A-V. - SCATTEROMETER MATHEMATICAL MODEL  
COMPUTER PROGRAM

```

*LIST
1      % SCAT SMD CALLED SMAIN MAY 7 1975
2      IMPLICIT REAL (A-Z)
3      COMMON /ANROUT/ PINT(6)
4      COMMON /DIGOUT/ DIGO(6)
5      INTEGER IPOL
6      COMMON /KK/PV,PH, TNV, TNL, PSCAT, IFIL, IGAIRN, ICMDA, IMODE, BW, %
7      LAH, LAV, TNANT, LSAV, LSAH, TND, LSD, TNRFQ, LSC, LC, TNSCTX, LSG
V, %
8      TNG, VH, TNLWG, LSWGV, LSWGH, VV, LGV, TNE, LSGH, LGH, TNALTX, L12
C, %
9      TNL1WG, LS1WG, TNLRJ, LSRJT, LSRJR, LRJ, TNL2WG, LS2WG, TNLWS, L
SMS, %
10     LCC, TN65, TNWGS, L1WGS, L2WGS, LD, TNF, LSEA, TNHDT, TNCOL, TNLS
F, %
11     LSF, LEA, VLPF, LSLPF, TNSYS, GTDA, TNL6PF, LS6PF, TNLBPF, LSBPF
GMA, %
12     TNLPD, LSPD, GIFF01, GIFF02, GIFFR, TNFILT, LPDFIL, TNLPCM, LSP
COM, %
13     GIF, GPLDET, IT, TNWS, TN40, TC
14     COMMON/KK1/DRIFT, DC
15     PV=1.E-10
16     PH=1.E-10
17     TNV=100.
18     TNH=100.
19     PSCAT=20.
20     IFIL=1
21     IGAIRN=1
22     ICMDA=1
23     IMODE=1
24     % : BWIN SET TO 0
25     LAH=.078412
26     LAV=.060105
27     TNANT=236.65
28     LSAV=1.055626
29     LSAH=1.072161
30     TND=299.95
31     LSD=1.048409
32     TNRFQ=297.75
33     LSC=1.027845
34     LC=.000123288
35     TNSCTX=280.15
36     LSGV=1.0218550
37     TNG=299.1
38     VH=1.263
39     TNLWG=236.65
40     LSWGV=1.
41     LSWGH=1.
42     VV=1.262
43     LGV=4.39 E-4
44     TNE=298.65
45     LSGH=1.01935
46     LGH=1.72 E-4
47     TNALTX=300.
48     L12C=.063895
49     TNL12C=276.4
50     TNL1WG=276.4
51     LS1WG=1.051405
52     LSRJT=1.051962
53     LSRJR=1.347132
54     TNLRJ=270.
55     LRJ=1.874 E-10

```

TABLE A-V. -- SCATTEROMETER MATHEMATICAL MODEL  
COMPUTER PROGRAM - Continued

```

56      TNL2WG=297.75
57      LS2WG=1.037265
58      TNLWS=297.75
59      LSWS=1.009253
60      LCC=1.90546 E-07
61      TN65=297.75
62      TNWGS=297.75
63      117  L1WGS=6.3095734 E-07
64      118  L2WGS=5.6234 E-07
65      LD=9.1877 E-4
66      TNF=299.2
67      LSEA=1.051869
68      TNHOT=392.2
69      TNCOL=318.3
70      TNLSF=299.2
71      LSF=1.028532
72      LEA=3.5495 E-3
73      VLPPF=1.1451
74      LSLPF=1.059864
75      TNSYS=1250.
76      GTDA=770.312
77      TNL6PF=297.75
78      LS6PF=1.462177
79      TNLBPF=289.3
80      109  LSBPF=1.
81      GMA=4.7315
82      TNLPD=289.3
83      110  LSPD=1.
84      111  GIFF01=1.064E10
85      112  GIFF02=1.
86      113  GIFFR=1.
87      TNFILT=276.85
88      LPDFIL=1.0
89      TNLPCM=276.85
90      114  LSPCOM=1.
91      115  GIF=1.
92      116  GPLDET=1.
93      IT=174.122
94      TNWS=297.75
95      TN40=297.75
96      TC=33.0
97      DRIFT=27. E-06
98      DC=4.9 E-03
99      %    : MAIN PROG ENTERS HERE.
100     %    : ACPT CONTROLS RECEIPT OF TEPMINAL INPUT CHANGES TO PA
PARAMETERS.
101     %1   CALL ACPT
102     %    WRITE(6,*)
103     %    WRITE(6,*) / INITIAL POWERS -- PV,PH...
104
105
106
107     WRITE(6,101) PV,PH
108     101 FORMAT(1H //// PV= ',E15.7,' PH= ',E15.7)
109     DO 100 IPOL=1,6
110     IF (IPOL.GE.5) ICMDA=5
111     IF (IPOL.EQ.5) IFIL=2
112     IF (IPOL.EQ.6) IFIL=1

```

TABLE A-V. - SCATTEROMETER MATHEMATICAL MODEL  
COMPUTER PROGRAM - Continued

```

113 CALL FILTER(IFIL,IMODE,ICMDA,BW)
114 CALL PNOISE(TNWS,BW,PNWS)
115 CALL PNOISE(TN40,BW,PN40)
116 CALL PNOISE(TNV,BW,PNV)
117 CALL PNOISE(TNH,BW,PNH)
118 CALL PNOISE(TNANT,BW,PNANT)
119 CALL PNOISE(TND,BW,PND)
120 CALL PNOISE(TNRFD,BW,PNRFD)
121 CALL PNOISE(TNG,BW,PNG)
122 CALL PNOISE(TNLWG,BW,PNLWG)
123 CALL PNOISE(TNE,BW,PNE)
124 CALL PNOISE(TNALTX,BW,PNALTX)
125 CALL PNOISE(TNL12C,BW,PNL12C)
126 CALL PNOISE(TNL1WG,BW,PNL1WG)
127 CALL PNOISE(TNLRJ,BW,PNLRJ)
128 CALL PNOISE(TNL2WG,BW,PNL2WG)
129 CALL PNOISE(TN65,BW,PN65)
130 CALL PNOISE(TNWGS,BW,PNWGS)
131 CALL PNOISE(TNF,BW,PNF)
132 CALL PNOISE(TNHOT,BW,PNHOT)
133 CALL PNOISE(TNCOL,BW,PNCOL)
134 CALL PNOISE(TNLSF,BW,PNLSF)
135 CALL PNOISE(TNSYS,BW,PNSYS)
136 CALL PNOISE(TNLBPF,BW,PNLBPF)
137 CALL PNOISE(TNLPD,BW,PNLPD)
138 CALL PNOISE(TNFILT,BW,PNFILT)
139 CALL PNOISE(TNSCTX,BW,PNSCTX)
140 CALL PNOISE(TNLPCM,BW,PNLPCM)
141 IF (IPOL.EQ.3) PV=0.
142 IF (IPOL.EQ.3) PH=0.
143 CALL CPUL(PV,PNV,PH,PNH,LAV,LAH,P1,P2)
144 CALL CL(P1,PNANT,LSAV,PVAF)
145 CALL CL(P2,PNANT,LSAH,PHAF)
146 CALL CL(PNRFD,PND,LSD,PCD)
147 CALL CX(PCD,PNRFD,LD,PCD)
148 CALL CL(PCD,PNRFD,LSC,PCC)
149 CALL CX(PCC,PNRFD,LC,PCC)
150 IF (IPOL.EQ.2) GO TO 2
151 IF (IPOL.EQ.4) GO TO 2
152 % : IPOL=2 IMPLIES HORIZONTAL
153 CALL CL(PCC,PNG,LSGV,PLV)
154 CALL VSWR(PHAF,PLV,VH,VSWRH)
155 CALL CL(VSWRH,PNLWG,LSWGH,P)
156 CALL CL(P,PNG,LSGV,PP)
157 CALL VSWR(PVAF,PP,VV,VSWRV)
158 CALL CL(VSWRV,PNLWG,LSWGV,PWG)
159 CALL CL(PWG,PNG,LSGV,PLG)
160 CALL CX(PLG,P,LGV,PVH)
161 GO TO 3
162 2 CALL CL(PCC,PNG,LSGH,PLH)
163 CALL VSWR(PVAF,PLH,VV,VSWRV)
164 CALL CL(VSWRV,PNLWG,LSWGV,P)
165 CALL CL(P,PNG,LSGH,PP)
166 CALL VSWR(PHAF,PP,VH,VSWRH)
167 CALL CL(VSWRH,PNLWG,LSWGH,PWG)
168 CALL CL(PWG,PNG,LSGH,PCG)
169 CALL CX(PCG,P,LGH,PVH)
170 3 CONTINUE
171 CALL CX(PNALTX,PNSCTX,LWG,PNL12C)
172 CALL CX(PNL12C,PNSCTX,L12C,P12DBC)
173 IF (IPOL.EQ.5) CALL CX(PNALTX,PSCAT,LWG,PNL12C)
174 IF (IPOL.EQ.5) CALL CX(PNL12C,PSCAT,L12C,P12DBC)
175 CALL CL(P12DBC,PNL1WG,LS1WG,PL1WG)
176 CALL CL(PL1WG,PNLRJ,LSRJ,PRJ)
177 CALL CL(PRJ,PNL2WG,LS2WG,PL2WG)
178 CALL CL(PL2WG,PNLWS,LSWS,PWS)
179 PCP=PVS
180 IF (IPOL.EQ.3) PCP=PNWS
181 IF (IPOL.EQ.4) PCP=PNWS
182 CALL CX(PN65,PCP,LCC,P65C)
183 IF (IPOL.EQ.4) P65C = PN40
184 CALL CL(PVH,PNRFD,LSC,P40DB)
185 CALL CX(P40DB,P65C,LC,P40DB)

```

TABLE A-V. - SCATTEROMETER MATHEMATICAL MODEL  
COMPUTER PROGRAM - Continued

```

186      CALL CL(P40DB,PND,LSD,PCD)
187      CALL CX(PNWGS,PL2WG,L1WGS,PWGS)
188      CALL CX(PNWGS,PWGS,L2WGS,PWGS)
189      IF(IPOL,LE,4.)PWGS = PNRFO
190      CALL CX(PCD,PWGS,LD,PCD)
191      CALL CL(PCD,PNE,LSEA,PCE)
192      PNHC=(PNHOT+PNCOL)/2.
193      CALL CL(PNHC,PNLSF,LSF,PLF)
194      CALL CX(PCE,PLF,LEA,PCE)
195      CALL VSWR(PCE,PNRFO,VLPF,PLPF)
196      CALL CL(PLPF,PNRFO,LSLPF,PLPF)
197      PNDIS=PLPF+PNSYS
198      PGTD = GTDA+PNDIS
199      CALL CL(PGTD,PNLSF,LS6PF,P6PF)
200      CALL CL(P6PF,PNLRJ,LSRJ,P2RJ)
201      CALL CX(P2RJ,PNL1WG,LRJ,P2RJ)
202      CALL CL(P2RJ,PNLSF,LS6PF,P6PF)
203      GPBPF=GMA+P6PF
204      CALL CL(GPBPF,PNLPD,LSPD,PPD)
205      PIFP01=GIFP01+PPD
206      PIFPR=GIFPR+PIFP01
207      PIFP02=GIFP02+PIFPR
208      CALL CL(PIFP02,PNFILT,LPDFIL,PPDL)
209      CALL CL(PPDL,PNLPCM,LSPCOM,PPCL)
210      CALL GAINS(IPOL,IGAIN,GIF,PPCL)
211      PIFG=PPCL*GIF
212      CALL FILG(ICMDA,IMODE,IFIL,PIFG,PIF6)
213      CALL GAINT(IFIL,IMODE,ICMDA,TNFILT,RATIO)
214      PIFG = PIFG*RATIO
215      %      WRITE(6,*) 'RATIO = ', RATIO
216      CALL DETIT (IMODE,IPOL,ICMDA,IGAIN,IT)
217      CALL DETTC (IMODE,IPOL,ICMDA,TC)
218      CALL DDRIFT(IFIL,TC,DRIFT)
219      CALL DDC(IFIL,IGAIN,TC,DC)
220      IF(IPOL,LE,2) WRITE(6,*) 'ICMDA=',ICMDA,' ***IMODE=',I
MODE, ' ***IFIL=',IFIL,' ***IGAIN=',IGAIN
221      %      WRITE(6,*) 'DC = ',DC,' *** DRIFT = ',DRIFT
222      PPLD=PIFG*IT/TC*GPLDET
223      PDAO=PPLD+(IT*DRIFT+(IT/TC)*DC)
224      PINT(IPOL) = PDAO
225      %      WRITE(6,*) 'TC = ',TC,' *** IT = ',IT,' *** B
W = ',BW
226      %      WRITE(6,*) 'PINT(',IPOL,')=',PINT(IPOL)
227      100 CONTINUE
228      WRITE(6,*) 'VVERT = ',PINT(1)
229      WRITE(6,*) 'VHOR = ',PINT(2)
230      WRITE(6,*) 'VNOISEV = ',PINT(3)
231      WRITE(6,*) 'VNOISEH = ',PINT(4)
232      WRITE(6,*) 'VCAL1 = ',PINT(5)
233      WRITE(6,*) 'VCAL2 = ',PINT(6)
234      CALL ADCON(IFIL)
235      WRITE(6,*) 'DVVERT = ',DIG0(1)
236      WRITE(6,*) 'DVHOR = ',DIG0(2)
237      WRITE(6,*) 'DNVERT = ',DIG0(3)
238      WRITE(6,*) 'DNHOR = ',DIG0(4)
239      WRITE(6,*) 'DVCAL1 = ',DIG0(5)
240      WRITE(6,*) 'DVCAL2 = ',DIG0(6)
241
242      %      ! MAIN PROG EXITS HERE.
243      STOP
244      END

^Q
SRU'S12.3
IEDIT PNOISE
^LIST
1      %      ! 'PNOISE' -- COMPUTES NOISE POWER.
2      SUBROUTINE PNOISE(TN,BW,PN)
3      PN=(1.98 E-23)*TN*BW
4      RETURN
5      END

^Q
SRU'S1.3

```

TABLE A-V. -- SCATTEROMETER MATHEMATICAL MODEL  
COMPUTER PROGRAM - Continued

```

!EDIT CPOL
^LIST
1      %      : 'CPOL' -- COMPUTES POLARIZATION POWER.
2      SUBROUTINE CPOL(PV,PNV,PH,PNH,LAV,LAH,P1,P2)
3      REAL LAV,LAH
4      P1 = (PV+PNV)*(1.-LAV)+LAV*(PH+PNH)
5      P2 = (PH+PNH)*(1.-LAH)+LAH*(PV+PNV)
6      RETURN
7      END

^Q
SRU'S: .4
!EDIT CL
^LIST
1      %      : 'CL' -- COMPUTES POWER LOSS.
2      SUBROUTINE CL(TI,TE,AL,TD)
3      TD = (TI + TE * (AL - 1.)) / AL
4      %      WRITE(6,*) ' CL= ',TD
5      RETURN
6      END

^Q
SRU'S: .4
!EDIT CX
^LIST
1      %      : 'CX' -- COMPUTES CROSSTALK.
2      SUBROUTINE CX(TI,TX,AL,TD)
3      TD = TI + (TX - TI) * AL
4      %      WRITE(6,*) ' CX= ',TD
5      RETURN
6      END

^Q
SRU'S: .3
!EDIT VSWR
^LIST
1      %      : 'VSWR' -- COMPUTES POWER DISCONTINUITY WITHIN MODEL.
2      SUBROUTINE VSWR(TI,TR,V,TD)
3      TD=TI*.4*(V/(V+1.))**.2+TR*((V-1.)/(V+1.))**.2
4      %      WRITE(6,*) ' VSWR= ',TD
5      RETURN
6      END

^Q
SRU'S: .4
!EDIT FILTER
^L
1      %      : 'FILTER' -- DETERMINES FILTER BANDWIDTH.
2      SUBROUTINE FILTER(AFIL,AMODE,ACMDA,BW)
3      DIMENSION ABW(3,5)
4      DATA ABW/64890.,64445.,64930.,71270.,70870.,73775.,7950
5.,%
5      79330.,80465.,84570.,87405.,84990.,89425.,89750.,91995./
6      IFIL=AFIL
7      ICMDA=ACMDA
8      IMODE=AMODE
9      GO TO (1,1,2,2,2,1,1),IMODE
10     1      BW=ABW(IFIL,ICMDA)
11     RETURN
12     2      BW=ABW(IFIL,5)
13     RETURN
14     END

^Q
SRU'S: .4

```



TABLE A-V. - SCATTEROMETER MATHEMATICAL MODEL  
COMPUTER PROGRAM - Continued

!EDIT GAINS

```

^L
1      %      : 'GAINS' -- LOGICALLY SELECTS AUTOMATIC GAIN FACTOR.
2      SUBROUTINE GAINS(IPOL,AGAIN,GIF,PPCL)
3      DIMENSION GAIN(4)
4      DATA GAIN/1.,.1007135,.0082848,.0008044/
5      IGAIRN =AGAIN
6      GO TO(1,1,2,2,3,3),IPOL
7      IF(IGAIRN-10.) 10,20,20
9      IF(PPCL.LE..94) IGAIRN=1
10     IF(PPCL.GT..94) IGAIRN=2
11     IF(PPCL.GT.9.333) IGAIRN=3
12     IF(PPCL.GT.113.4607) IGAIRN=4
13     GO TO 9
14     2      IGAIRN=1
15     GO TO 9
16     3      IGAIRN=4
17     GO TO 9
18     20     IGAIRN = IGAIRN -10
19     9      GIF =GAIN(IGAIRN)
20     AGAIRN = IGAIRN
21     RETURN
22     END

```

^Q

SRU'S:1.4

!EDIT FILG

```

^L
1      %      : 'FILG' -- EQUALIZES GAIN BETWEEN FILTERS.
2      SUBROUTINE FILG(ACMDA,AMODE,AFIL,PIFG,POFG)
3      DIMENSION RGAIN(3,5)
4      DATA RGAIN/1.15,1.15,1.10,1.16,1.15,1.15,1.15,1.15,1.20
5      , %      .21,1.17,1.21,1.05,1.02,1.06/
6      ICMDA=ACMDA
7      IFIL= AFIL
8      IMODE=AMODE
9      GO TO (1,1,2,2,1,1) ,IMODE
10     POFG=PIFG*RGAIN(IFIL,ICMDA)
11     %      : WRITE(6,*)'RGAIN(IFIL,ICMDA) =' ,RGAIN(IFIL,ICMDA)
12     RETURN
13     2      POFG=PIFG*RGAIN(IFIL,5)
14     %      : WRITE(6,*)'RGAIN(IFIL,5) =' ,RGAIN(IFIL,5)
15     RETURN
16     END

```

^Q

SRU'S:1.4

!EDIT DETTC

```

^L
1      %      : 'DETTCC' -- DETERMINES TIME CONSTANT.
2      SUBROUTINE DETTC(AMODE,IPOL,ACMDA,TC)
3      ICMDA=ACMDA
4      IMODE=AMODE
5      IF(IPOL.GE.5) GO TO 20
6      10     GO TO (11,12,12,12,12,16,17) ,IMODE
7      11     TC=4.0
8      RETURN
9      12     TC=33.0
10     IF (ICMDA.EQ.5) TC=10.22
11     RETURN
12     16     TC=10.22
13     RETURN
14
15     17     TC=4.0
16     RETURN
17     20     TC=10.22
18     RETURN
19     END

```

^Q

SRU'S:1.4

TABLE A-V. - SCATTEROMETER MATHEMATICAL MODEL  
COMPUTER PROGRAM - Continued

!EDIT DETIT

^L

```

1      %      : 'DETIT' -- DETERMINES INTEGRATION TIME.
2      SUBROUTINE DETIT (AMODE,IPOL,ACMDA,AGAIN,AT)
3      IMODE=AMODE
4      ICMDB=ACMDA
5      AITPP=2.187
6      IF (ICMDA.EQ.1) AITPP=2.353
7      IF (IPOL.GE.5) GO TO 20
8      GO TO (11,12,12,12,12,16,17) ,IMODE
9      11      AT=AITPP*(10.-AGAIN)
10     IF (IPOL.GE.3) AT=27.063
11     RETURN
12     12      GO TO (121,122,123,124,125) ,ICMDA
13     121     AT=AITPP*(75.-AGAIN)
14     IF (IPOL.GE.3) AT=125.532
15     RETURN
16     122     AT=AITPP*(65.-AGAIN)
17     IF (IPOL.GE.3) AT=125.532
18     RETURN
19     123     AT=AITPP*(58.-AGAIN)
20     IF (IPOL.GE.3) AT=57.990
21     RETURN
22
23     124     AT=AITPP*(40.-AGAIN)
24     IF (IPOL.GE.3) AT=57.990
25     RETURN
26     125     AT=AITPP*(24.-AGAIN)
27     IF (IPOL.GE.3) AT=24.094
28     RETURN
29     16      AT=AITPP*(15.-AGAIN)
30     IF (IPOL.GE.3) AT=13.686
31     RETURN
32     17      AT=AITPP*(9.-AGAIN)
33     IF (IPOL.GE.3) AT=6.544
34     RETURN
35     20      AT= 20.488
36     RETURN
37     END

```

^Q

SRU'S:.6

!EDIT DDRIFT

^L

```

1      %      : 'DDRIFT' -- DETERMINES DRIFT RATE.
2      SUBROUTINE DDRIFT (AFIL,TC,DRIFT)
3      DIMENSION DRATE(3,3)
4      IFIL=AFIL
5      DATA DRATE/.163,.210,.206,.060,.083,.079,.017,.027,.031
6
7      IF (TC.EQ.4) ITC=1
8      IF (TC.EQ.10,22) ITC=2
9      IF (TC.EQ.33) ITC=3
10     DRIFT=DRATE(IFIL,ITC)*.001
11     RETURN
12     END

```

^Q

SRU'S:.4

TABLE A-V. - SCATTEROMETER MATHEMATICAL MODEL  
COMPUTER PROGRAM - Continued

```

!EDIT DDC
^L
1      %      : 'DDC' -- DETERMINES DC OFFSET VALUE.
2      SUBROUTINE DDC (AFIL,AGAIN,TC,DC)
3      DIMENSION DOFF(3,4,3)
4      DATA DOFF/6.4,4.6,4.8,3.8,4.0,4.0,3.5,4.0,3.9,5.0,4.0,3
.6,%
5      6      .4,5.0,4.7,3.8,4.4,3.9,3.5,4.4,3.8,5.0,4.4,3.5,      %
6      6      .1,4.9,4.4,3.8,4.3,3.7,3.5,4.3,3.6,5.0,4.3,3.3/
7      IFIL=AFIL
8      IGAIn= AGAIN
9      IF (TC.EQ.4) ITC=1
10     IF (TC.EQ.10,22) ITC=2
11     IF (TC.EQ.33) ITC=3
12     DC=.001*DOFF(IFIL,IGAIN,ITC)
13     RETURN
14     END

^Q
SRU'S:1.4
!EDIT ADCON
^L
1      %      : 'ADCON' -- ANALOG VOLTAGE TO DIGITAL COUNT CONVERTER.
2      SUBROUTINE ADCON(AFIL)
3      COMMON /ANROUT/AVV,AVH,ANV,ANH,AC1,AC2
4      COMMON /DIGOUT/DVV,DVH,DNV,DNH,DC1,DC2
5      REAL VOLTS(20), VOLT1(20), VOLT2(20), VOLT3(20)
6      REAL CNTS(20)
7      DATA VOLT1/-.004,.002,.007,.0206,.0373,.0765,.154,.310,
.6242,1.245
.003/
8      DATA VOLT2/-.007,.001,.0065,.0156,.033,.0737,.151,.309,
.6208,%
9      1.246,2.493,3.746,4.37,4.684,4.84,4.919,4.959,4.975,4.995,
5.005/
10     DATA VOLT3/-.003,.003,.0083,.0209,.0422,.0797,.1573,.31
5,.623,1.2
9,5.010/
11     DATA CNTS/0.,1.,2.,4.,8.,16.,32.,64.,128.,256.,512.,768
.,896.,960.
12     IFIL=AFIL
13     GO TO (1111,2222,3333),IFIL
14     1111 DO 991 I = 1,20
15     991 VOLTS(I) = VOLT1(I)
16     GO TO 999
17     2222 DO 992 I = 1,20
18     992 VOLTS(I) = VOLT2(I)
19     GO TO 999
20     3333 DO 993 I = 1,20
21     993 VOLTS(I) = VOLT3(I)
22     999 CALL AKITRP(VOLTS,CNTS,AVV,DVV,20)
23     CALL AKITRP(VOLTS,CNTS,AVH,DVH,20)
24     CALL AKITRP(VOLTS,CNTS,ANV,DNV,20)
25     CALL AKITRP(VOLTS,CNTS,ANH,DNH,20)
26     CALL AKITRP(VOLTS,CNTS,AC1,DC1,20)
27     CALL AKITRP(VOLTS,CNTS,AC2,DC2,20)
28     RETURN
29     END

^Q
SRU'S:1.5

```

TABLE A-V. - SCATTEROMETER MATHEMATICAL MODEL  
COMPUTER PROGRAM - Continued

```

IEDIT AKITRP
  L
  1      %      1 'AKITRP' -- INTERPOLATIVE LINE SMOOTHING.
  2      SUBROUTINE AKITRP (XX,YY,XD,YD,N)
  3      REAL T(2),M(5),XX(1),YY(1),XD,YD,X(6),Y(6)
  4      IF (N.GE.3) GO TO 1
  5      WRITE(1,1000)N
  6      1000  FORMAT(32H AKITRP - N MUST BE .GE. # N = ,I5)
  7      STOP
  8      1      DO 2 I = 2,N
  9      XXMXD = (XX(I-1)-XD)*(XX(I)-XD)
 10      IF (XXMXD.LE.0.) GO TO 33
 11      2      CONTINUE
 12      WRITE(1,1001)XX(1),XX(N),XD
 13      1001  FORMAT(1H , ' AKITRP  XD MUST BE BETWEEN ,E15.7, ' AND
 14      ,E15.7, ' XD = ,E15.7)
 15      WRITE(6,*) 'PV = ',PV, ' PH = ',PH
 16      STOP
 17      33      CONTINUE
 18      3      K = 3
 19      4      X(K) = XX(I+K-4)
 20      Y(K) = YY(I+K-4)
 21      K = K - 1
 22      IF (K.LE.0) GO TO 5
 23      IF (I+K-4.GE.1) GO TO 4
 24      IF (K.EQ.1) GO TO 6
 25      X(2) = XX(1)+XX(2)-XX(3)
 26      Y(2) = YY(1)+YY(2)-YY(3)
 27      X(1) = 2.*XX(1)-XX(3)
 28      Y(1) = 2.*YY(1)-YY(3)
 29      Y(1) = Y(2)+(X(1)-X(2))*(Y(2)-YY(1))/(X(2)-XX(1))+YY(1)
 30      (XX(1)-XX(3))
 31      GO TO 5
 32      6      X(1) = X(2)+X(3)-XX(3)
 33      Y(1) = Y(2)+Y(3)-XX(3)
 34      (X(3)-XX(3))
 35      K = 4
 36      7      X(K) = XX(I+K-4)
 37      Y(K) = YY(I+K-4)
 38      K = K + 1
 39      IF (K.GT.6) GO TO 10
 40      IF (I+K-4.LE.N) GO TO 7
 41      IF (K.EQ.6) GO TO 9
 42      X(5) = X(4)+X(3)-X(2)
 43      Y(5) = Y(4)+Y(3)-X(4)
 44      (Y(3)-Y(2))/(X(3)-X(2))
 45      X(6) = 2.*X(4)-X(2)
 46      Y(6) = Y(5)+(X(6)-X(5))*(Y(5)-Y(4))/(X(5)-X(4))+Y(4)-Y(
 47      (X(4)-X(3))-(Y(3)-Y(2))/(X(3)-X(2))
 48      GO TO 10
 49      9      X(6) = X(5)+X(4)-X(3)
 50      Y(6) = Y(5)+(X(6)-X(5))*(Y(5)-Y(4))/(X(5)-X(4))-Y(
 51      (Y(4)-Y(3))/(X(4)-X(3))
 52      10      DO 11 K = 1,5
 53      11      M(K) = (Y(K)-Y(K+1))/(X(K)-X(K+1))
 54      DO 12 K = 1,2
 55      T(K) = (ABS(M(K+3)-M(K+2))*M(K+1)+ABS(M(K+1)-M(K))*M(K+2)
 56      (ABS(M(K+3)-M(K+2))+ABS(M(K+1)-M(K)))
 57      IF ((M(K).EQ.M(K+1)).AND.(M(K+2).EQ.M(K+3)))
 58      T(K) = (M(K+1)+M(K+2))/2.
 59      12      CONTINUE
 60      P0 = Y(3)
 61      P1 = T(1)
 62      P2 = (3.*(Y(4)-Y(3))/(X(4)-X(3))-2.*T(1)-T(2))/(X(4)-X(
 63      (T(1)+T(2)-2.*(Y(4)-Y(3))/(X(4)-X(3)))/(X(4)-X(3))
 64      DX = XD-X(3)
 65      DXDX = DX*DX
 66      YD = P0+P1*DX+P2*DXDX+P3*DX*DXDX
 67      RETURN
 68      END
  SRU'S: 9

```

TABLE A-V. - SCATTEROMETER MATHEMATICAL MODEL  
COMPUTER PROGRAM - Concluded

```

EDIT GAIN
^L
1      %      : 'GAIN' -- DETERMINE TEMPERATURE BIASED FILTER GAIN R
RATIO.
2      SUBROUTINE GAIN(AFIL,AMODE,ACMDA,TEMP,RATIO)
3      DIMENSION RATIOG(3,3,5)
4      DATA RATIOG/.982,1.,.865,.932,1.,.889,.865,1.,.839,  %
5      .977,1.,.863,.933,1.,.888,.837,1.,.831,.984,1.,.862  %
6      .944,1.,.882,.860,1.,.826,1.04,1.,.851,.984,1.,.875,  %
7      .872,1.,.822,1.12,1.,.837,.971,1.,.878,.964,1.,.819/
8      IFIL = AFIL
9      IMODE = AMODE
10     ICMDA = ACMDA
11     TEMPIN = TEMP - 273.15
12     IF (TEMPIN-24.44) 10,20,30
13     10     TMPINR = 1.0
14     IF (TEMPIN+10.) 12,22,32
15     12     WRITE(6,*) '♦♦WARNING♦♦SCAT TEMP LESS THAN -10DEG CENT,
TEMPIN =', %
16     TEMPIN
17     32     GO TO 8
18     22     GO TO (4,4,5,5,5,4,4) ,IMODE
19     4     RATIO = RATIOG(1,IFIL,ICMDA)
20     RETURN
21     5     RATIO = RATIOG(1,IFIL,5)
22     RETURN
23     20     RATIO = 1.
24     RETURN
25     30     TMPINR = 3.
26     IF (TEMPIN-30.) 13,23,33
27     23     GO TO (6,6,7,7,7,6,6) ,IMODE
28     6     RATIO = RATIOG(3,IFIL,ICMDA)
29     RETURN
30     7     RATIO = RATIOG(3,IFIL,5)
31     RETURN
32     33     WRITE(6,*) '♦♦WARNING♦♦SCAT TEMP EXCEEDS 30DEG CENT, TEM
PIN =',%
33     TEMPIN
34     13     GO TO 9
35     8     GO TO (1,1,2,2,2,1,1) ,IMODE
36     1     RATIO = RATIOG(TMPINR,IFIL,ICMDA)
37     GO TO 3
38     2     RATIO = RATIOG(TMPINR,IFIL,5)
39     3     SLOPY = (1.-RATIO)/34.44
40     TEMPIN = 24.40 - TEMPIN
41     BYY = 1.-(SLOPY*TEMPIN)
42     RATIO = BYY
43     RETURN
44     9     GO TO (19,19,29,29,29,19,19) ,IMODE
45     19     RATIO = RATIOG(TMPINR,IFIL,ICMDA)
46     GO TO 39
47     29     RATIO = RATIOG(TMPINR,IFIL,5)
48     39     SLOPY = (1.-RATIO)/5.56
49     TEMPIN = TEMPIN -24.44
50     BYY = 1.-(SLOPY*TEMPIN)
51     RATIO = BYY
52     RETURN
53     END

```

```

^Q
SRU'S:1.8
IOFF
USAGE ON 05/07/75 AT 07:50:25
SRU'S:11.6      ELAPSED TIME: 00:23:08
GOOD BYE.

```

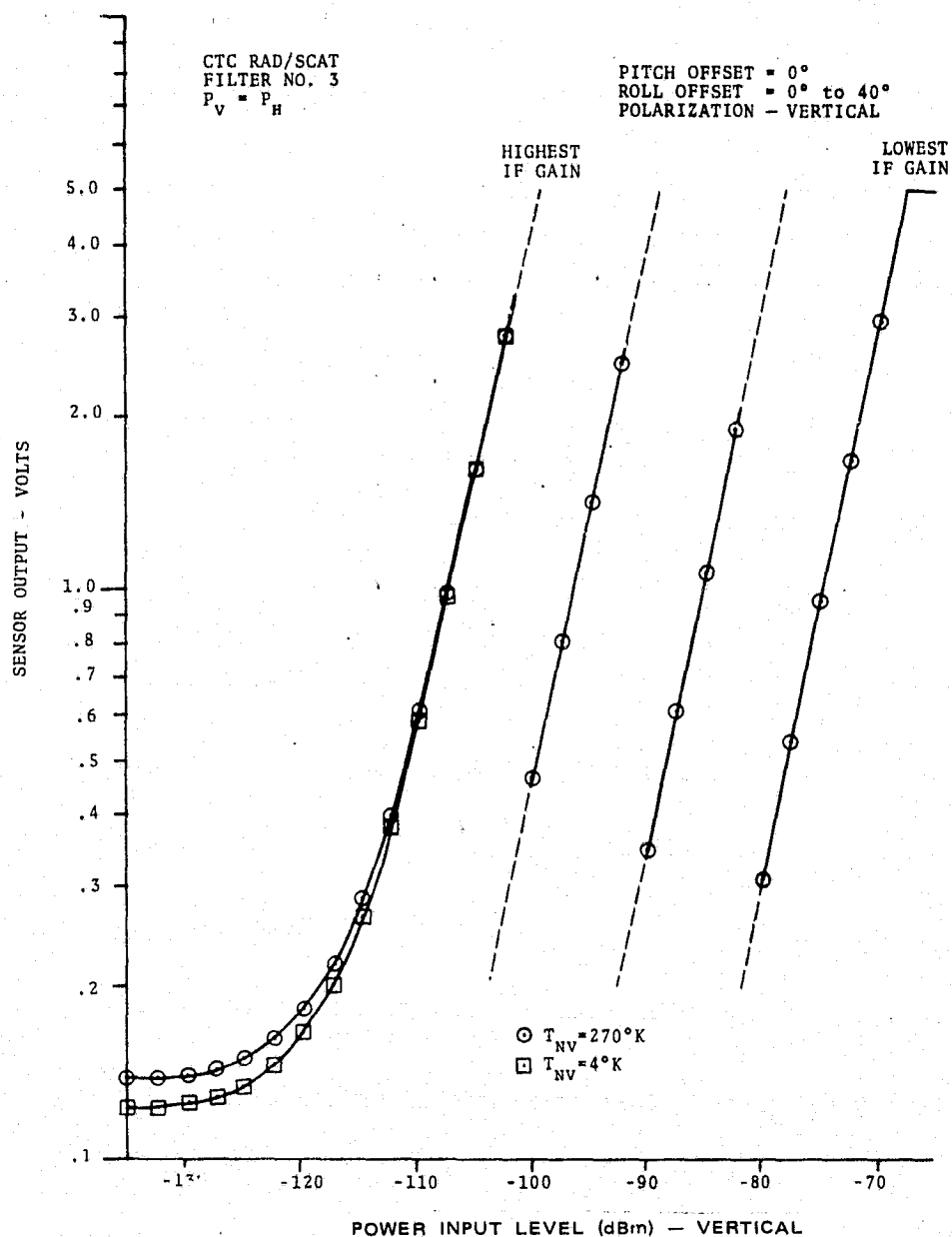


Figure A-10. - S-193 Scatterometer volts output versus power input for two radiometric antenna temperatures.

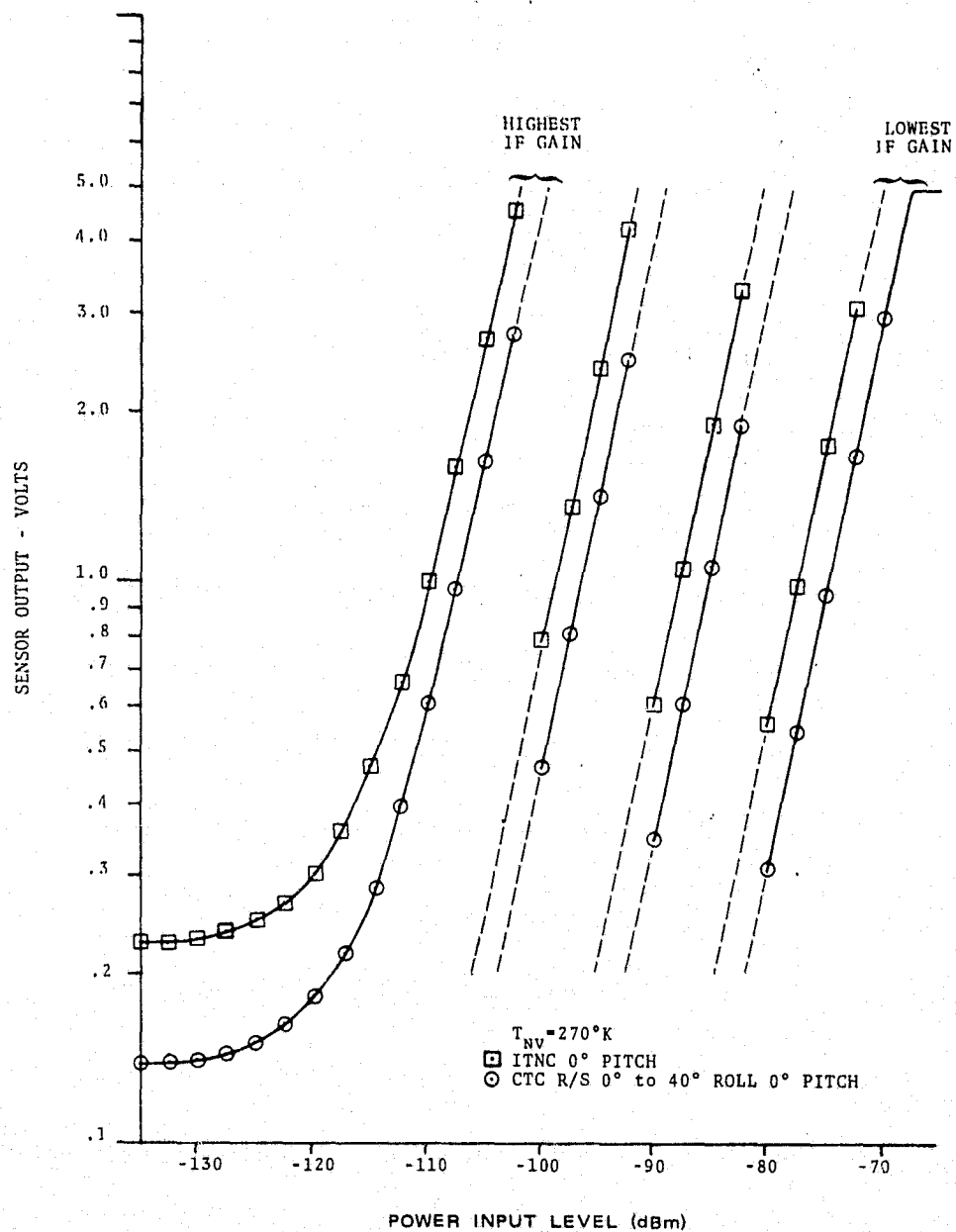


Figure A-11. — S-193 Scatterometer volts output versus power input for two modes — CTC R/S and ITNC.

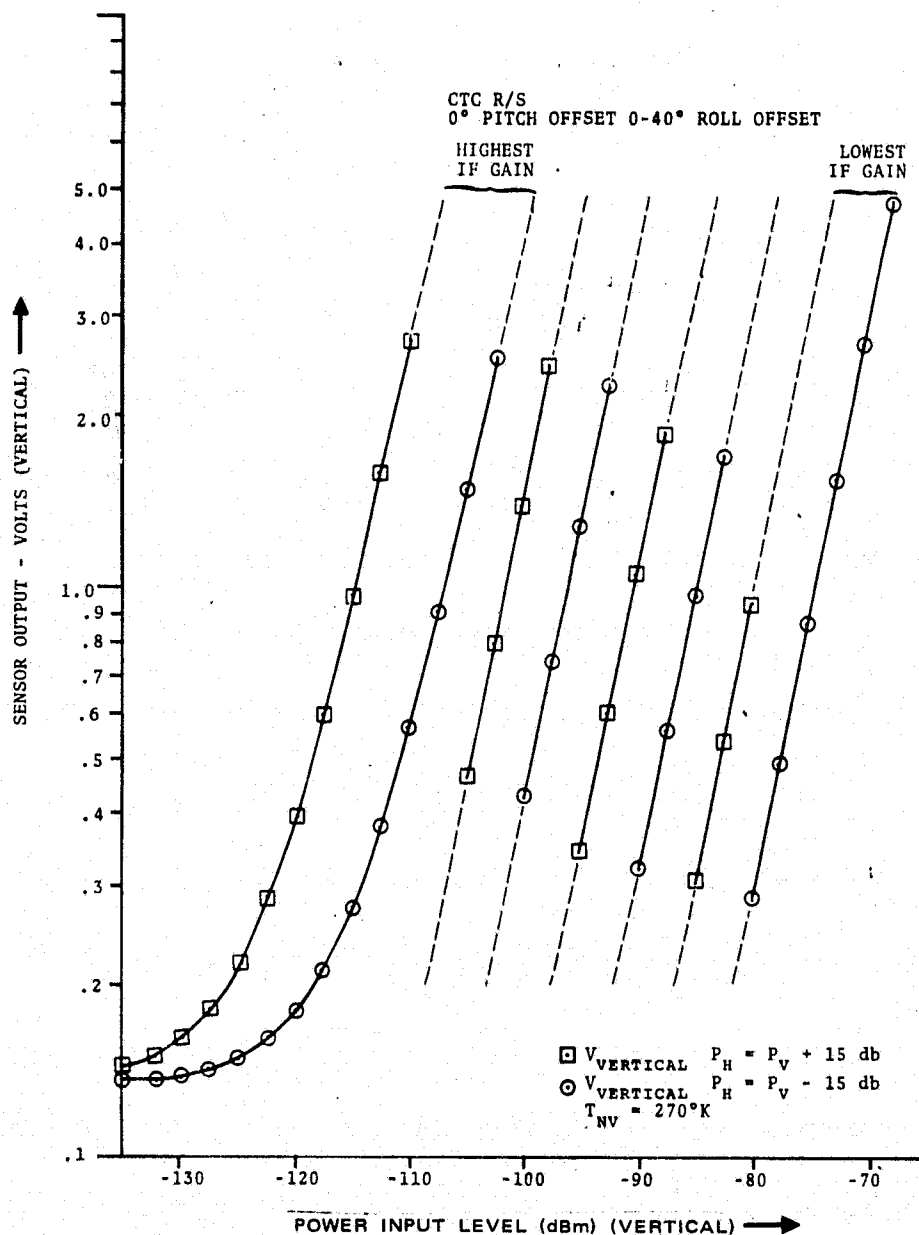


Figure A-12. — S-193 Scatterometer volts output versus power input for a difference of 15 dB between vertical and horizontal input power.



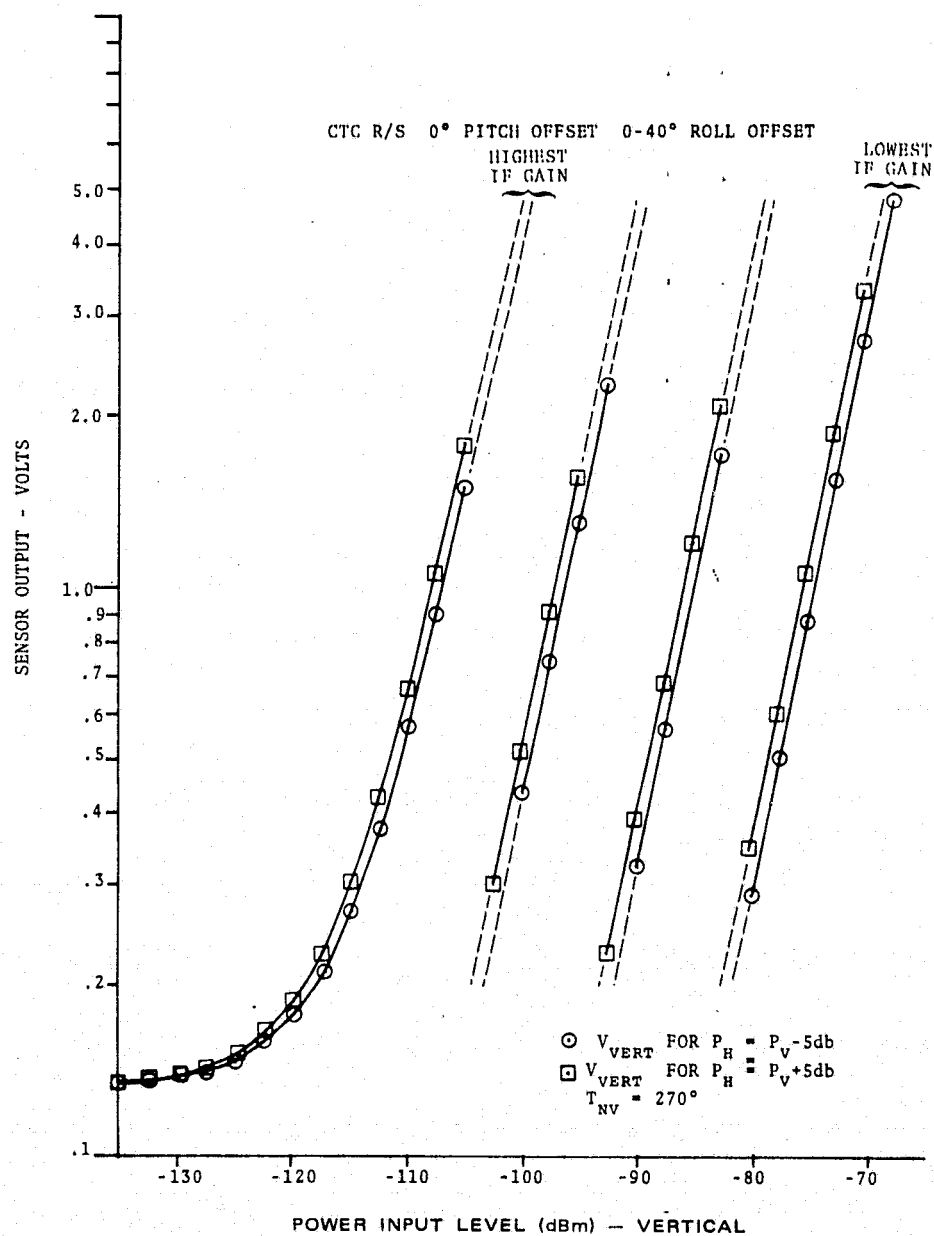


Figure A-13. - S-193 Scatterometer volts output versus power input for a difference of 5 dB between vertical and horizontal input power.

The affect of the cross-polarization leakage on the S-193 Scatterometer output is illustrated in figure A-12. The input versus output has been drawn for two cases. In the first case the vertical incoming power ( $P_V$ ) is 15 dB higher than the horizontal incoming power ( $P_H$ ). The output vertically polarized voltage is not significantly different from  $P_V = P_H$  case. The reason for this is that the leakage from horizontal is very low because of the lower magnitude of the horizontally polarized power. In the second case, the vertically polarized incoming power is 15 dB below the horizontally polarized power. Now the leakage, due to higher  $P_H$ , is significant. The vertically polarized output is the sum of two contributions - vertical incoming power and leakage from the horizontal port. This leads to an increase in the output power.

There is another way of interpreting figure A-12. For the unlikely cases where the horizontally polarized power is 15 dB above the vertically polarized power, the proper curve should be used to determine the incoming vertical power from the sensor output. If this is not done and the output is calculated using the characteristic curve where  $P_V$  is large (15 dB or more) as compared with  $P_H$ , then an error will result. This resultant error will depend upon the magnitude of the input signal. The cross-polarization assumes significance since the difference in horizontally and vertically polarized incoming power is unknown for remotely sensed rough scenes.

Serious errors can result from using one curve for the calculation of input power from the output measured voltage. It is interesting to note that the errors in estimating the

input power will decrease if the incoming vertically and horizontally polarized powers differ by a less amount which is the usual case. This is why only one set of curves has been used in the S-193 production data processing. This is illustrated in figure A-13, where  $P_V$  and  $P_H$  differ by 5 dB for each plot. In figures A-11, A-12, and A-13, the radiometer temperature of the surrounding scene was taken to be 270°K.

The scatterometer mathematical model presented in this report is not valid for the Skylab-4 (SL-4) mission. This is due to a drastic change in cross-polarization and antenna pattern. It is, however, possible to modify the present scatterometer computer model to reflect these changes.

## APPENDIX B

### DATA PROCESSING TECHNIQUES

## APPENDIX B

### DATA PROCESSING TECHNIQUES

#### 1.0 S-193 SCATTEROMETER DATA PROCESSING

##### 1.1 S-193 RADIOMETER/SCATTEROMETER PROCESSING FLOW

The first step in the Skylab-acquired data processing is to duplicate the 28-track Earth Resources Experiment Package (EREP) tape. From this tape two 14-track tapes are developed (figure B-1). These tapes contain Interrange Instrumentation Group Format A (IRIG A) time converted from the original time words on one of their tracks. One of the 14-track tapes contains the S-192 sensor data and the other contains S-190A, S-191, S-193, and S-194 sensor data. From the latter 14-track tape (the S-193 data on this tape is on a frequency modulated subcarrier), a nine-track digital S-193 Radiometer/Scatterometer tape is prepared.

This tape (also known as S061-4 product) is time edited and has data in raw pulse code modulated (PCM) counts.

From S061-4 the raw processed tape (S061-2) containing data in PCM counts is generated directly (figure B-2). Calibration data and Skylab Best Estimate of Trajectory (SKYBET) Ephemeris Data tapes are used in data processing to generate computer-compatible tapes (CCT's, S061-1), tabulations (S062-A, B, C), and plots (S063-D, 6). The output product data flow is shown in figure B-2. The detailed definition of each product is given in Earth Resources Production Processing Requirements for EREP electronic sensors document (reference 40). The production data processing program can

Figure B-1. - S-193 Radiometer/Scatterometer data processing flow.

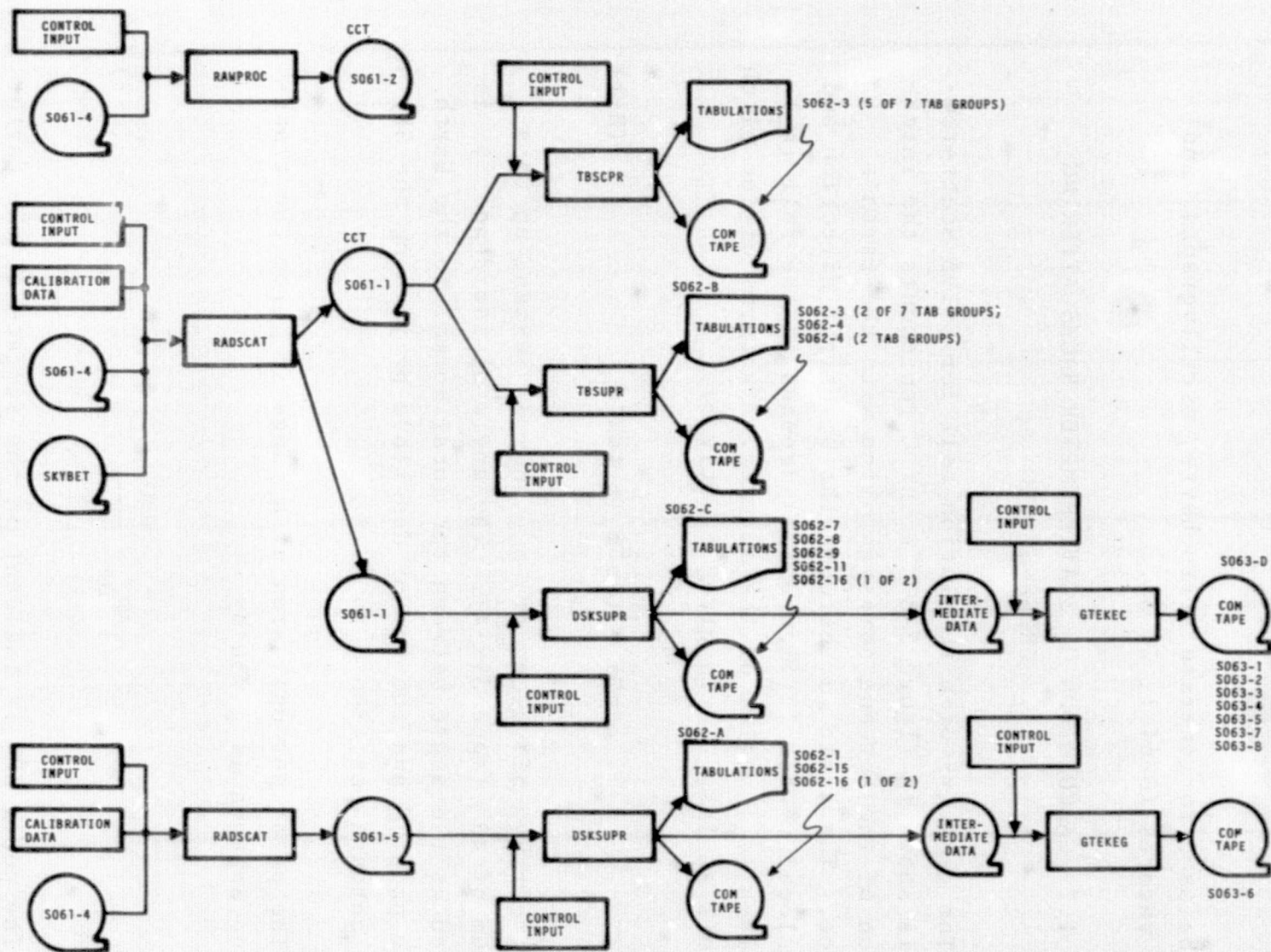


Figure B-2. — S-193 Radiometer/Scatterometer output product data flow.

also be used to generate stripcharts, oscillographs, and event records (S064-1, 2, 3).

## 1.2 CALCULATION OF SCATTEROMETER BACKSCATTERING CROSS SECTION

The geometry of a resolution cell for S-193 Scatterometer is shown in figure B-3. Point C represents the intersection of the antenna boresight line with the Earth's surface. The angle  $\alpha$  between the boresight direction and the Z-local vertical (figure B-3) depends on the roll ( $\phi_r$ ) and pitch ( $\phi_p$ ) angles of the antenna. In terms of the pitch and roll angles,  $\alpha$  is given exactly by

$$\tan^2 \alpha = \tan^2 \phi_r + \tan^2 \phi_p \quad (\text{B-1})$$

The range of values of  $\phi_r$  and  $\phi_p$  extend up to a maximum of  $48^\circ$  (appendix A). The angle of incidence  $\theta$  is defined as the angle between the local normal to the Earth at the point C and the vector described by joining the Skylab S-193 antenna position S to C.

The power per unit area at a range  $r$  from the transmitting antenna is given by

$$\Delta P_a = \frac{P_T G_t}{4\pi r^2} \quad (\text{B-2})$$

The power  $\Delta P_a$  is incident on the surface of the Earth.  $P_T$  is the power radiated by the transmitting antenna in watts,



B-5

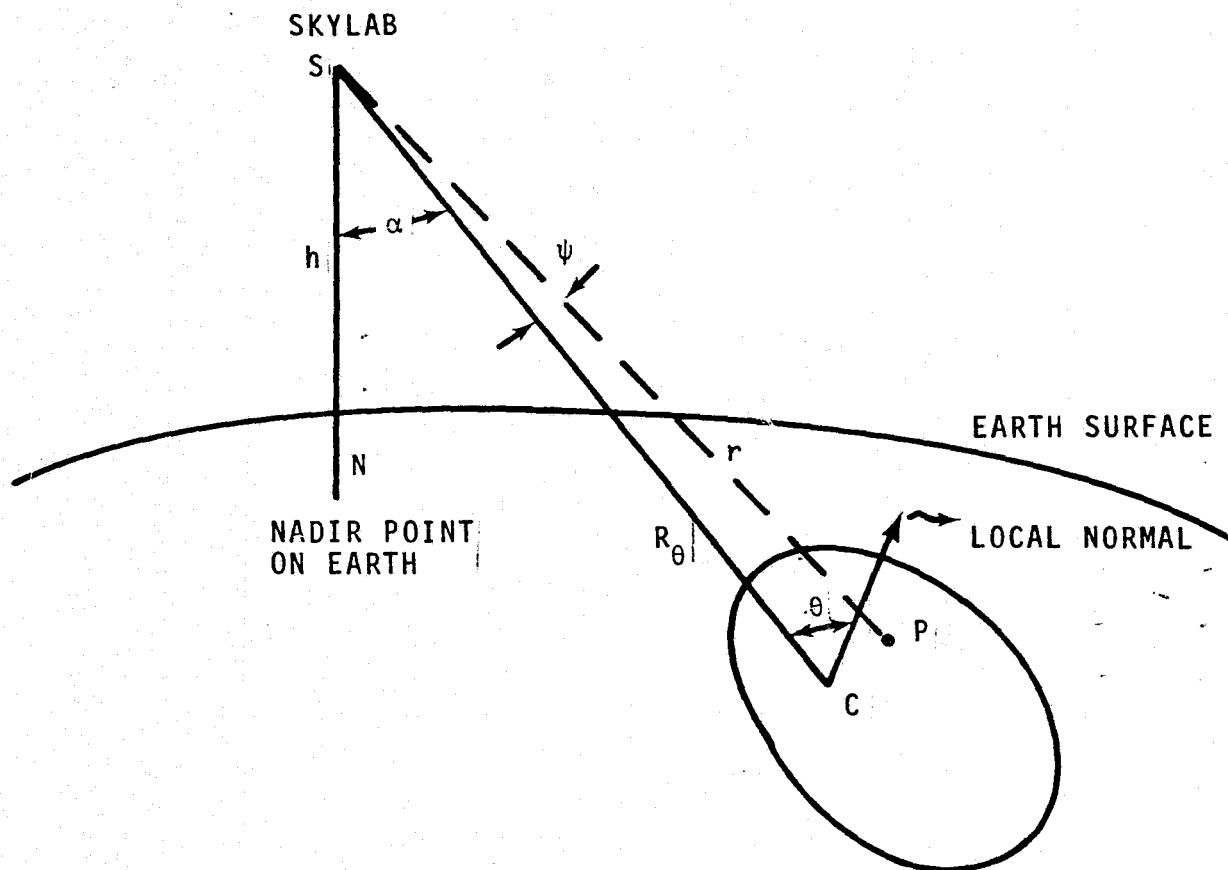


Figure B-3. — S-193 Scatterometer resolution cell geometry.

and  $G_T$  is the gain of the antenna in the direction of the resolution cell. This incident power is scattered in the space surrounding the resolution cell. The scattered power at the surface can be expressed as

$$\Delta P_s = \Delta P_a \cdot \sigma_o \quad (B-3)$$

where  $\sigma_o$  is the scattering cross section of the surface per unit area.  $\Delta P_s$  travels back to the receiving antenna (this can be the same as transmitting antenna but polarization of reception may be different). The power per unit area at the receiver is given by

$$\Delta P_{ar} = \frac{\Delta P_s}{4\pi r^2} \quad (B-4)$$

The receiving antenna has an effective receiving aperture or effective area  $A_r$ . Thus, the received power from a unit surface area is

$$\Delta P_r = \frac{\Delta P_s}{4\pi r^2} \cdot A_r \quad (B-5)$$

Combining equations (B-2) through (B-5), the power received as a result of scattering from unit surface is

$$\Delta P_r = \left( \frac{P_T G_t}{4\pi r^2} \right) \sigma_o \left( \frac{A_r}{4\pi r^2} \right)$$

The S-193 Scatterometer operates essentially in a continuous wave (CW) mode. The carrier frequency of 13.9 GHz is pulse modulated (125 pps) with a 62.5 percent duty cycle. This assures small modulation sidebands and the transmitter wavelength ( $\lambda$ ) can be assumed a constant.

The receiving antenna aperture is given by

$$A_r = \frac{\lambda^2 G_r}{4\pi} \quad (B-6)$$

where  $G_r$  is the gain of the receiving antenna. From equations (B-5) and (B-6)

$$\Delta P_r = \frac{P_T \sigma_o G_t G_r}{(4\pi)^3 r^4} \quad (B-7)$$

The total power received ( $P_R$ ) from an illuminated area can be calculated from equation (B-7) by integrating over the reflecting area:

$$P_R = \frac{P_T \lambda^2}{(4\pi)^3} \int_A \frac{G_t G_r \sigma_o}{r^4} dA \quad (B-8)$$

where  $dA$  is the element of the reflecting area.

In evaluating (B-8) two approximations can be made:

- For the ground scenes considered in this report,  $\sigma_o$  can be considered a constant over the area  $A$ .

- The error caused by assuming  $r = R_\theta$  over a resolution cell for  $\alpha = 48^\circ$ , will amount to an error of 0.02 dB in the value of  $P_R$  (or  $\sigma_o$ ).

With the preceding assumptions the radar backscattering cross section is given by (reference 3):

$$\sigma_o(\theta_1, \phi_1) = \frac{(4\pi)^3 \cdot R_\theta^4}{\lambda^2} \cdot (L_1 L_2) \frac{P_R}{P_T} \frac{1}{\int_A G_o^2(\theta_1, \phi_1) f(\theta, \phi) dA}$$

(B-9)

where

$L_1, L_2$  = path losses through intervening medium for transmission and reception

$G_o(\theta_1, \phi_1)$  = one way antenna gain in the direction of the antenna boresight

$f(\theta, \phi)$  = two-way antenna gain pattern in any direction ( $\psi$ ) (figure B-3) specified by angles  $\theta$  and  $\phi$ .

The value of  $\sigma_o$  is to be related to the surface parameters of the remotely sensed scene. For this purpose the location of the field-of-view (FOV) has been calculated for each value of  $\sigma_o$ . The details of this calculation are given in Earth Resources Production Processing Requirements for ERPP Electronic Sensors document (reference 40). The values of  $R$  and the local angle of incidence  $\theta$  are also calculated using the FOV program and the SKYBET tape.

The approximate value of the antenna pattern integral in equation (B-9) is given by (reference 54):

$$\int G_O^2(\theta_1, \phi_1) f(\theta, \phi) da = G_O^2 I_O H_O^2 R^2 \sec \alpha \quad (B-10)$$

In equation (B-10),  $H_O$  is the nominal altitude of the Skylab (taken as 435 kilometers for calculating  $I_O$ ).  $G_O$  is the gain of the S-193 antenna. Equation (B-10) assumes a pencil beam antenna. The University of Kansas has performed integrations for the antenna pattern equation (B-10). These values are dependent on the receiving and transmitting polarization states of the antenna. For SL-2 and SL-3, the values of  $I_C = G_O^2 I_O H_O^2$  are shown below:

<u>Transmitting antenna polarization</u>	<u>Receiving antenna polarization</u>	<u><math>I_C</math></u>
V	V	$6.778 \times 10^4$
H	H	$7.146 \times 10^4$
V	H	$6.745 \times 10^4$
H	V	$6.745 \times 10^4$

The ratio of  $(P_R/P_T)$  is a function of the sensor operating modes and sensor output voltages. This ratio is given by:

$$\frac{P_R}{P_T} = \frac{K_C}{K_R K_T} \left[ \frac{(IT)_C}{(IT)_S} \times \frac{(TC)_S}{(TC)_C} \times \frac{F_C}{F_S} \times \frac{G_C}{G_S} \right] AC \text{ (DF)}$$

$$\times \left\{ \frac{V'_S - V'_N \left[ \frac{(IT)_S}{(IT)_N} \times \frac{(TC)_N}{(TC)_S} \times \frac{F_S}{F_N} \times \frac{G_S}{G_N} \right]}{V'_C} \right\} \quad (B-11)$$

In equation (B-11),

- $K_C$  = scatterometer calibration path attenuation
- $K_R$  = loss unique to the receive path
- $K_T$  = loss unique to the transmit path
- IT = integration time with subscripts S, N, C to denote signal and noise, noise, or calibrate, respectively (mode, gain, and angle dependent)
- TC = integration time constant with subscripts S, N, C to denote signal and noise, noise, or calibrate, respectively (mode and angle dependent)
- $G_S, G_N, G_C$  = scatterometer gain for signal, noise, calibrate, respectively
- $F_S, F_N, F_C$  = scatterometer filter gain for signal, noise, calibrate, respectively (filter, gain, pitch angle, and  $T_{IP}$  dependent)
- AC(DF) = angle correction to account for filter attenuation encountered in ITC mode at 48° angle for the LCF filter because the antenna only achieved 43°. For all other modes and/or angles, AC = 1. At 48° ITC:

$$AC = \text{antilog}_{10} [a_0 + a_1 DF + a_2 DF^2 + a_3 DF^3 + a_4 DF^4 + a_5 DF^5] \quad \text{for} \quad 0.44 < DF < 0.48 \text{ MHz}$$

$$AC = 1 \text{ for } DF \geq 0.48 \text{ MHz}$$

No calculation is made for  $DF < 0.44$  MHz or for MCF or HCF filters.

$$a_0 = 693762.396$$

$$a_1 = -7550134.85$$

$$a_2 = 32845532.2$$

$$a_3 = -71395735.3$$

$$a_4 = 77541217.8$$

$$a_5 = -33662017.0$$

DF = Doppler frequency

$$V'_S = V_S - [q(T_{IP}) \times IT_S/TC_S] - [IT_S \times \text{drift}]$$

$$V'_S = V_N - [q(T_{IP}) \times IT_N/TC_N] - [IT_N \times \text{drift}]$$

$$V'_C = V_C - [q(T_{IP}) \times IT_C/TC_C] - [IT_C \times \text{drift}]$$

$T_{IP}$  = internal processor temperature A012-193

$q$  = scatterometer voltage correction constant  
(filter, gain, and time constant dependent)

$V_S$  = measured signal plus noise voltage

$V_N$  = measured noise voltage (the next value following  $V_S$  for ITC mode, for other modes polarization and command angle of  $V_N$  must match  $V_S$  )

$V_C$  = measured calibrate voltage\* (scatterometer calibration 1 or 2 is used, depending on which has the greater  $V'_C/F_C$  ratio)

drift = integrator drift correction, a function of the time constant and filter

The values of the parameters  $K_C$ ,  $K_R$ ,  $K_T$ ,  $(IT)_S$ ,  $(IT)_N$ ,  $(IT)_C$ ,  $(TC)_S$ ,  $(TC)_N$ ,  $(TC)_C$ , drift,  $q$ ,  $G_S$ ,  $G_N$ ,  $G_C$ ,  $F_S$ ,  $F_N$ , and  $F_C$  are given in EREP Calibration Data document (reference 55). The voltage values of  $V_S$ ,  $V_N$ , and  $V_C$  are contained in the measurements A063-193 and A064-193 depending on the scatterometer status.

Relative voltages are also computed for the three components signal, noise, and calibration as follows:

$$V''_S = (V'_S/G_S) \times [(TC)_S/(IT)_S]$$

$$V''_N = (V'_N/G_N) \times [(TC)_N/(IT)_N]$$

$$V''_C = [V'_C/G_C] \times [(TC)_C \times (IT)_C]$$

### 1.3 TIME TAGGING AND DATA SEQUENCE

The S-193 Scatterometer operates in several scanning modes and submodes. Details of these modes are given in appendix A. During each scan, data is recorded in a particular sequence depending on the mode chosen. The integration times depend on the mode. The raw data products (processed using

---

\*Can be entered by control data.



NASA/Data Systems and Analysis Division (DSAD) computer program) tabulate the data in the same order as the acquisition sequence. The times have been properly scaled from Airlock Module Time (AMT) to GMT. The time used in the raw data products will henceforth be called the Data Stream Time (DST). In equation (B-11) proper values of  $V_N$  are to be subtracted from  $V_S$ . For instance, if the receive polarization is vertical, noise corresponding to the vertical receive channel following the signal should be used for  $V_N$ . The production processing program has been developed on the basis of one pass processing. Consequently, the sequence in which the computations are done are not the same as the data acquisition sequence. However, the tabulated scatterometer data in product S062-11, reflects actual data acquisition times.

When relating a particular measurement to the ground scene, it is necessary that the coordinates of the illuminated area be calculated at the time the measurement was taken. A study showed that corrections had to be done to arrive at the center of the measurement time (CMT). Since each scatterometer measurement is collected for a finite period of time,  $CMT(t_m)$  should represent the center of this period, accurate to a 3-sigma confidence limit of 9 milliseconds;

$$t_m = t_s - \Delta t$$

where

$t_s$  = starting time of the measurement

$\Delta t$  = half of the data collection period

For ITNC and CTNC radiometer measurements:

$\Delta t = 130$  msec for  $48.0^\circ$  and  $40.1^\circ$  command angles

$\Delta t = 66$  msec for  $29.4^\circ$  and  $15.6^\circ$  command angles

$\Delta t = 31$  msec at  $0.0^\circ$  command angle

For ITNC and CTNC scatterometer measurements:

$\Delta t = 4 \times (N - G)$  msec

G = scatterometer gain setting number (D005A193)

N = 74 for command angle  $48.0^\circ$

N = 64 for command angle  $40.1^\circ$

N = 57 for command angle  $29.4^\circ$

N = 39 for command angle  $15.6^\circ$

N = 23 for command angle  $0.0^\circ$

For ITC radiometer measurements:

$\Delta t = 18$  msec

For ITC scatterometer measurements:

$\Delta t = 4 \times (9 - G)$  msec

For CTC radiometer measurements:

$\Delta t = 18$  msec for radiometer/scatterometer

$\Delta t = 31$  msec for radiometer only

For CTC scatterometer measurements:

$$\Delta t = 4 \times (N - G) \text{ msec}$$

N = 14 for radiometer/scatterometer

N = 11 for scatterometer only

Data products S062-7, S062-11, S062-16 tab group two, S063-1, S063-2, S063-3, S063-4, S063-5, S063-7, and S063-8 have  $t_m$  on them. All other products have  $t_s$ . Product S061-1 also has the difference  $t_s - t_m$  used for each FOV calculation.

The times given for the statistical data products are the times of the first measurement of the sample to be averaged. The angles and other data given on the "averaged scattering cross section" tabulations are the average value of the samples.

#### 1.4 TABULATED ANGLES FOR SCATTEROMETER DATA

A particular S-193 measurement is taken for a finite amount of time. This time depends on the mode, type of data (radiometer or scatterometer), and roll/pitch angles. In ITC and CTC mode the antenna angles are varying during the measurement period. Before an accurate FOV calculation can be made for these modes, roll and pitch angles were interpolated to the corrected data measurement time ( $t_m$ ). The corrected roll/pitch angles ( $A_m$ ) were computed by using the equation (reference 40):

$$A_m = A - (A' - A) (\Delta t) / (t_s' - t_s)$$

for  $|A' - A| < 3^\circ$

where

$A_m$  = corrected roll/pitch

$A$  = uncorrected roll/pitch

$A'$  = previous uncorrected roll/pitch

$\Delta t$  = see paragraph 1.3

$t_s$  = uncorrected roll/pitch time

$t'_s$  = previous uncorrected roll/pitch time

The angles given in this report are the corrected angles  $A_m$  and corresponding angles of incidence.

### 1.5 POLARIZATION LABEL

The polarization labels applied to the production processed data are the same as the data stream. These labels do not follow the normal convention in some modes. In literature, the polarization is defined by the scattering geometry. The polarization labels for intrack modes (no roll), are correct. The crosstrack (zero pitch) polarizations should be relabeled so that vertical (V) is changed to horizontal (H). In other modes where neither pitch nor roll is zero (for example, cross-track contiguous mode with  $15.0^\circ$ ) care must be exercised in interpreting the data. In the analysis presented in this report normal polarization convention has been followed. The polarization labels given in the production-processed data have been properly interpreted in the comparisons with theoretical values of backscattering cross sections.

## 1.6 CORRECTION FOR 48° ITC SCATTEROMETER DATA

The actual maximum attained angle for the ITC mode is approximately 43° instead of 48°. The sharp Doppler filter characteristic curve introduces large errors for the actual angle attained. These errors have been removed by involving proper correction [AC(DF)] factors in the production data processing program. The procedure for correcting data involves calculating the Doppler frequency using SKYBET data corresponding to the attained angle. The attenuation due to the Doppler filter was determined by interpolating the filter characteristics. The scatterometer backscattering data was then corrected for filter attenuation. The data analyzed in this report has been corrected for the effects of Doppler filter attenuation.

## 1.7 MISCELLANEOUS SCATTEROMETER DATA PROCESSING REMARKS

For the field-of-view calculations the SKYBET tape computations assume a "perfect Z-local vertical" vehicle attitude whenever this data was not available.

The accuracy of the EREP pointing has been determined to be 0.7° per axis  $3\sigma$  ( $\sigma$  is the standard deviation).

There are some data dropouts in the S-193 production-processed data products. Wherever it was important for Sensor Performance Evaluation, the raw data was used to calculate the scattering cross sections.

Calibration data used in the S-193 data processing was taken from the S-193 acceptance test data. The range of

temperatures used during these tests were not as wide as were encountered during the Skylab data takes. Interpolations and extrapolations were done to obtain the values for the temperature-dependent variables. The effect of these is not serious since ratios are used in the computation of  $\sigma_0$ .

The antenna scan performance differed from that before launch. The integration times could also be different from those given as a result of the system acceptance test. For the case when no signal was received (deep space), the average signal plus noise power density when equated to the average noise power density yielded a set of noise integration times slightly different from those given in the acceptance test data. Details of the scan performance and noise analysis are given in S-193 Sensor Performance Report (reference 32). The integration times for the noise were revised to reflect the new values as recommended in reference 32.

The backscattering cross section is reported in decibels (dB) relative to 1. After the value of  $\sigma_0$  is computed using equation (B-9), the output value from production data processing is

$$\sigma_0 \text{ (dB)} = 10 \log_{10} \sigma_0$$

The value is computed by calculating the average value of  $\sigma_0$  and converting this to decibels.

At the end of a S-193 Radiometer/Scatterometer data take, the scatterometer is switched to standby (STBY) position.

In this configuration, the transmitter is shut off and the receiver is still on. The radiometer is switched to STBY (standby) approximately 2 seconds later. The scatterometer data during its STBY operation at the end of a radiometer/scatterometer is invalid, since no valid signal is received. The average values of  $\sigma_0$  reported for such data takes is also in error. For this reason, average values of  $\sigma_0$  were computed using valid data avoiding also the use of default values in such a computation.

The data processing equations used in production data processing program assumes a linear model for the sensor. The acceptance test data (reference 55) shows that for power received by the antenna in excess of -70 dBm and less than -115 dBm the system is nonlinear.

## 2.0 AIRCRAFT DATA PROCESSING

NASA/JSC, 13.3 GHz scatterometer underflight data was acquired during the SL-2 mission. This data will be used for comparison with spacecraft-acquired data.

The 13.3 GHz scatterometer is a continuous-wave Doppler radar system, designed to measure reflectivity per unit area as a function of the angle of incidence ( $\theta$ ). The scatterometer antenna illuminates a fan-shaped area (approximately  $120^\circ$  along the aircraft flightpath), and the data is gathered for vertical-transmit, vertical-receive polarization states only. As a result of the forward motion of the aircraft, Doppler frequency shifts are introduced and the signal returned

by a ground resolution cell can be retrieved by bandpass filtering at the corresponding Doppler frequencies (figure B-4). The returned energy may be separated using the Doppler equation as a function of incidence angle

$$f_D = \frac{2V_A}{\lambda} \sin \theta \quad (B-12)$$

where

$f_D$  = Doppler frequency

$V_A$  = aircraft ground velocity

$\lambda$  = wavelength of the transmitted power

$\theta$  = angle of incidence

The returned energy is received from all angles of incidence simultaneously and is divided equally into two channels, one of which is 90° out of phase with the other. The data for each channel, detected by a direct-rf-to-audio conversion technique, is amplified and recorded on an FM tape recorder. The fore-and-aft beam data are separated by use of a sign sensing technique (reference 56). To calibrate the system, a ferrite modulator is used to provide an absolute power reference level of the transmitted signal. The  $\sigma_0$  versus  $\theta$  information is obtained by subtracting known system losses and aircraft attitude and velocity factors and comparing the remainder with a reference signal level.

The radar cross section per unit area is given by the equation



$$\sigma_o(\theta) = \frac{P_R}{P_T} \frac{2(4\pi)^3}{\lambda^3} \frac{Vh^2}{\Delta f_D} \frac{1}{\int_{-\psi_1}^{\psi_2} G_T(\psi)_\theta G_{R_\theta}(\psi) d\psi}$$

(B-13)

where

$P_T$  = transmitted power

$P_R$  = power received in the Doppler window defined by  $\Delta f_D$

$G_T, G_R$  = transmitting antenna and receiving antenna gain, respectively, as a function of  $\theta$  (incidence angle) and  $\psi$  (crosstrack angle)

$h$  = altitude of the aircraft

$\psi$  = crosstrack angle (figure B-4)

Equation (B-13) may be rearranged for computer calculations as

$$\begin{aligned} \sigma_o(\theta) = & RC + 20 \log h + 10 \log V + 20 \log \frac{E_i}{E_r} \\ & + 10 \log \frac{BW_R}{BW_i} + R(D) - G_O^2 F'(\theta) + Z(\theta) \end{aligned}$$

(B-14)

where

$RC$  = radar offset constant

$h$  = aircraft height

$E_i$  = average radar data at  $i$ th filter

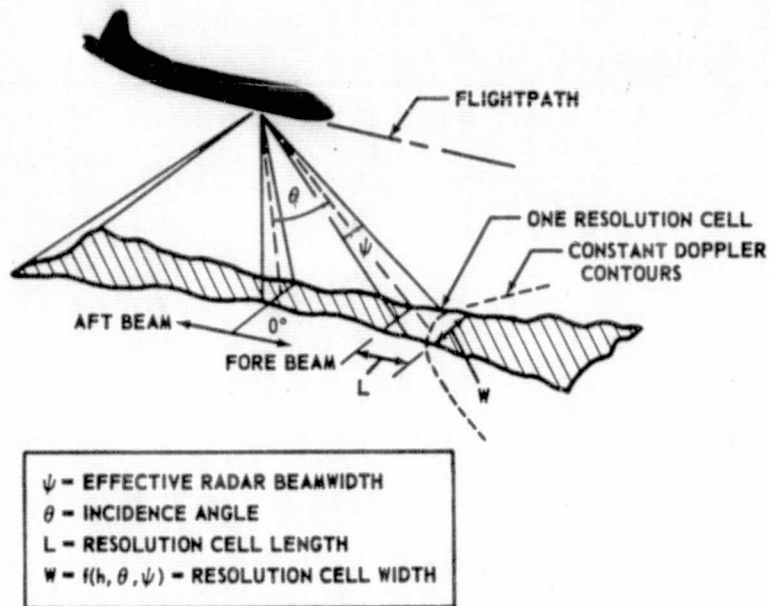


Figure B-4. — 13.3 GHz scatterometer resolution cell geometry.

$E_r$  = average reference data  
 $BW_i$  = bandwidth of  $i$ th filter  
 $R(D)$  = system rolloff  
 $Z(\theta)$  = any system errors which can be determined  
 $G_O^2 F'(\theta)$  = two-way antenna gain  
 $BW_R$  = reference bandwidth

The radar offset constant RC is computed from the following equation

$$RC = 10 \log_{10} 2(4\pi)^3 + FMC - 10 \log_{10} P_T - 30 \log_{10} \lambda$$

where

FMC = ferrite modulator constant

A detailed description of the program can be found in reference 56. The calibration data and detailed evaluation of the 13.3 GHz scatterometer system is given in reference 57.